

RL-TR-96-80
Final Technical Report
June 1996



SILICON OPTOELECTRONICS

Massachusetts Institute of Technology

Sponsored by
Advanced Research Projects Agency

APPROVED FOR PUBLIC RELEASE; DISTRIBUTION UNLIMITED.

The views and conclusions contained in this document are those of the authors and should not be interpreted as necessarily representing the official policies, either expressed or implied, of the Advanced Research Projects Agency or the U.S. Government.

19960807 052

Rome Laboratory
Air Force Materiel Command
Rome, New York

DECLASSIFIED

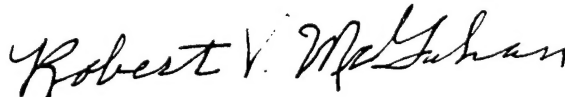
RL-TR- 96-80 has been reviewed and is approved for publication.

APPROVED:



DR. RICHARD A. SOREF
Project Engineer

FOR THE COMMANDER:



DR. ROBERT V. MCGAHAN
Director
Electromagnetics & Reliability Directorate

DESTRUCTION NOTICE - For classified documents, follow the procedures in DOD 5200.22M, Industrial Security Manual or DOD 5200.1-R, Information Security Program Regulation. For unclassified limited documents, destroy by any method that will prevent disclosure of contents or reconstruction of the document.

If your address has changed or if you wish to be removed from the Rome Laboratory mailing list, or if the addressee is no longer employed by your organization, please notify Rome Laboratory/ (EROC), Rome NY 13441. This will assist us in maintaining a current mailing list.

Do not return copies of this report unless contractual obligations or notices on a specific document require that it be returned.

SILICON OPTOELECTRONICS

Prof. L.C. Kimerling

Contractor: Massachusetts Institute of Technology
Contract Number: F19628-92-K-0012
Effective Date of Contract: 20 May 1992
Contract Expiration Date: 20 September 1995
Short Title of Work: Silicon Optoelectronics

Period of Work Covered: May 92 - Dec 95

Principal Investigator: Prof. L.C. Kimerling
Phone: (617) 253-5383

RL Project Engineer: Dr. Richard A. Soref
Phone: (617) 377-2380

Approved for public release; distribution unlimited.

This research was supported by the Advanced Research
Projects Agency of the Department of Defense and was
monitored by Dr. Richard A. Soref, RL/EROC,
80 Scott Drive, Hanscom AFB MA 01731-2909.

REPORT DOCUMENTATION PAGE			Form Approved OMB No. 0704-0188	
<small>Public reporting burden for this collection of information is estimated to average 1 hour per response, including the time for reviewing instructions, searching existing data sources, gathering and maintaining the data needed, and completing and reviewing the collection of information. Send comments regarding this burden estimate or any other aspect of this collection of information, including suggestions for reducing this burden, to Washington Headquarters Services, Directorate for Information Operations and Reports, 1215 Jefferson Davis Highway, Suite 1204, Arlington, VA 22202-4302, and to the Office of Management and Budget, Paperwork Reduction Project (0704-0188), Washington, DC 20503.</small>				
1. AGENCY USE ONLY (Leave Blank)		2. REPORT DATE June 1996		3. REPORT TYPE AND DATES COVERED Final May 92 - Dec 95
4. TITLE AND SUBTITLE SILICON OPTOELECTRONICS			5. FUNDING NUMBERS C - F19628-92-K-0012 PE - 61102F PR - 2305 TA - D2 WU - 10	
6. AUTHOR(S) Prof. L.C. Kimerling				
7. PERFORMING ORGANIZATION NAME(S) AND ADDRESS(ES) Massachusetts Institute of Technology Materials Science and Engineering Department 77 Massachusetts Avenue Cambridge MA 02139			8. PERFORMING ORGANIZATION REPORT NUMBER N/A	
9. SPONSORING/MONITORING AGENCY NAME(S) AND ADDRESS(ES) Advanced Research Projects Agency 3701 North Fairfax Drive Arlington VA 22203-1714			10. SPONSORING/MONITORING AGENCY REPORT NUMBER RL-TR-96-80	
Rome Laboratory/EROC 80 Scott Drive Hanscom AFB MA 01731-2909				
11. SUPPLEMENTARY NOTES Rome Laboratory Project Engineer: Dr. Richard A. Soref/EROC/(617) 377-2380				
12a. DISTRIBUTION/AVAILABILITY STATEMENT Approved for public release; distribution unlimited.			12b. DISTRIBUTION CODE	
13. ABSTRACT (Maximum 200 words) This silicon optoelectronics program is the first comprehensive investigation of a silicon compatible, optical interconnection technology. The objective of the program is to establish processes, compatible with integrated circuit fabrication, for the integration of photonic interconnection with silicon electronics. The diffusivity and the solubility of Er in silicon was measured and the Er-Si-O ternary phase diagram was determined. Split lot test structures confirmed that Er did not cross-contaminate adjacent wafer locations or adjacent wafers in the same lot. The contractor designed, fabricated, and tested the first Si:Er LED with sharp line electroluminescence at 1.54 microns, operating at 300K. To model device performance, the contractor developed a global theory of Er excitation by minority carrier recombination, and monolithically integrated Si:Er LEDs with waveguides and drive electronics to demonstrate the optical and electronic compatibility of Silicon Optoelectronics. The high index contrasts of Si/SiO ₂ provided excellent coupling efficiency with low optical loss on SOI (silicon-on-insulator) substrates. The best LED internal quantum efficiencies ranged from 1-5%. The 3 dB modulation rate cutoff for the LED/MOSFET structure was 25 kHz. An optical test bench to measure waveguide losses by the cut-back techniques was developed. Waveguides with world record, low loss of 35 dB/cm were fabricated by control of polycrystalline Si (see reverse)				
14. SUBJECT TERMS Silicon, Erbium, Light emitting diodes, Optical waveguides			15. NUMBER OF PAGES 172	
			16. PRICE CODE	
17. SECURITY CLASSIFICATION OF REPORT UNCLASSIFIED	18. SECURITY CLASSIFICATION OF THIS PAGE UNCLASSIFIED	19. SECURITY CLASSIFICATION OF ABSTRACT UNCLASSIFIED	20. LIMITATION OF ABSTRACT UL	

13. (Cont'd)

deposition conditions and surface roughness. This highly successful program has provided a foundation of Silicon Optoelectronics as a low-cost, high-bandwidth solution for quiet communications and interconnection.

Contents

1	Executive Summary	9
2	Diffusivity and Solubility of Er in Si	12
2.1	Introduction	12
2.2	Experimental	13
2.3	Silicon:erbium reactivity	14
2.4	Erbium diffusivity and solubility	18
2.5	Conclusion	24
3	Excitation and De-excitation Processes	27
3.1	Introduction	27
3.1.1	General	27
3.1.2	Energy flow for recombination at rare earth centers in semiconductors	28
3.2	Experimental	30
3.3	Efficiency of Electroluminescence of Er in Si	30
3.4	Results	31
3.4.1	Dependence of emission intensity on temperature and pumping power	31
3.4.2	Electroluminescence decay curves	34
3.4.3	Energy back transfer by the impurity Auger effect via excess carriers	40
3.4.4	Energy back transfer by the impurity Auger effect via equilibrium free carriers	45
3.4.5	Evidence for a second back transfer process	47
3.5	Conclusion	49
4	Electronic Structure of Erbium Centers in Silicon	52
4.1	Introduction	52
4.2	Results and Discussion	53
5	Optical Activity of Erbium-Doped Silicon	59
5.1	Introduction	59
5.2	Experiment	61
5.3	Si:Er with Oxygen Co-implantation	61

5.4	Si:Er with F Co-implantation	66
5.5	Si:Er Process Simulation	78
5.5.1	Si:Er Process Model	79
5.5.2	Results and Discussion	82
6	4.5 MeV Discrete Si:Er LED	93
6.1	Introduction	93
6.2	Qualification of Er-Doped Si for IC Fab	93
6.3	First room-temperature LED	94
6.4	Si:Er LED Design and Fabrication	99
6.4.1	Design	99
6.4.2	Fabrication	101
6.5	Electrical Characterization	105
6.6	Optical Characterization	108
6.6.1	Electroluminescence and Photoluminescence	108
6.6.2	Quantum Efficiency	112
6.6.3	Junction Profile	115
6.6.4	Substrate Concentration	120
6.7	Summary	121
7	Si:Er LED Integration	124
7.1	Introduction	124
7.2	Process Design	124
7.3	CMOS Fabrication	125
7.4	Electrical Characterization	128
7.5	Optical Characterization	128
7.6	Summary	141
8	UHV-CVD Reactor	143
8.1	Introduction	143
8.2	Description of System	144
8.3	Safety Features	145
8.4	Growth of Si and Si _{1-x} Ge _x Films	147
8.4.1	Silicon Films	147
8.4.2	Si _{1-x} Ge _x Films	147
9	Polysilicon Waveguides for Optoelectronics Integrated Circuits	151
9.1	Introduction	151
9.2	Experimental Methods	152
9.3	Results	153
A	Papers and Talks	159
A.1	Papers	159
A.2	Talks	160

List of Figures

2.1	X-ray diffraction phase identification of Er_3Si_5 , Er_2O_3 , and ErN , formed by reacting erbium and silicon in vacuum, O_2 , and N_2	15
2.2	SEM image of cross section of vicinal Si (111) surface, heat treated at 1165C for 24h under Er vapor. The bottom graph illustrates the observed terrace structure of the 4° miscut Si (111) surface.	15
2.3	Proposed ternary phase diagram of the Er-Si-O system between 450C and 1100C. Two ternary phases on the Er_2O_3 and SiO_2SiO_2 tie line are Er_2SiO_5 and $Er_2Si_2O_7$	17
2.4	Comparison of Er^{3+} photoluminescence spectra in Si:Er and Er_2O_3 . .	18
2.5	SIMS depth profiles of Si:Er before and after diffusion annealing at 1300C for 1h. The dotted line represents an expected normal diffusion profile.	19
2.6	Equilibrium solubility limit of Er in Si at different annealing temperatures.	21
2.7	Precipitation density of Si:Er for a 900C, 30 min anneal vs. Er peak concentration. The line shows a fit using homogeneous nucleation theory.	22
2.8	Diffusivity of Er in Si determined by SIMS and precipitation formation.	23
2.9	Comparison of the experimental migration energy E_m with ΔU_{el} calculated using the elastic energy model for Er and 3d transition metal atoms. Data for 3d transition metal atoms are taken from Utzig . . .	23
3.1	(a) Excitation and deexcitation processes of Er in Si. All processes in bold letters are comprised in a model which is presented in section 3.4.3 to describe the low temperature Er luminescence phenomena. (b) Exciton-electron Auger recombination process. (c) Energy back transfer from the excited Er 4f shell by impurity Auger process with free carriers.	29
3.2	PL intensity vs. temperature for two different excitation laser powers (sample C).	32
3.3	PL intensity vs. excitation power for three different temperatures (sample C).	32
3.4	Temperature dependence of 1/e decay time (top) and intensity (bot.) measured at low power (PL, 60mW, sample A).	34
3.5	Pulse scheme for the EL decay experiments.	35
3.6	EL decay at 40K for different bias conditions during decay cycle (sample C)	35

3.7	EL decay at 100K under reverse and zero bias conditions (sample C).	36
3.8	EL decay at 40K for different drive currents (sample C).	36
3.9	EL spectra at 40K for different bias conditions (resolution 8Å, sample C).	37
3.10	EL spectra at 40K for different drive currents at 40 K (resolution 8Å, sample C).	37
3.11	Spreading resistance and Er -SIMS profiles of a) sample C (LED, deep implanted); b) sample A (Er/O deep implanted and annealed) .	38
3.12	EL decay curves at 40K for zero bias and two different forward bias (corresponding to 2mA and 6mA forward current) during decay (sample C). A two exponential fit yields: 50μs/670μs (intensity ratio 2:1) for zero bias; 33μs/202μs (intensity ratio 3:1) for 2mA; 23μs/67μs (intensity ratio 8:1) for 6mA.	39
3.13	PL decay curves at 4K for two different laser powers, solid lines simulated profiles with rate equations (8a) to (8c) .	40
3.14	PL two-beam experiment at 4K: decay time vs. cw laser power; symbols measured data, solid line fitted by Eq. (3.6), dashed line simulation result (implanted and annealed sample).	41
3.15	Simulation results: power dependence at 4K; data points (symbols) from 4K curve in Fig. 3.3. ; solid line simulated with $\tau_r=1\text{ms}$, $\tau_e=4\mu\text{s}$, $a=10^{-12}\text{cm}^3\text{s}^{-1}$, $c_{A,x}=1\times 10^{-10}\text{cm}^3\text{s}^{-1}$, $c_{A,Er}=10^{-12}\text{cm}^{-3}\text{s}^{-1}$. Inset: simulated decay curves for high generation rates ($G=10^{22}\text{cm}^{-3}\text{s}^{-1}$) illustrating the effect of impurity Auger back transfer on the decay curve. The intensity is normalized.	43
3.16	Power dependence of the boron bound exciton line intensity (4K, sample A, PL spectrum in inset). Solid line fitted with equation (3.13).	45
3.17	Low power PL decay curves and fitted exponentials (60mW, sample A); 4K: one exponential (1290ms), 100K two exponentials (270μs and 1033μs).	46
3.18	Temperature dependence of the short PL decay component (60mW, sample A); solid line fitted with equation (3.16)	47
3.19	Temperature dependence of the short PL decay component (60mW, sample A); solid line fitted with equation (3.16)	48
4.1	SCF energy spectrum of the $\text{Er}_i\text{Si}_{14}\text{H}_{24}$ cluster	54
4.2	SCF energy levels of different charge states of the $\text{Er}_i\text{Si}_{14}\text{H}_{24}$ cluster, from neutral to triply ionized (a - d)	55
4.3	Schematic diagram of the SCF energy levels of $\text{Si}_{35}\text{H}_{36}$, $\text{V}_{\text{Si}}\text{Si}_{34}\text{H}_{36}$, and $\text{Er}_s\text{Si}_{34}\text{H}_{36}$ clusters	56
5.1	Photoluminescence intensities of Si:Er doped with oxygen are compared with those of Si(Cz):Er, Si(FZ):Er as a function of annealing temperatures. Data for Si(Cz):Er and Si(Fz):Er labeled by Δ , \bullet , and \circ are taken from reference [6].	63

5.20	The comparison of the experimental PL intensity with the simulated Er PL intensity, simulated using the same parameters as in Figure 5-19, as a function of annealing time at 800°C. $F_{peak} = 4 \times 10^{18} \text{cm}^{-3}$	86
5.21	The simulated light emission intensity vs the total amount of F atoms retained in Si after 800°C isothermal annealing. The F atoms is expressed as the ratio of the total Er atoms in Si:Er.	86
6.1	(a) A typical Si:Er LED cross section view. (b) SEM picture of an Si:Er LED top view.	96
6.2	Electroluminescence and photoluminescence spectra of a typical Si:Er LED at $T = 100\text{K}$ and 300K	97
6.3	Si:Er LED EL spectra under different drive current densities.	97
6.4	A typical Si:Er LED EL intensity temperature dependence.	98
6.5	(a) Mesa pattern and Si dry etch.(b) N^+ junction pattern and implantation.(c) P^+ substrate contact pattern and implantation.	102
6.6	(a) N^+ junction annealing and drive-in. (b) Er/O pattern with $4 \mu\text{m}$ photoresist and 4.5 MeV implantation.(c) Er/O annealing and LTO passivation.	103
6.7	(a) Contact pattern and etch. (b) AlSi metal deposition. (c) AlSi metal pattern and dry etch.	104
6.8	(a) Typical I-V characteristics of an Si:Er LED and a reference diode. (b) Junction profiles of two Si:Er LEDs with different n^+ emitter depth and a reference diode.	106
6.9	(a) Deviation of voltage drop (ΔV) from ideal. (b) ΔV vs. linear current to determine resistance R_s	107
6.10	(a) Medici simulated and measured I-V curves for Si:Er diode. (b) Si:Er diode leakage current area dependence.	109
6.11	Photoluminescence and electroluminescence experimental setup. . . .	110
6.12	Si:Er LED EL drive current density dependence at both $T = 300\text{K}$ (a) and $T = 100\text{K}$ (b).	111
6.13	(a) Si:Er LED light power output at $T = 100\text{K}$. (b) Si:Er LED internal quantum efficiency at $T = 100\text{K}$	114
6.14	(a) A typical Er EL intensity vs. drive current density. (b) Si:Er LED light emission intensity vs. junction depth in n-type substrate. The dashed line with error bar is the measurement, and the dotted line is the simulation.	117
6.15	(a) Cross section view of an Si:Er LED on n-type substrate. (b) Suprem3 modeled junction depth profiles.	118
6.16	(a) Spreading resistance profiles of three Si:Er LEDs with different n^+ emitter depth. (b) EL and PL comparison of three Si:Er LEDs with different n^+ emitter depth. The center line is PL measurement, the dotted line is EL measurement, and the solid line is the simulation. . .	119
6.17	Er PL intensity vs. substrate concentration.	121

5.2	The affect of annealing time on the luminescence spectra of Si:Er-O after 900°C isothermal annealing. The insert shows the PL peak intensity of Si:Er-O decays with annealing time.	63
5.3	The impact of longer annealing time on high resolution spectra of Si:Er doped with oxygen.	64
5.4	An Arrhenius relationship of the Er^{3+} PL intensity of Si:Er doped with oxygen after high temperature annealing. The samples are Er doped n or p type Fz-Si co-doped with $1 \times 10^{18} \text{cm}^{-3}$ oxygen.	66
5.5	The effect of F co-implantation on the PL peak intensity of Si:Er after 30 min anneal. Horizontal dashed line is the PL intensity in Si:Er with $1 \times 10^{18} \text{cm}^{-3}$ oxygen after 900°C, 30 min heat treatment.	67
5.6	Comparison of the effect of O and F on the Si:Er PL intensity at 4.2 K.	67
5.7	PL spectra of Si:Er with F concentration of $5 \times 10^{19} \text{cm}^{-3}$ and $4 \times 10^{18} \text{cm}^{-3}$. The spectrum resolution is 4 Å.	69
5.8	The PL spectra of Si:Er with $\text{F} = 5 \times 10^{19} \text{cm}^{-3}$ as a function of measurement temperature.	69
5.9	The PL peak intensity (at 4.2 K) vs the annealing temperature as a function of the F concentration in Si:Er-F for a 30 min anneal.	71
5.10	Schematic drawing of the physican processes taken place in Si:Er-F during heat treatment.	72
5.11	SIMS depth profiles of Er in Si:Er-F after 800°C and 1100°C anneal for 1/2 hour.	72
5.12	SIMS depth profiles of F in Si:Er-F after heat treatments. Initial F level is at $4 \times 10^{18} \text{cm}^{-3}$ and marked with a dashed line. Er profile remains constant.	73
5.13	The effect of F out-diffusion on the light emission intensity of Si:Er. Total retained F atoms after the heat treatment is expressed as the ratio of total Er atoms.	74
5.14	The effect of annealing time on the PL intensity of Si:Er-F. The samples with $[\text{F}]_{\text{peak}} = 4 \times 10^{18} \text{cm}^{-3}$ are annealed at 800°C. The others are annealed at 900°C. The lines are drawn to guide the eye.	74
5.15	The effect of annealing time on the PL intensity of Si:Er during 800°C isothermal annealing. The insert shows the PL peak intensity of Si:Er evolves with the annealing temperature.	75
5.16	The evolution of the Si:Er-F PL spectra as a function of annealing temperature during an isochronal anneal. The F peak concentration in Si:Er is $4 \times 10^{18} \text{cm}^{-3}$	76
5.17	A schematic drawing of the Si:Er process simulator.	79
5.18	The concentration profiles of total F in Si:Er after 800°C, 30 min anneal (a); 800°C, 10 h anneal (b); generated with parameters $D_0 = 5 \times 10^{-4}$, $\Delta H_3 = -2.5 \text{eV}$, $\alpha/D(\text{F}) = 0.1$ and $C_b = 10^{12}$; and are compared with the experimental profiles measured by SIMS.	84
5.19	The concentration profiles of ErF , ErF_2 , ErF_3 , free [Er] and [F] in Si:Er after 800°C, 30 min anneal are generated using the same parameters as in Figure 5-19.	85

7.1	(a) Si:Er LED/waveguide integration on BESOI substrate. (b) Si:Er LED/MOSFET integration on BESOI substrate.	126
7.2	(a) NMOS p-well pattern and implant. (b) LED p-well pattern and implant. (c) p-well first half drive-in. (d) LED n^+ arsenic pattern and implant.	129
7.3	(a) LED arsenic/p-well drive-in. (b) n-well field threshold pattern and implant. (c) Active area pattern and nitride etch.	130
7.4	(a) p-well field pattern and implant. (b) LOCOS isolation. (c) NMOS threshold and punchthrough pattern and implant.	131
7.5	(a) PMOS threshold and punchthrough pattern and implant. (b) Gate oxidation and polysilicon gate pattern and etch. (c) NMOS source/drain and nwell contact pattern and implant.	132
7.6	(a) LED mesa pattern and etch. (b) PMOS source/drain and p-well contact pattern and implant. (c) Er/O pattern and implant.	133
7.7	(a) Schematic circuit configuration showing MOSFET in series with Si:Er LED. (b) Schematic top view of the circuit. (c) CMOS/Si:Er LED cross section view.	134
7.8	(a) Drain current vs. drain voltage for n-channel $W/L = 20/2$, $V_b = 0V$, $V_G = 1V$ to $5V$. (b) Drain current vs. drain voltage for p-channel $W/L = 30/3$, $V_b = 0V$, $V_G = -1V$ to $-5V$	135
7.9	(a) Subthreshold slope = 81 mV/decade for n-channel, $W/L = 20/2$, $V_{ds} = 50 \text{ mV}$. (b) Subthreshold slope = 85 mV/decade for p-channel, $W/L = 30/3$, $V_{ds} = -50 \text{ mV}$	136
7.10	(a) Transconductance vs. gate voltage for n-channel, $W/L = 20/2$, $V_d = 3V$. (b) Transconductance vs. gate voltage for p-channel, $W/L = 30/3$, $V_d = -3V$	137
7.11	A typical I-V curve of a MOSFET integrated Si:Er LED	138
7.12	Light emission from a MOSFET integrated Si:Er LED on BESOI substrate at high and low drive current densities.	139
7.13	(a) Er light emission intensity vs. drive current density. (b) Er light modulation by MOSFET gate voltage.	140
7.14	Er light emission modulation frequency curve. The intensity decrease at frequencies below about 50 kHz is due to Er, the drop beyond 50 kHz is due to the measurement system response time.	141
8.1	UHV-CVD reactor	146
8.2	PL (at $4K$) of Si grown at $575C$ for 30 min	148
8.3	PL (at $4K$) of $Si_{.95}Ge_{.05}$ grown at $850C$ for 60 min	148
8.4	XTEM of SiGe quantum wells (35 \AA) grown at 750 C	149
9.1	Spectral Reflectance data for crystalline Si, $560C$ and $625C$ polySi. The $560C$ sample exhibits reflectance similar to that of crystalline Si, indicating that its surface is less rough than the polySi deposited at $625C$	154

9.2	Measured loss (squares), calculated loss due to surface roughness (diamonds), and estimated bulk loss (triangles) as a function of surface roughness. The estimated bulk loss is determined by subtracting the calculated loss from the measured loss. Samples (from left to right) are 560C, 625C CMP, 580C and 625C. Differences in estimated bulk loss are attributed to microstructural effects.	156
9.3	Estimated bulk loss dependence on deposition temperature.	156

Chapter 1

Executive Summary

This Silicon Optoelectronics program is the first comprehensive investigation of a silicon compatible, optical interconnection technology. The projects range from fundamental research supporting emitter and waveguide materials physics to technology demonstrations of devices and circuits. This highly successful program has provided the basis for paradigm changing advances in optoelectronics, such as silicon lasers, waveguides, optical amplifiers and modulators, for integrated optical interconnection.

The objective of the program is to establish processes, compatible with integrated circuit fabrication, for the integration of photonic interconnection with silicon electronics. Our approach is to create technology building blocks under the constraints of the conventional silicon fabline process tools, the current circuit design rules and the projected systems performance requirements. Silicon Optoelectronics offers the advantages of low cost, high yield components based on accepted, high volume process technologies; reduced interconnection power dissipation by elimination of the RC contributions of fineline electronic wires; and reduced interconnection density by multiplexing on high bandwidth optical waveguides.

Erbium-doped silicon was selected as the most promising materials system for integrated light emitters. The system gives electroluminescence (EL) at $\lambda = 1.54\mu\text{m}$, the commercial telecom and datacom standard, and the output signal can be amplified by conventional Er-doped fiber amplifiers. This program was designed to work in collaboration with Rome Laboratories, Hanscom to understand the Si:Er system, to develop a test capability to evaluate materials and devices, and to fabricate demonstration devices.

We performed the first electronic structure calculations for Si:Er using the X- α , scattered wave formalism. The f-electrons were treated explicitly as valence electrons to assess matrix and ligand interactions. We found that the tetrahedral field of the silicon host provides a symmetry-breaking crystal field that allows the parity-forbidden, Er^{3+} optical transition to be allowed. Ligands act to enhance dipole coupling for excitation processes and to enhance Er solubility by complexing.

We measured the diffusivity $D_{\text{Er}} = 10^{-15}\text{cm}^2/\text{s}$ at 900C and the solubility, $C_{s(\text{max})} = 5 \times 10^{16}\text{cm}^{-3}$ of Er in silicon. We determined the Er-Si-O ternary phase diagram. Er reduces both Si and SiO_2 to form stable compounds, Er_3Si_5 and Er_2O_3 , respectively. The slow diffusivity, low solubility and compound stability make Er safe for the

conventional silicon fabline. Split lot test structures confirmed that Er did not cross-contaminate adjacent wafer locations or adjacent wafers in the same lot.

We designed, fabricated and tested the first Si:Er LED with sharp line ($\Delta\lambda = 100\text{\AA}$) electroluminescence at $\lambda = 1.54\mu\text{m}$ operating at 300K. This achievement involved definition of the process windows for a series of standard processes using the MIT Microsystems Technology Laboratories CMOS fabline. This approach utilized advanced fabrication tools and yielded a reproducible path for large quantity production.

Er association with highly electronegative ligands was found to be essential for optical efficiency. We determined process windows for oxygen and fluorine ligand complexes. Fluorine offered the best performance, because it has a higher diffusivity that allows association reactions at lower temperatures. A process simulator was constructed to optimize complex formation and to limit dissociation and out-diffusion of the ligands.

Two process paths were explored to maximize the concentration of Er in solution: ion implantation and UHV-CVD film growth. Ion implantation is currently the more fabline compatible, and it was used in all device fabrication. UHV-CVD provides the best opportunity for inclusion of high concentrations of Er by low temperature growth where precipitation is slow. We designed and constructed a UHV-CVD system featuring SiH_4 , P_2H_5 , B_2H_6 , GeH_4 and various MO-Er source gases. The system provided Si-Ge heterostructures for optical confinement and photon detection. Growth of Si and SiGe with sharp interfaces was achieved in the 500C - 1000C range.

To model device performance we developed a global theory of Er excitation by minority carrier recombination. The f-electron manifold, which is responsible for luminescence, is excited by an intracenter Auger process following exciton recombination. Er in silicon is a very efficient recombination center which is excited $\times 10^6$ more efficiently by electronic injection than by optical pumping. A detailed study of the temperature dependence of luminescence intensity, lifetime and pumping power dependence revealed an internal back transfer process that limits quantum efficiency. When the back transfer rate exceeds the spontaneous emission rate, both emission intensity and excited state lifetime decrease. At low temperature, Auger coupling to free carriers controls back transfer. The spontaneous emission time must be decreased to defeat this efficiency loss.

We have monolithically integrated Si:Er LEDs with waveguides and drive electronics to demonstrate the optical and electronic compatibility of Silicon Optoelectronics. The high index contrast of Si/SiO₂ provides excellent coupling efficiency with low optical loss ($<1\text{ dB/cm}$) on SOI (silicon-on-insulator) substrates. A SiO₂ film thickness of only 0.5 - $1\mu\text{m}$ is required for optical confinement at $\lambda = 1.54\mu\text{m}$. Monolithic integration of drive electronics required considerable effort in design and process integration to preserve the Si:Er process/performance window. Our design evolved in consultation with industry collaborators to be a backend, interconnection approach. The LEDs showed excellent performance. The best internal quantum efficiencies ranged from 1 - 5%. The 3dB modulation rate cutoff for the LED/MOSFET structure was 25kHz.

Realization of an optical interconnection level above the waferplane requires the

use of polycrystalline Si waveguides. We developed an optical test bench to measure waveguide losses by the cut-back technique. A robust polishing method was devised that yields $\pm 3\%$ variation in coupling efficiency. By control of polycrystalline Si deposition conditions and surface roughness, we fabricated waveguides with world record, low loss of 35dB/cm. We expect to improve further on this performance by modification of grain boundary properties.

This highly successful program has provided a foundation for Silicon Optoelectronics as a low-cost, high-bandwidth solution for quiet communications and interconnection. This study has revealed three areas of immediate focus for the realization of complete system integration: 1) a silicon laser based on high Er concentrations and shorter spontaneous emission times; 2) a silicon waveguide modulator operating at 1GHz; and 3) a SiGe photodetector at $\lambda = 1.54\mu\text{m}$.

Acknowledgments

We wish to acknowledge the seminal contributions and encouragement in this work by Richard Soref and Joe Lorenzo, Rome Labs, Hanscom (silicon waveguides and testing) and Lt. Col. Gernot Pomrenke, AFOSR (Si:Er LEDs). John Poate and Dale Jacobson of AT&T Bell Laboratories collaborated on the Er implantation. Partial support by the Semiconductor Research Corporation provided the systems driver and compatibility standards for much of this work.

Partial support was also provided by the AT&T Ph.D. Scholarship Program, the Fundacao de Amparo a Pesquisa do Estado de Sao Paulo, and the Deutsche Forschungsgemeinschaft.

We are also indebted to collaborations with Digital Equipment Corporation, Hewlett Packard and Intel Corporation for helpful discussion during the course of this work.

Chapter 2

Diffusivity and Solubility of Er in Si

2.1 Introduction

The limiting factors to increased functionality of silicon based integrated circuits (ICs) are interconnection density, interconnect driver-related power dissipation and systems bandwidth. The integration of optoelectronic devices for interconnection provides an immediate solution of the above in the form of multiplexed outputs; absence of interconnect line capacitance and resistance; and an unlimited ($\sim 10^{15} Hz$) bandwidth capacity. In addition, new capabilities in parallel architectures, immunity from electromagnetic interference and package integration present the opportunity for breakthrough applications.

One of the components for optoelectronic interconnects is a silicon based light emitter. Because of the indirect nature of the band gap, light emission in silicon is very inefficient. Therefore, research in recent years focussed on the search for efficient Si based light emission. One of the potential systems that was identified is erbium doped silicon [1, 2, 3]. Silicon acts as a host material for Er that, through an intra f-shell transition, emits light at $1.54\mu m$, a wavelength that is already technologically utilized for fiber communication. This inneratomic transition provides temperature independence of the emission wavelength and a narrow linewidth towards high temperatures.

A good understanding of the Er:Si materials system is imperative in order to optimize the optically active Er centers in Si. In recent years, much progress has been made. Important contributions are the light emission enhancement from oxygen and other impurity ligands [2, 3], the achievement of room temperature Er luminescence [3], and the development of the first room temperature Er:Si LED [4]. However, many fundamental materials properties are not well understood. The processing conditions for Si:Er are far from optimal. Many key issues are yet to be solved such as Er solubility and diffusivity in Si and the impact of impurities, defects and annealing temperature on the optical activity of Er in Si.

The predominant technique to introduce Er into Si is by implantation [2, 3, 4,

5]. Er peak concentrations of 10^{18}cm^{-3} can be achieved without permanent lattice damage [3], while co-implantation with oxygen stabilizes Er at 10^{20}cm^{-3} without significant precipitation [5]. Oxygen co-implantation is very effective in enhancing the Er luminescence. However, there is very little existing information about oxygen-erbium-silicon reactivity and the Er-Si-O ternary system in the current literature.

Increasing light emission in Si:Er and improving the LED device performance of this defect system depend on how the optically active Er centers in Si can be effectively maximized. The maximum number of optically active Er centers which can be introduced in Si:Er is constrained by the kinetic and equilibrium factors of the Er:Si system. Er diffusion and solubility in Si are the basic kinetics and equilibrium parameters in Si:Er. Therefore, Er equilibrium and metastable solubility limits and Er diffusivity in Si are critical for the optimal process design to achieve superior performance in Si:Er devices.

Si:Er compatibility with Si IC processing is one of its major advantage of Si:Er over other optoelectronic semiconductor materials. Transition metal elements such as Au, Cu, Fe etc. are detrimental to the Si fabline because of their fast diffusivity and formation of effective recombination centers. Preliminary evidence shows that Er implanted in Si does not diffuse as fast as transition metal elements in Si [2]. Since Er is a very efficient recombination center in Si, it is critical to provide further evidence of a slow Er diffusion in Si and to ensure its compatibility with existing Si fablines.

The purpose of this research is to create an IC compatible process technology for optical interconnection. This chapter will review our results on Er:Si reactivity, diffusivity and solubility which establish silicon fabline compatibility. The Er-Si reactivity, especially in the presence of O_2 , is studied through annealing of a thermally evaporated erbium layer on etched Si wafers. The reacted phases are identified through X-ray phase analysis. The Er-Si-O ternary phase diagram is established. The implications of phase stability on Si:Er processing will be discussed. Photoluminescence characteristics of Si:Er and other Er compounds formed in the process are also analysed to establish the unique characteristics of the Si:Er luminescence.

2.2 Experimental

Experiments on Er-Si reactivity were carried out through the heat treatment of thin Er films on silicon in various processing ambients. A thin layer of erbium, typically ranging from 100 Å to 1000 Å was vacuum deposited on an etched silicon substrate in an Edwards 306A thermal evaporator with a base pressure of 10^{-6}Torr . The silicon surface was cleaned with organic solvents and followed by an etch in a 20:1 HNO_3 and HF acid mixture. The sample was then dipped into 5% HF to passivate the silicon surface for the transfer to the evaporator. The deposited Er/Si was immediately transferred into an annealing furnace for annealing in various controlled ambients at temperatures ranging from 450C - 1000C.

Glancing angle X-ray diffraction, performed with a Rigaku X-ray diffractometer was used to identify the different erbium phases formed on the silicon surface after the heat treatment. The glancing angle of less than 5° was used to enhance the powder

diffraction patterns from the thin film layer on the surface. A JCPDS computer data base [6] was used to identify the different phases. Photoluminescence measurements of the related Er compounds formed on the Si surface were carried out at 4.2 K. The samples were excited using an argon-ion laser at 488 nm. The excitation power was varied from 0.1 -1.5 W. The luminescence was collected and measured with a 0.75 m Spex monochromator and detected by a cooled North Coast Ge detector.

To determine the diffusivity and solubility of Er in Si, Er was implanted into silicon at 5.25 MeV with an implantation dose to produce an Er peak concentration of $1 \times 10^{18} \text{ cm}^{-3}$. The diffusion was carried out in a two step annealing process. The pre-diffusion annealing at 850C in Ar ambient was used to anneal the implantation damage without affecting the Er profile. A SIMS analysis confirmed that the Er profiles in Si remain unchanged after a 850C - 900C anneal. Diffusion annealing was carried out at temperatures between 1150C and 1300C in encapsulated quartz ampoules. The quartz ampoule was evacuated to a base pressure of 10^{-6} Torr and the backfilled with purified Ar before sealing. The Er SIMS depth profile was measured in a VG IX-70 SIMS microanalyser.

2.3 Silicon:erbium reactivity

The phase stability of Si:Er in typical process ambients was determined by the evaporation of pure erbium on etched silicon substrates, followed by heat treatment in controlled ambients. Erbium reacts easily at elevated temperatures. Depending on different annealing ambients, various erbium compounds are formed.

Figure 2.1 shows the thin film X-ray diffraction spectra for vacuum, air and nitrogen ambients. Polycrystalline Er_2O_3 is formed after a complete oxidation of the Er film during a 450C, 1h anneal in air. ErN is formed after a 650C anneal for 1 h in a N_2 ambient. In vacuum, a multiphase combination of silicides is often observed with some fraction of Er_2O_3 , unless extreme care is taken. The best condition for single phase silicide formation, Er_3Si_5 , was found to be (450C, 3 h) under a vacuum of 10^{-5} Torr.

The silicide, Er_3Si_5 , is the most stable compound in the series of silicides ErSi , ErSi_2 , and Er_3Si_5 . The reacted film exhibits a rough morphology on Si(100), but is planar and highly textured along the (001) plane on Si(111). The lattice mismatch between $\text{Er}_3\text{Si}_5(001)$ and Si(111) is small (1.2%) [7], providing a basis for this interface to be of low energy. This conclusion was tested by exposing a substrate of vicinal Si (111), miscut 4° toward $\langle 110 \rangle$, to erbium vapor at 1160C for 24h in a sealed quartz ampoule. The vapor pressure of erbium is above 10^{-3} Torr at 1100C. Figure 2.2 shows a scanning electron micrograph of a cross section of a reacted sample. The schematic cross-sectional view of the Si surface is illustrated in the bottom part of Fig. 2.2 and the ratio of the height and width of the terrace structure is consistent with a 4° miscut of a vicinal Si(111) surface. This result is consistent with studies on epitaxial growth of ErSi_{2-x} ($x = 0.3$) using UHV erbium e-beam evaporation and MBE. Epitaxial ErSi_{2-x} has been formed through in-situ annealing of an UHV evaporated erbium layer at 350C - 450C [8] or rapid thermal annealing of a thin Er film

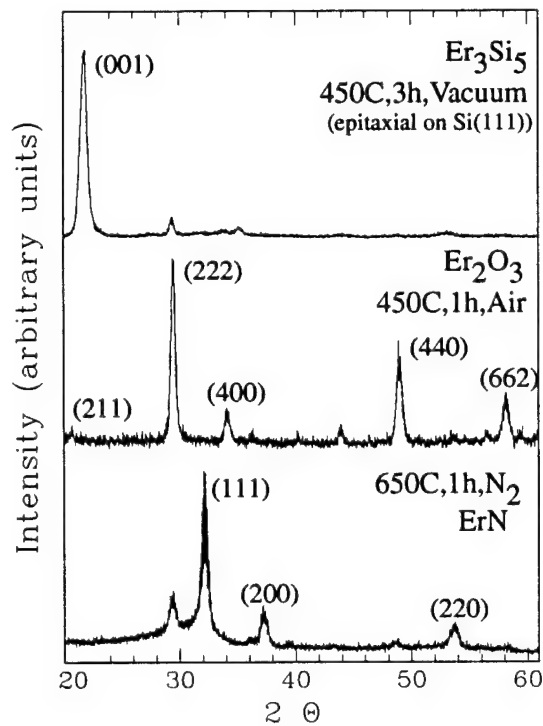


Figure 2.1: X-ray diffraction phase identification of Er_3Si_5 , Er_2O_3 , and ErN , formed by reacting erbium and silicon in vacuum, O_2 , and N_2 .

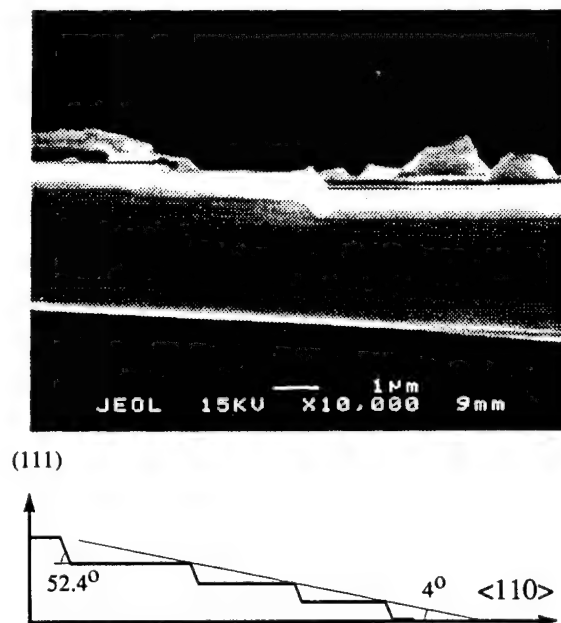


Figure 2.2: SEM image of cross section of vicinal Si (111) surface, heat treated at 1165°C for 24h under Er vapor. The bottom graph illustrates the observed terrace structure of the 4° miscut Si (111) surface.

on Si at 950C [7]. We conclude that the formation of an (001) Er_3Si_5 texture and of Si(111) terraces upon heat treatment in vacuum at 1160C define this interface to be lowest in energy for the Si:Er system.

Heat treatment of Er on SiO_2 in vacuum and Er_3Si_5 in an oxygen containing ambient in the range $450C < T < 1100C$ yields Er_2O_3 . Thus, erbium reacts similar to titanium with respect to silicon [9]. The oxidation of Er_3Si_5 can be explained by comparing the formation enthalpy of each Er compound involved in the reaction. Er_2O_3 is a very stable compound. Its formation enthalpy at 298K is [10]

$$\Delta H(Er_2O_3) = -453.6kcal/mol \quad (2.1)$$

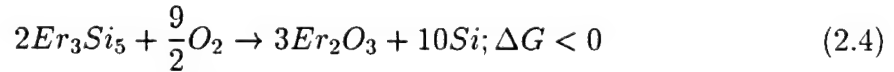
There are no data available for the formation energy of Er_3Si_5 . However, it can be estimated based on a model proposed by Andrews and Phillips [11]. They have correlated the heat of formation ΔH of a silicon-rich silicide formed on n-type Si with its Schottky barrier height F_b in a linear relationship.

$$F_b = 0.83 - 0.18(\Delta H) \quad (2.2)$$

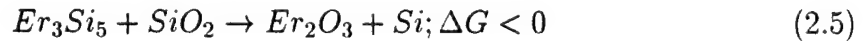
F_b is reported to be 0.39 eV for Er_3Si_5 [12]. This yields a formation energy of $\Delta H = -55kcal/mol$ of Er for Er_3Si_5 . The corresponding entropy change (ΔS) of the oxidation reaction is mainly due to the change of entropy of O_2 . $\Delta S(O) = 24cal/K$ per mol of O ($1/2 O_2$) [13]. The free energy change of the total reaction can be computed

$$\Delta G = \Delta H - T\Delta S \quad (2.3)$$

An oxidation reaction as follows can easily occur when Er_3Si_5 is in the presence of O_2 since the overall free energy change of the reaction (ΔG) is negative.



At 298K, $\Delta G = -966.4kcal$. Likewise, the reaction between Er_3Si_5 and SiO_2 can also proceed



The formation energy for SiO_2 is $\Delta H = -215.94kcal/mol$ [11]. Since all phases in the reaction are solid, the entropy changes are insignificant when compared with the enthalpy changes. $\Delta G = -59.1kcal$ at 298K.

Combining the analysis of the X-ray diffraction data and the existing binary phase diagrams among Er, Si, and O [1], a ternary phase diagram for the ER-Si-O system is proposed in Figure 2.3. Er_2O_3 , the dominant phase, will capture the erbium activity under any oxidizing condition. As indicated in Fig. 2.3, in the presence of O_2 the oxidation of Er_3Si_5 occurs. Er_2O_3 and Si are formed. The oxidation can further proceed to form SiO_2 or the Er-Si-O ternary phases, Er_2SiO_5 and $Er_2Si_2O_7$ [6]. Both have been observed in our experiments.

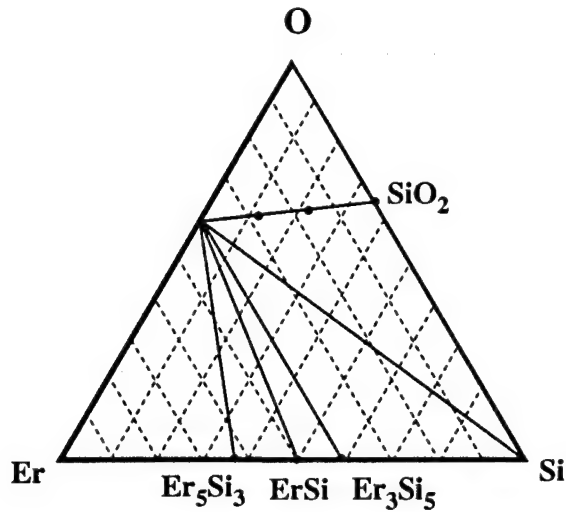


Figure 2.3: Proposed ternary phase diagram of the Er-Si-O system between 450C and 1100C. Two ternary phases on the Er_2O_3 and SiO_2SiO_2 tie line are Er_2SiO_5 and $Er_2Si_2O_7$.

A further test of this phase diagram can be done by looking at the reaction of Er on SiO_2 . No tie line exists between Er and SiO_2 in Fig. 2.3. Therefore, SiO_2 is reduced by erbium to form Er_2O_3 and erbium silicides. This reaction was confirmed by the annealing of an erbium layer on an oxidized silicon substrate. We observe the formation of Er_2O_3 and Er_2SiO_5 after the annealing of the erbium layer deposited on an oxidized Si substrate at 1150C for 9h in an Ar ambient. Using $^{16}O(d,)^{14}N$ nucleation reaction technique, Wu et al. reported a reduction of the SiO_2 layer by the erbium layer during the annealing of erbium on a thermally oxidized Si substrate at 500C for 2h [3].

Knowing the relative phase stability of the Er-Si-O system can help in understanding the effect of oxygen co-implantation on Er:Si. The Er-Si-O ternary phase reaction can be considered as the result of breaking 10 Er-Si bonds and forming 9 Er-O bonds in the presence of O. It can be inferred that O in Si:Er breaks an Er-Si bond to form a Er-O bond. In other words, Er prefers to cluster with O in Si:Er. This is consistent with the findings in Si:Er. Oxygen has been shown to greatly enhance light emission in Si:Er [2, 3]. Since the Er-O bond is very stable, the above process should be independent of heat treatment procedures of Si:Er with oxygen co-implantation. This inference is consistent with experimental results on Si:Er.

Of the reaction products Er_2O_3 , Er_3Si_5 and ErN , only Er_2O_3 is optically active with an Er^{3+} emission at $1.54\mu m$. Er_3Si_5 does not give rise to an Er luminescence because it is a semimetal with a resistivity $< 10 Wcm$ at temperatures $< 50K$ [18]. ErN does not show any light emission either. Therefore we infer that ErN is metallic too and therefore conductive and absorbing. This conclusion is strengthened by the fact that in silicon both O and N provide optically activating ligand fields for erbium.

Figure 2.4 shows a comparison of the optical spectra of Er implanted in Si (900C, 30 min) and poly-crystalline Er_2O_3 (450C) at 4.2 K. Spectral features of the Er^{3+}

at $1.54\mu\text{m}$ are a result of the crystal field splitting of the ground state and the first excited state of the Er 4f electron. The crystal field varies depending on the symmetry, the ligand field strength, and the host material. Therefore, the different number of peaks and their spacing in the spectra of Si:Er and Er_2O_3 imply different symmetry and ligand field of the Er on the different host materials. The distinction can be used as fingerprints for the Er compounds. There are two reproducible differences: 1) the primary emission shifts to shorter wavelengths for Si:Er; and 2) the multiple crystal field split emission bands for Er are absent for Er_2O_3 . These differences are critical in determining whether erbium emission originates in a surface oxide or bulk silicon.

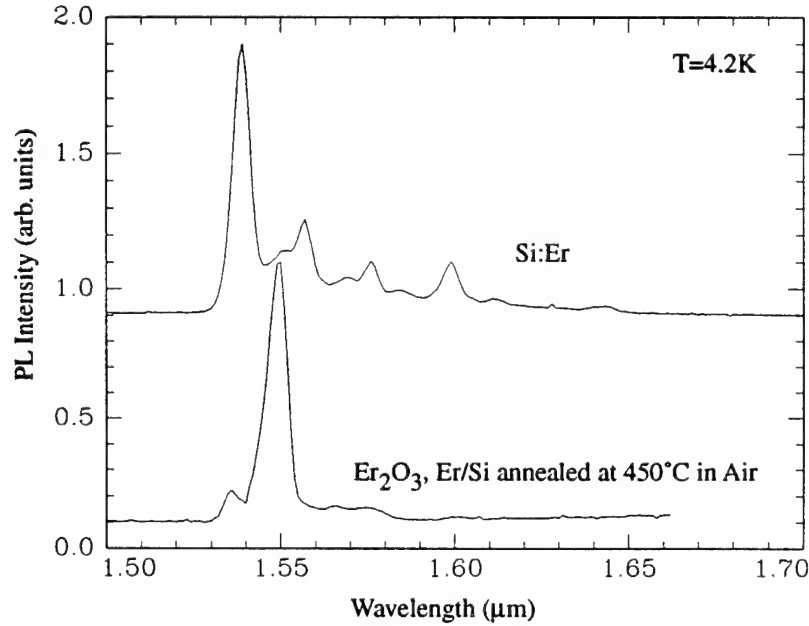


Figure 2.4: Comparison of Er^{3+} photoluminescence spectra in Si:Er and Er_2O_3 .

2.4 Erbium diffusivity and solubility

The internal quantum efficiency of Si:Er for light emission is dependent on the dominant role of erbium in the generation- recombination processes in the silicon host. Thus, it is necessary to establish that the Er diffusivity is small enough during processing to prohibit cross-contamination of adjacent devices, wafers and process equipment. In addition, a high solubility of Er in Si is desirable because the optical power out is proportional to the Er concentration [Er] [19]. Direct measurements of the Er diffusivity are experimentally difficult. Two different diffusivities for Er were reported between 1100C and 1250C [3, 9]. These diffusivities are given as $D_{\text{Er}} = 2 \times 10^{-3} \exp -2.9\text{eV}/kT \text{cm}^2/\text{s}$ and 6×10^{-15} to $4 \times 10^{-13} \text{cm}^2/\text{s}$, respectively, for this temperature region. The inconsistency of these results may be explained by surface reactions between Er, Si, and O. In addition, a low solubility of Er in Si posts challenges for the detection of Er in an equilibrium diffusion experiment.

Figure 2.5 shows a typical Secondary Ion Mass Spectroscopy (SIMS) profile of Er implanted silicon before and after diffusion annealing. Erbium was implanted to a peak concentration of $3 \times 10^{18} \text{ cm}^{-3}$ at an energy of 5.25 MeV. After heat treatment at 850C, 1/2 hour no change from the as-implanted profile was observed. A subsequent heat treatment of 1300C, 1 hour, results in contraction of the profile rather than the broadening normally observed for Group III and V dopants in silicon (dashed lines). A second aspect of the profile is a constant $[Er] \sim 10^{16} \text{ cm}^{-3}$ away from the implanted distribution.

The narrowing of the distribution unambiguously connotes precipitation at the peak of the distribution. Thus, the precipitates, as well as the surfaces, act as sinks for the Er to reach its equilibrium solubility. By assuming that complete point defect equilibrium is reached by 1300C, 1 hour, we define the flat portion of the distribution as the solid solubility ($[Er]_{sol}$) of Er in Si.

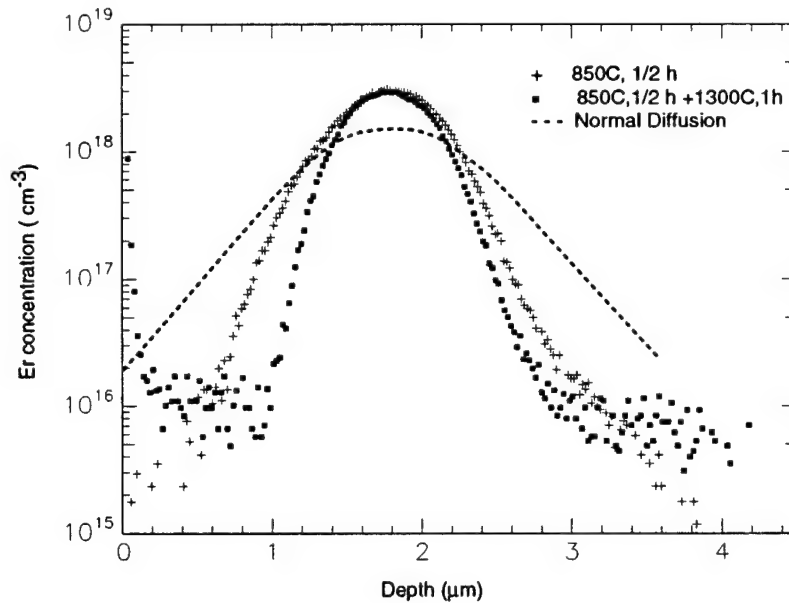


Figure 2.5: SIMS depth profiles of Si:Er before and after diffusion annealing at 1300C for 1h. The dotted line represents an expected normal diffusion profile.

Because of the low solubility of Er in Si, a direct observation of Er diffusion requires SIMS analysis of an Er profile with a peak concentration below its solubility limit of 10^{16} cm^{-3} . The limit of Er detection makes this difficult to accomplish experimentally using SIMS. A modified diffusion model however, incorporating the dissolution of the precipitates, can be used to model the observed changes in Er profiles. As a result, the diffusivity of Er in Si can be extracted.

In the model, Er diffusion is assumed to be the rate limiting step for the narrowing of the Er profile. In other words, the dissolution process of subcritical Er-Si precipitates at the extreme is fast enough to maintain local equilibrium with solute Er, which out-diffuses to the surface. This assumption is critical. Otherwise, the

observed narrowing of the Er profile would be determined by the rate of precipitates dissolution instead of Er out-diffusion. In this respect, the extracted diffusivity from the model may not represent the true diffusivity, but instead indicate only a lower bound of Er diffusivity at these temperatures. Furthermore, to simplify the model, the Er-Si precipitation is assumed to take place instantaneously for concentrations above its equilibrium solid solubility at such high temperatures (1150C - 1300C). For Er below its solid solubility,

$$\frac{dEr}{dt} = D_{Er} \frac{d^2 Er}{dx^2} \quad (2.6)$$

Er in the form of the precipitates is immobile and assumed to remain in a Gaussian distribution. The peak concentration is unchanged after short time anneals. This assumption is consistent with our SIMS observations after 1h anneal. However, the assumption would break down at much longer time anneals when significant depletion of the precipitates reduce the Er peak concentrations. Therefore, for $[Er]$ in the region of the precipitates, exceeding the equilibrium solid solubility $[Er]_{sol}$,

$$[Er] = C_p \exp -x^2/R^2 \quad (2.7)$$

where C_p is the Er peak concentration ($1 \times 10^{18} cm^{-3}$). R is the straggle for Er profiles and contracts as the diffusion and precipitate dissolution process proceeds.

To maintain mass conservation, the Er out-diffusion rate J is equal to the rate of Er reduction in the precipitation region. Therefore,

$$J = -D \frac{dEr}{dx} = \frac{d}{dt} \int C_p \exp -x^2/R^2 dx \quad (2.8)$$

The problem is similar to a moving boundary problem in diffusion studies and can be solved numerically. The finite difference method is used here to solve equation (2.5). Er diffusivity in Si is obtained by comparing simulated profiles with SIMS profiles. The best fits for Er diffusivities in Si at different annealing temperatures are listed in Table 2.1.

Temperature (C)	Diffusivity (cm ² /s)
1300	5×10^{-10}
1250	6×10^{-11}
1200	5×10^{-11}

Table 2.1: Er diffusivities in Si at different annealing temperatures based on the analysis of Er SIMS profiles

The flat plateau in the Er profiles represent the equilibrium solubility of Er in Si as mentioned earlier. Figure 2.6 shows the Er equilibrium solubilities in Si at different annealing temperatures. They are in the range of $10^{16} cm^{-3}$, similar to S in Si and retrograded at $\sim 1200C$ [22]. The equilibrium solid solubility $[Er]_{sol}$ is significantly less than the value of $1 \times 10^{18} cm^{-3}$ reported by Eaglesham et al. as an onset for Er-Si

precipitation at 900C [14]. Because of the slow Er diffusivity, its equilibrium solid solubility can be significantly different from the threshold concentration for the onset of precipitation. The metastable threshold concentration may be controlled by either kinetics or equilibrium factors.

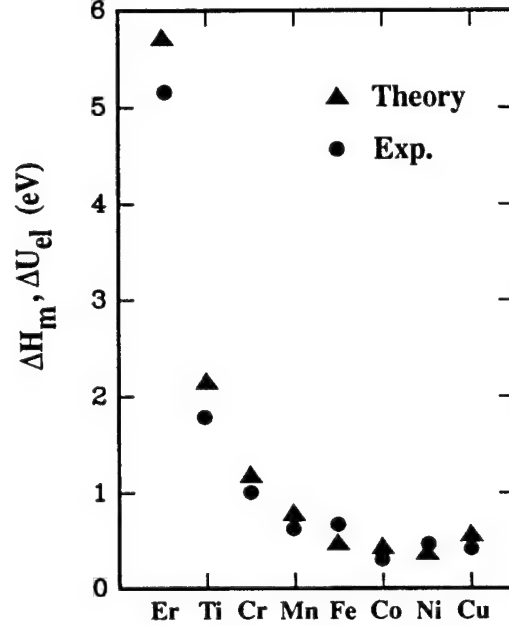


Figure 2.6: Equilibrium solubility limit of Er in Si at different annealing temperatures.

The observed precipitation results from Eaglesham et al. can be further analysed by diffusion limited precipitation theory. In the homogeneous nucleation precipitation theory, the density of precipitates can be derived in the following equations.

$$N_p \sim \int I(T, t) dt \quad (2.9)$$

$$= \alpha \frac{2D_{Er}}{a_0^2} [Er] \exp -\frac{F}{kT} t \quad (2.10)$$

where I is the nucleation rate and α is the shape factor. For spherical precipitates, $\alpha = 1$. a_0 is the silicon interlattice distance (2.76 \AA), t is the annealing time, D_{Er} is the Er diffusivity, and F is the nucleation barrier for Er-Si precipitates.

Figure 2.7 shows our fit (line) of the data from Eaglesham et al. [14] (filled squares) to a diffusion limited precipitation model. The data exhibit two key features: an 'incubation' stage of $[Er]$ of $2 \times 10^{18} \text{ cm}^{-3}$ at 900C, 30 min, and a linear increase in precipitation density with $[Er]$ beyond that concentration. The linear increase of precipitates with $[Er]$ is consistent with a nucleation limited precipitate density. The incubation stage represents a time minimum required for Er atoms to associate at the temperature and is also dependent on the Er concentration. The observed value of 10^{18} cm^{-3} sets a lower limit of the diffusivity $D_{Er} > 6 \times 10^{-16} \text{ cm}^2/\text{s}$ at 900 C.

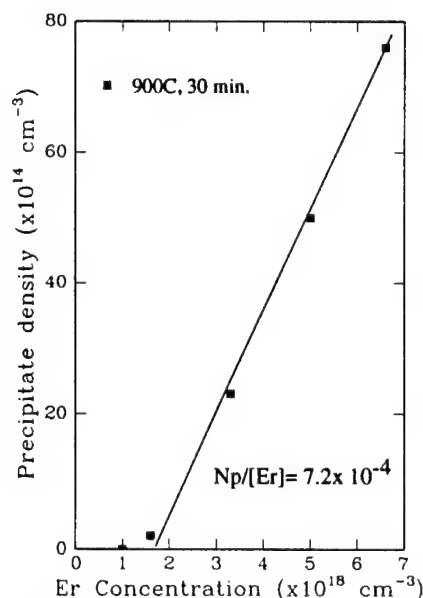


Figure 2.7: Precipitation density of Si:Er for a 900C, 30 min anneal vs. Er peak concentration. The line shows a fit using homogeneous nucleation theory.

The slope of the data $N_p/[Er] = 7.2 \times 10^{-4}$ is very sensitive to D_{Er} and F in the analysis. A two parameter fit yields $D_{Er} = 10^{-15} \text{ cm}^2/\text{s}$ and $F = 1.57 \text{ eV}$. The nucleation barrier is similar to values discussed for oxygen precipitation in silicon [24].

Figure 2.8 shows the diffusivities from our SIMS measurements and the precipitation data. From these data a migration enthalpy for Er diffusion in Si of $5.1 \pm 0.3 \text{ eV}$ is obtained. The migration enthalpy of Er is similar of that of Ge diffusion in Si [22]. Since Er has a large atomic radius $r_a = 1.78 \text{ \AA}$, it is not surprising that Er is a slow diffuser in Si. The migration enthalpy for Er diffusion in Si can be estimated using an elastic energy model [25]. In the model, a diffuser migrates interstitially and moves from tetragonal interstitial sites (T site) to hexagonal interstitial sites (H site) in Si. The migration enthalpy for interstitial diffusion is derived mainly from the elastic energy difference at the saddle point, H site, and at the equilibrium point, T site. The same approach has successfully explained the diffusion of dissolved 3d transition metal atoms in Si [25].

For Er diffusion in Si the model predicts a migration energy of $E_m = 5.7 \text{ eV}$. The experimental migration energy and the from the model calculated energy are plotted in Figure 2.9 with those for 3d transition metals in Si. The general agreement is good. This suggests that Er diffuses interstitially in Si. This conclusion is consistent with the theoretical prediction that the minimum energy configuration for an isolated Er atom in Si is an Er^{3+} at a tetrahedral interstitial site [15].

The metastable threshold concentration can be further altered by modifying either kinetics or equilibrium factors in Si:Er. Recently, Polman et al. reported an incorporation of much higher concentrations ($\sim 10^{20} \text{ cm}^{-3}$) of Er in crystalline Si by solid phase epitaxy of Er -implanted amorphized Si [5]. The limit for Er incorporation

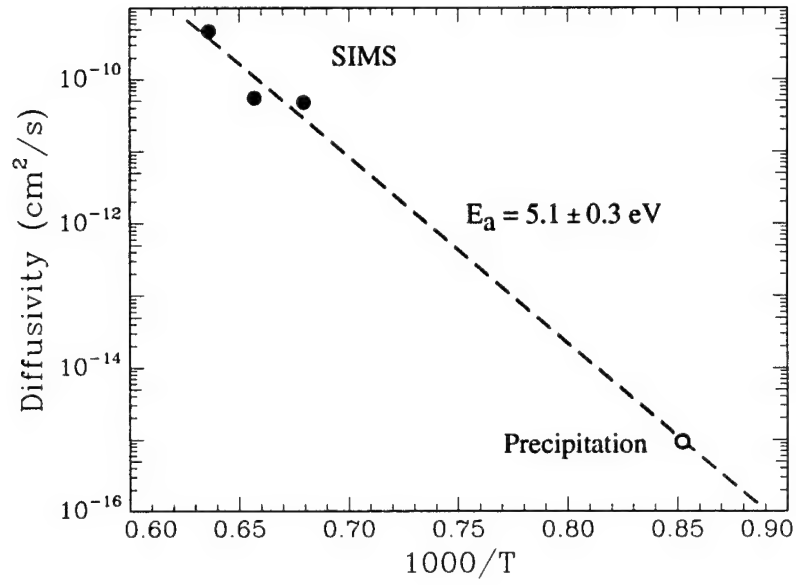


Figure 2.8: Diffusivity of Er in Si determined by SIMS and precipitation formation.

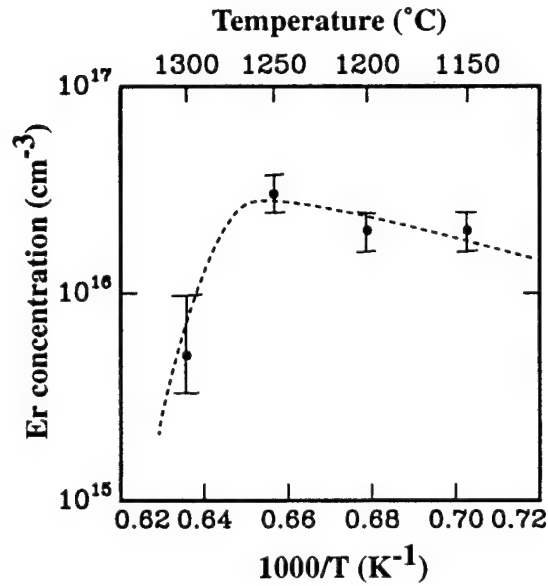


Figure 2.9: Comparison of the experimental migration energy E_m with ΔU_{el} calculated using the elastic energy model for Er and 3d transition metal atoms. Data for 3d transition metal atoms are taken from Utzig

was temperature dependent, decreasing from $1.2 \times 10^{20} \text{cm}^{-3}$ after 15 min anneal at 600C to $6 \times 10^{19} \text{cm}^{-3}$ after 15s anneal at 900C. A much higher migrational barrier for Er precipitation must be in place than in Eaglesham's observation. Conversely, the precipitation kinetics can also be enhanced and therefore reduce the metastable Er concentration. In a Si:Er sample with a flat Er concentration of $5 \times 10^{17} \text{cm}^{-3}$, created by multiple implantations, 20% ErSi_2 precipitates were reported [27]. The precipitation enhancement was likely due to high defect densities created during the multiple Er implants. Impurity doping can alter the equilibrium conditions in Si:Er.

2.5 Conclusion

We found that the Er_3Si_5 (001) plane and the Si (111) plane yield the lowest energy interface because of their close lattice match. Vicinal Si (111) reacts with Er at 1160C and forms (111) terrace structures. A ternary phase diagram for the Er-Si-O system is determined based on X-ray phase identification for the temperature range between 450C to 1100C. Er_3Si_5 is oxidized in the presence of O_2 and Er reduces SiO_2 on a Si substrate, similar to titanium. Optically, only Er_2O_3 luminesces among Er compounds formed during heat treatment. These findings confirm the results that Er precipitates as ErSi_{2-x} ($x = 0.3$) in Si and Er clusters with O to form complexes in Si:Er with O co-implantation. Luminescence studies on various Er compounds established a unique spectrum for Si:Er, which can be used to fingerprint products of Si:Er processing.

Er diffusion and its solubility in Si were studied based on the analysis of Er SIMS profiles in Si after high temperature annealing. It is found that Er is a slow diffuser with moderate solubility in Si. The equilibrium solid solubility for Er is in the range observed for S in Si with $[\text{Er}]_{\text{sol}} \sim 10^{16} \text{cm}^{-3}$ between 1150 and 1300C. Si:Er processing should be comparable with standard Si IC processing and should not contaminate the existing Si fabline. Metastable Er can be incorporated into Si at the concentrations far exceeding its equilibrium solid solubility.

The values for D_{Er} are similar to those observed for Ge in silicon [9] and $[\text{Er}]_{\text{sol}}$ is in the range observed for S in silicon [10]. The process relevant conclusions are as follows: 1) erbium is a slow diffuser with moderate solubility and should not contaminate during silicon IC processing; 2) implanted erbium can be maintained in a metastable solid solution at concentrations two orders of magnitude higher than its solid solubility.

Bibliography

- [1] H. Ennen, J. Schneider, G. Pomrenke, and A. Axmann, Appl. Phys. Lett. 43, 943 (1983).
- [2] P.N. Favennec, H.L. Haridon, D. Moutonnet, M. Salvi, and M. Ganneau, Jpn. J. Appl. Phys. 29, L524 (1990)
- [3] J. Michel, J.L. Benton, R.F. Ferrante, D.C. Jacobson, D.J. Eaglesham, E.A. Fitzgerald, Y.-H. Xie, J.M. Poate and L.C. Kimerling, J. Appl. Phys. 70, 2672 (1991).
- [4] B. Zheng, J. Michel, F. Ren, L.C. Kimerling, D.C. Jacobson, and J.M. Poate, Appl. Phys. Lett. 64, 2842 (1994)
- [5] A. Polman, J.S. Custer, E. Snoeke, and G.N. van den Hoven, Appl. Phys. Lett. 62, 507 (1993)
- [6] JCPDS (Joint Committee on Powder Diffraction Standard)
- [7] J.A. Knapp and S.T. Picraux, Appl. Phys. Lett. 48, 466 (1986).
- [8] M.P. Siegal, F.H. Kaatz, and W.R. Graham, Appl. Sur. Sci. 38, 162 (1989)
- [9] S.P. Murarka, Silicides for VLSI Applications, (Academic Press, Orlando, 1983), p.142.
- [10] National Bureau of Standards, Selected Values of Chemical Thermodynamic Properties, Tech. Notes 270-7, p. 65
- [11] J.M. Andrews and J.C. Phillips, Phys. Rev. Lett. 61, 2118 (1992)
- [12] K.N. Tu, R.D. Thompson, and B.Y. Tsau, Appl. Phys. Lett. 38, 626 (1981)
- [13] K. Kenigh, The Principal of Chemical Equilibrium, 4th edition, Cambridge University Press, pp.426 (1981)
- [14] CRC, Handbook of Chemistry and Physics, 71th edition, P4.8-21
- [15] W.G. Moffatt, The Handbook of Binary Alloy Phase Diagram, General Electric Company, p 6.78 and 11.84 (1984)

- [16] C.S. Wu, D.M. Scott, and S.S. Lau, J. Appl. Phys. 58,? (1985)
- [17] I.Sagnes, G. Vincent, and P.A Badoz, J.Appl.Phys. 72, 4295 (1992)
- [18] Y.-H. Xie, E.A. Fitzgerald and Y.-J. Mii, J. Appl. Phys. 70, 3223 (1991).
- [19] D.E. Nazzyrov, G.S. Kulikov, and R.Sh. Malkovich, Sov. Phys. Semicon. 25, 997 (1991)
- [20] V.V. Ageev, N.S.Aksenova, V.N. Kokovina, and E.P. Troshina, ozv. Leningr. Elektrotekh. Inst. No. 221, 80 (1977)
- [21] S.M. Sze, Physics of Semiconductor Devices, 2nd ed. (John Wiley & Sons, New York,1981) p. 69.
- [22] D.J. Eaglesham, J. Michel, E.A. Fitzgerald, D.C. Jacobson, J.M. Poate, J.L.Benton, A. Polman, Y.-H. Xie and L.C. Kimerling, Appl. Phys. Lett. 58, 2797 (1991).
- [23] P.E. Freeland, K.A. Jackson, C.W. Lowe, and J.R. Patel, Appl. Phys. Lett. 30, 31 (1977).
- [24] J. Utzig, J. Appl. Phys. 65, 3868 (1989)
- [25] M. Needles, M.A. Schluter, and M. Lannoo, Phys. Rev. B 47, 15533 (1993)
- [26] D.L. Adler, D.C. Jacobson, D.J. Eaglesham, M.A. Marcus, J.L. Benton, J.M. Poate, and P.H. Citrin, Appl. Phys. Lett. 61, 2118 (1992)

Chapter 3

Excitation and De-excitation Processe

3.1 Introduction

3.1.1 General

Since the first report in 1983 [1] the luminescence of Er in Si has increasingly attracted both scientific and technology motivated research. By building the first Si based Light Emitting Diode (LED) operating at room temperature at $\lambda = 1.54 \mu\text{m}$ we have shown that Er doping of Si is a viable approach towards a Si microphotonic technology [2, 3]. Our objective is to establish an integrated circuit (IC) compatible process technology for integration of optical interconnection with Si electronics. Current research in the field addresses the materials properties of the Si:Er system [4, 5, 6] optical activation and luminescence enhancement by codoping of impurities [7, 8, 9, 10, 11] and the physics of the Er luminescence [12, 13, 11].

In this chapter we present a detailed analysis of the excitation and deexcitation processes of the Si:Er center. The sharp line luminescence at $1.54 \mu\text{m}$ arises from the $^4\text{I}_{13/2} \Rightarrow ^4\text{I}_{15/2}$ transition from the excited, inner $4f^{11}$ shell of the Er^{3+} configuration. In contrast to other luminescent processes in semiconductors rare earth luminescence arises from spin state transitions, i.e., it does not directly involve changes of charge state or occupancy of bands or band gap states. The luminescence of Er in Si is electroluminescence (EL) in that excitation involves the generation of electron hole pairs followed by a nonradiative energy transfer of the recombination energy to the Er inner $4f$ shell [8]. Theoretical evaluation of the excitation process suggest that an intra-center Auger process [1] provides the energy transfer to the $4f$ shell by electric dipole and exchange interaction. The efficiency of this process is greatly enhanced if a state in the band gap associated with the Er center allows a localization of energy in the form of bound excitons. In section 3.4.4 we show that at low temperatures the dominant processes after excess carrier generation are the formation of excitons and their subsequent recombination by Auger processes. Recombination by nonradiative energy transfer to free carriers competes with the Si:Er excitation process (Fig. 3.1a,3.1b). We show in section 3.3 that the electroluminescence of Er in Si is far more

efficient than direct optical pumping of Er doped fibers for optical amplifiers.

3.1.2 Energy flow for recombination at rare earth centers in semiconductors

It is important to understand the kinetic regimes of energy flow for recombination at rare earth centers in semiconductors. The rate limiting step for electron hole recombination is the dissipation of the energy difference between the initial and final states. Figure 3.1a depicts a serial sequence of energy transfer comprised of four regimes. For a serial sequence of events the slowest process dominates. In regimes I, III and IV parallel processes compete for the energy flow. For parallel processes the fastest mechanism will dominate. All processes preceding or competing with the Auger Er excitation will determine the emission intensity without affecting the luminescence decay time. In regime IV both the decay time and the emission intensity are controlled by the fastest of the two processes. For slow nonradiative back transfer processes the spontaneous emission lifetime of the excited state of the RE center is observed. For fast back transfer the rate of nonradiative energy flow is observed and the radiative emission is reduced.

As an internal, discrete to discrete 4f state transition the Er luminescence energy is independent of band gap and, hence, does not change with temperature. The emission intensity, however, strongly decreases by as much as three orders of magnitude as the temperature increases from 4K to 300K. We consider three different possible causes for the observed thermal quenching.

- 1) The total number of optically active, excitable Er centers decreases, for example by a temperature controlled structural transition to a nonluminescent configuration.

- 2) The pumping efficiency decreases by processes occurring between the electron hole pair generation and the Er excitation. These are the processes in regimes I to III of Fig 3.1a, such as competing recombination processes, e.g. via deep traps and Auger processes (Fig. 3.1b), or the decrease of the excitation efficiency by thermalization of carriers from an Er related state in the band gap.

- 3) The radiative efficiency decreases by a nonradiative energy back transfer from the excited Er 4f shell (regime IV of Fig.3.1a).

Possible energy back transfer mechanisms are multiphonon emission processes or impurity Auger processes involving the energy transfer by electric dipole or exchange interaction between the 4f electrons and free or bound carriers (Fig. 3.1c). This work demonstrates that energy back transfer processes are responsible for the thermal quenching of the Er luminescence in Si. The direct evidence for back transfer processes is the correlation of photoluminescence decay time and intensity. A decrease of Si:Er decay time by a shortening of the spontaneous emission time should lead to an increase of luminescence intensity. We observe a decrease of lifetime with a concurrent loss of emission intensity. This correlation argues strongly for a fast competing nonradiative processes of energy back transfer from the excited Er center to the crystal host. We show that the impurity Auger effect decreases the excited state lifetime of Er in Si and controls the thermal quenching in the temperature range from 4K to 100K.

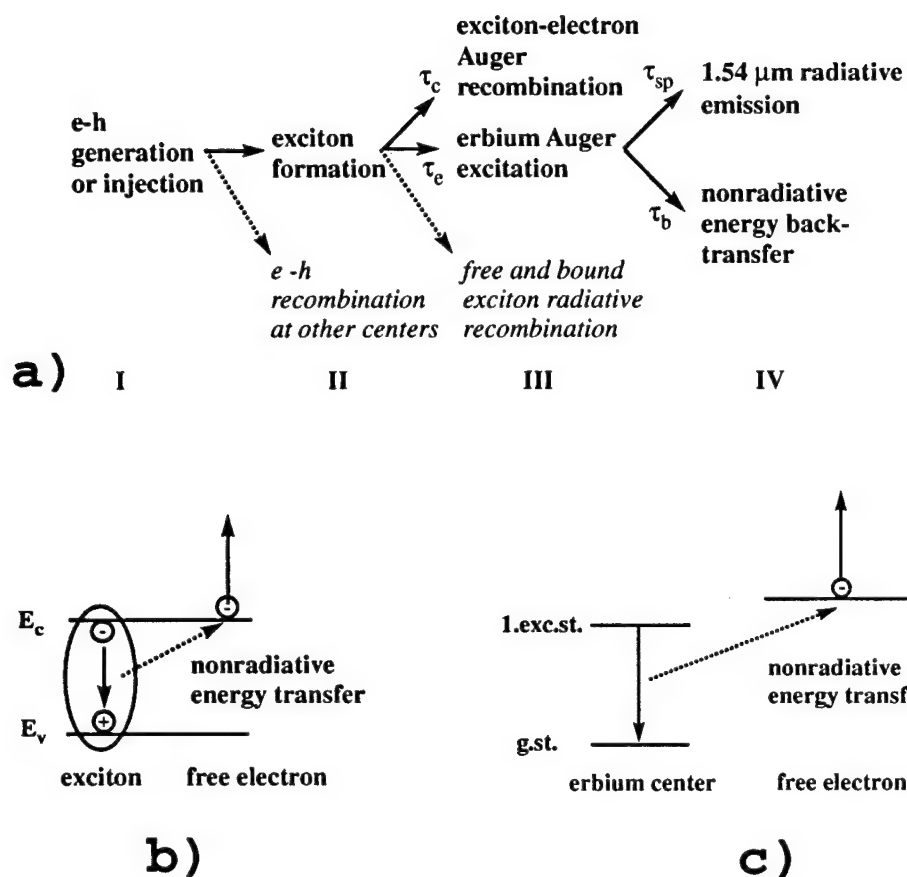


Figure 3.1: (a) Excitation and deexcitation processes of Er in Si. All processes in bold letters are comprised in a model which is presented in section 3.4.3 to describe the low temperature Er luminescence phenomena. (b) Exciton-electron Auger recombination process. (c) Energy back transfer from the excited Er 4f shell by impurity Auger process with free carriers.

Measurements of the dependence of PL intensity vs. excitation power show that at 4 K the internal quantum efficiency decreases by three orders of magnitude with increasing pump power. We demonstrate that the Auger processes, impurity Auger and exciton-electron Auger recombination, can reduce both the pumping and the radiative efficiency of Si:Er (Fig.3.1a to 3.1c).

3.2 Experimental

Boron doped Czochralski grown Si wafers were implanted with Er and O resulting in peak concentrations of $5 \times 10^{17} \text{ cm}^{-3}$ and $3 \times 10^{18} \text{ cm}^{-3}$. We used two different implantation energies 4.5 MeV and 400keV for Er which correspond to peak depths of $1.4 \mu\text{m}$ (deep) and $0.130 \mu\text{m}$ (shallow), respectively. The oxygen implant energies were chosen accordingly to match the Er profiles. For this paper we consider four types of samples: sample A (deep implant) and sample B (shallow implant) were subsequently annealed at 900°C for 30 minutes in an argon ambient. Mesa LED structures were fabricated with an As n+ emitter by implantation prior to the Er/O implantation. For sample C (deep implant) the emitter implant was annealed at 1000°C for two hours. After Er/O implantation the Si:Er centers were activated by the same $900^\circ\text{C}/30 \text{ min}$ anneal. For sample D the (shallow) As/Er/O LED implants were annealed together at 800°C for 30 min. After annealing open Al front contacts were formed[2]. For photoluminescence (PL) spectra a mechanically chopped $\lambda=488\text{nm}$ Ar ion laser beam provided the excitation. For EL spectra the devices were forward biased with a pulsed voltage generator. A liquid nitrogen (LN) cooled Ge detector, a grating spectrometer and a lock-in amplifier were used for signal detection. For the decay measurements the latter components were replaced by a $1.54 \mu\text{m}/40\text{nm}$ band pass filter, a LN cooled InGaP detector, a current amplifier and a digital oscilloscope. The measurement system response time was $20 \mu\text{s}$.

3.3 Efficiency of Electroluminescence of Er in Si

Er doping is employed in glass hosts for commercial lasers and optical amplifiers. These devices operate by optical pumping at $\lambda=960 \text{ nm}$. In contrast the pumping of Si:Er is always mediated by electron-hole recombination. The efficiencies of these two different excitation mechanisms may be compared by relating the incident current (photons or electrons) to the emitted photon current, whereas the current is the flux integrated over the full sphere. Optical excitation is commonly characterized by the photon capture cross section σ_o as defined by the equation

$$\Phi_{out} = \sigma_o \Phi_{in} N_{Er} \quad (3.1)$$

where N_{Er} is the density of Er centers integrated over the depth. For the case of Er incorporation by ion implantation this value corresponds to the implanted Er dose. Φ_{in} and Φ_{out} are the incident and the emitted photon fluxes. To calculate the "effective photon capture cross section" for Si:Er from our photoluminescence experiments at 4

K, we intentionally abstract from all processes between photon absorption by the Si host and light emission from the Si:Er center. The lowest and the highest laser powers which we applied are $10\mu\text{W}$ and 1.6W . Losses due to cryostat windows and Si surface reflection reduce the power by about 70%. At the argon ion laser wavelength of $\lambda=488\text{ nm}$ the coupled incident photon fluxes (Φ_{in}) are of $7.4\times 10^{12}\text{ s}^{-1}$ and $1.2\times 10^{18}\text{ s}^{-1}$, respectively. Taking into account the extraction losses due to total internal reflection and light collection due to the experimental geometry, we obtain, at 4K, typical total output powers of $0.15\text{ }\mu\text{W}$ and $10\mu\text{W}$ which correspond to emitted photon fluxes (Φ_{out}) of $1.2\times 10^{12}\text{ s}^{-1}$ and $7.8\times 10^{13}\text{ s}^{-1}$ at $\lambda=1.54\text{ }\mu\text{m}$ for the two different injection levels. With the Er dose $N_{Er}=3\times 10^{13}\text{ cm}^{-2}$ equation (1.1) yields the values for the "effective photon capture cross section" of $\sigma_o=5.2\times 10^{-15}\text{ cm}^2$ and $\sigma_o=2.2\times 10^{-18}\text{ cm}^2$ for the low and the high power excitation, respectively.

Compared to the value of $\sigma_o=2\times 10^{-21}\text{ cm}^2$ for Er in glass hosts [3] we can conclude that the electrical excitation of the Er 4f shell luminescence is three to six orders of magnitude more efficient in Si than optical excitation in glass hosts. The internal quantum efficiency η_i , however, is low compared to III-V band edge luminescence: it decreases from 5% to 0.002% for the lowest and highest power. In the next section we show that the decrease of η_i and σ_o with excitation power is due to Auger processes that decrease both the pumping and the radiative efficiency.

3.4 Results

3.4.1 Dependence of emission intensity on temperature and pumping power

Fig. 3.2 shows the dependence of PL intensity on temperature in a semi-log plot for two different pumping powers. There are two distinct regimes indicating two different mechanisms which are responsible for the thermal quenching of the emission intensity. A double exponential fit (solid line), by the equation

$$I(T) = I_o \left[1 + c_1 \exp\left(-\frac{E_1}{kT}\right) + c_2 \exp\left(-\frac{E_2}{kT}\right) \right]^{-1} \quad (3.2)$$

gives activation energies of $E_1=10\text{ meV}$ and $E_2=160\text{ meV}$ for both pumping laser powers. The fitting parameters c_1 and c_2 can be understood as coupling coefficients for two activated processes. They depend, however, on excitation power because the quenching rate $I(T)/I_0$ decreases with increasing excitation power. In section 3.4.4 and 3.4.5 we present evidences that the two apparent processes are back transfer processes.

Figure 3.3 presents the dependence of PL intensity on laser power for different temperatures in a log-log plot. In this plot the slope of the curves increases with increasing temperature. The log-log plot reveals that particularly at the two lower temperatures the dependence cannot be described by a simple power law. The calculation of the internal quantum efficiency in the preceding section indicated a decrease of three orders of magnitude in the measured range of 5 decades of incident laser

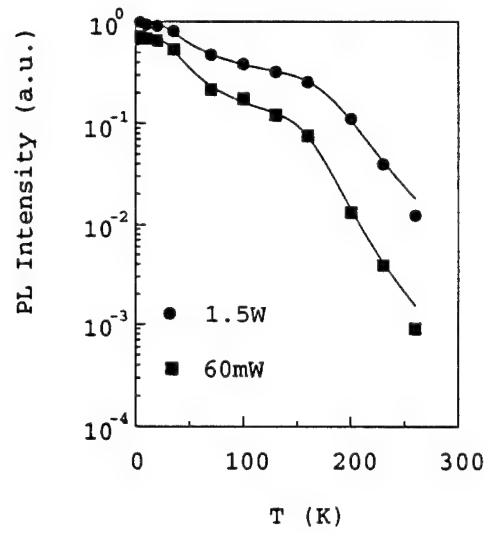


Figure 3.2: PL intensity vs. temperature for two different excitation laser powers (sample C).

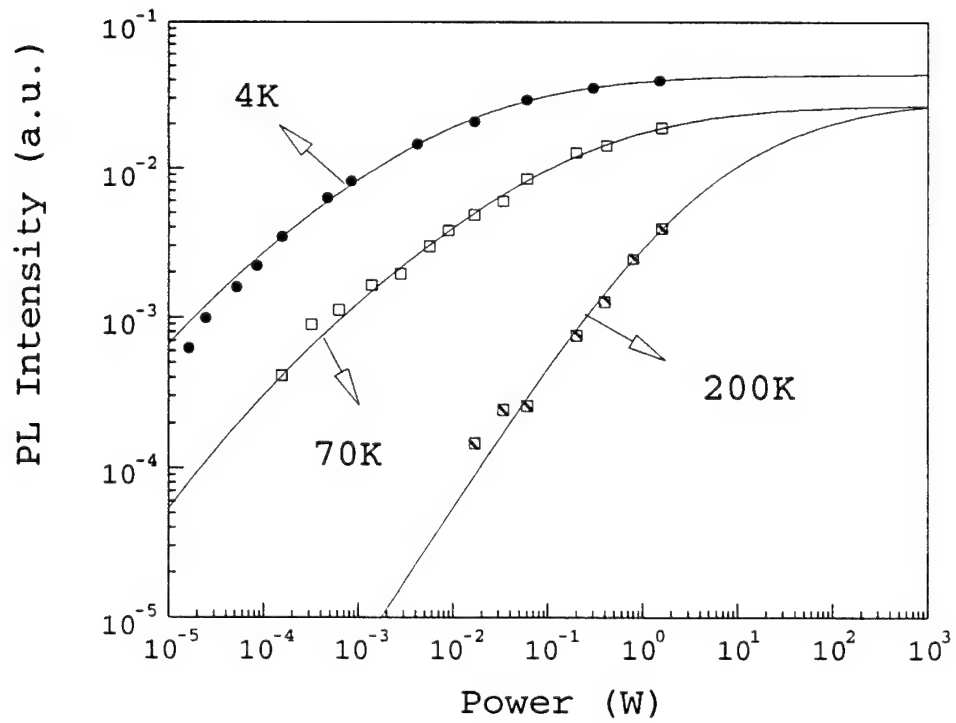


Figure 3.3: PL intensity vs. excitation power for three different temperatures (sample C).

powers (10 μ W to 1.6W). We show below that the decrease of the total efficiency is caused by Auger processes affecting both the pumping efficiency η_{pump} and the radiative efficiency η_{rad} .

$$\eta = \eta_{pump}\eta_{rad} = \frac{1}{\left(1 + \frac{\tau_c}{\tau_{ex}}\right)} \frac{1}{\left(1 + \frac{\tau_b}{\tau_{sp}}\right)} \quad (3.3)$$

The first factor (η_{pump}) reflects the temporal branching in regime III (Fig. 3.1a) by processes (τ_c) competing with the excitation (τ_e). The second factor (η_{rad}) represents back transfer processes (τ_b) competing in regime IV with spontaneous emission time (τ_{sp}). In the case of Auger processes with excess carriers we expect that each factor contains an excitation power dependence on carrier density. As shown later (in section 3.4.3) the excess carrier density is controlled by the bimolecular formation of excitons which suggests a square root dependency on generation rate, i.e. pumping power. Indeed we find that all three curves can be fit by the following function of pumping power p :

$$I(p) = \eta \frac{p}{h\nu} = \frac{c_3 + p}{(c_4 + \sqrt{p})(c_5 + \sqrt{p})} \quad (3.4)$$

where c_3 , c_4 , c_5 are fitting parameters. At 4K the output intensity apparently saturates at high powers (slope equals to zero). This maximum intensity value corresponds to the fitting parameter c_3 . All curves were fitted independently. The parameter c_3 varies only by about 40% for the three temperatures. The parameters c_4 and c_5 increase with increasing temperature: 4K: $c_4 = 0.002$, $c_5 = 0.125$; 70K: $c_4 = 0.006$, $c_5 = 0.5$; 200K: $c_4 = 3$, $c_5 = 3$. Since parameter c_3 remains approximately constant, this fitting function predicts saturation at about the same intensity at high pump powers independent of measurement temperature, as evident in Fig. 3.3. The fitting function (Eq. 3.4) is the analytical steady state solution of a set of rate equations which we present in section 3.4.3.

Fig. 3.4 compares the temperature dependence of the PL decay time (1/e time) with that of the PL intensity. The decay curves were measured at low laser powers (60 mW). As pointed out in the introduction, the simultaneous decrease of both intensity and decay time with increasing temperature is strong evidence for a competing non-radiative process that decreases the radiative efficiency of the Si:Er center. The decay time corresponds to an effective, internal lifetime τ_{eff} of the excited Si:Er center:

$$\frac{1}{\tau_{eff}} = \frac{1}{\tau_{sp}} + \frac{1}{\tau_b} \quad (3.5)$$

reflecting the decay of excited Er centers N_{Er}^* by radiative transitions (τ_{sp}) and competing back transfer processes (τ_b) to the ground state (regime IV in Fig. 3.1a). When the probability of the nonradiative transitions is greater than the spontaneous emission time, the decay time will decrease and a higher generation rate is required to achieve the same steady state population of N_{Er}^* . This construct is consistent with the changes of the PL power dependence with temperature. As the PL intensity is proportional to N_{Er}^* / τ_{sp} the PL intensity will decrease, or more power is needed

to achieve the same PL intensity. In equation (3.4) for the power dependence this decrease of efficiency with temperature is reflected by the increase of the parameters c_4 or c_5 . The physics of the temperature dependent loss process is contained in the variation of b and c with temperature.

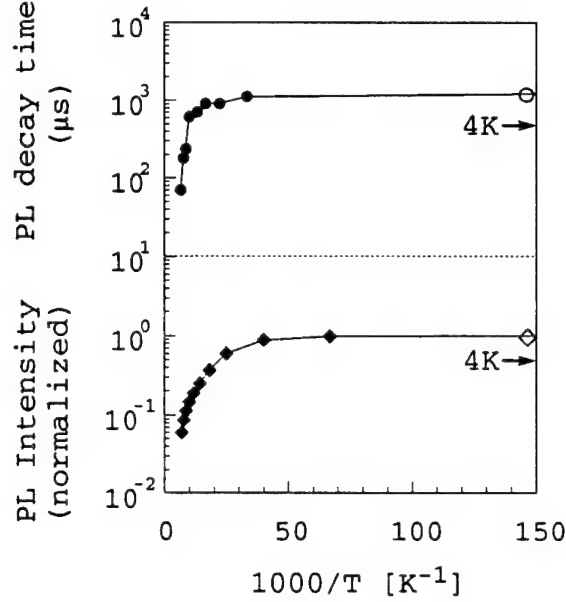


Figure 3.4: Temperature dependence of $1/e$ decay time (top) and intensity (bot.) measured at low power (PL, 60mW, sample A).

The increasing slope of the PL vs. power curves and the extrapolation to high powers indicate that for all temperatures the intensity would saturate at the same level if enough power could be provided. This behavior confirms that the total number of optically active Er centers N_{Er} is independent on temperature.

3.4.2 Electroluminescence decay curves

In the following section we investigate the processes which decrease the radiative efficiency with increasing pump power and temperature. In order to evaluate the participation of free carriers via an impurity Auger process (Fig. 3.1c) we measured EL decay curves at 40 K applying different bias conditions during the decay half cycle (Figure 3.5, LED B). Fig 3.6 shows that under zero bias conditions the decay signal is composed of a fast and a slow component. Fitting two exponentials to the measured profiles we obtain $1/e$ decay times of $82\mu\text{s}$ and $770\mu\text{s}$ contributing to the signal in an intensity ratio of 1:1. Under reverse bias the contribution of the fast component however is strongly decreased and the two exponential fit yields $110\mu\text{s}$ and 1ms and with an intensity ratio of 2:5. A small forward bias results in a very fast decay ($380\mu\text{s}$ and $49\mu\text{s}$, intensity ratio 1:3). At higher temperatures the effect of reverse bias on the contribution of the long component is even more pronounced. At 100K (Figure 3.7) the two exponential fit yields $20\mu\text{s}/700\mu\text{s}$ (intensity ratio 8:1)

under zero bias and $33\mu\text{s}/820\mu\text{s}$ (intensity ratio 1:1) under reverse bias. We observed a related phenomenon by pumping with different drive currents and measuring the EL decay under zero bias conditions.

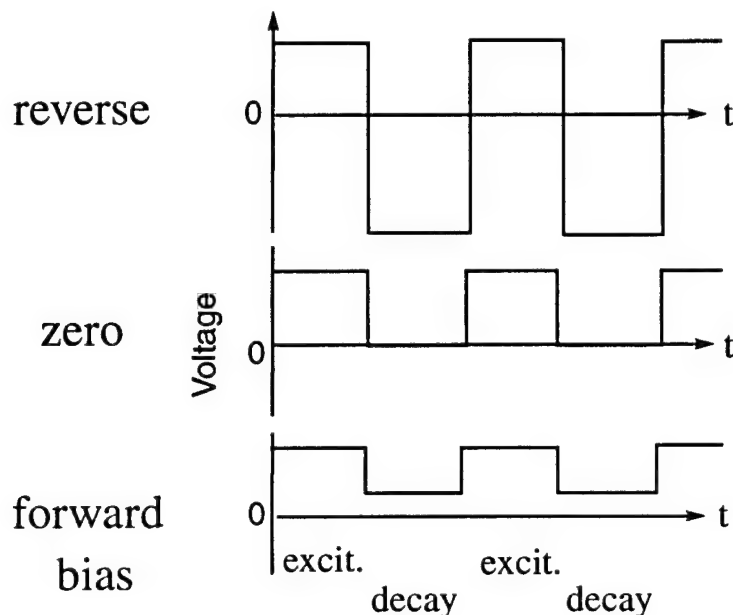


Figure 3.5: Pulse scheme for the EL decay experiments.

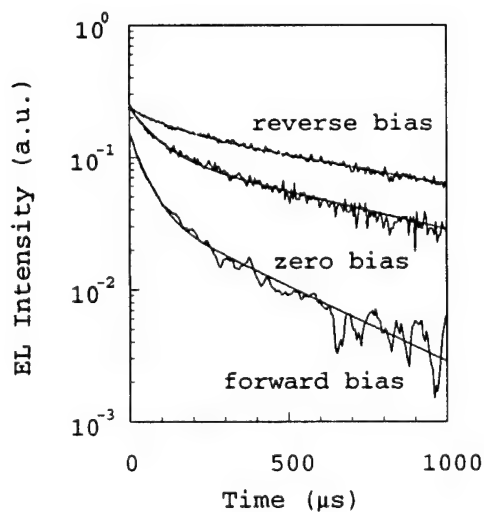


Figure 3.6: EL decay at 40K for different bias conditions during decay cycle (sample C)

Figure 3.8 shows three $930\mu\text{s}$ with an intensity ratio 1:2. Increasing the drive current to 70 mA the intensity ratio of fast ($40\mu\text{s}$) to slow ($675\mu\text{s}$) component becomes 4:1. To examine these two components we recorded EL spectra at different bias

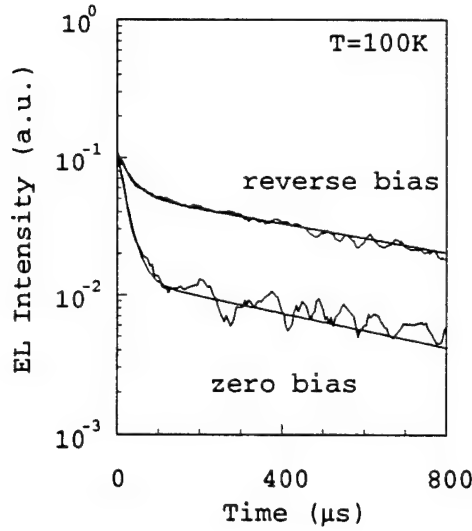


Figure 3.7: EL decay at 100K under reverse and zero bias conditions (sample C).

conditions during decay (Fig. 3.9) and for different drive currents followed by zero bias (Fig. 3.10) during the decay. The spectra are identical regardless of the different decay profiles. The EL decay experiments show that the effective lifetime decreases for forward bias relative to reverse bias conditions. The change of bias from forward to reverse bias corresponds to an increase of the depletion layer width.

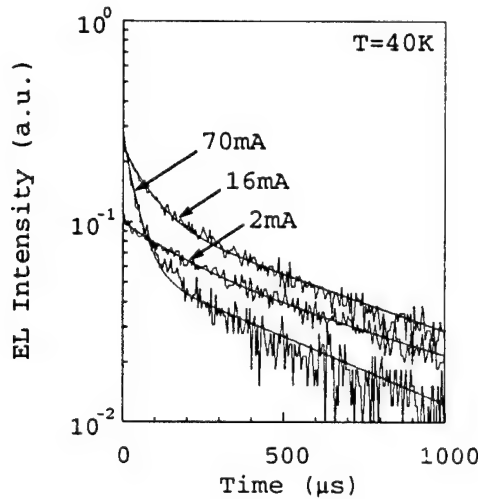


Figure 3.8: EL decay at 40K for different drive currents (sample C).

Figure position of the junction (at a depth of $1.6\mu\text{m}$) is controlled by donors introduced by Er/O implantation and annealing. Capacitance-Voltage (C-V) measurements at 40K give depletion region widths of $0.4\mu\text{m}$ and $1\mu\text{m}$ under zero and reverse bias (16V) respectively. The Er doped layer, therefore, is mostly depleted under the applied reverse bias voltage. At the measurement temperature a large fraction of the Er layer is outside the depletion region at zero bias. Taking into account

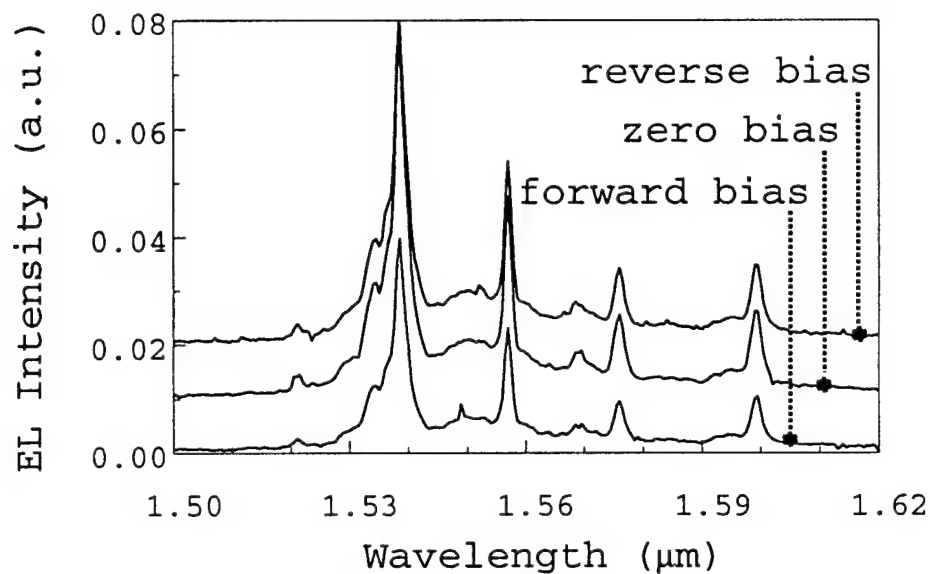


Figure 3.9: EL spectra at 40K for different bias conditions (resolution 8Å, sample C).

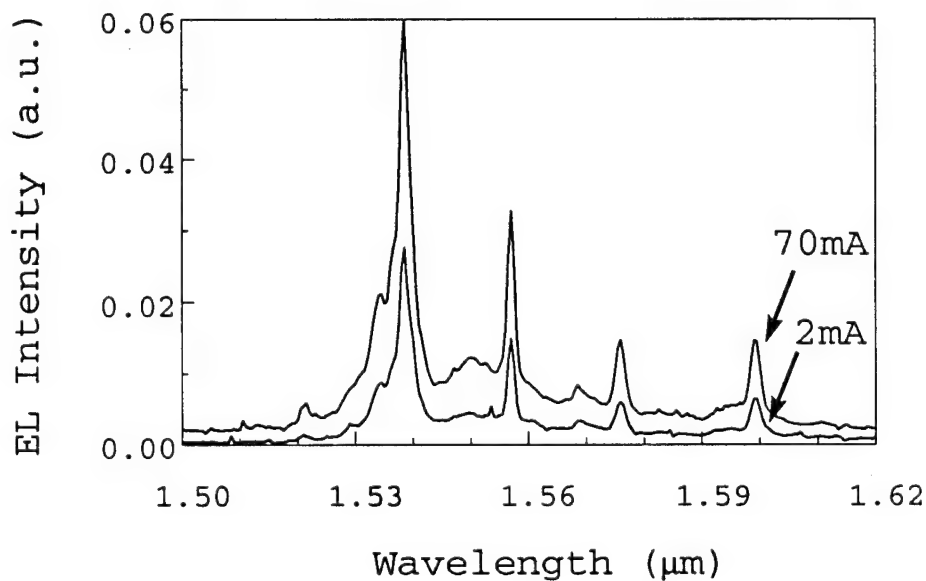


Figure 3.10: EL spectra at 40K for different drive currents at 40 K (resolution 8Å, sample C).

that the doping profile is almost symmetric near the junction, we estimate from the SIMS profile fractions of 46%, 44% and 10% of Er ions in the n-type, depletion, and p-type regions, respectively, for zero bias. For reverse bias we obtain about 23% (n), 75% (depl.) and 2% (p). Therefore the decrease of decay time at zero bias implies that the probability of the competing nonradiative process (in regime IV of Fig. 3.1a) is dependent on the availability of equilibrium free carriers.

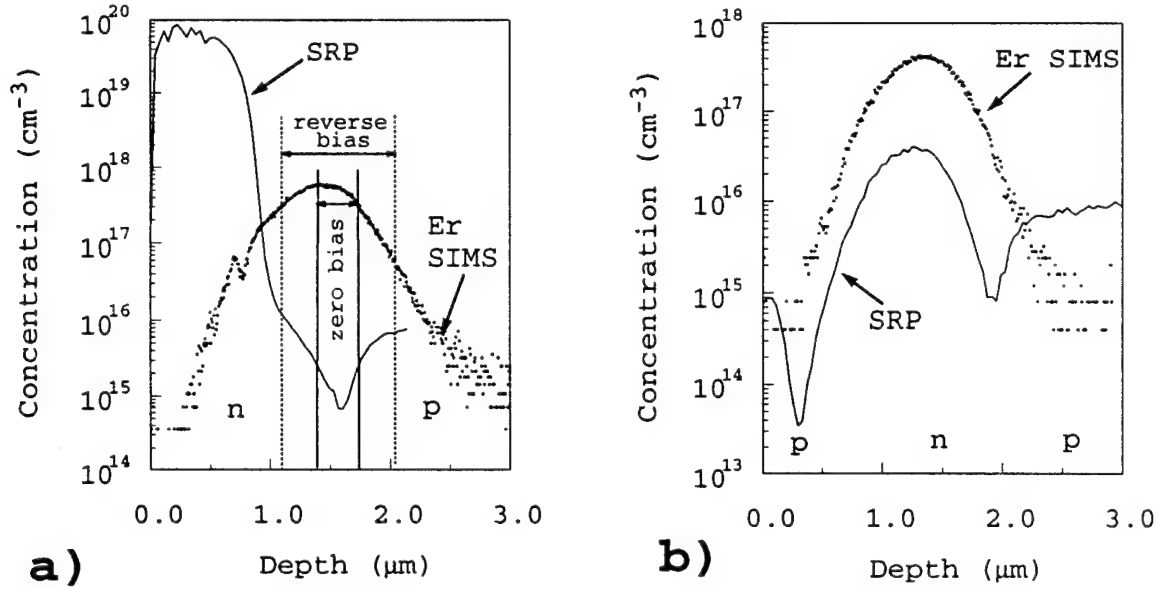


Figure 3.11: Spreading resistance and Er-SIMS profiles of a) sample C (LED, deep implanted); b) sample A (Er/O deep implanted and annealed)

As shown below (section 3.4.4) the carrier density in the n region is controlled by deep and shallow donors. If the equilibrium free carrier density increases above 40K we expect at higher temperatures a strong short component for zero bias decay which is confirmed in Fig. 3.7. The decrease of the zero bias decay time with increasing temperature and its recovery under reverse bias support the correlation between the probability of the competing nonradiative process and the availability of equilibrium free carriers. The interchange of decay time and equilibrium free carriers is a strong evidence for the luminescence quenching by an impurity Auger process. The energy of the excited luminescence center is transferred to free carriers by electron dipole or exchange interaction (Fig.3.1c). This process is responsible for effective luminescence quenching at Mn in ZnS [8, 18] as well as Mn, Gd and Tb in CdF₂ [19, 3]. The changes of the decay curves due to different drive currents (Fig. 3.8) and due to forward bias during the decay (Fig. 3.8 and Fig. 3.12) indicate that the quenching can also be induced by the injected excess carriers. The contribution of the short decay components increases with injection level. The presence of excess carriers during the decay also leads to an increase of the short contribution and the decay time of the long component decreases as the forward current during decay is increased (Fig. 3.12). This result leads to an explanation for the shape of the decay profiles under zero bias conditions: the excess carrier density decreases rapidly after switching from forward

to zero bias. The excess carriers outside the zero bias depletion region can either recombine or diffuse to the junction yielding a time dependent probability of the Auger quenching.

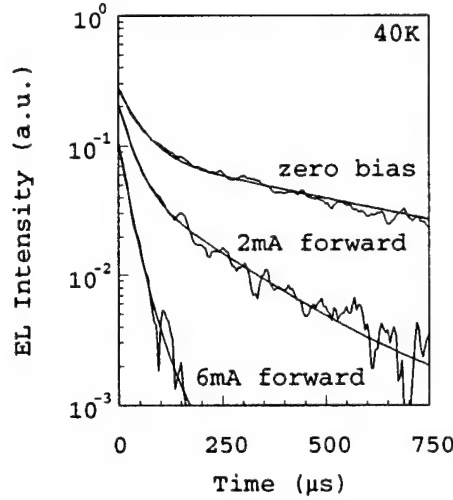


Figure 3.12: EL decay curves at 40K for zero bias and two different forward bias (corresponding to 2mA and 6mA forward current) during decay (sample C). A two exponential fit yields: $50\mu\text{s}/670\mu\text{s}$ (intensity ratio 2:1) for zero bias; $33\mu\text{s}/202\mu\text{s}$ (intensity ratio 3:1) for 2mA; $23\mu\text{s}/67\mu\text{s}$ (intensity ratio 8:1) for 6mA.

The effect of luminescence quenching by excess carriers is particularly evident in Fig. 3.8: the EL intensity for the highest drive current (70mA) drops below the EL intensity of the 16mA and the 2mA decay (the intensity scale is identical for all three decay curves). The influence of the excess carrier decay on the EL decay participates in the back transfer mechanism, which decreases the effective excited Er lifetime. The analytical fitting by two exponentials is therefore only an approximation which is convenient to describe the convoluted change of the decay curves. Increasing the driving current and, hence, the carrier density in the Er region results in an increase of the fast contribution. In order to quantitatively investigate the processes discussed above it is important to consider that the effects on the EL decay curves are due to spatial inhomogeneity, time and temperature dependent phenomena. In the next two sections we show how we can separate the impurity Auger effect by excess carriers on one hand and by equilibrium free carriers on the other hand. PL decay curves at 4 K for different pumping powers and a PL two-beam experiment correlates the back transfer deexcitation (regime IV) with excess carriers. The results can be simulated with a set of rate equations which couple the excited Er 4f shell to excess carriers by the impurity Auger effect. The temperature dependence of PL decay curves at low powers of implanted and annealed samples yield the evidence for the back transfer via free equilibrium carriers.

Two decay components with power dependent ratios of their contribution have also been observed by Coffa et al [13]. Their interpretation as two different Er species is not consistent with our investigation since the relative contributions can be controlled

by applying different bias conditions during the decay. Fig. 3.12 shows that the decay time under forward bias decreases continuously as the forward bias is increased. Therefore the decrease of decay time by increasing drive current or increasing forward bias during decay cannot be ascribed to the saturation of an Er species with a long lifetime. Such saturation would rather result in a change of the intensity ratio of the long and short components, but not in a decrease of the decay time constants of each component. In addition to that, the EL spectra give no evidence of different species since they are identical for all cases (Fig. 3.9 for different bias during decay and Fig. 3.10 for different drive currents).

3.4.3 Energy back transfer by the impurity Auger effect via excess carriers

The role of excess carrier impurity Auger back transfer is supported by PL decay curves for two different laser powers at 4K of implanted and annealed samples (sample A, without additional emitter implant) as shown in Fig. 3.13. The low temperature and the absence of a collecting junction results in a considerably longer time for the decay of the excess carrier density. The observed initial decay time therefore is much longer ($\sim 200\mu\text{s}$). In order to separate the effect of excess free carriers from equilibrium carrier quenching we performed a two-beam PL experiment at 4K: a chopped HeNe Laser (8 mW) was used for excitation and the 488 nm Ar ion laser provided a cw background generation.

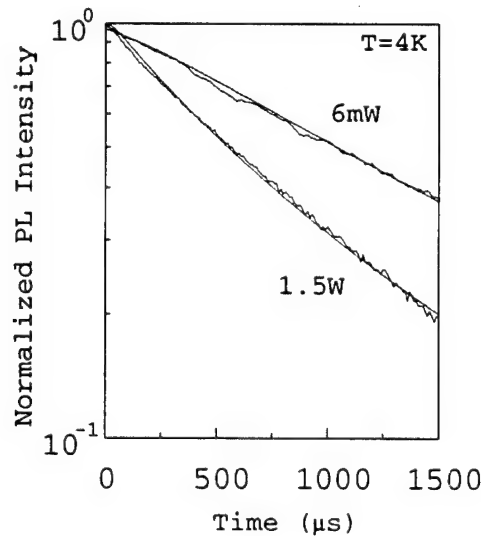


Figure 3.13: PL decay curves at 4K for two different laser powers, solid lines simulated profiles with rate equations (8a) to (8c)

As shown in Fig. 3.14 the increase of the cw laser power results in a strong decrease in the $1/e$ decay time. This result is analogous to the case of decay during forward bias in Fig. 3.12. A similar experiment was performed by Benyattou et al [9]. They showed that free carrier Auger processes decrease the pumping efficiency of

Er in GaAs. However no influence of cw background generation on decay time was observed. Since the excess carrier lifetimes are much shorter in III-V compounds than in Si a considerable photon flux is required to generate an appreciable injection level. The dependence of decay time on cw laser power, i.e. generation rate G , provides, moreover, insight into the excitation process. In the inset of Fig. 3.14 we replotted the data as $1/\tau_{eff} - 1/\tau_o$ vs. the square root of pumping power and obtained a linear relationship. τ_o is the decay time without secondary illumination.

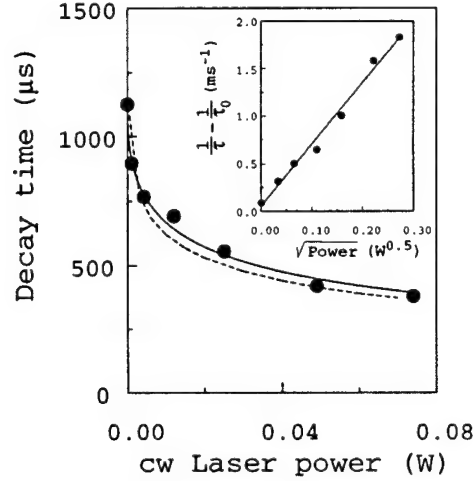


Figure 3.14: PL two-beam experiment at 4K: decay time vs. cw laser power; symbols measured data, solid line fitted by Eq. (3.6), dashed line simulation result (implanted and annealed sample).

Therefore the

$$\tau_{eff} = \frac{\tau_o}{1 + c_6 \sqrt{G}} \quad (3.6)$$

By rewriting Eq. (3.5) with $\tau_{nr}^{-1} = c_A n$ for an Auger-type process

$$\frac{1}{\tau_{eff}} = \frac{1}{\tau_{sp}} + c_A n \quad (3.7)$$

we find that the excess carrier concentration n is proportional to the square root of the generation rate G . This functional dependence implies that the excess carrier concentration is controlled by a bimolecular formation of excitons. At these low temperatures all e-h recombination processes can be disregarded because of the indirect bandgap of Si and the low probability of multiphonon processes. Recombination processes therefore always involve excitons. This supports the role of excitons in the Si:Er excitation process, as it has been proposed previously [1]. The following three rate equations, involving the excess carrier density n , the density of excitons N_x and the concentration of excited Er centers N_{Er}^* , can reflect all the features of the excitation and deexcitation processes (see Fig.3.1a to 3.1c):

$$\frac{dn}{dt} = G - an^2 \quad (3.8)$$

$$\frac{dN_x}{dt} = an^2 - c_{A,x}nN_x - \frac{N_x}{\tau_e} \left(1 - \frac{N_{Er}^*}{N_{Er}}\right) \quad (3.9)$$

$$\frac{dN_{Er}^*}{dt} = \frac{N_x}{\tau_e} \left(1 - \frac{N_{Er}^*}{N_{Er}}\right) - N_{Er}^* \left(\frac{1}{\tau_{sp}} + c_{A,Er}N_e\right) \quad (3.10)$$

Equation (3.8) describes the generation of carriers and the formation of excitons. The last term reflects the results of the two beam experiment. The excess carrier density is controlled by bimolecular formation of excitons. The form of the functional dependence of PL intensity on power Eq. (3.4) indicated that there are two loss mechanisms the rates of which increase with the excess carrier density. We identified one as the impurity Auger back transfer (regime IV). The second one is most likely the loss of excitons by Auger-type processes with free carriers (regime III) which is accounted for by the second term in equation (3.9). The third term in the exciton equation describes the excitation (τ_e) of the Er (regime III). The factor in brackets at the last term considers saturation due to a limited number of excitable Er ions N_{Er} . The last equation (3.10) for the concentration of excited Er reflects the two possible deexcitation paths (regime IV): radiative emission with spontaneous emission time τ_r and impurity Auger quenching which is proportional to the density of free carriers.

Figure 3.15 demonstrates the good agreement between the simulated and measured power dependence. The fitting function Eq. (3.4) can be derived from the analytical solution for the steady state in the limit of $N_{Er}^* \ll N_{Er}$ given by

$$I(G) = \frac{N_{Er}^*}{\tau_{sp}} = \frac{G}{\left(1 + \frac{\tau_e}{c_{A,x}} \sqrt{\frac{G}{a}}\right) \left(1 + \frac{\tau_{sp}}{c_{A,Er}} \sqrt{\frac{G}{a}}\right)} \quad (3.11)$$

The fact that $N_{Er}^* \ll N_{Er}$ holds indicates that under the present experimental conditions, i.e. Er peak concentration and depth, the maximum light output at low temperatures is limited by the Auger processes and not by the number of excitable Er ions. Due to the complex structure of the real samples (spatial inhomogeneity, surface, implantation defects etc.) this model provides only a semi-quantitative description. In the following paragraphs we apply these rate equations to describe the PL decay curves, the power dependence of the emission intensity and the two beam experiment and discuss the reasonableness and the consistency of the parameters. Assuming that the maximum applied power (1.6W in a beam spot of 2mm diameter) corresponds to a generation rate of $10^{21} \text{cm}^{-3} \text{s}^{-1}$ we obtain the following set of parameters: $\tau_{sp}=1\text{ms}$, $\tau_e=4\mu\text{s}$, $a=10^{-12} \text{cm}^3 \text{s}^{-1}$, $c_{A,x}=1 \times 10^{-10} \text{cm}^3 \text{s}^{-1}$, $c_{A,Er} = (0.2 \text{ to } 1) \times 10^{-12} \text{cm}^3 \text{s}^{-1}$. The solid lines in Fig. 3.13 show the simulated decay profiles for two different excitation powers, demonstrating that the observed fast component appears indeed at high generation rates and is due to the initial decay of excess carrier. The inset of Figure 3.12 compares simulated normalized decay curves with $c_{A,Er}=0$ and $c_{A,Er}=10^{-12} \text{cm}^3 \text{s}^{-1}$. In the case of $c_{A,Er}=0$, i.e. no back transfer, there is no influence of the other loss process (regime III) on the decay time, i.e. in this case the excitonic Auger recombination. The dashed line in Figure 3.14 illustrates the excellent results of the application of the model and the parameters to the PL two beam experiment.

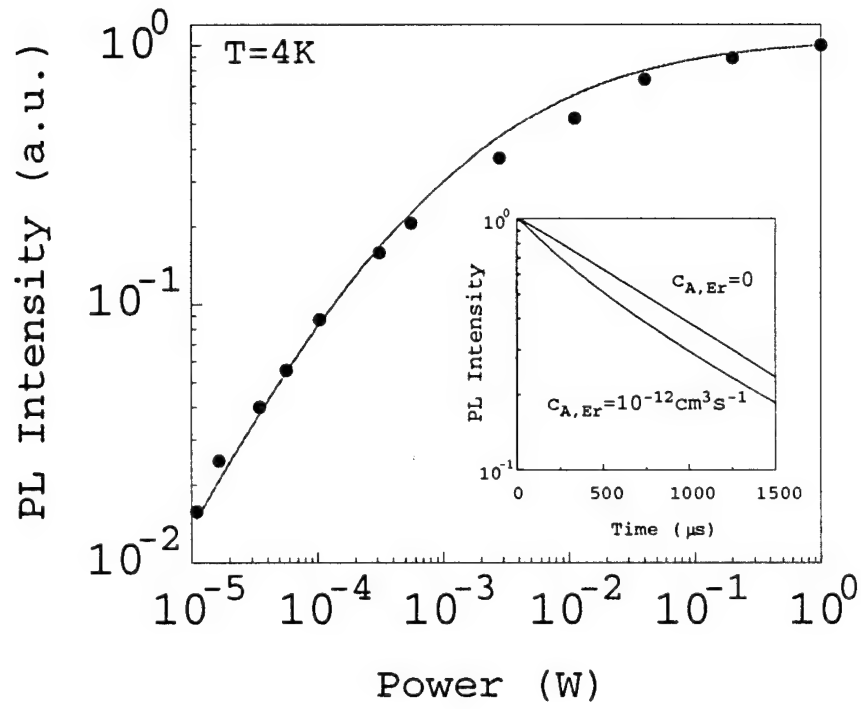


Figure 3.15: Simulation results: power dependence at 4K; data points (symbols) from 4K curve in Fig. 3.3. ; solid line simulated with $\tau_r=1\text{ms}$, $\tau_e=4\mu\text{s}$, $a=10^{-12}\text{cm}^3\text{s}^{-1}$, $c_{A,x}=1\times 10^{-10}\text{cm}^3\text{s}^{-1}$, $c_{A,Er}=10^{-12}\text{cm}^3\text{s}^{-1}$. Inset: simulated decay curves for high generation rates ($G=10^{22}\text{cm}^{-3}\text{s}^{-1}$) illustrating the effect of impurity Auger back transfer on the decay curve. The intensity is normalized.

The process of excitonic Auger recombination for low carrier concentrations in Si has been investigated by Hangleiter et al [22]. They discussed the electron-hole-electron recombination processes considering the effect of electron hole correlation due to Coulombic interaction which enhance the probability of Auger processes particularly at low temperatures and low carrier densities. Introducing an electron-hole correlation factor g_{eeh} the rate for Auger recombination becomes $R = g_{eeh} c_A n^2 p$. The correlation factor depends on the carrier concentration and temperature. From Fig. 2 in [22] one obtains a simple relationship $g_{eeh} = 5 \times 10^{17} \text{cm}^3/n$ which fits the experimental and theoretical data of that paper well in the concentration range between 10^{16}cm^{-3} and 10^{18}cm^{-3} . With the free carrier Auger coefficient for high concentrations [14], $c_A = 2 \times 10^{-31} \text{cm}^{-6} \text{s}^{-1}$, this leads to $R = 1 \times 10^{-12} \text{cm}^{-3} \text{s}^{-1}$. In our simple three particle model (free electrons, excitons and Er centers) we split the electron-hole-electron interaction into two subsequent steps: exciton formation and exciton-electron Auger recombination (see Fig.3.1b). Since the total rate is given by the slower process we can conclude that the values obtained from our simulations ($a = 10^{-12} \text{cm}^3 \text{s}^{-1}$, $c_{A,x} = 1 \times 10^{-10} \text{cm}^3 \text{s}^{-1}$) agree very well with this work. Note that our simulations (equations (3.8) to (3.10)) and the fitting to the experimental results cover only the low temperature PL (4K) where all background carriers are frozen and only excess carriers ($n=p$) are considered. The model assumptions regarding exciton formation and exciton electron Auger recombination can also be confirmed by measuring the power dependence of the boron bound exciton line at $1.14 \mu\text{m}$. The binding of an exciton at the neutral boron and the subsequent radiative recombination is a competitive process in regime III. Since the emission intensity is proportional to the number of excitons, we obtain:

$$N_x = \frac{G}{\left(\frac{1}{\tau_e} + c_{A,x} \sqrt{\frac{G}{a}}\right)} \quad (3.12)$$

$$PL_{B-BE} = \frac{c_7 p}{c_8 + \sqrt{p}} \quad (3.13)$$

Fig. 3.16 demonstrates that the intensity of the boron exciton line (see inset) follows this dependence over four decades of excitation laser power.

The coefficient for the impurity Auger effect was calculated by Langer [3, 24]. Assuming only electric dipole interaction a simple formula was obtained for the impurity Auger coefficient $c_{A,Imp}$ and the critical density n_o where radiative and radiationless processes have equal rates:

$$c_{A,Imp} c_{A,Imp} = (n_o \tau_{sp})^{-1} \quad (3.14)$$

$$n_o = 4\pi^{\frac{5}{2}} n_r^5 \lambda_o^{\frac{-7}{2}} \sqrt{\frac{m^* \alpha_B}{m_o \alpha_o}} \quad (3.15)$$

n_r is the refractive index, λ_o is the transition wavelength, m^* and m_o are the effective and the free electron mass, respectively, $\alpha_o = 1/137$ and α_B is the Bohr electron radius. Substituting the symbols with the corresponding values for Er in Si ($\lambda_o = 1.54 \mu\text{m}$, $\tau_r = 1 \text{ms}$) we obtain: $n_o = 7.6 \times 10^{14} \text{cm}^{-3}$ and $c_{A,Er} = 1.4 \times 10^{-12} \text{cm}^{-3} \text{s}^{-1}$ which is in good agreement with our value obtained from the simulations.

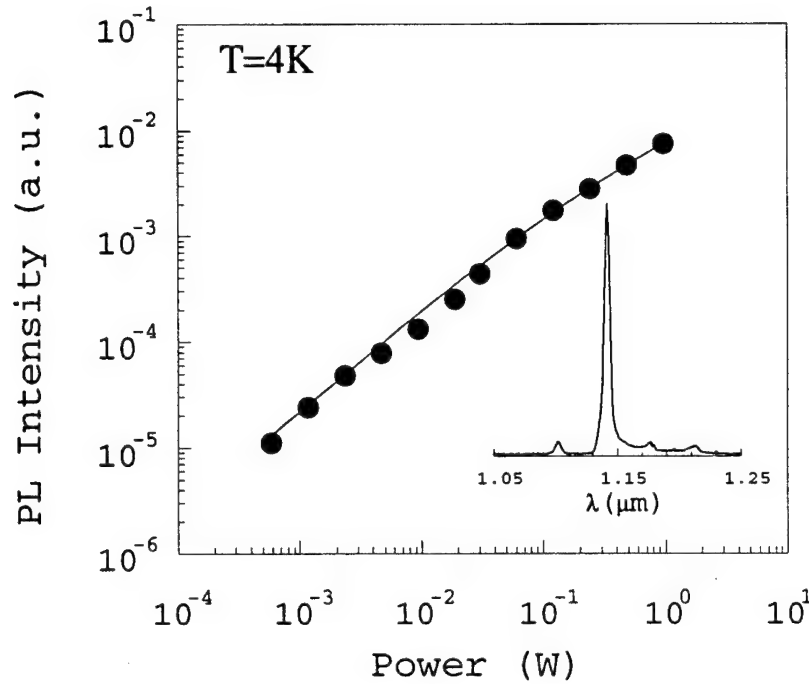


Figure 3.16: Power dependence of the boron bound exciton line intensity (4K, sample A, PL spectrum in inset). Solid line fitted with equation (3.13).

3.4.4 Energy back transfer by the impurity Auger effect via equilibrium free carriers

Spreading resistance measurements on Er/O implanted and annealed samples revealed the type conversion of a large fraction of the implanted layer from p-type to n-type (Fig.3.11b, sample A). The comparison with the SIMS profile shows that most of the implanted Er lies in the n-type region as well as in the depletion region of the second junction. Temperature dependent Hall effect measurements on a shallow implanted sample (sample B) show the presence of shallow and deep donors after the implantation and annealing process with thermal activation energies of 20meV and 160meV [25]. As the concentration of shallow donors ($\sim 5 \times 10^{16} \text{cm}^{-3}$) is about six times higher than the shallow boron acceptors ($8 \times 10^{15} \text{cm}^{-3}$) the apparent activation energy measured for temperatures above 70 K corresponds to the half of the true ionization energy of 40meV (i.e. negligible compensation). In the following section we show that these shallow donor states provide the electrons for the impurity Auger back transfer process.

Fig. 3.17 shows the PL With increasing temperatures a fast component appears. We can rule out the effect of excess carriers discussed in the previous section. There is no fast component at 4K. For a given pumping power the quenching effect via excess carriers should be most pronounced at low temperatures where the excess carrier lifetimes are long enough. Considering the spatial distribution of the Si:Er centers presented in Fig. 3.11b we propose that the two decay components correspond to

the decay of Er centers in the n-type ($n>0$) and the depletion region ($n=0$). In the n-type region the concentration of equilibrium free electrons increases with increasing temperatures by ionization of the shallow donor states. These free carriers reduce the effective excited state lifetime of Si:Er centers in this region by the impurity Auger effect. While the temperature dependence of the contributions, i.e. ratio of intensities, of the fast and the slow component depend on the distribution of generated carriers and the spatial distribution of donors, the decay time should have a simple temperature dependence. Rewriting equation (3.6) with the thermally activated concentration of carriers we obtain:

$$\tau_{eff} = \left[\frac{1}{\tau_{sp}} + c_9 \exp\left(-\frac{E_A}{kT}\right) \right]^{-1} \quad (3.16)$$

In Fig. 3.18 we plot the short decay time as a function of temperature. The solid line is a fit with equation (3.16). We obtain $\tau_r=1290\mu s$, $c=0.067$ and $E_A = 24\text{meV}$. The activation energy of 24 meV is in good agreement with the free carrier activation energy obtained from the Hall effect measurement.

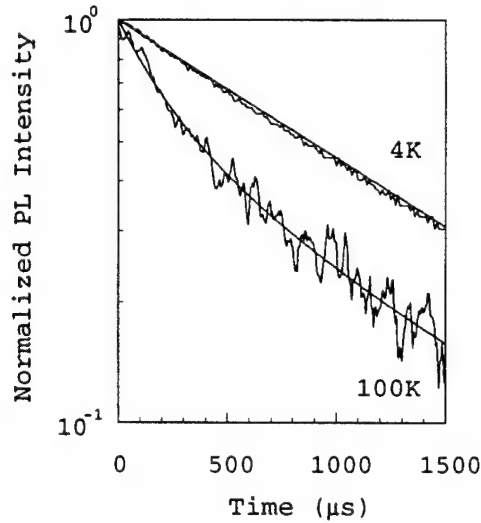


Figure 3.17: Low power PL decay curves and fitted exponentials (60mW, sample A); 4K: one exponential (1290ms), 100K two exponentials ($270\mu s$ and $1033\mu s$).

In order to estimate the upper limit of the contribution of the impurity Auger effect with equilibrium free carriers to the thermal quenching of intensity we replace $c_A A$ and n of equation (3.7) with the impurity Auger coefficient obtained from our simulations ($c_A=10^{-12} \text{ cm}^{-3} \text{ s}^{-1}$) and the maximum carrier concentration at 300K obtained from SRP of sample A (Fig. 3.16, $n=2 \times 10^{-16} \text{ cm}^{-3}$). We obtain an effective lifetime of $20\mu s$. Compared to the spontaneous emission time of 1ms this would account only for a quenching by a factor of $\tau_r/\tau_{eff}=50$ which is much less than observed for low laser powers ($\sim 10^3$). It is evident however that the first step of thermal quenching between 4K and 100K (Fig. 3.2) can be attributed to impurity Auger back transfer with equilibrium free carriers. The apparent activation energy $E_1=10\text{meV}$ for intensity

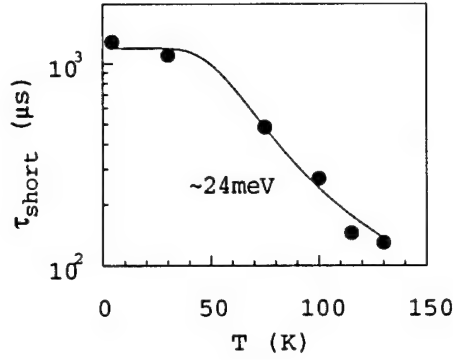


Figure 3.18: Temperature dependence of the short PL decay component (60mW, sample A); solid line fitted with equation (3.16)

quenching obtained from the fitting by Eq. (3.2) is different from the value obtained from the initial decay time because the total emission intensity is determined by Si:Er centers in all three regions (n, p and depletion layer). The disagreement between the observed quenching rate of emission intensity and the extrapolated lifetime quenching by impurity Auger effect suggests that the observed activation energy of 160meV cannot be due to impurity Auger quenching by free carriers which are released from deep donors at E_c -160meV. In the next section we present experimental evidence for this important conclusion. We reveal the presence of a second back transfer process from Si:Er which is responsible for the thermal quenching above 100K.

3.4.5 Evidence for a second back transfer process

In the preceding section we have shown that the fast component in the low power PL experiment, which arises at higher temperatures, can be attributed to the impurity Auger effect via free equilibrium carriers in the n-type region. In Fig. 3.19 we plot the temperature dependence of the long component corresponding to the Er centers in the depletion region (circles). Due to the absence of free equilibrium carriers the decay time is almost constant in the range from 4K to 100K. For higher temperatures, however, also the long component decreases rapidly. The solid line is a fit with equation (3.16) which yields an activation energy of about 150 meV. In order to examine the role of the depletion region width we performed a corresponding EL experiment on a processed 400keV LED (sample D). The EL decay curves were measured under reverse bias conditions. Fig. 3.19 (diamonds) demonstrates that the long decay component shows the same dependence as in the PL experiments. Above 100K the long component decreases rapidly with the same activation energy (150 meV) and it falls below the system response time at temperatures above 150K. We have shown by the EL experiments (section 3.4.2, Figs. 3.6 and 3.7) that the contribution of the long component can be controlled by the reverse bias.

This observation is consistent with the attribution of the long decay component of the EL decay to Si:Er centers inside the depletion region. By temperature dependent C-V measurements we confirmed that the reverse bias depletion layer width of the

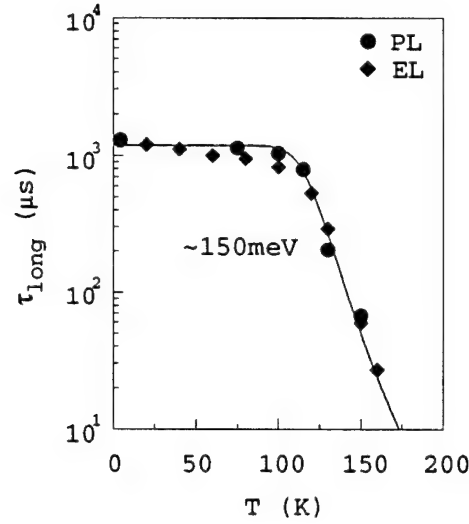


Figure 3.19: Temperature dependence of the short PL decay component (60mW, sample A); solid line fitted with equation (3.16)

shallow implant LED decreases only by about 5% from 100K to 300K. This small decrease is consistent with the asymmetric junction of the shallow implant device (not shown here). The narrower distribution of Er for the shallow implant (peak depth at 130 nm) ensures that at all Er centers are inside the large reverse bias depletion region (800nm). Hence, despite the absence of free carriers we can observe a strong decrease of the excited Er lifetime. This result leads to the important conclusion that the thermal quenching above 100K must be caused by a different, nonradiative energy back transfer mechanism. The activation energy of 150meV corresponds approximately to the second activation energy obtained from the temperature dependence of the emission intensity (Fig. 3.2 and equation (3.2)). The energy is close to the deep donor level which we obtained from Hall effect. Er/O related states in the bandgap close to E_C -160meV have been previously found by other groups by Deep Level Transient Spectroscopy (DLTS) measurements [10, 11, 15]. In references [10, 11] the authors proposed the thermalization of the exciton bound to a E_C -150meV band gap state as the quenching mechanism for the luminescence of Er in Si. This, however, would only decrease the pumping efficiency (regime III, Fig.3.1) and should not result in the decrease of the effective excited state lifetime, as discussed above. The paper by Coffa [13] reported the decrease of the 1/e time of the two observed decay component with temperature. This was attributed to back transfer processes. In [11], however, the decay curves were fitted with two decay components with 1/e times apparently independent on temperature of $\sim 50\mu s$ and $\sim 800\mu s$ decay components decrease subsequently with increasing temperature below the time resolution of our system ($20\mu s$). As a possible second back transfer process we suggest the nonradiative energy transfer from the excited Si:Er to the excitation of a carrier bound to the 160meV donor level. This would require thermal energy to compensate the energy mismatch between the 0.81eV 4f transition energy and the distance between valence band and donor level

$\Delta E = (E_c - 0.16 \text{ eV}) - 0.81 \text{ eV} = 0.15 \text{ eV}$. A similar process has been proposed for Yb in InP by Taguchi et al. [27].

3.5 Conclusion

We have shown that the thermal quenching of the Er luminescence in Si is caused by nonradiative energy back transfer processes. The total number of excitable Er remains constant with temperature. We have demonstrated that the impurity Auger process is the dominant quenching mechanism for Er in Si below 100K. The observed fast initial decay component at high pumping powers was attributed to the decay of the excess carrier concentration which results in a time dependent probability of the nonradiative energy back transfer. Considering exciton formation, exciton-electron Auger recombination and the impurity Auger effect with free (excess) carriers the power dependence, the decay curve and the PL-two beam experiment can be well described by analytic simulation. The thermal quenching above 100K is due to an additional back transfer which is yet to be identified.

Bibliography

- [1] H. Ennen, J. Schneider, G. Pomrenke, and A. Axmann, Appl. Phys. Lett. 43, 943 (1983).
- [2] B. Zheng, J. Michel, F.Y.G. Ren, L.C. Kimerling, D.C. Jacobson and J.M. Poate, Appl. Phys. Lett. 64, 2842 (1994).
- [3] F.Y.G. Ren, J. Michel, Q. Sun-Paduan, B. Zheng, H. Kitawa, D.C. Jacobson, J.M. Poate and L.C. Kimerling, Mat. Res. Soc. Symp. Proceedings, 301, 87 (1993).
- [4] D. J. Eaglesham, J. Michel, E.A. Fitzgerald, D.C. Jacobson, J. M. Poate, J. L. Benton, A. Polman, Y.-H. Xie, and L.C. Kimerling, Appl. Phys. Lett. 58, 2797 (1991).
- [5] S. Coffa, F. Priolo, G. Franzo, V. Bellani, A. Carnera, and C. Spinella, Phys. Rev B. 48, 11782 (1993).
- [6] A. Polman, J.S. Custer, E. Snoeks and G.N. van den Hoven, Nucl. Instrum. Methods B 80/81, 653 (1993).
- [7] P. Favennec, H. L'Haridon, D. Moutonnet, M. Salvi and M. Gauneau, J. Appl. Phys. 29, L524 (1990).
- [8] F.Y.G. Ren, J. Michel, D.C. Jacobson, J.M. Poate and L.C. Kimerling, Mat. Res. Soc. Symp. Proceedings 316, 493 (1994).
- [9] J. Michel, J.L. Benton, R.F. Ferrante, D.C. Jacobson, D.J. Eaglesham, E.A. Fitzgerald, Y.-H. Xie, J.M. Poate, and L.C. Kimerling, J. Appl. Phys. 70, 2672 (1991).
- [10] S. Libertino, S. Coffa, G. Franzo, and F. Priolo, J. Appl. Phys. 78, 3867 (1995).
- [11] F. Priolo, G. Franzo, S. Coffa, A. Polman, S. Libertino, R. Barklie and D. Carey, J. Appl. Phys. 78, 3874 (1995).
- [12] J. Michel, F.Y. Ren, B. Zheng, D.C. Jacobson, J.M. Poate, and L.C. Kimerling, Materials Science Forum 143-147, 707 (1994).
- [13] S. Coffa, F. Priolo, G. Franzo, V. Bellani, A. Carnera, and C. Spinella, Phys. Rev. B 48, 11782 (1993).

- [14] S. Coffa, G. Franzo, F. Priolo, A. Polman, and R. Serna, *Phys. Rev. B.* 49, 16313 (1994).
- [15] I.N. Yassievich and L.C. Kimerling, *Semicond. Sci. Technol.* 7, 1 (1993).
- [16] W. J. Miniscalco, *J. Lightwave Technol.* 9, 234 (1991).
- [17] N.T. Gordon and J.W. Allen, *Solid State Commun* 37 1441 (1981).
- [18] J.M. Langer, A. Lemanska-Bajorek, A. Suchocki, W. Walukiewicz, and B. Wiktor, *J. Luminescence* 24/25, 889(1981).
- [19] A. Suchocki and J.M. Langer, *Phys. Rev. B.* 39, 7905 (1989).
- [20] J.M. Langer, *Electroluminescence*, Springer Proceedings in Physics, S. Shionoya and H. Kobayashi (Eds), Vol. 38, pp 16-23, Springer Verlag, Berlin Heidelberg 1989.
- [21] T. Benyattou, D. Seghier, G. Guillot, R. Moncorge, P. Galtier, and M.N. Charasse, *Appl. Phys. Lett.* 58, 2132 (1991).
- [22] A. Hangleiter and R. Hcker, *Phys. Rev. Lett.* 65, 215 (1990).
- [23] D.B. Laks, G.F. Neumark, A. Hangleiter, and S.T. Pantelides, *Phys. Rev. Lett.* 61, 1229 (1988).
- [24] J. M. Langer, *J. Luminescence* 40&41, 589 (1988).
- [25] J. Palm, S. Nelson, A. Agarwal, B. Zheng, S. Ahn, and L.C. Kimerling, to be published.
- [26] J.L. Benton, J. Michel, L.C. Kimerling, D.C. Jacobson, Y.-H. Xie, D.J. Eaglesham, E.A. Fitzgerald, and J.M. Poate, *J.Appl. Phys.* 70, 2667 (1991)
- [27] A. Taguchi, K.Takahei, and Y. Horikoshi, *J. Appl. Phys.* 76, 7288 (1994).

Chapter 4

Electronic Structure of Erbium Centers in Silicon

4.1 Introduction

The properties of rare earth ions in solids have been studied in detail for decades. However, until recently this research has been predominantly restricted to ionic crystals, such as oxides and fluorides. Absorption and fluorescence spectra with sharp lines in the visible or infrared regions have been observed in these ionic materials where the RE ions are mostly in the 3+ charge state [1]. The identification of free ion levels from ionic material spectra was highly successful and the lower levels for almost all of RE ions have been identified by interpreting the spectra as transitions between the excited and ground spin-orbit states of the ions weakly split by the crystal field [2]. The studies of RE ions have been extended to more covalently bonded hosts such as tetrahedral III-VI semiconductors, and luminescence of 4f ions has been observed [3]. The study of the luminescence properties of RE ions in semiconductors such as GaAs, InP, and Si just gained interest in the 1980s due to their optoelectronic potential for dc-pumped 4f-doped light emitting diodes (LEDs) and lasers [4]. Since the first discovery of sharp line luminescence spectra from Er in III-V semiconductors and Si by Ennen *et al.* [4], exciting possibilities for creating optical devices in Si and for integrating electrical and optical devices in circuits fabricated in silicon have been proposed. Erbium impurities in silicon have the important technological property of exhibiting sharp luminescence at 1.54 μm which can be excited either optically or electronically [4]. The 1.54 μm luminescence is interpreted as the result of an intra-4f transition and should be assigned to transitions from the first excited spin-orbit state $^4I_{13/2}$ to the $^4I_{15/2}$ ground state of Er^{3+} ($4f^{11}$) which are weakly split by the crystalline field [4]. However, almost nothing is known about the chemical nature of erbium impurities in silicon. In fact, neither the Er lattice location nor the oxidation state is well known. Moreover, it is not known whether Er exists as an isolated impurity or whether it forms complexes with other impurities. Even though it has been demonstrated that co-implantation with O, C, N, and F enhances the 1.54 μm luminescence of Er in silicon [5], the first step to understand the nature

of the chemical behavior of partially filled 4f shell in covalently bonded Si crystal, is to study the electronic structure of an isolated Er impurity.

The first theoretical study of Si:Er system was done by Delerue and Lannoo using a tight-binding Green's-function technique [6]. The Er 4f states were treated as a frozen core and the 5d and 6s shells were considered in the electronic structure calculations. The results showed that there were no 5d-derived gap states and the 4f states were found to be resonant in the Si valence band, leaving 3+ as the only oxidation state. Another theoretical simulation, using first-principle calculations, was done by Needels *et al.* in a 32-atom supercell of Si with the framework of the density-functional theory and relativistic norm-conserving pseudopotentials [7]. The 4f electrons were treated as core electrons and it was found that Er^{3+} at a tetrahedral interstitial site is the minimum energy configuration. The common point between these theoretical simulations is that they supposed an atomic like point of view for Er, as in metals, i.e., they considered that Er 4f states could be treated as core states, in spite of Si being a covalently bonded semiconductor.

In this work, we report on self-consistent one-electron electronic structure calculations for isolated interstitial and substitutional Er impurity in Si using the multiple-scattering molecular cluster model [8, 9] which has been used successfully to describe the electronic structure of impurities in semiconductors [10]. The Hedin-Lundqvist approach is used to describe the local exchange-correlation potential [11]. A non-empirical muffin-tin overlapping spheres model is adopted [12]. The 4f atomic orbitals are treated as valence states in order to investigate whether the interaction between Er 4f states and Si host atoms plays an important role in determining the electronic properties of the centers. Moreover, the evaluation of this interaction is required to achieve the crystal field splitting energy which is expected to be close to 0.1 eV with or without including multiplet interactions for compact 4f states. As relativistic effects should be important to describe Er atom, a quasirelativistic one-electron theory is adopted [13]. Even though spin-orbit term is not included in this approach, it has been shown that this approach could lead to equivalent results for valence levels when compared with full relativistic scheme [11]. Therefore, in this work, we can find out if relativistic calculations are important to describe Er in Si. Since the approach used here is only capable of describing one electron states, the transitions between ground and excited multiplet states are not evaluated. The cluster used in our studies to simulate the substitutional Er impurity is a 71-atom cluster, which comprises a central Er atom surrounded by 34 Si atoms (four shells of neighbors) and 36 H terminators. The tetrahedral interstitial Er impurity was simulated by a 39-atom cluster which comprises 14 Si atoms (three shells of neighbors), 24 H terminators, and the Er atom, which is placed at the center of the cluster.

4.2 Results and Discussion

In order to analyse the results related to the impurities, we must start by reporting the results of the electronic structure calculation for the perfect clusters which simulate the Si crystal. The values of 1.6 eV and 10.7 eV were obtained for the crystal band

gap and valence band width, respectively, for the 38-atom cluster. For the 71-atom cluster, these values are 1.2 eV and 13.5 eV. These results are in good agreement with experimental data [1] and show that the selected clusters are a good start point to simulate the Er impurities.

The SCF energy spectrum of the $\text{Er}_i\text{Si}_{14}\text{H}_{24}$ cluster is shown in Figure 1. In order to better characterize the impurity levels we selected the Er 4f-related levels and some valence energy levels from the complete spectrum. The molecular orbitals are classified according to the irreducible representations of the T_d point group. The numbers between square brackets denote the occupancy of the levels and within parentheses is given the orbital configuration for each energy level inside the Er sphere. The first interesting feature that emerges from the simulations is that the Er 4f-related states are strongly localized energy levels, they have a $4f^{12.08}$ configuration; they show a very weak interaction with Si neighbors; and they are located closed the bottom of the conduction band (CB). The crystal field splitting energy (CFS) is 0.43 eV. This energetic localization could be understood by analyzing the selected valence energy levels shown in Figure 1. Those levels describe a weak covalent interaction between the impurity and the Si crystal valence states. The t_2 levels have contributions in the Er sphere that are related with the 4f, 5d and 6p Er orbitals. These contributions are related with the 4f and 6s orbitals for the a_1 levels, with the 5d orbitals for e states, and with 4f orbitals for t_1 energy levels. By adding all contributions inside the Er sphere related with all the Si valence states we obtain the configuration $4f^{0.31}6s^{0.19}5d^{1.09}6p^{0.68}$ showing that the total number of electrons inside the Er sphere in the crystal valence band (VB) is 2.27.

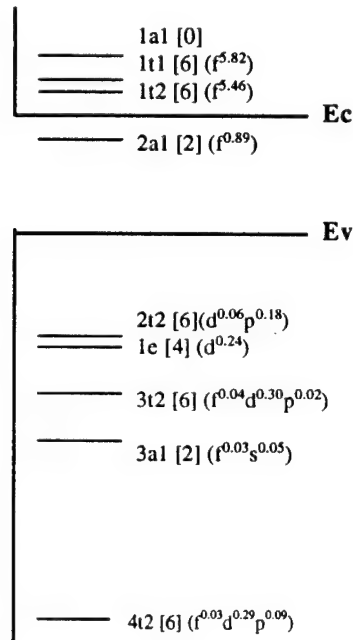


Figure 4.1: SCF energy spectrum of the $\text{Er}_i\text{Si}_{14}\text{H}_{24}$ cluster

From this results it is clear that, besides 4f and 6s orbitals, the 5d and 6p excited

states play an important role in describing the interactions between the Er_i impurity and Si crystal. In addition to that, the 4f orbitals are involved in the hybridization process showing contributions in the covalent interaction. Even though the neutral cluster shows a close shell configuration, we can say that Er_i center is not stable because it displays occupied energy levels in the CB.

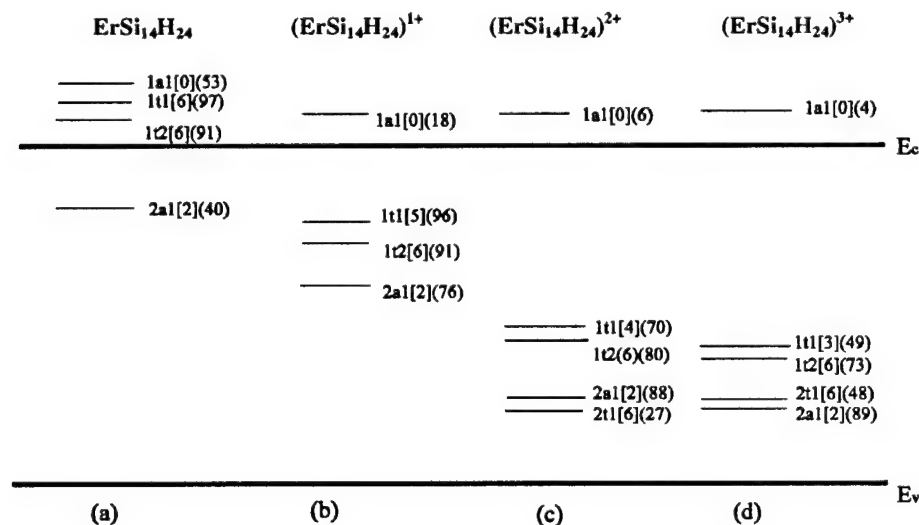


Figure 4.2: SCF energy levels of different charge states of the $\text{Er}_i\text{Si}_{14}\text{H}_{24}$ cluster, from neutral to triply ionized (a - d)

In order to have a better understanding of this behavior, three positively charged states were simulated and the results show that the 4f-derived states are located in the Si band gap. These results are shown in Figure 2 and, as we can see, when one electron is removed from the $1t_1$ orbital in order to simulate the $1+$ charged state, the $1a_1$ level turns to be delocalized and the CFS can be evaluated by taking in consideration only the $1t_1, 1t_2$, and $2a_1$ levels and its value is 0.23 eV. Even though a larger interaction between the Er_i and Si host atoms takes place, the CFS is almost unchanged when the $2+$ and $3+$ states are simulated. The total number of electrons in the crystal VB, inside the Er sphere, slightly increase as electrons are removed from $1t_1$ gap level as shown in Table 8.1. The number of electrons (n) in the Er 4f-derived gap states is also shown. Although our calculations show that n decreases when electrons are taken out from the pure 4f t_1 state, the total charge inside the Er_i sphere does not decrease in the same ratio, showing that the Aldane and Anderson mechanism is operative, supporting the role of covalent effects [3].

This fact confirms the necessity of treating the 4f orbitals as valence states. Among the results obtained by the simulation of the charged states for Er_i center, the $3+$ state displays an electronic configuration close to $4f^{11}$ and a 0.18 eV CFS. The simulations using the spin-unrestrict formalism show that the exchange split is larger than the CFS and all the configurations present high spin. As the highest occupied gap energy level has t_1 symmetry, the clusters in the $1+$ and $2+$ states have an open shell configuration and probably are unstable with respect to Jahn Teller distortions, which

Cluster	Er	VB	n	$\Delta(\text{CFS})$ (eV)
$\text{ErSi}_{14}\text{H}_{24}$	$5s^{1.96}5p^{5.28}4f^{12.39}6s^{0.19}5d^{1.09}6p^{0.68}$	$4f^{0.31}6s^{0.19}5d^{1.09}6p^{0.68}$	12.08	0.43
$(\text{ErSi}_{14}\text{H}_{24})^{1+}$	$5s^{1.96}5p^{5.28}4f^{12.39}6s^{0.24}5d^{1.15}6p^{0.71}$	$4f^{0.61}6s^{0.24}5d^{1.15}6p^{0.71}$	11.78	0.23
$(\text{ErSi}_{14}\text{H}_{24})^{2+}$	$5s^{1.96}5p^{5.34}4f^{12.32}6s^{0.16}5d^{1.15}6p^{0.64}$	$4f^{0.86}6s^{0.16}5d^{1.15}6p^{0.64}$	11.46	0.17
$(\text{ErSi}_{14}\text{H}_{24})^{3+}$	$5s^{1.96}5p^{5.34}4f^{12.15}6s^{0.18}5d^{1.42}6p^{0.65}$	$4f^{0.61}6s^{0.18}5d^{1.42}6p^{0.65}$	11.13	0.18

Table 4.1: Electronic configuration of $\text{Er}_i\text{Si}_{14}\text{H}_{24}$ cluster for different charged states, n is the number of pure 4f electrons.

we have not investigated. It is worth mentioning that the Er 5s and 5p atomic orbitals were considered as valence states and they give rise to two atomic-like energy levels below the bottom of the VB. When quasirelativistic calculations were done, the results showed that the overall features described above unchanged and the only significant change was that the 5s and 5p orbitals showed a more localized character. In conclusion, we find Er_i^{3+} is the most stable state in T_d symmetry with a gap electronic configuration close to $4f^{11}$, a CFS of 0.18 eV and a spin $S = 3/2$.

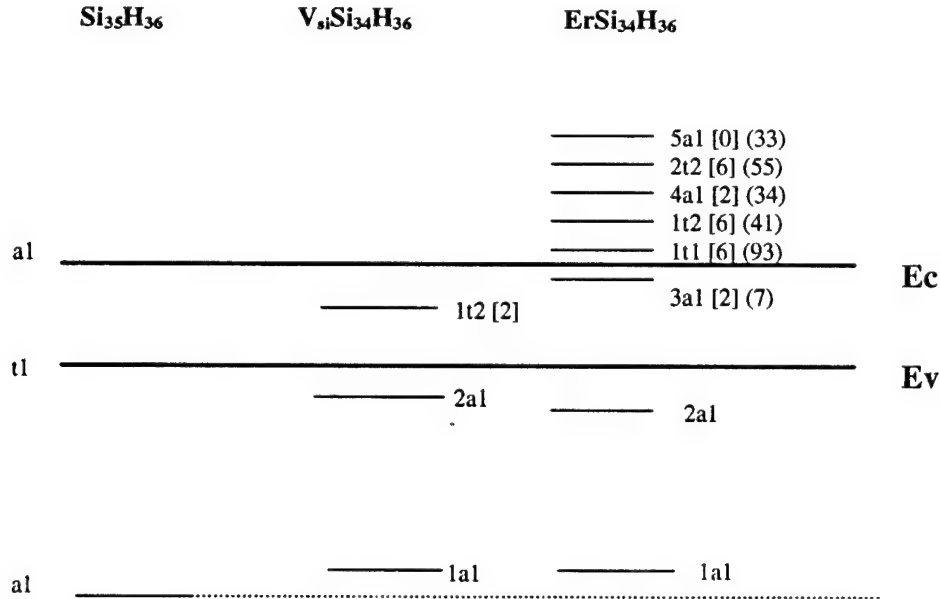


Figure 4.3: Schematic diagram of the SCF energy levels of $\text{Si}_{35}\text{H}_{36}$, $\text{V}_i\text{Si}_{34}\text{H}_{36}$, and $\text{Er}_i\text{Si}_{34}\text{H}_{36}$ clusters

The SCF electronic states of the $\text{Er}_i\text{Si}_{34}\text{H}_{36}$ cluster are shown in Figure 3. The results for the band edge of $\text{Si}_{35}\text{H}_{36}$ cluster, as well as for the ideal Si vacancy, simulated by the $\text{V}_i\text{Si}_{34}\text{H}_{36}$ cluster are shown. The numbers between parentheses denote the percentage of charge, normalized to one electron, inside the Er_i sphere. The occupancy of the levels is given within square brackets. This figure is not scaled. The $\text{Er}_i\text{Si}_{34}\text{H}_{36}$ cluster orbitals, from $3a_1$ to $5a_1$, are 4f-related energy levels and can be

described by a $4f^{12.08}$ configuration. Except for $3a_1$ orbital, all Er 4f states are located in the crystal CB. The CFS is 0.66 eV. By comparing the results obtained for the Si vacancy and the Er_s center, we can infer that the Er 4f states do not reconstruct the Si vacancy dangling-bonds and interact with the t_2 vacancy energy level and Si CB states. As in the case of Er_i , the Er_s energy spectrum displays valence energy levels that have contributions in the Er sphere related with 4f, 5d, 6s and 6p atomic orbitals. the valence energy levels' configuration $4f^{0.39}6s^{0.51}5d^{1.24}6p^{0.53}$. Although the neutral cluster show a close shell configuration, the center is not stable because of the occupied energy levels in the CB. A positive charge state cluster was simulated and the results are exactly the same displayed by the neutral state. Quasirelativistic calculations were done and, as in the case of Er_i center, the results showed that this corrections are not important to describe the valence states.

In conclusion, among the configuration studied in this work, the Er_i^{3+} center is the most stable structure which shows 4f related energy levels in the crystal band gap with a small crystal field splitting, a $4f^{11}$ configuration and spin $S = 3/2$. The Er_s center is unstable since the results show occupied energy levels in the CB. Hybridization among Er 4f, 6s, 5d and 6p atomic orbitals is observed and is responsible for the weak interaction between the impurity and the Si crystal. The analysis of our results lead to the conclusion that when 4f orbitals are treated as valence states, hybridization among impurity 4f, 6s, 5d and 6p orbitals drives the 4f related energy levels to be located in the Si band gap for the Er_i center and in the CB for Er_s center. We can also conclude that ligands, such as O, N, F and C, are not required for parity breaking since the Er_i electronic structure results show a weak interaction between Er and Si host atoms, which is enough to split the 4f states.

Bibliography

- [1] H. M. Crosswhite e H. W. Moos, "*Optical Properties of Ions in Crystals*", John Wiley & Sons, New York, 1967.
- [2] G. H. Dieke, "*Spectra and Energy Levels of Rare Earth Ions in Crystals*", John Wiley & Sons, New York, 1968.
- [3] M.R.Brown, A.F.J.Cox,W.S.Shand, and J.M. Williams, in "Advances in Quantum Eletronics", edited by D.W. Goodwin (Academic, London, 1974), vol.2 p.69
- [4] H. Ennen and J. Schneider, Appl. Phys. Lett. **43**,943 (1983); *ibid* **46**,381 (1985).
- [5] J. Michel, J. L. Benton, R. F. Ferrante, D.C. Jacobson, D.J. Eaglesham, E.A. Fitzgerald, Y.-H. Xi, J. M. Poate, and L. C. Kimerling, J. Appl. Phys. **70**,2672 (1991).
- [6] C. DeLerue and M. Lannoo, Phys. Rev. Lett. **67**, 3006 (1991); Mater. Sci. Forum **143-147**, 699 (1994).
- [7] M. Needles, M. Schlüter, and M. Lannoo, Phys. Rev. B **47**,15553 (1993).
- [8] K. H. Johnson, in "*Advances in Quantum Chemistry*", edited by P.O. Löwdin (Academic,New York,1973),vol. 7, p. 143.
- [9] J. C. Slater, "*The Self-Consistent Field for Molecules and Solids*"(McGraw Hill,New York,1974)
- [10] L. V. C Assali and J. R. Leite, Phys. Rev. B, ;Phys. Rev. Lett. ; Mater. Sci Forum ;*ibid*, ;
- [11] L. Hedin and B. I. Lundqvist, J. Phys. C **4**,2064 (1971).
- [12] J. C. Norman Jr., Mol. Phys. **31**,1191 (1976).
- [13] C. Y. Yang and S. Rabii, Phys. Rev. A **12**, 362 (1975).
- [14] D. A. Case and C. Y. Yang, J. Chem. Phys. **72**, 3443 (1980).
- [15] A. Frova and P. Handler, Phys. Rev Lett. **14**,178 (1965); W. B. Grobman and D. E Eastman, Phys. Rev. Lett. **29**,1508 (1972).
- [16] A. Zunger,Solid State Physics **39**,275 (1985).

Chapter 5

Optical Activity of Erbium-Doped Silicon

5.1 Introduction

The future of Si:Er as an optoelectronic semiconductor material relies on successful development of high performance Si:Er photonic devices. Maximizing the concentration of optically active Er centers in Si:Er is a necessary step to achieve strong light emission and to obtain good Si:Er device performance. Significant progress has been made in recent years to improve Si:Er performance. Many questions still remain, as discussed in Chapter 2. The exact structure of optically active Er centers is not yet known. The current challenge in Si:Er research is to further enhance light emission intensity by optimizing processing conditions.

As was described in Section 2.2.3, the brightest $1.54\mu m$ emission of Si:Er thus far comes from Si:Er material co-implanted with selected electronegative impurities [6][7]. The co-doped electronegative impurities such as O, F, C and N⁻ form ligands with Er^{3+} in Si and are necessary to achieve Er optical activity in Si [20][6]. The EXAFS study on the local structure of Er^{3+} in Er doped Czochralski-grown (Cz) silicon and erbium-doped Float-zone grown (Fz) silicon indicates that Er^{3+} is dominantly surrounded by oxygen atoms in Si(Cz):Er, conversely, in Si(Fz):Er which yields very weak light emission, Er^{3+} is mainly surrounded by Si atoms [51].

In this chapter, the impact of oxygen co-implantation on the Er light emission will be discussed further. Oxygen was the first and is the most common impurity element used to enhance the light emission in Si:Er, largely because it is an impurity in concentration $\sim 10^{18} \text{cm}^{-3}$ in Cz-Si. The heat treatment process of Si:Er with oxygen ligands will be analyzed in the first section to help design optimized processing.

In the following section, a systematic study of the interaction of Er^{3+} with fluorine ligand in Si is presented to confirm our understanding of the physical processes occurring during Si:Er heat treatment and of the structure of the optically active Er centers. Fluorine was chosen as a prototype dopant primarily because it interacts strongly with Er in Si. We found that the light intensity from Si:Er co-doped with fluorine was 100 times stronger than with oxygen doping at the same level. In addition, fluorine is a low concentration impurity in Si compared with 10^{18}cm^{-3} oxygen in Cz silicon and 10^{16}cm^{-3} oxygen level in Fz silicon. This low background allows us to observe the interaction of Er^{3+} and F under a wider range of F concentrations. Furthermore, because fluorine should have a sizable solubility in Si due to its small atomic radius (0.57\AA), F in Si should remain in solution during heat treatment. Finally, the F level in Si can be more precisely profiled experimentally using Secondary Ion Mass Spectroscopy (SIMS) because the relative sensitivity factor of F is two orders of magnitude better than that of O in Si for SIMS measurements [56]. The SIMS depth profiles of F in Si provide valuable microstructural information concerning the physical processes in Si:Er during heat treatment.

In the last section, a simulation model based on the solid state reactions and ligand out-diffusion is constructed to simulate the physical processes taking place during Si:Er heat treatment. The simulated results are compared with the PL intensities and SIMS depth profiles in Si:Er to demonstrate the important role of the complex dissociation and the out-diffusion of the ligands such as F and O during Si:Er heat treatment.

5.2 Experiment

Er ion implantation was performed at room temperature. For Si:Er with oxygen co-implantation (Si:Er-O), 5.25 MeV or 4.5 MeV Er implantations were used to produce an Er profiles with projected ranges R_p at $1.78\mu m$ and $1.5\mu m$, respectively. The Er peak concentration was $1 \times 10^{18} cm^{-3}$. Additional oxygen co-implantation at 1.08 MeV produced an oxygen profile which matched the Er profile. The oxygen peak concentration was $1 \times 10^{18} cm^{-3}$. For studies of Si:Er with F ligand (Si:Er-F), 1 MeV Er implantation was used with an implantation dose of $1 \times 10^{13} cm^{-2}$ to produce an Er profile with a peak concentration of $5 \times 10^{17} cm^{-3}$ at a depth of $0.3\mu m$. F co-implants were done with an ion energy of 150 keV to match the Er spatial profile. The F dose was varied from $1.0 \times 10^{13} cm^{-2}$ to $1.0 \times 10^{15} cm^{-2}$ to give a corresponding F peak concentration $[F]_{peak}$ from $5 \times 10^{17} cm^{-3}$ to $5 \times 10^{19} cm^{-3}$. A 500Ω -cm Fz Si substrate was chosen to provide a low oxygen background level ($< 10^{16} cm^{-3}$).

The heat treatment was carried out in a conventional quartz furnace, purged continuously with Ar gas. The samples were placed between two clean Si wafers to minimize any impurity contamination. Photoluminescence (PL) measurements (see Appendix A for details) were done at 4.2 K with a 2 W argon ion laser emitting at 488 nm, a 0.75 m Spex spectrometer and a cooled Ge detector. The excitation power was varied from 0.3 W to 1.5 W to saturate the Er^{3+} centers. The Si:Er light intensity was measured at the PL peak emission intensity at $\lambda = 1.54\mu m$.

5.3 Si:Er with Oxygen Co-implantation

Post-implantation annealing is critical to remove implantation damage and to optically activate Er in Si. The Er light emission in Si is very sensitive to the processing temperature and time. Figure 5-1 shows the effect of annealing temperature on the light emission of Si:Er co-doped with oxygen. At low annealing temperature, large amount of displacement defects introduced by the implantation are still present. The dominant optically active centers are erbium-defect complexes. No significant differ-

ence in PL intensity due to the oxygen level in Si is observed. At higher temperature annealing ($T \geq 800^\circ\text{C}$), the dominant optically active centers are erbium-oxygen ($\text{Er} - \text{O}_x$) complexes. We observe a significant increase in the PL intensity from high levels of oxygen in Cz-Si and from the additional oxygen co-implantations. At even higher temperature, $\text{Er} - \text{O}_x$ complexes start to dissociate. The oxygen out-diffusion at the high temperature significantly reduce the free oxygen concentration in Si:Er. Therefore, the number of optically active erbium-oxygen complexes and the PL intensity in Si:Er decrease.

The optimum annealing temperature to obtain the maximum light emission from erbium-doped Cz-silicon is 900°C . This optimum temperature shifts to a lower temperature with additional oxygen co-implantation as shown in Figure 5-1. A similar shift of the optimum annealing temperature to a lower temperature was also observed in Si:Er-F system as the F implantation dose increased (see the following section). The reason for this shift is the fast rate of the Er-O association to form the optically active centers because of the shorter diffusion distance with a larger concentration of oxygen.

The annealing time also has a significant effect on the Er^{3+} luminescence intensity in Si:Er. Figure 5-2 shows the effect of heat treatment time on the Er light emission in Si:Er with oxygen co-implantation. The PL peak intensity (shown in the insert) reaches its maximum after an 1/2h anneal and starts to decrease rapidly for annealing beyond 1h. The PL intensity decays more slowly at longer annealing times. The spectra of the Er^{3+} light emission at $\lambda = 1.54\mu\text{m}$ is also shown in Figure 5-2. They evolve into simpler spectra as the annealing time prolongs. The development of the spectra is believed to result from the changes of the local environment around optically active Er centers.

High resolution spectra show more clearly the evolution of PL spectra of Si:Er as the annealing time increases. Figure 5-3 compares the high resolution spectrum of Si:Er-O annealed for 1/2h with that of Si:Er-O annealed for 32h at 900°C . The spectral resolution in Figure 5-3 is 2\AA , as compared with 40\AA resolution in Figure 5-2. After 1/2h annealing, there are many clearly defined lines present in the spectrum

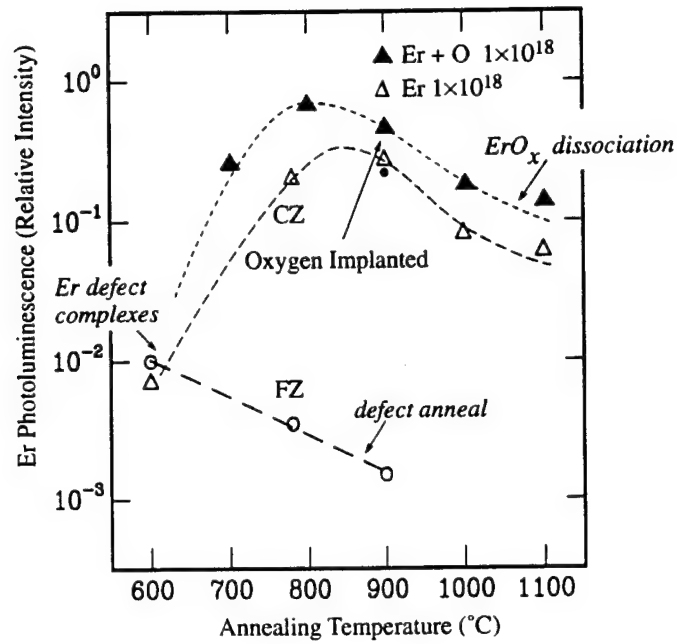


Figure 5-1: Photoluminescence intensities of Si:Er doped with oxygen are compared with those of Si(Cz):Er, Si(Fz):Er as a function of annealing temperatures. Data for Si(Cz):Er and Si(Fz):Er labeled by Δ , \bullet and \circ are taken from reference [6].

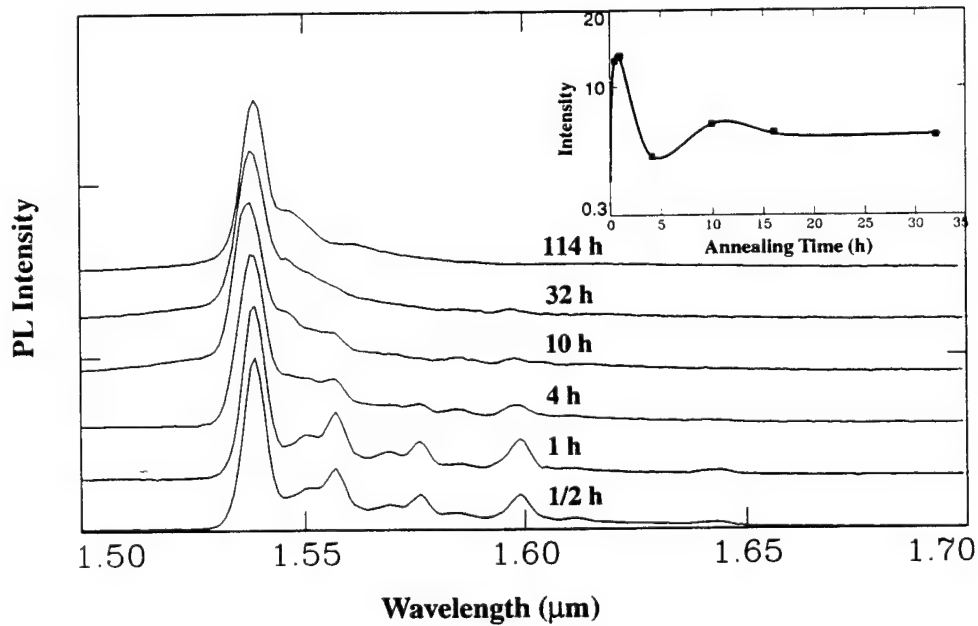


Figure 5-2: The effect of annealing time on the luminescence spectra of Si:Er-O after 900°C isothermal annealing. The insert shows the PL peak intensity of Si:Er-O decays with the annealing time.

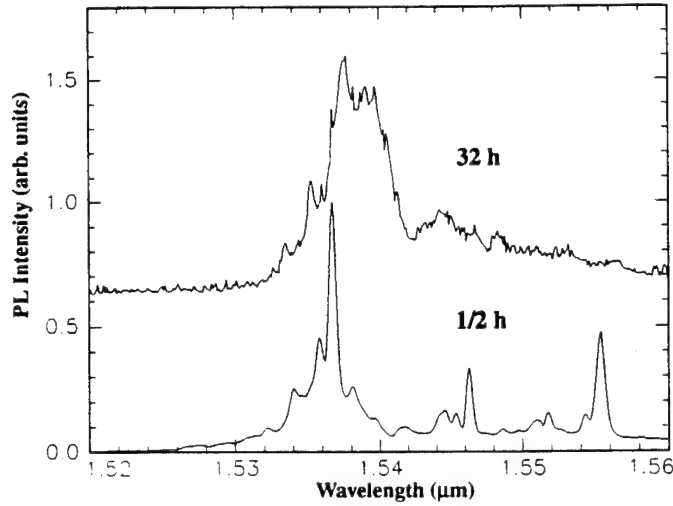


Figure 5-3: The impact of longer annealing time on high resolution spectra of Si:Er doped with oxygen.

in Figure 5-3. The luminescence lines indicate that there is more than one optically active Er center in Si:Er because the characteristic 5-line spectrum is lost, the additional centers must occupy sites with lower symmetry than T_d . There appear to be a limited number of luminescence centers with well-defined structures after the 1/2 h anneal. In contrast, after 32 h annealing, Si:Er spectrum shows no separable spectral lines around $\lambda = 1.54\mu m$ and display primarily inhomogenous broadening. It is similar to the inhomogenous broadening of the spectral lines in rare earth doped mixed ionic crystal [57]. This broadening signifies the contribution of many more Er-related luminescence centers in different symmetry sites.

A similar evolution of Er^{3+} spectra is also observed as the annealing temperature increases. A $1000^{\circ}C$, 1/2 hour anneal yields a spectrum similar to the $900^{\circ}C$, 4-10h anneal in terms of both spectral features and photoluminescence intensity. In other words, an equivalent impact on the Er PL spectra can be achieved by either high temperature and short time annealing or low temperature and long time annealing. This result suggests that the post-implantation heat treatment process of Si:Er is kinetically limited, most likely controlled by a diffusion process. A similar impact on the Er^{3+} spectra due to the heat treatment was also observed in Si:Er-F.

The role of a diffusion controlled process is further supported by the additive effect on the Er light emission of sequential processing cycles. For each process cycle, the effects on the PL intensity and the spectral features are additive. In other words, the effect of two separate 900°C , 30 min anneals is equivalent to that of one one-hour annealing at 900°C . Furthermore, the heat treatment process involving the optically active Er centers is irreversible. In an experiment in which Si:Er samples with oxygen were first annealed between $1100 - 1300^{\circ}\text{C}$ for 1h, little effect on the PL intensity (or a slight decrease of PL intensity) was produced by an additional 30min anneal at 900°C . Similarly, no effect on PL intensity was observed in Si:Er from a 450°C and up to 100h annealing, following a 900°C , 30min annealing [6].

At high temperature, the PL intensity decreases significantly, as shown in Figure 5-4. The heat treatment process at $T \geq 1000^{\circ}\text{C}$ is dominated by the dissociation of Er-O complexes and outdiffusion of O ligand. Fast out-diffusion rate at these temperatures results in a significant reduction in the concentration of the optically active centers in Si:Er. At such high temperature, Er diffusion becomes significant and Er silicide starts to precipitate. The Er precipitation process results in a further reduction of the light emission intensity. The activation energy ($\sim 4.5\text{eV}$) in Figure 5-4 represents the rate of this kinetic process determined by the Er-O complex dissociation and the O ligand outdiffusion and the Er silicide precipitation. For actual Si:Er devices, such high temperature processing should be avoided.

In summary, it is found the optically active centers in Si:Er-O are metastable after post-implantation heat treatment. Increasing annealing time has the same impact on the optically active Er centers as increasing annealing temperature in the temperature range between $900 - 1100^{\circ}\text{C}$ for Si:Er with oxygen co-implantation. The optimum annealing temperature of Si:Er shifts to a lower temperatures with increasing oxygen co-implantation doses.

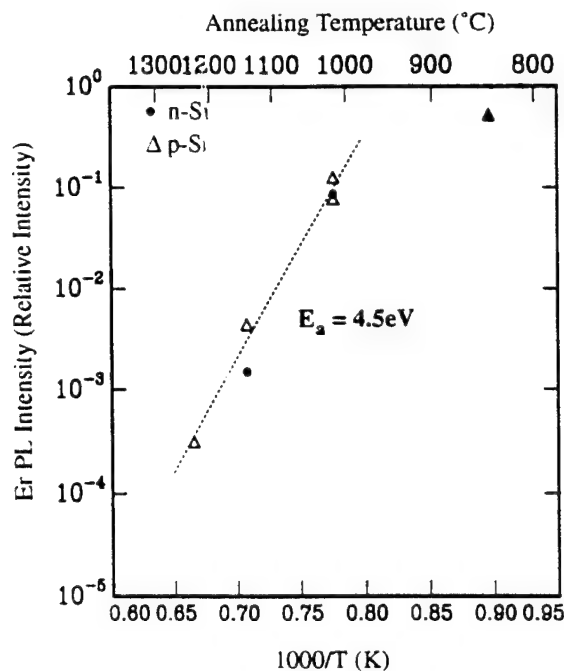


Figure 5-4: An Arrhenius relationship of the Er^{3+} PL intensity of Si:Er doped with oxygen after high temperature annealing. The samples are Er doped n or p type Fz-Si co-doped with $1 \times 10^{18} cm^{-3}$ oxygen.

5.4 Si:Er with F Co-implantation

Figure 5-5 shows the light emission enhancement in Si:Er using F co-implantation (Si:Er-F). The magnitudes of the luminescence peak intensity at 4.2 K are shown here as a function of F concentration in Si:Er for different annealing temperatures of a 1/2 hour anneal. The maximum luminescence intensity from Cz Si ($1 \times 10^{18} cm^{-3}$ oxygen) with the same Er concentration is marked with the horizontal dashed line. The oxygen anneal was optimum at $900^\circ C$ for 1/2 hour for Er in Cz-Si. In comparison, fluorine has a clear advantage over oxygen in Si:Er. Figure 5-6 compares the effect of O and F co-implantation on the Er PL intensity at 4.2K. Both samples have the same Er concentration and undergo the same $900^\circ C$, 30 min anneal. The Er emission with $[F]_{peak} = 4 \times 10^{18} cm^{-3}$ is two orders of magnitude stronger than Er in Cz-Si with oxygen level at $1 \times 10^{18} cm^{-3}$. For $[F]_{peak} = 1 \times 10^{18} cm^{-3}$, the Er light emission intensity is a factor of ten greater than oxygen, as seen in Figure 5-5.

The light emission from Si:Er increases with the initial F implantation concen-

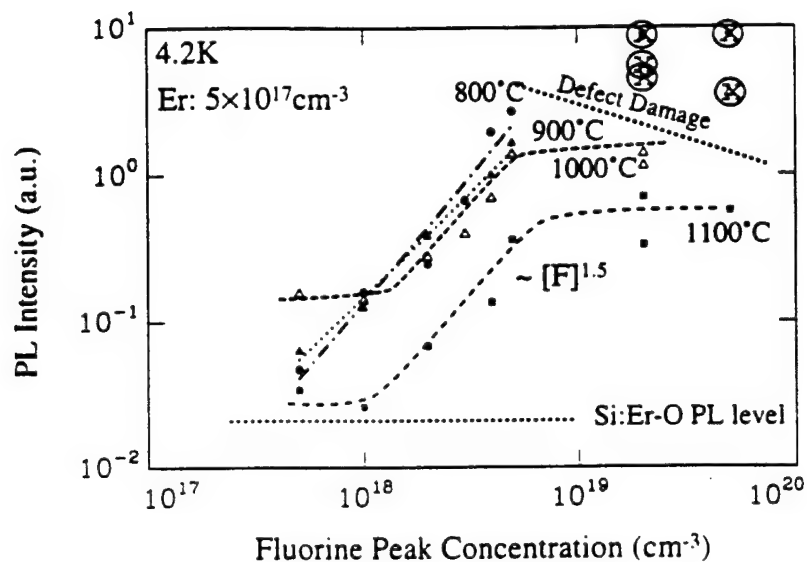


Figure 5-5: The effect of F co-implantation on the PL peak intensity of Si:Er after 30 min anneal. Horizontal dashed line is the PL intensity in Si:Er with $1 \times 10^{18} \text{ cm}^{-3}$ oxygen after 900°C , 30 min heat treatment.

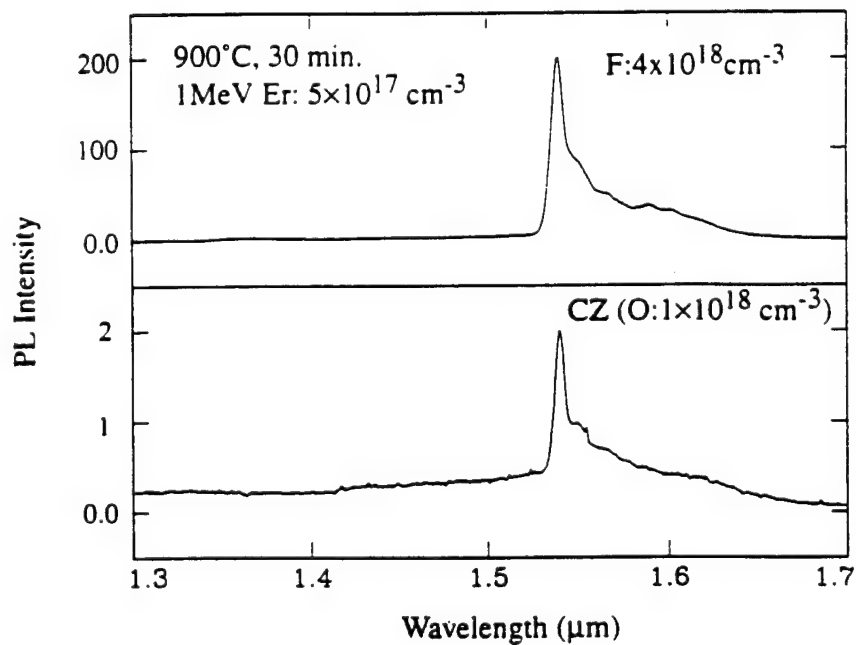


Figure 5-6: Comparison of the effect of O and F on the Si:Er PL intensity at 4.2 K.

tration, and is increased by two orders of magnitude when the $[F]_{peak}$ is raised from $5 \times 10^{17} cm^{-3}$ to $5 \times 10^{18} cm^{-3}$ with the same Er profile, in Figure 5-5. The lines in Figure 5-5 are the least square fits for the light intensity of Si:Er after the same heat treatment process. All heat treatments show a similar slope of ~ 1.5 in the log-log plots in the temperature range $800 - 1100^\circ C$. This $[F]^{1.5}$ dependence of the PL intensity on the initial F level in Si:Er indicates that an Er-F complex is the source of the light emission in Si:Er-F. It is important to note the $[F]^{1.5}$ dependence provides only a rough engineering guide for determining the initial F implantation dose. F out-diffuses significantly between $800 - 1100^\circ C$ after 1/2 hour annealing and the amount of F atoms retained in Si varies depending on the F outdiffusion and the Er-F complexes dissociation processes taking place in Si:Er-F at different annealing temperature. It is shown later in the chapter that the luminescence intensity is linearly proportional to the total amount of F atoms retained in Si:Er-F after the heat treatment.

For F peak concentrations exceeding $\sim 10^{19} cm^{-3}$, the light intensities at $1.54\mu m$, which are labeled as \otimes in Figure 5-5, are artificially high. Figure 5-7 compares the high resolution spectrum of high F concentration ($[F]_{peak} = 5 \times 10^{19} cm^{-3}$) with that of low F concentration ($[F]_{peak} = 4 \times 10^{18} cm^{-3}$), after a $900^\circ C$, 30 min anneal. The spectral resolution is 4\AA . The sharp emission lines from Er^{3+} in Si:Er-F ($[F]_{peak} = 5 \times 10^{19} cm^{-3}$) are superimposed on a broad background spectrum.

The broad feature associated with high $[F]$ ($[F]_{peak} = 5 \times 10^{19} cm^{-3}$) is different from the sharp Er^{3+} emission at $\lambda = 1.54\mu m$. The broad spectrum is likely related with the significant implantation damage at high $[F]$. The peak of the broad spectrum shifts at different measurement temperature, as shown in Figure 5-8. The peak position moves from $1.52\mu m$ to $1.56\mu m$ as the PL sampling temperature is increased from 4.2 K to 225 K. Conversely, the sharp emission from Er^{3+} in Si maintains a constant wavelength position, independent of the measurement temperature.

Furthermore, the broad background spectrum disappears after the material is annealed at high temperature between $1000 - 1100^\circ C$. However, after high temperature annealing, the Er light intensity decreases significantly due to the dissociation of Er-F

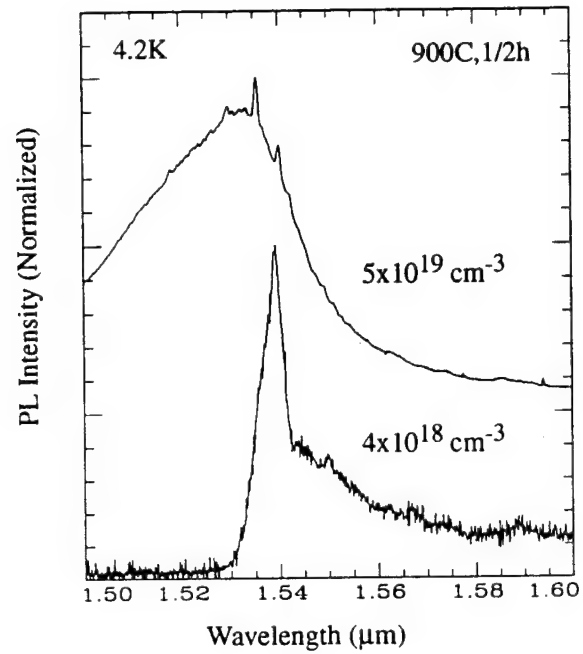


Figure 5-7: PL spectra of Si:Er with F concentration of $5 \times 10^{19} \text{ cm}^{-3}$ and $4 \times 10^{18} \text{ cm}^{-3}$. The spectrum resolution is $= 4 \text{ \AA}$.

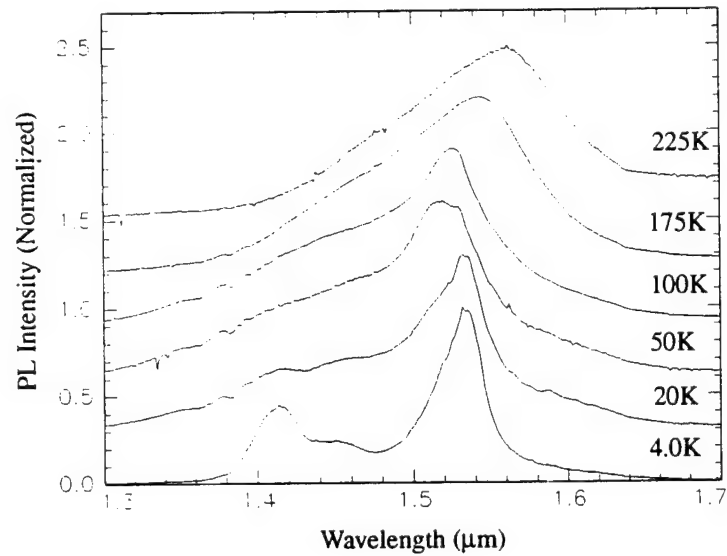


Figure 5-8: The PL spectra of Si:Er with $F = 5 \times 10^{19} \text{ cm}^{-3}$ as a function of measurement temperature.

complexes and a fast F out-diffusion rate. There is no advantage combining high F implants with high temperature annealing to enhance the light emission in Si:Er.

The optimum annealing condition varies with the initial F peak concentration. As indicated in Figure 5-9, the processing temperature to achieve the maximum Si:Er light emission after 1/2 hour annealing decreases from 1000°C to 800°C as $[F]_{\text{peak}}$ increases from $5 \times 10^{17} \text{cm}^{-3}$ to $5 \times 10^{18} \text{cm}^{-3}$. At higher F concentration, fewer diffusion jumps of F to Er sites are required to form optically active complexes because of a shorter average separation between Er and F. A similar argument was presented in the previous section to explain the similar impact on the optimum annealing temperatures of high O implantation dose. Furthermore, it was reported the F out-diffusion rate was faster with a higher F concentration in Si [58]. It is because the limiting steps for the F out-diffusion in Si are the formation of F containing species such as SiOF_2 and SiF_4 and the desorption of those F containing species from Si surface [58]. The reaction rate to form those F containing species is $[F]$ dependent and increases significantly at a high F concentration. Therefore, at higher F concentration, smaller percentage of the initial F dose is retained in Si after the same temperature annealing. The absolute PL intensity remains higher with a higher initial F dose after the same heat treatment. However, the luminescence intensity decays fast and the optimum annealing temperature shifts to a lower temperature.

The light emission intensity in both Si:Er-F (Figure 5-9) and Si:Er-O (Figure 5-1) shows a characteristic behavior as a function of annealing temperature. A schematic drawing of the main physical processes taken place in Si:Er-F during heat treatment is shown in Figure 5-10. This characteristic annealing behavior can be understood as the competition of three different processes: (1) implantation damage recovery; (2) F out-diffusion; and (3) complex formation and dissociation. The Si:Er light intensity and the concentrations of optically active Er centers are determined by the dominant process at different temperatures. Specifically, below $800 - 900^{\circ}\text{C}$, the dominant process is damage recovery and the formation of Er-F complexes. An increase of the PL intensity is expected as the annealing temperature increases. Above $800 - 900^{\circ}\text{C}$, F out-diffusion becomes dominant. The out-diffusion of F in Si:Er reduces the number

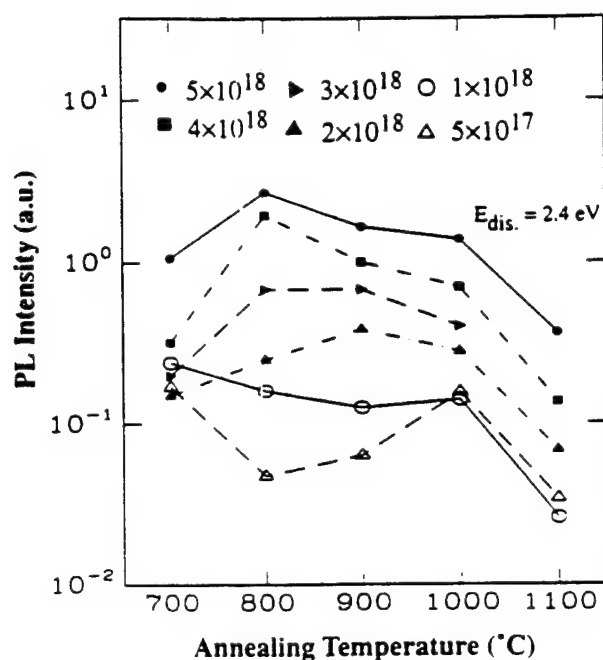


Figure 5-9: The PL peak intensity (at 4.2 K) vs the annealing temperature as a function of the F concentration in Si:Er-F for a 30 min anneal.

of the Er-F complexes and the luminescence intensity. Above 1100°C, F out-diffusion is very fast and the dissociation kinetics of the Er-F complex becomes the rate limiting process. A 2.4 eV activation energy of the dissociation process can be measured from Figure 5-9, based on reduction of the luminescence intensity between 1000 – 1100°C.

The SIMS depth profiles of Er and F in Si after heat treatment are shown in Figure 5-11 and 5-12, respectively. The Er profile remains basically unchanged during annealing between 800 – 1100°C. A small degree of Er accumulation at the surface is seen in Figure 5-10 and indicates that Er out-diffusion has started to occur at 1100°C. The slight variation in the Er peak concentration in Figure 5-11 is due to the experimental noise. F out-diffusion dominates the heat treatment process of Si:Er-F. Significant F out-diffusion occurs at 800°C after 1/2 hour and 10 hour anneals with the F distribution maintaining coincidence with the Er distribution. The majority of the bonded F in Er-F complexes dissociates and out-diffuses at 1100°C for 30 min, confirming the dissociation process. The total F atoms retained in Si after heat treatment can be calculated by integrating the F depth profile. The Er light intensity

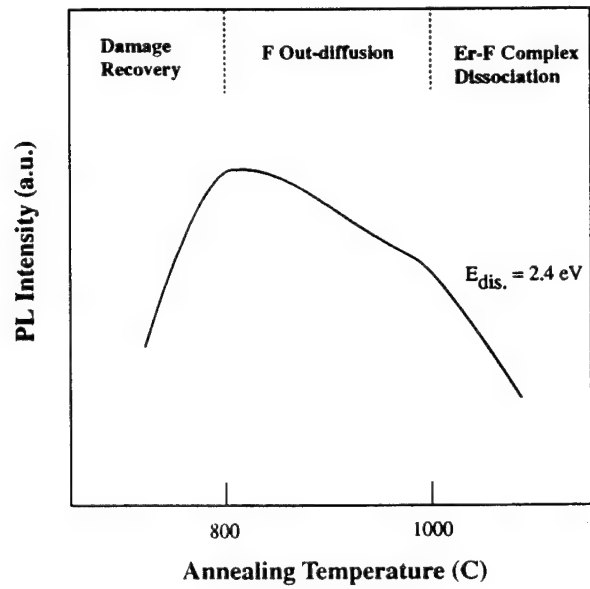


Figure 5-10: Schematic drawing of the physical processes taken place in Si:Er-F during heat treatment.

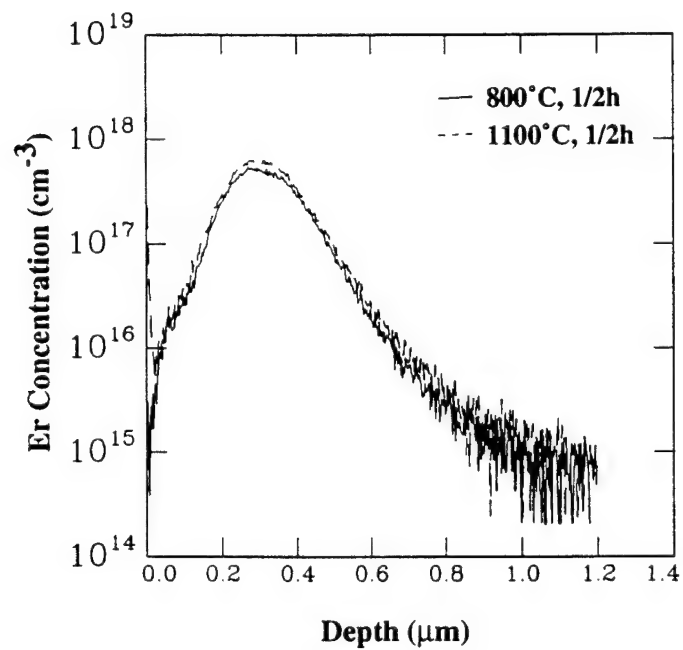


Figure 5-11: SIMS depth profiles of Er in Si:Er-F after 800°C and 1100°C anneal for 1/2 hour.

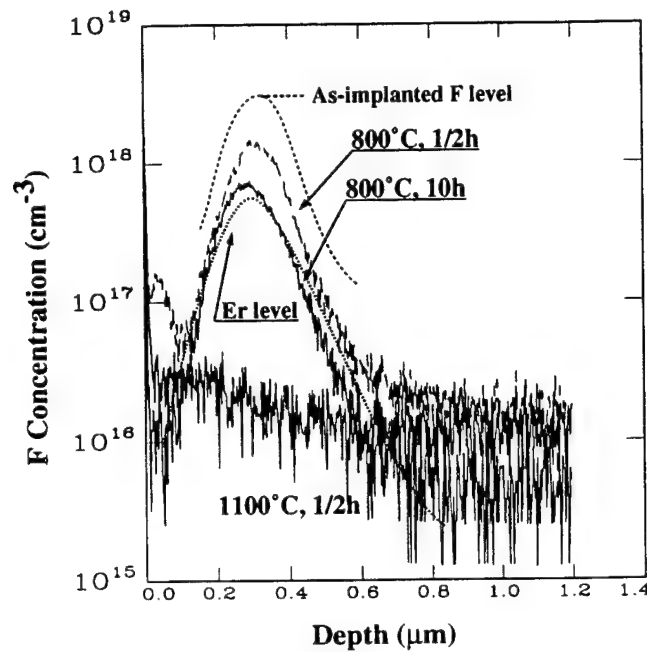


Figure 5-12: SIMS depth profiles of F in Si:Er-F after heat treatments. Initial F level is at $4 \times 10^{18} \text{ cm}^{-3}$ and marked with dashed line. Er profile remains constant.

is linearly proportional to the total F retained in Si, as shown in Figure 5-13. This result further confirms that the Er-F associates are the source of the luminescence in Si:Er-F. In other words, the Er-F associates are the optically active Er centers in Si:Er doped with fluorine ligand.

The annealing time also affects the light emission of Si:Er-F. Figure 5-14 shows the effect of annealing time on the PL intensity at $\lambda = 1.54 \mu\text{m}$. The light emission in Si:Er reaches a maximum after 1/2 hour annealing and then slowly decreases with additional annealing time. This behavior is consistent with the long term F out-diffusion (decreasing the PL intensity) at 800°C and 900°C , superimposed on the initial damage recovery/ Er-F complex formation process (increasing the PL intensity) described earlier.

The emission spectra of Si:Er also varies with the annealing time. Figure 5-15 shows the effect of annealing time on the Si:Er PL spectra at 800°C . The shifts of the peak and the development of a less complex spectrum are noticeable. These changes suggest that the local ligand fields around the optically active Er^{3+} consolidate from

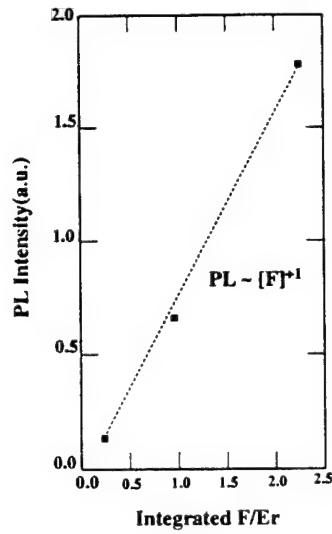


Figure 5-13: The effect of F out-diffusion on the light emission intensity of Si:Er. Total retained F atoms after the heat treatment is expressed as the ratio of total Er atoms.

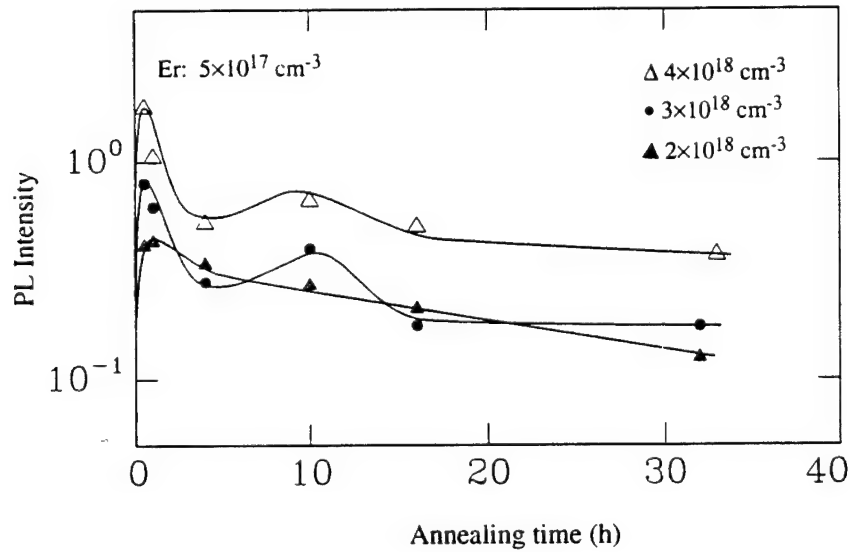


Figure 5-14: The effect of annealing time on the PL intensity of Si:Er-F. The samples with $[F]_{peak} = 4 \times 10^{18} \text{ cm}^{-3}$ are annealed at 800°C . The others are annealed at 900°C . The lines are drawn to guide the eye.

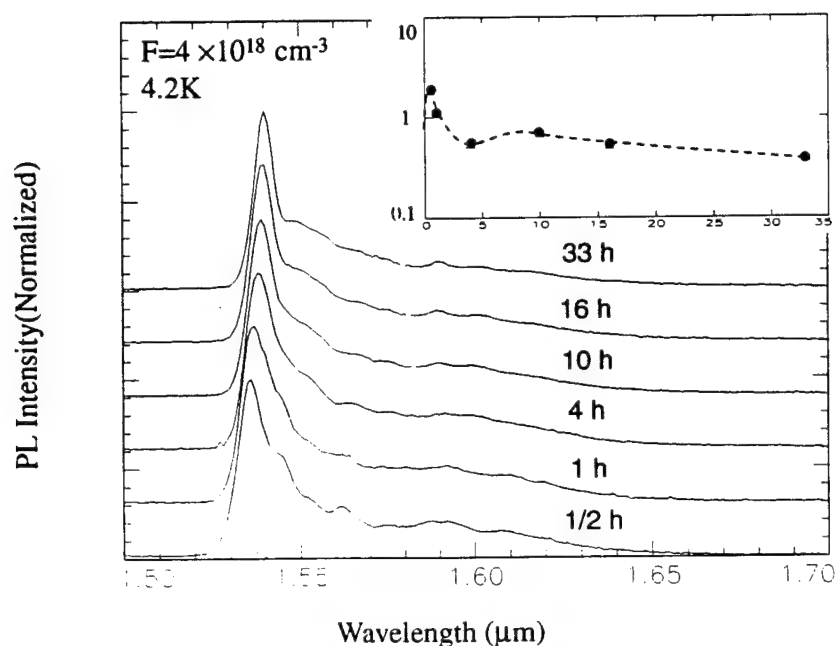


Figure 5-15: The effect of annealing time on the PL intensity of Si:Er during 800°C isothermal annealing. The insert shows the PL peak intensity of Si:Er evolves with the annealing time.

many different centers to a single more stable type. The same changes on the Si:Er spectral features take place with increasing annealing temperature, but to a much greater extent, as shown in Figure 5-16. The impact on the PL intensity due to increasing annealing temperature has already been discussed, shown in Figure 5-9. A longer time anneal has the same impact on the luminescence intensity and the spectral features as a higher temperature anneal. Table 5.1 lists the annealing conditions to yield the equivalent luminescence intensity and spectrum in Si:Er-F.

The same effect of high annealing temperature as of long annealing time on the light emission and on the optically active Er centers are seen in both Si:Er-F and Si:Er-O. The optically active Er centers after 900°C , 30 min anneal are metastable. The post-implantation heat treatment process is kinetically controlled by a ligand out-diffusion process.

In summary, fluorine is very effective in increasing light emission in Si:Er. We have achieved two orders of magnitude enhancement in light emission at low temperature over the commonly-used ligand, oxygen. The light intensity increases linearly with

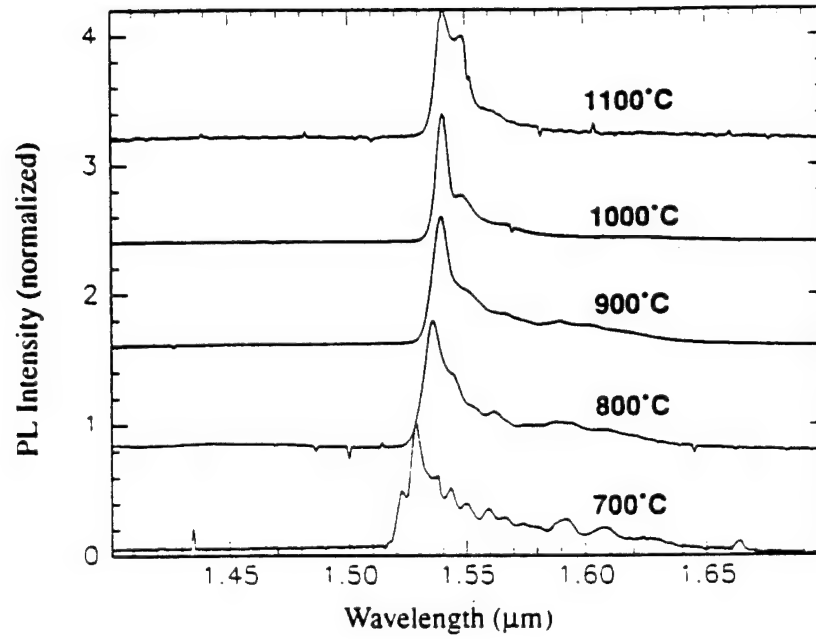


Figure 5-16: The evolution of the Si:Er-F PL spectra as a function of annealing temperature during an isochronal anneal. The F peak concentration in Si:Er is $4 \times 10^{18} \text{ cm}^{-3}$.

Table 5.1: The annealing conditions to yield equivalent light emission intensity and spectrum in Si:Er-F

Si:Er-F sample	Processing conditions	Equivalent conditions
$F=4 \times 10^{18}$	800°C , 10 h	900°C , 30 min.
$F=3 \times 10^{18}$	900°C , 10 h	1000°C , 30 min.
$F=2 \times 10^{18}$	900°C , 4-10 h	1000°C , 30 min.
$F=1 \times 10^{18}$	900°C , 1-4 h	1000°C , 30 min.

total F atoms retained in Si after heat treatment. The light intensity after a 1/2 hour anneal has a $[F]^{1.5}$ dependence with the initial F implanted peak concentration between $5 \times 10^{17} \text{cm}^{-3}$ and $5 \times 10^{18} \text{cm}^{-3}$. Er-F associates are the optically active Er centers and the source of the light emission in Si:Er with F co-implants. The optimum heat treatment condition to achieve the maximum light emission depends on the interaction of the three processes occurring in the heat treatment: (1) implantation damage recovery; (2) F out-diffusion; and (3) complex formation and dissociation. The optimum heat treatment temperature decreases from 1000°C to 800°C for an 1/2 hour anneal as the F implantation concentration increases. For implanted F peak concentrations above 10^{19}cm^{-3} , the damage dominates the luminescence at $\lambda = 1.54 \mu\text{m}$. The processing advantage of fluorine is most likely due to its high diffusivity which allows Er-F to associate at the temperature where the associate is stable and where Er diffusion and precipitation are limited.

5.5 Si:Er Process Simulation

In order to establish an optimum process for a Si:Er device, a process model has been constructed to simulate the solid state reactions of Si:Er during heat treatment processes. For actual device processing, for example that of a light emitting diode, Si:Er may undergo several annealing processes besides the post-implantation anneal. Each high temperature process will have an impact on the optically active Er centers and, therefore, affect the final performance of a Si:Er device. A good process simulator allows one to predict the impact and streamline process design to improve final device performance. The success of the simulation model helps confirm our understanding of the annealing process and provides further insight into the Si:Er defect chemistry.

A good device process simulator employs a concise physical model capable of describing the actual internal material processes occurring during heat treatment. The internal material processes taking place during the Si:Er heat treatment process are complex. As pointed out in Section 5.4, there are three major processes controlling material performance: (1) implantation damage recovery; (2) impurity ligand out-diffusion; and (3) Er-impurity complex formation and dissociation. Depending on the processing temperature, one of the three processes dominates and determines the optically active Er centers in Si:Er. Besides these major processes, other processes also occur in Si:Er such as the formation of the Er-defect complexes at low temperatures, and the Er diffusion and the formation of $ErSi_{2-x}$ precipitates at very high temperatures.

A flow chart for the Si:Er process simulator described in the following section is shown in Figure 5-17. Based on the initial processing conditions such as Er and F ligand profiles, the model simulates the solid state reactions and ligand out-diffusion in Si:Er, calculates the number of the optically active Er centers and the luminescence intensity. The model includes two of the major processes occurring in Si:Er during the heat treatment, namely the formation and dissociation of Er-impurity complexes and the outdiffusion of ligand impurity atoms. It does not include the processes occurring at very low and very high temperatures: the processes of implantation

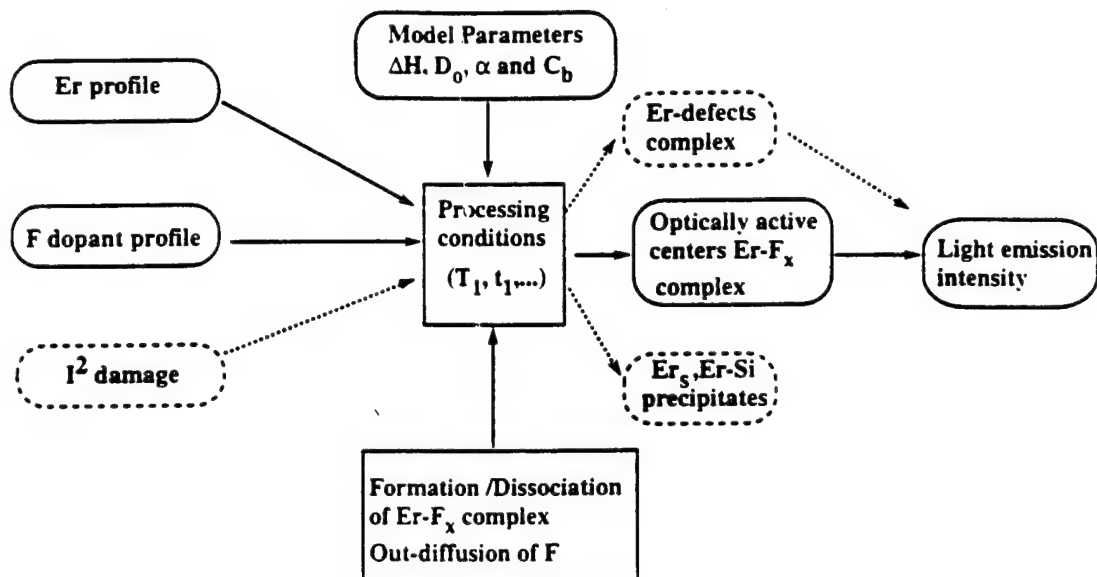


Figure 5-17: A schematic drawing of the Si:Er process simulator.

damage recovery and Er silicide precipitation. The recovery of implantation damage is fast at the normal processing temperature and becomes a dominant rate limiting process only at low temperature. Er diffusion and precipitation becomes significant only at very high temperature, see Chapter 4. At such high temperature, Si:Er loses most of its optical activity due to Er-ligand dissociation and ligand outdiffusion. For actual Si:Er devices, such high temperature processing should be avoided.

5.5.1 Si:Er Process Model

The simulation will be presented in terms of the Si:Er-F materials system. There are three Er-F complexes, ErF , ErF_2 and ErF_3 , in Si:Er doped with F. The association reactions for each of the Er-F associates are as follows:



where Kf_i and Kr_i are the forward and the backward reaction rate for each reaction ($i=1, 2$ and 3) respectively, and the ratio of the forward and the backward reaction rate is the equilibrium reaction constant of the reaction.

$$K_i = \frac{Kf_i}{Kr_i}$$

Si:Er-F can be regarded as a dilute solution of Er and F in Si, and therefore the equilibrium reaction constant for the first reaction (5.1) can be estimated as

$$K_1^{-1} = \frac{Kr_1}{Kf_1} = \frac{[Er] \times [F]}{[ErF]} = \frac{C_s}{\theta} \text{Exp}[\Delta H_1/kT]$$

where C_s is the density of lattice sites and is equal to $5 \times 10^{22} \text{cm}^{-3}$ in silicon. θ is the number of ways one F atom can neighbor one Er atom and is taken as the site coordination number. $\theta = 4$ in Si. $\Delta H_1 (< 0)$ is the enthalpy of the reaction.

Similarly, the equilibrium reaction constants for other two reactions, K_2 and K_3 , can be estimated as follows.

$$K_2^{-1} = \frac{Kr_2}{Kf_2} = \frac{[ErF] \times [F]}{[ErF_2]} = \frac{C_s}{\theta} \text{Exp}[\Delta H_2/kT]$$

and

$$K_3^{-1} = \frac{Kr_3}{Kf_3} = \frac{[ErF_2] \times [F]}{[ErF_3]} = \frac{C_s}{\theta} \text{Exp}[\Delta H_3/kT]$$

where ΔH_2 and ΔH_3 are the reaction enthalpy for the reaction (5.2) and (5.3) respectively.

Fluorine is the dominant mobile species in Si:Er-F and diffuses rapidly by an interstitial mechanism in silicon [59]. In comparison, Er diffuses very slowly at temperatures between $800-1100^\circ\text{C}$ and is practically immobile. Er is treated as immobile in this model and so are the Er-F associates. The association barriers between F and Er, ErF, and ErF_2 are small due to a small migration energy associated with F diffusion in Si (shown later in the same section). Assuming no long range attraction.

the forward reaction rate can be estimated as

$$Kf_1 = Kf_2 = Kf_3 = 4\pi aD_F$$

where D_F is F diffusivity in Si and a is the nearest neighbor distance. For F in Si, $a = 2.76\text{\AA}$.

If the Er-F association reactions occurred in the gas phase, the enthalpy for each F and Er association reaction would be calculated based on the values of standard enthalpy, listed in Table 2.3. In that case, $\Delta H_1 = 45\text{kcal/mol} = 1.95\text{eV}$, $\Delta H_2 = 119\text{kcal/mol} = 5.16\text{eV}$ and $\Delta H_3 = 130\text{kcal/mol} = 5.64\text{eV}$. These values are reduced in Si:Er because of the screening effect by the silicon lattice. Although the exact binding energy for each reaction in the silicon lattice is not clear, a reasonable starting point estimate is to assume that the enthalpy value for each reaction in the solid is proportional to that in gas phase. $\Delta H_1 : \Delta H_2 : \Delta H_3 = 1.95 : 5.16 : 5.64$

F is the only mobile species in this model. The free F diffusivity is concentration independent due to the low F concentration in Si and its interstitial (mono-molecular) diffusion mechanism. According to Fick's second law, we have F diffusion as

$$\frac{dF}{dt} = D_F \frac{d^2 F}{dx^2} \quad (5.4)$$

There are no direct experimental measurements reported for the F diffusivity in silicon. However, experimental studies on F implanted in Si shown F out-diffuses very fast in Si [58][60]. First principle theory predicted interstitial F diffusion in Si with a migration energy of 0.7eV [59]. In the simulation performed in the next section, the diffusivity of fluorine in Si between $800 - 1100^\circ\text{C}$ is assumed to have an Arrhenius relationship.

$$D_F = D_0 \exp\left[\frac{-E_m}{kT}\right]$$

where $E_m = 0.7\text{eV}$ and $D_0 = 10^{-3} - 10^{-5}$, a typical value for an interstitial diffusion in Si.

The desorption of F containing species at the silicon surface limits the fluorine out-diffusion [58]. So at the surface,

$$J_F = \alpha(C_F^o - C_b) \quad (5.5)$$

where C_F^o is the F concentration at the silicon surface and α is the mass transport coefficient describing the desorption rate of volatile F containing species at the surface. C_b is the F concentration in the gas flow and it is very small.

The light emission in Si:Er is linearly proportional to the number of optically active Er centers. In this model, the ErF_3 associate is postulated as the stable optically active center in Si:Er-F. Therefore, a normalized luminescence intensity from Si:Er-F can be calculated as

$$PL \propto \int [ErF_3] dx \quad (5.6)$$

The ErF_3 assumption is based on the following reasoning. First of all, it is very likely that the ErF_3 complex gives the strongest Er^{3+} light emission among the Er-F associates. Luminescence in Si:Er arises from the non-symmetric ligand fields around Er^{3+} . Because of the strong bonding between Er and F in ErF_3 , ErF_3 most likely has the strongest crystal field around Er^{3+} ions, therefore, ErF_3 yields strong Er^{3+} luminescence. Secondly, ErF_3 is the overwhelmingly dominant Er-F associate in Si:Er because of its strong enthalpy energy ΔH_3 . Even if ErF and ErF_2 are optically active and yield similar Er^{3+} luminescence intensity, their contributions to the light emission are insignificant if the gas phase binding energy enthalpies scale the solid state values. However, the model cannot decide which Er-F associates are optically active. If ErF_3 turns out to be completely optically inactive in comparison to ErF and/or ErF_2 , the simulated luminescence intensity from this model has to be modified accordingly.

5.5.2 Results and Discussion

The mathematical equations of the model describing the processes of the ligand out-diffusion and the complex formation and dissociation in Si:Er-F are listed in Ap-

pendix C. The simulations were performed using the dial-an-operator feature of the simulation software PEPPER [61]. PEPPER is a general finite element partial differential equation solver for the diffusion-type problems. There are four independent parameters in this model, the reaction enthalpy for ErF_3 complex reaction ΔH_3 , the pre-exponential factor for F diffusivity D_0 , the mass transport coefficient α (or α/D ratio) and the residual F concentration C_b in the gas flow. The last two parameters describe the F desorption at the surface and in general do not affect the results significantly. C_b is small and set to be $\sim 1 \times 10^{12} \text{cm}^{-3}$ in the simulation. The ratio of α/D determines F concentration at the surface and a typical value of $\alpha/D \sim 0.1$ was used in the simulation [62]. ΔH_3 and D_0 are the fitting parameters, determined using the Levenberg-Marquardt optimizer PROFILE [63]. The values act as self-consistency checks when compared with the experiment data. The SIMS profiles of F at 800°C are used as the reference profiles for the optimizer.

Figure 5-18 shows the comparison of the simulated and the experimental SIMS F profiles in Si:Er after annealing at 800°C for 1/2h and 10h. The F concentration given by the simulation is calculated using

$$F = [F] + [ErF] + [ErF_2] * 2 + [ErF_3] * 3$$

where $[F]$, $[ErF]$, $[ErF_2]$ and $[ErF_3]$ are the concentration profiles for each F-related species in Si:Er-F. $\Delta H_3 = -2.5 \text{eV}$ and $D_0 = 5 \times 10^{-4} \text{cm}^2/\text{s}$ are the best fitting parameters, used in the simulation.

The fitting value for reaction enthalpy ΔH_3 agrees well with the activation energy of the dissociation of 2.4 eV in Si:Er-F, which was determined from the PL intensity in Figure 5-9. $D_0 (= 5 \times 10^{-4} \text{cm}^2/\text{s})$ is within the typical range for interstitial diffusion. Figure 5-19 shows the individual concentration profiles of each species in Si:Er doped with F after 800°C , 30 min anneal. Since F diffuses very fast, the majority of the free F is out-diffused after 30 min at 800°C . The F level is controlled by the surface mass transport coefficient α and C_b and the Er-F association reactions. The majority of F in Si:Er is bonded to Er in the form of ErF_3 . ErF_3 is essential to explain

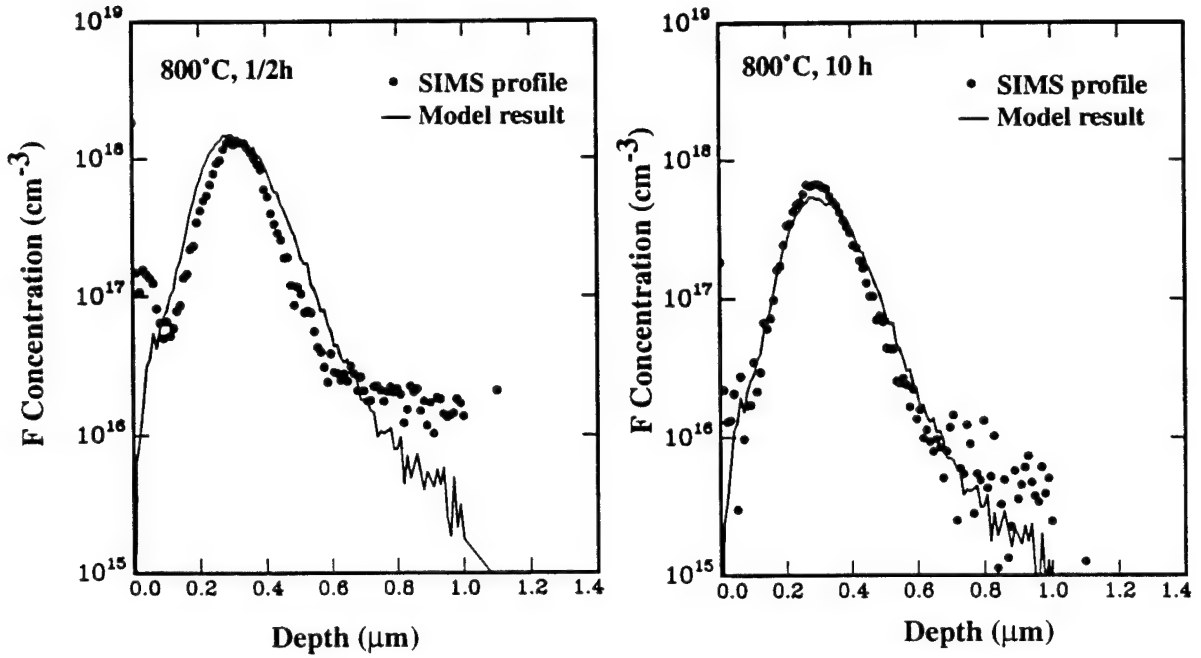


Figure 5-18: The concentration profiles of total F in Si:Er after 800°, 30 min anneal(a); 800°, 10h anneal(b); generated with parameters $D_o = 5 \times 10^{-4}$, $\Delta H_3 = -2.5\text{eV}$, $\alpha/D(F) = 0.1$ and $C_b = 1 \times 10^{12}$; and are compared with the experimental profiles measured by SIMS.

the F peak concentration in the SIMS profile which is ~ 3 times higher than the implanted Er peak concentration of $5 \times 10^{17}\text{cm}^{-3}$ after 30 min anneal at 800°C, shown in Figure 5-12. The free [Er] concentration $\sim 2 \times 10^{16}\text{cm}^{-3}$ is far lower than the implanted Er concentration. The ErF and ErF_2 levels are very low compared with the concentration levels of ErF_3 and free Er due to their relatively small reaction enthalpies.

With longer annealing time, the model predicts that the ErF_3 concentration level will decrease. The free [Er] concentration increases, as well as the ErF level. However, the ErF and ErF_2 levels are still insignificant in comparison with ErF_3 and free [Er] levels.

A decrease of the ErF_3 concentration level with annealing time suggests a reduction of the light emission intensity of Si:Er-F. We use the relative PL output as a measure of the optically active ErF_3 concentration. Figure 5-20 compares the simulated light emission intensity with the experimental PL intensity of Si:Er-

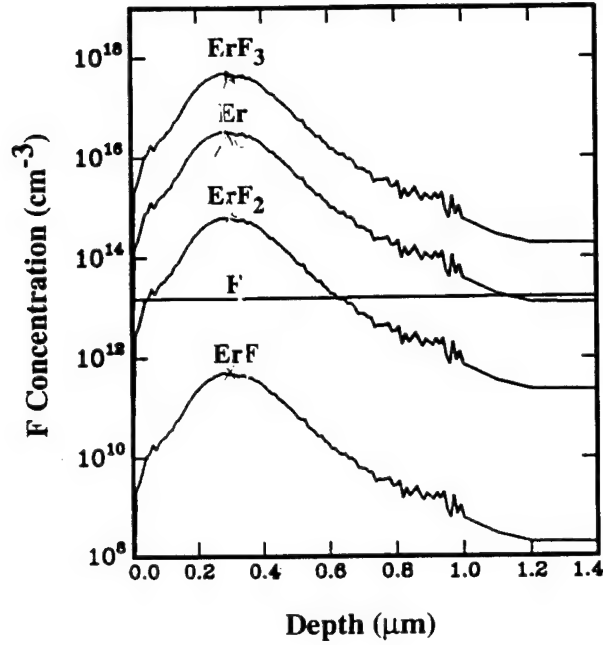


Figure 5-19: The concentration profiles of ErF , ErF_2 , ErF_3 , free $[Er]$ and $[F]$ in Si:Er after 800°, 30 min anneal, are generated using the same parameters as in Figure 5-19.

F of $F_{peak} = 4 \times 10^{18} cm^{-3}$. The same simulation parameter values were used, $\Delta H_3 = -2.5 eV$ and $D_o = 5 \times 10^{-4} cm^2/s$. The PL intensity after a 30 min anneal is normalized to the experimental value for comparison. The simulation shows a general decay of the light intensity with longer annealing time and agrees well with the experiment. The sharp decrease in the PL intensity is not captured by the simulation. This decrease is due to the process of implantation defect anneal, which the model ignores.

Figure 5-21 shows the simulated luminescence intensity as a functional of total F atoms retained in Si after the annealing for various time span at 800°C. The result confirms that the light emission in Si:Er-F is linearly proportional to the total amount of F atoms retained in Si, as shown in Figure 5-13 in the SIMS measurements. This result is expected since the majority of F atoms is in the form of ErF_3 after the heat treatment and the luminescence intensity is linearly proportional to the ErF_3 concentration.

In summary, the simulated results confirms the physical processes during Si:Er

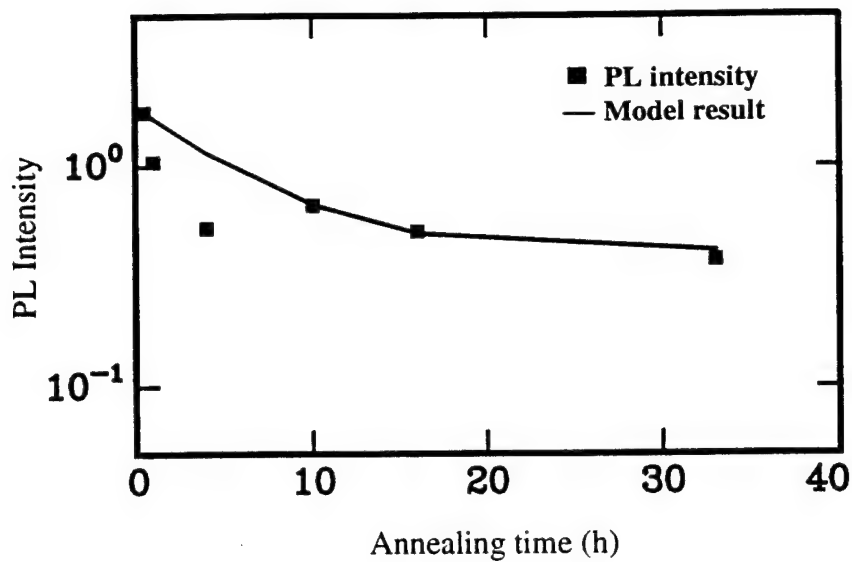


Figure 5-20: The comparison of the experimental PL intensity with the simulated Er PL intensity, simulated using the same parameters as in Figure 5-19, as a function of annealing time at 800°C . $F_{\text{peak}} = 4 \times 10^{18} \text{cm}^{-3}$.

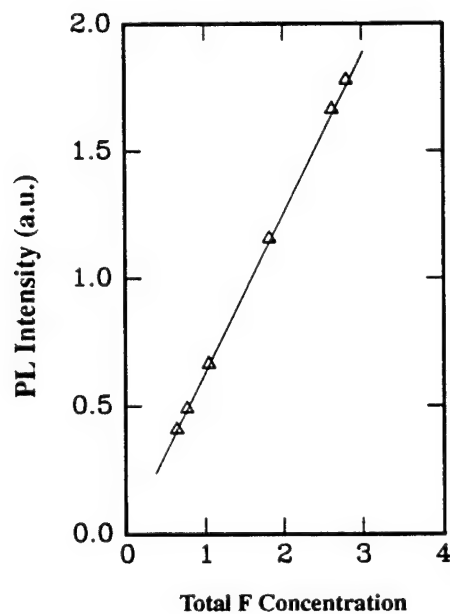


Figure 5-21: The simulated light emission intensity vs the total amount of F atoms retained in Si after 800°C isothermal annealing. The F atoms is expressed as the ratio of the total Er atoms in Si:Er.

heat treatment. They show that the complex dissociation and outdiffusion of ligands such as F and O are the dominant processes during the heat treatment of Si:Er and determine the reduction of the light emission intensity. ErF_3 is the dominant species formed in the heat treatment of Si:Er-F and is likely the optically active Er center in Si:Er-F.

In Si:Er-F, the formation of the optically active Er center requires an association of one Er atom with three F ligands. Increasing the light emission intensity by maximizing the concentration of the optically active Er center can be achieved only by increasing the Er and F concentrations simultaneously in a 1:3 ratio. The implantation damage anneal limits the maximum luminescence intensity in an implanted Si:Er-F. High temperature heat treatment may anneal away all the implantation damage, and at the same time, increase the ligand outdiffusion and the complex dissociation. As a result, the luminescence intensity decreases significantly.

Other low temperature processes are preferred to ion implantation to incorporate metastable Er and ligand F in Si. Low temperature Chemical Vapor Deposition (LTCVD) ($< 800^\circ C$) is likely a superior process because LTCVD is capable of introducing high concentrations of metastable Er and F ligand during the epitaxial growth of the silicon material. Furthermore, the LTCVD process does not create high level of defects as the ion implantation. Post-growth heat treatment after the LTCVD process may be not necessary. The outdiffusion of F ligand and the dissociation of the Er-F complex are minimized. The high concentration of the optically active ErF_3 associate is predicted with the LTCVD process. The light emission intensity can be significant enhanced.

Bibliography

- [1] National Research Council(U.S), Material science and Engineering for the 1990s, National Academy of Science(1989).
- [2] C.K.N.Patel, Lasers-Invention to Application, Edited by J.H. Ausubel and H.D. Langford, National Academy Press(1987).
- [3] A.Y.Cho and A.M.Glass, *AT&T Tech. Journal*. Vol.69, No.6, P77-91(1990).
- [4] H. Ennen, J. Schneider, G. Pomrenke and A. Axmann, *Appl. Phys. Lett.* 43, 943(1983).
- [5] H. Ennen, G. Pomrenke, A. Axman, K. Eisch, W. Haydl and J. Schneider, *Appl. Phys. Lett.* 46, 381(1985).
- [6] J. Michel, J.L. Benton, R.F. Ferrante, D.C. Jacobson, D.J. Eaglesham, E.A. Fitzgerald, Y.-H. Xie, J.M. Poate, and L. C. Kimerling, *J. Appl. Phys.* 70, 2672(1991).
- [7] S. Coffa, F. Priolo, G. Franzo, V. Bellani, A. Carnera, and C. Spinella, *Mat. Res. Soc. Symp. Proc.* Vol.301, p.125 (1993).
- [8] F.Y.G. Ren, J. Michel, Q.Sun-Paduan, B.Zheng, H. Kitagawa, D.C. Jacobson, J.M. Poate, and L.C. Kimerling, *Mat. Res. Soc. Symp. Proc.* Vol.301, p.87(1993).
- [9] B. Zheng, J. Michel, F.Y.G. Ren, D.C. Jacobson, J.M. Poate, and L.C.Kimerling, (submitted to *Appl. Phys. Lett.*).

- [10] J. Michel, L.C. Kimerling, J.L. Benton, D.J. Eaglesham, E.A. Fitzgerald, D.C. Jacobson, J.M. Poate, Y.-H. Xie, and R.F. Ferrante, Material Science Forum, Vol. 83-87, p.653 (1992).
- [11] F. Priolo, S. Coffa, G. Franzo, to be published, Mat. Res. Soc. Symp. Proc. 316(Pittsburgh, PA, 1994).
- [12] Y.-H. Xie, E.A. Fitzgerald and Y.-J. Mii, J. Appl. Phys. 70, 3223(1991).
- [13] A. Yariv, Optical Electronics, 3rd Ed. Holt, Rinehard and Winston, Inc. New York, 1985.
- [14] A. Yariv, Quantum Electronic, John Wiley and Sons, Inc., New York, 1967.
- [15] A.A. Kaminskii, Laser Crystals, 2nd Edition, Springer-Verlag,1990, pp166.
- [16] Y.S. Tang, K.C. Heasman, W.P. Gillin and B.J.Sealy, Appl. Phys. Lett. 55,432(1989).
- [17] K. Thonke, H.U. Hermann and J. Schneider, J. Phys. C21,5881(1988).
- [18] I. Yassievich, L.C. Kimerling, Semicond. Sci. and Tech. 8, 718(1993).
- [19] A.A. Kaminskii, Laser Crystals, 2nd Edition, Springer-Verlag,1990, pp327.
- [20] P.N. Favenneec, H.L. Haridon, D. Moutonnet, M. Salvi and M. Gauneau, Japan. J. Appl. Phys. 29, L524 (1990).
- [21] W.G. Moffatt, The Handbook of Binary Alloy Phase Diagram, General Electric Company, p6.78 and p11.84(1984).
- [22] JCPDS (Joint Committee on Powder Diffraction Standard).
- [23] J.A. Knapp and S.T. Picraux, Appl. Phys. Lett. 48(7), 1986.
- [24] I. Sagnes, G. Vincent, and P. A. Badoz, J. Appl. Phys. 72, 4295(1992).
- [25] M.P. Siegal, F.H. Kaatz and W.R. Graham, Appl. Sur. Sci. 38, 162(1989).

- [26] J. -Y. Duboz and P.A. Badoz et al, App. Sur. Sci. 38, 171(1989).
- [27] J.E.E. Baglin, F. M. d'Heurle, and C.S. Petersson, J. Appl. Phys. 52, 2841(1981).
- [28] Natinal Bureau of Standards, Selected Values of Chemical Thermodynamic Properties, Tech. Notes 270-7, p.65.
- [29] D.J. Eaglesham, J. Michel, E.A. Fitzgerald, D.C. Jacobson, J.M. Poate, J.L. Benton, A. Polman, Y.-H. Xie and L.C. Kimerling, Appl. Phys. Lett. 58, 2797 (1991).
- [30] V.F. Masterov and L.F. Zakharenkov, Sov. Phys. Semicond. 24(4), 1990.
- [31] C. Lhomer, B. Lambert, Y. Toudic, A. L. Corre, M. Gauneau, F. Clerot, and B. Sermage, Semicond. Sci. Technol. 6, 916(1991).
- [32] Y.S. Tang, Zhang Jingping, K.C. Heasman and B.J. Sealy, Solid State Comm. 72, 991(1989).
- [33] H. Przybylinska, J. Enzenhofer, G. Hendorfer, M. Schoisswohl, L. Palmetshofer and W. Jantsch, Proceedings of ICDS 17, Gmunden, Austria(1993).
- [34] M. Needles, M. A. Schluter, and M. Lannoo, Phys. Rev. B, 47, 15533(1993).
- [35] J. Michel, F.Y.G. Ren, B. Zheng, D.C. Jacobson, J.M. Poate, and L.C. Kimerling, Materials Science Forum, Vol. 143-147, p.707(Tran. Tech. Publications Ltd., Aedermannsdorf, 1994).
- [36] D.E. Nazzyrov, G.S. Kulikov, and R. Sh. Malkovich, Sov. Phys. Semicond. 25, 997(1991)
- [37] V.V. Ageev, N. S. Aksenova, V.N. Kokovina, and E.P. Troshina, ozv. Leningr. Elektrotekh. Inst. No. 211,80(1977).
- [38] J.L. Benton, J. Michel, L.C. Kimerling, D.C. Jacobson, Y.-H. Xie, D.J. Eaglesham, E.A. Fitzgerald, J.M. Poate, J. Appl. Phys. 70, 2667(1991).

- [39] H.B. Dietrich, P.B. Klein, and B.J. Mrstik, SPIE Vol.530, Advanced Applications of Ion Implantation(1989).
- [40] F.P. Widdershoven and J.P.M. Naus, Materials Science and Engineering, B4,71(1989).
- [41] J. L. Benton, D.J. Eaglesham, M. Allmonte, Ph. Citrin, M.A. Marcus, D.L. Adler, D.C. Jacobson, and J.M. Poate, Mat. Res. Soc. Symp. Proc. Vol.301, p.119(1993).
- [42] H. Efeoglu, J. H. Evans, T.E. Jackson, B. Hamilton, D. C. Houghton, J. M. Langer, A. R. Peaker, D. Perovic, I. Poole, N. Ravel, Phemment, and C.W. Chan, Semicond. Sci. Technol. 8, 236(1993).
- [43] C.A. Millar, T.J. Whitley, and S. C. Fleming, IEE proceedings, 137, 155(1990).
- [44] H. Isshiki, H. Kobayashi, S. Yugo, T. Kimura, and T. Ikoma, Appl. Phys. Lett. 58, 484(1991).
- [45] CRC, Handbook of Chemistry and Physics, Ed. D.R Lide, 71th(1991) P4.8-21.
- [46] Murarka, Silicides for VLSI technology, Academic Press, Orlando, pp142(1983).
- [47] J.M. Andrews and J.C. Phillips, Phys. Rev. Lett. 35, 56 (1975).
- [48] K.N. Tu. R.D. Thompson and B. Y. Tsau, Appl. Phys. Lett. 38(8), 626(1981).
- [49] K. Kenbigh, The Principle of Chemical Equilibrium, 4th edition, Cambridge Univ. Press, pp426(1981).
- [50] C.S.Wu, D.M. Scott, and S.S. Lau, J. Appl. Phys. 58 (3)(1985).
- [51] D.L. Adler, D.C. Jacobson, D.J. Eaglesham, M.A. Marcus, J.L. Benton, J.M. Poate, and P.H. Citrin, Appl. Phys. Lett. 61, 2118(1992).
- [52] S.M. Sze, Physics of Semiconductor Devices, 2nd edition, John Wiley & Sons, New York (1981), p. 69.

- [53] J. Utzig, J. Appl. Phys. 65, 3868(1989).
- [54] P.E. Freeland, K.A. Jackson, C.W. Lowe, and J.R. Patel, Appl. Phys. Lett. 30, 31(1977).
- [55] A. Polman, J.S. Custer, E. Snoeke, and G. N. van den Hoven, Appl. Phys. Lett. 62, 507(1993).
- [56] R.G. Wilson, F.A. Stevie, and C. W. Magee, Secondary Ion Mass Spectroscopy, John Wiley & Sons, Inc. App.E.17(1989).
- [57] A.A. Kaminskii, Laser Crystals, 2nd Edition, Springer-Verlag, 1990, pp23.
- [58] S.P. Jeng, T.-P. Ma, R. Canteri, M. Anderle and G.W. Rubloff, Appl. Phys. Lett. 61, 1310(1992).
- [59] C.G. van de Walle, F.R. McFeely, and S.T. Pantelides, Phys. Rev. Lett. 61, 1967 (1988).
- [60] M.Y. Tsai, D. S. Day, B.G. Streetman, P. Williams, and C. A. Evans, J. Appl. Phys. 50, 188 (1979).
- [61] B.J. Mulvaney, W.B. Richardson and T. L. Crandle, IEEE Trans. Comp. Aid. Des. 8, 336(1989).
- [62] D.R. Sadoway, 3.21 Class Notes.
- [63] G. J. L Ouwerling, The PROFILE/PROF2D User's Manual(Delft University of Technology, 1987).
- [64] P.B. Klein and G.S. Pomrenke, Electron. Lett. 24, 1503(1988).
- [65] P.B. Klein, Solid State Commun. 65, 1097(1988).
- [66] A. Taguchi, M. Taniguchi, and K. Takahei, Appl. Phys. Lett. 60, 966(1992).
- [67] A. Kozanechi, K. Karpinska, and Z. Kalinski, Appl. Phys. Lett. 62, 84(1993).

Chapter 6

4.5 MeV Discrete Si:Er LED

6.1 Introduction

4.5 MeV Er implantation was chosen for Si:Er LEDs due to our previous experience on implantation conditions and subsequent annealing procedure. Er was implanted to a peak concentration below the precipitation limit and coimplanted with oxygen. A process window of 900C/30mins/ N_2 ambient was defined to activate Er optical activity [1, 2].

We successfully demonstrated the first room temperature operation of an Si:Er LED with 4.5 MeV Er implantation [1, 3] as described in section 6.3. However, a low internal quantum efficiency was observed. A detailed electrical and optical characterization and analysis was carried out to understand and to improve the efficiency of Si:Er LEDs.

Er implanted Si wafers were first processed to confirm that Si:Er does not contaminate IC fab. Section 6.2 explains the details of this qualification experiment. Section 6.4 presents Si:Er LED design principles and fabrication procedures. Electrical characterization of Si:Er LEDs are presented in section 6.5, followed by optical characterization of Si:Er LEDs in section 6.6.

6.2 Qualification of Er-Doped Si for IC Fab

Er has a diffusivity of about $6 \times 10^{-16} \text{cm}^2/\text{s}$ and a solubility of about 10^{16}cm^{-3} at 900C, which gives about $0.01 \mu\text{m}$ diffusion length after 30 min annealing at 900C. Due to the low solubility and diffusivity of Er in Si [4], Er is expected to be compatible with Si IC fab. However, since Er does introduce deep level states according to DLTS work [5] it is important to experimentally confirm that Er does not contaminate IC fab.

The wafers were grouped in three different groups: group A, group B, and group C. Group A wafers are for furnace control, group B wafers are Er wafers where Er was implanted only into the central area, while group C wafers are contamination control wafers. Group A was processed first to ensure that the furnace itself was not contaminated. Group B (Er wafers) was then processed in the same furnace to

deliberately "contaminate" the furnace, followed by group C to test if any furnace contamination happened. All three groups of wafers were cleaned and processed in identical and tightly controlled conditions. A furnace was dedicated to the experiment and the RCA station was cleaned after each Er wafer cleaning.

n^+ /p diodes and MOS capacitors were fabricated on all the wafers with the same processing conditions and furnace. 1kÅ dry thermal oxide was first grown at 950C as a screen layer for boron field implantation. Boron was implanted at an energy of 80keV and a dose of $5 \times 10^{13} \text{cm}^{-2}$. Oxide was then wet stripped and a 7kÅ wet oxide was grown to drive in boron. A photolithography step was carried out to define the active diode region and the oxide window was opened by wet etching. A 1kÅ dry thermal oxide is grown again after the photoresist was wet stripped. Phosphorus was then implanted through 1kÅ oxide at a dose of $2 \times 10^{15} \text{cm}^{-2}$ and an energy of 70keV. Phosphorus implant was annealed at 900C for 30 min in N_2 ambient and further driven-in with an extra long time annealing at 1000C for 90 min to form n^+ /p diodes.

C-V data of both furnace control wafers and contamination wafers have a voltage shift less than 0.2V after Bias/Temperature/Stressing (200C/10V/5min). A 0.3V threshold voltage difference between these two wafers is normal for different runs with slightly different oxide thickness.

I-V characteristics of the $50 \times 50 \mu\text{m}^2$ diodes fabricated on furnace control wafers and on non-Er region of the Er wafers were practically identical. An average break down voltage of 21.5V and leakage current of $1.6 \times 10^{-6} \text{A/cm}^{-2}$ at 10V reverse bias voltage was observed. The leakage current values of the diodes on non-Er region of the Er wafers are the same as those of the control wafers. A similar break down voltage but a higher leakage current of $4.0 \times 10^{-6} \text{A/cm}^{-2}$ was measured for the Er diodes. The Er region of Er wafers showed higher leakage current due to the residual Er implantation damage and the Er related deep level states in the diode space charge regions.

C-t measurements showed that there was no degradation of the minority carrier lifetime between furnace control wafers and contamination wafers. The recovery time of 570 sec and 200 sec were measured for two different furnace control wafers. The spread of data is due to the fact that the wafers were manually loaded and therefore the quenching history was different. The recovery time was 300 sec for the contamination control wafer. The difference between furnace control wafers and contamination wafers is under normal distribution.

In conclusion, the data show that Er does not contaminate other wafers and the furnace, and furthermore also does not contaminate the unimplanted region of the same wafer. Though Er introduces deep level states, the low diffusivity and solubility of Er in Si makes Si:Er compatible with Si IC fab.

6.3 First room-temperature LED

The starting wafers were boron-doped p-type (100) oriented silicon Cz wafers (0.5-2 Ωcm). n^+ /p junctions were formed by a high dose phosphorus implant. The back sides

of the wafers were boron implanted to achieve good ohmic contacts. A heat treatment of 900 C/30 min/ N_2/H_2 was carried out to remove the implantation damage and to activate dopants. Erbium was then implanted at an energy of 4.5 MeV with a peak concentration of $1 \times 10^{18} \text{ cm}^{-3}$. An oxygen coimplant with the same peak concentration was designed to spatially overlap the erbium implant. The first mask step defined the active mesa areas. Silicon mesas were then formed by reactive ion etching to provide isolation between different diodes. High temperature (900C/30 min/ O_2) dry oxidation followed by low temperature oxide deposition at 450C was used to activate the erbium optical activity and to passivate the mesa etch-induced surface damage. Contact openings were defined by the second mask step and aluminum was sputter deposited. A final photolithography step followed by an aluminum dry etch defined the LED metal contact pattern. A 450C aluminum contact annealing completed the fabrication. A typical device cross section is shown in Figure 6.1.

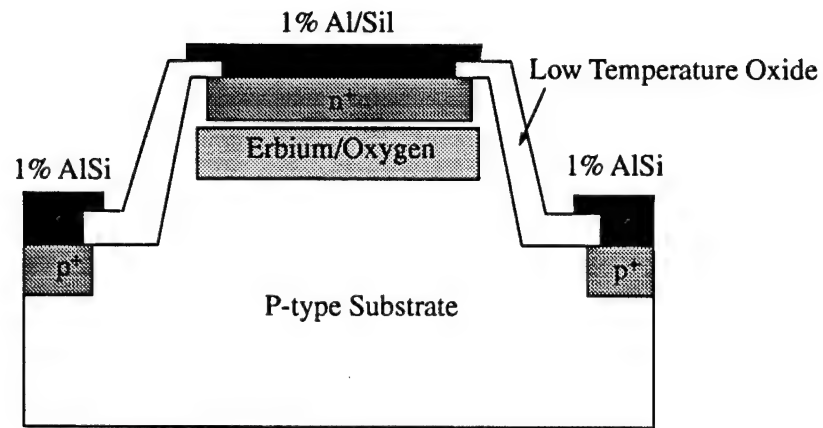
Figure 6.2 shows typical electroluminescence (EL) spectra from a surface-emitting erbium-doped silicon LED, observed at both 100 K and room temperature. A sharp luminescence linewidth (100 Å) at $\lambda = 1.54 \mu\text{m}$ is produced at both operating temperatures. No line shift of the peak wavelength with temperature is observed, consistent with Er^{3+} intra-4f shell transition.

The EL spectrum and line intensities depend on the drive current density. Shown in Figure 6.3 are the EL spectra taken at 100 K with different drive currents. Only the Er^{3+} luminescence at $\lambda = 1.54 \mu\text{m}$ is observed at low drive current densities. At higher drive current densities, the Er^{3+} luminescence saturates and free exciton and defect related luminescence bands appear. The defect related luminescence spectra are likely to be the dislocation related D lines [6]. The two main peaks at 1.35 and 1.44 μm are close to the peak wavelength of D 3 (1.33 μm) and D 2 (1.42 μm), while the background feature around 1.54 μm coincides with D 1 (1.53 μm).

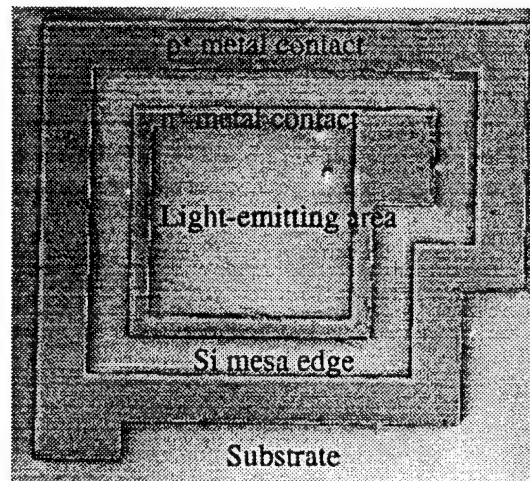
The dislocation lines are unique to processed devices. No D lines have been observed in the PL spectra on Er-implanted, unpatterned Cz wafers. Exciton (band edge) and dislocation related luminescence provide alternate radiative recombination paths which compete with the Er^{3+} luminescence. The relative dominance of the Er^{3+} luminescence at low drive current densities (Fig. 6.3) shows that the Er^{3+} centers are the most efficient radiative recombination centers.

At 100 K, the Er^{3+} EL peak intensity saturates at a drive current density of about 2 A/ cm^2 , while it saturates at about 5 A/ cm^2 at room temperature. The band-edge related luminescence peak intensity also increases with the drive current density, as expected, and no saturation is observed. The saturation of the Er^{3+} EL peak intensity at relatively low drive current densities is due to the long lifetime (~ 1 ms) of the first excited state ($^4I_{13/2}$) of the Er^{3+} center [7].

When all of the centers have been pumped to an excited state, the emitted light intensity is at an asymptotic maximum. We are investigating two hypotheses for the difference in the drive current density required to saturate the EL peak intensity at 100 K and at room temperature [8]. An Auger process involving the exciton and an Er^{3+} complex is believed to be the excitation mechanism. In this process the exciton recombination energy excites the Er^{3+} from the ground state to a spin-orbit excited state. Any energy difference between the exciton recombination and the $\lambda = 1.54 \mu\text{m}$



(a)



(b)

Figure 6.1: (a) A typical Si:Er LED cross section view. (b) SEM picture of an Si:Er LED top view.

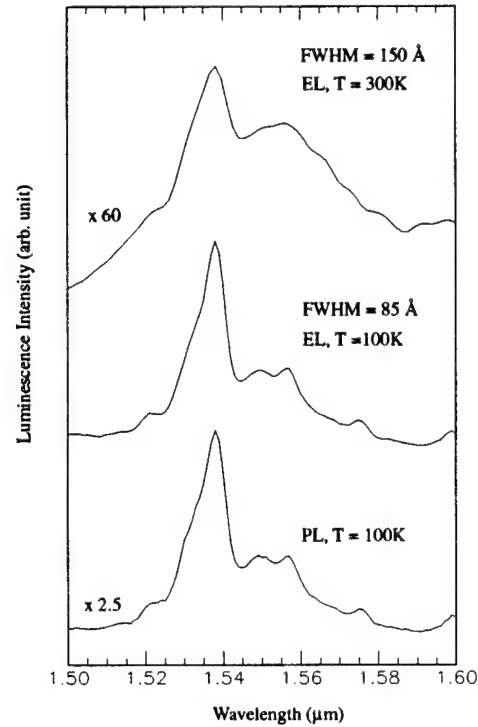


Figure 6.2: Electroluminescence and photoluminescence spectra of a typical Si:Er LED at $T = 100\text{K}$ and 300K .

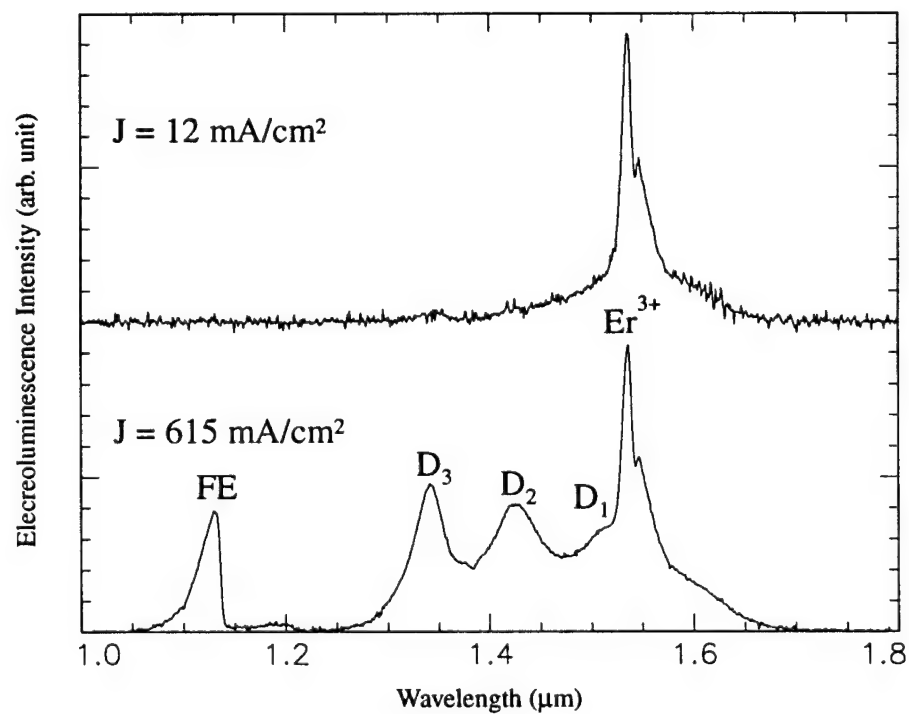


Figure 6.3: Si:Er LED EL spectra under different drive current densities.

luminescence must be dissipated by phonon emission [9]. If an Er^{3+} "gateway" state in the silicon energy gap participates in this Auger process, then carrier emission from this state at the higher temperatures will decrease the probability of the Auger excitation process, and therefore require higher drive currents to reach saturation. An alternative explanation is based on participation of an energy back transfer mechanism from the internal first excited state of Er^{3+} to the external silicon lattice [8] to deactivate the Er^{3+} . Either or both of these processes yield a less efficient Er^{3+} pumping process at room temperature.

The Er^{3+} EL peak intensity changes significantly with temperature as shown in Fig. 6.4. The EL peak intensity was monitored near its saturation value with a constant forward bias ($J=3 \text{ A/cm}^2$) over the entire temperature range. The linewidth of the Er^{3+} luminescence at $1.54\mu\text{m}$ broadens slightly from 85\AA at 100 K to 130\AA at 300 K. In this semilog plot different temperature regions can be identified. From 100 to 200 K, the EL intensity decays with an activation energy of approximately 17 meV. Above 200 K a much steeper decay with an activation energy of about 200 meV occurs. A similar behavior was observed in previous PL studies of Er^{3+} centers [2, 10]. At low temperature ($< 200 \text{ K}$), energy transfer to the Er^{3+} center by the Auger mechanism is most probable [9, 1]. The data of Fig. 6.3 show that the radiative recombination through Er^{3+} is more efficient than the free exciton or dislocation related radiative recombination processes. The decrease of the EL intensity above 200 K can be viewed effectively as a reduction in the number of optically active Er^{3+} centers.

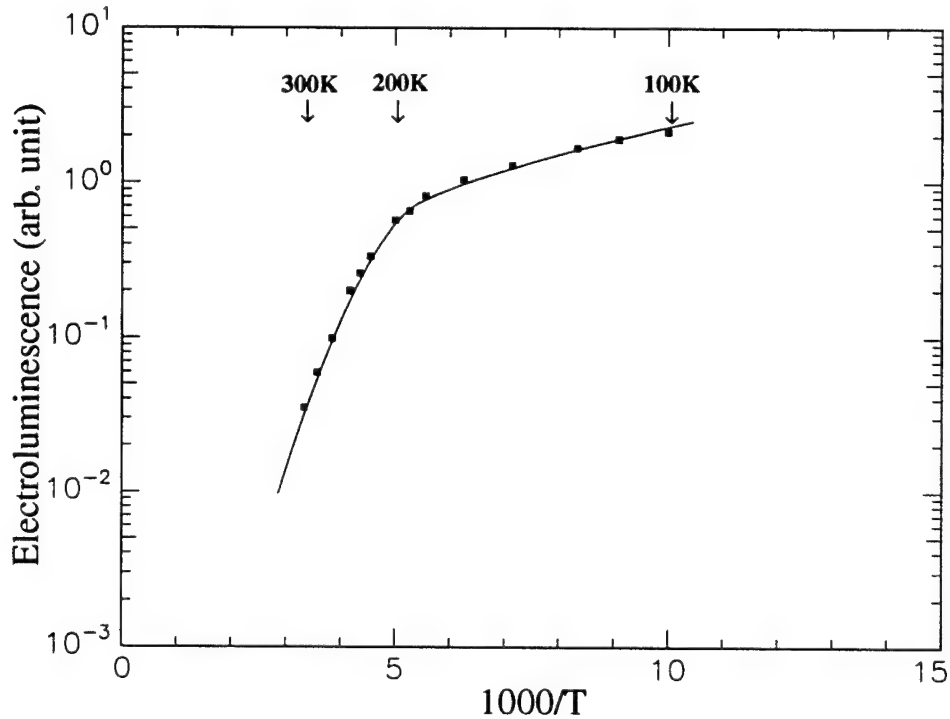


Figure 6.4: A typical Si:Er LED EL intensity temperature dependence.

A comparison of the efficiency of EL and PL was made at 100 K. PL was excited

at 488 nm (penetration depth $\sim 1\mu m$) with an excitation power of 1.5 W. The excitation of the Er^{3+} PL was due to photogenerated electron-hole pairs [2]. At this excitation power, the PL intensity was saturated. Correction for the power loss of the laser beam at lenses, quartz window of the cryostat, and the silicon surface, leaves about 430 mW laser power actually absorbed by the silicon. After the PL data were recorded, the diode was forward biased into optical saturation again, and the EL spectrum was taken with the same collection optics. The electrical power input for the diode was estimated to be about 200 mW. Assuming a 100% quantum efficiency for the production of electron-hole pairs, the ratio of the quantum efficiency of EL to PL was estimated as

$$\eta_{EL}/\eta_{PL} = (I_{EL}P_{PL})/(I_{PL}P_{EL}) = 4 \quad (6.1)$$

where I_{EL} and I_{PL} are the luminescence peak intensities and P_{EL} and P_{PL} are the power inputs for the EL and PL. This value is about two orders of magnitude higher than the ratio reported by Ennen ($\eta_{EL}/\eta_{PL} = 0.05$ at 77 K) [11]. This remarkable increase is due to both processing and device structure improvements.

6.4 Si:Er LED Design and Fabrication

6.4.1 Design

The design of Si:Er LEDs mainly consists of two parts: junction design - device issue and design of Er annealing - material issue. Ren's work [4] concluded that 900C / 30min / N_2 Er annealing is the optimum process condition for 4.5 MeV Er implant. The goal of the design is to optimize both device and material parameters to achieve high quantum efficiency. The elements of the external quantum efficiency η_{ext} are [12]

$$\eta_{ext} = \eta_{int} \times \eta_{opt} \times \eta_{IR} \quad (6.2)$$

where η_{int} is the internal quantum efficiency, η_{opt} is the optical or light extraction efficiency, and η_{IR} accounts for the LED series resistance effect.

As described in chapter 3, an Auger process involving electron-hole pair and Er complex is believed to be the basic Er 4f shell excitation mechanism. In this process the electron-hole recombination energy excites the Er complex from the ground state ($^4I_{15/2}$) to the spin-orbit excited state ($^4I_{13/2}$).

Internal quantum efficiency η_{int} can be further defined as

$$\eta_{int} = \eta_{excitation} \times \eta_{radiation} \quad (6.3)$$

where $\eta_{excitation}$ is the Er excitation efficiency which indicates the energy transfer efficiency from electron-hole pair recombination to Er 4f shell. In another words, this is the efficiency of an Er 4f electron excited from a ground state to a spin-orbit excited state ($^4I_{15/2} \rightarrow ^4I_{13/2}$). $\eta_{radiation}$ is the Er radiative recombination efficiency once the Er 4f shell is in the first excite state and emits photon at $1.54\mu m$ ($^4I_{13/2} \rightarrow ^4I_{15/2}$).

The Er 4f shell is localized and weakly coupled to the surrounding Si lattice [3, 14], and the nature of this weak bonding makes the excitation efficiency less efficient. From the physical materials point of view, at low temperature, this excitation process can be further viewed as a 2-step process: capture of an electron-hole pair at an Er site and the subsequent energy transfer from the electron-hole pair recombination to the Er 4f shell. The Er electron-hole capture efficiency is believed to be determined by its deep level states in the Si bandgap [3]. A high excitation efficiency ($\eta_{excitation}$) therefore requires an optimization of Er micro-environment to make the Er related deep level states to be the main recombination centers and the minimization of other lifetime killers.

From the device point of view, abundance of electron-hole pairs around the Er atoms is important for an effective excitation of Er atoms. This requires the implanted Er/O region to be close to the pn junction due to the exponential distribution of injected carriers and a short carrier diffusion length at the presence of Er. A detailed study on the junction depth on Er light emission will be presented in section 6.6. More efficient Er light emission from p-type substrates than n-type substrates requires p-type wafers as starting wafers. N^+ layer instead of n layer is used to ensure ohmic contact and also ensure efficient electron injection into Er implanted region.

Once Er 4f electrons are in the excited state ($^4I_{13/2}$), a relatively efficient recombination and a long spontaneous radiative lifetime (1ms) were observed [3, 7]. However, this long lifetime makes the radiative recombination process vulnerable to other fast competing recombination processes. A competing impurity Auger process is recently identified as an nonradiative energy back transfer from the excited Er to the Si lattice [15, 16]. This competing mechanism becomes important at high carrier concentration.

Overall, a high high excitation efficiency η_{int} is determined by the electron-hole pair mediated excitation efficiency, the relative abundance of optically active Er, and the effectiveness of other competing radiative and nonradiative processes. The other radiative recombination processes include bandedge luminescence and Er implant related dislocations lines (D-lines). The nonradiative recombination processes include free carrier Auger recombination, surface recombination, and recombination at deep level states (SRH). Both these non-radiative and radiative processes decrease the Er excitation efficiency ($\eta_{excitation}$). Besides, the non-radiative impurity Auger process decreases the Er radiative recombination efficiency ($\eta_{radiation}$).

Therefore a high η_{int} requires an optimization of the Er micro-environment such as an effective ligand field and a minimization of the crystal imperfection and damage from the vicinity of Er region. This requirement can be best met by processing Si:Er LEDs in IC fab where the processing environment and conditions are most strictly controlled.

Optical efficiency η_{opt} for a surface-emitting LED can be defined as [12]

$$\eta_{opt} = \eta_{abs} \times \eta_{ref} \times \eta_{cri} \quad (6.4)$$

where η_{abs} is an absorption effect, η_{ref} is a reflection effect due to silicon-air interface, and η_{cri} is a critical angle effect. Silicon is transparent at $1.54\mu m$ wavelength, therefore absorption is not significant. Reflection at silicon-air interface can be reduced by anti-

reflection coating at silicon surface. An increase of critical angle can also be achieved by coating the silicon surface with an intermediate medium such as a layer of oxide.

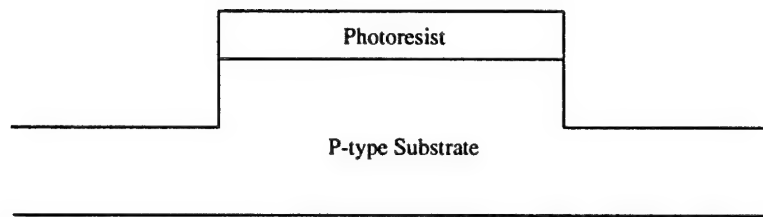
The IR effect (η_{IR}) is important when the LED series resistance is large. Low substrate doping leads to a large IR drop across the substrate and self-heating. Increase of the substrate doping certainly improves the IR drop. However due to free carrier Auger effect, carrier lifetime decreases as the substrate doping above $1 \times 10^{17} \text{cm}^{-3}$ [17, 18]. This nonradiative recombination effectively competes with Er optical recombination and decreases the Er light emission. A further discussion of this issue will be given in section 6.6.

6.4.2 Fabrication

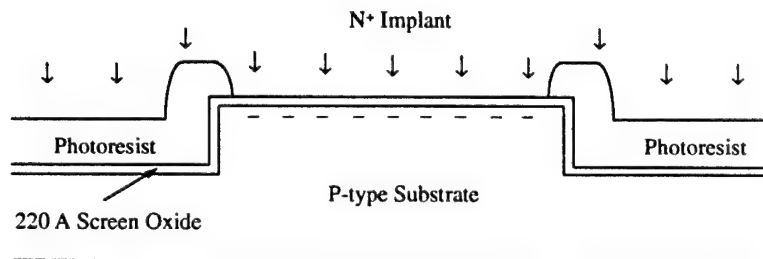
The fabrication of Si:Er LEDs took place in Integrated Circuits Laboratory (ICL). Various starting wafers were used for Si:Er LED fabrication. The best results were obtained from p-type ($1 \times 10^{16} \text{cm}^{-3}$) CZ wafers, so the following processing procedure assumes p-type CZ wafers.

The starting wafers were boron-doped p-type (100) oriented silicon CZ wafers ($0.5\text{-}2 \Omega \text{cm}$). Silicon mesa were first patterned and anisotropically dry-etched (using CCL_4/SF_6 chemistry) to provide isolation between different devices. A 220\AA thermal oxide was grown as a screen layer for junction implantation and also served as a passivation layer for Si mesa edge surface. N^+ /P junctions were then patterned and formed by high dose arsenic or phosphorus implantation as shown in Figure 6.5. A separate p^+ implantation was used to achieve good ohmic contacts to the substrate. A heat treatment of $950\text{C}/30\text{mins}/\text{O}_2 + 950\text{C}/30\text{mins}/\text{N}_2$ for phosphorus implant was carried out to remove the implantation damage and to activate dopants. For arsenic implant, a higher temperature annealing is required to drive arsenic close to the Er region. The wafers were then patterned for Er implantation. Due to the high implantation energy of Er, a $4\mu\text{m}$ thick photoresist was used as implantation mask. Er was implanted at an energy of 4.5 MeV with a peak concentration of $5 \times 10^{17} \text{cm}^{-3}$ to a peak depth of about $1.5\mu\text{m}$. An oxygen coimplant with the peak concentration of $3 \times 10^{18} \text{cm}^{-3}$ was designed to spatially overlap the Er implant. Both n^+ and Er implant were designed so that the implantation region is $10 \mu\text{m}$ away from the mesa edge as shown in Figure 6.6. The space charge region of the pn junction intersects only the top unetched Si surface, not the etched mesa edge surface, and therefore the leakage current due to the dry Si etching damage along the mesa edge was minimized.

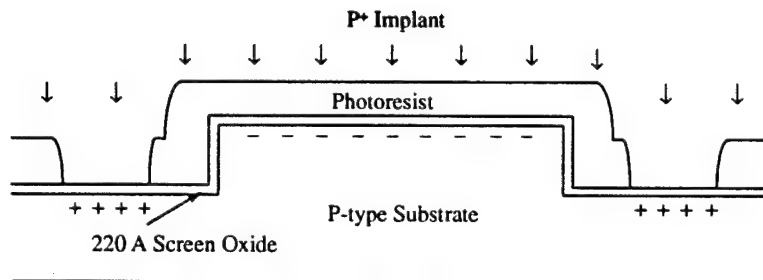
A high temperature ($900\text{C}/30\text{min}/\text{N}_2$) annealing was used to activate Er optically. This is a critical step for Er optical activation. ICL furnaces are idled at 800C . The boat-in of the wafers takes about 10 minutes. After the wafers are loaded, the furnace temperature stabilizes at 800C for 10 minutes. Then it starts to ramp to the desired process temperature at $10\text{C}/\text{min}$ rate (10 minutes for ramping from 800C to 900C). After it reaches the desired temperature, the furnace stabilizes at that temperature for another 10 minutes before it starts oxidation or annealing process. After the annealing, the furnace will first cool down to 800C at a rate of $-2.5\text{C}/\text{min}$ (40 minutes for cooling down from 900C to 800C), then it takes another 10 minutes to boat out. To accurately anneal Si:Er for 30 minutes at 900C , the furnace temperature was first



(a)

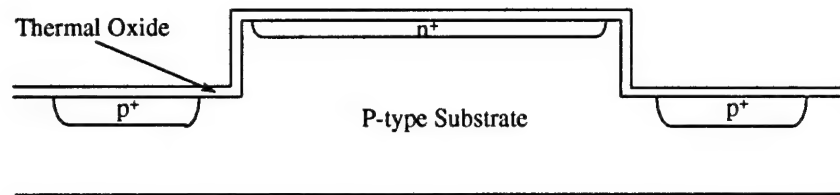


(b)

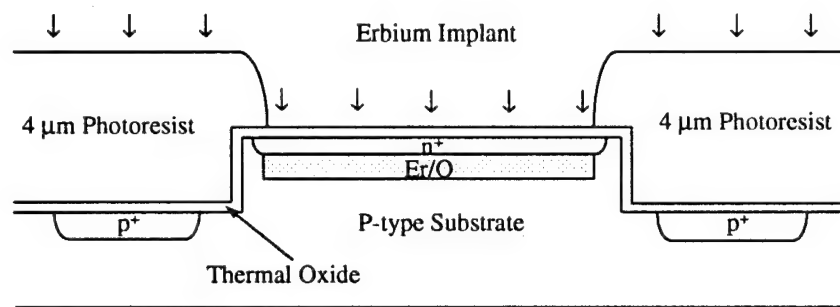


(c)

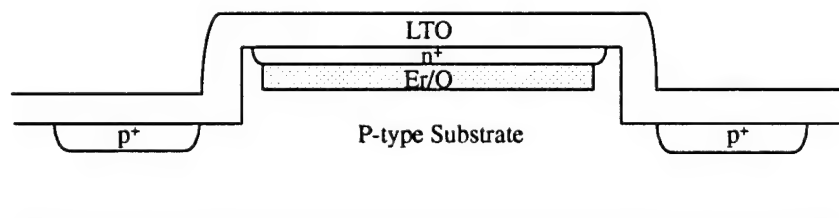
Figure 6.5: (a) Mesa pattern and Si dry etch.(b) N^+ junction pattern and implantation.(c) P^+ substrate contact pattern and implantation.



(a)

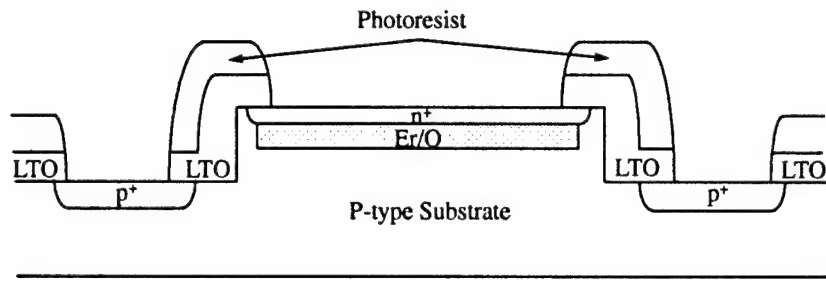


(b)

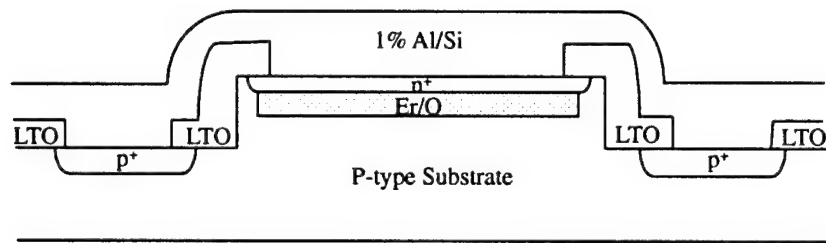


(c)

Figure 6.6: (a) N^+ junction annealing and drive-in. (b) Er/O pattern with $4\ \mu m$ photoresist and 4.5 MeV implantation. (c) Er/O annealing and LTO passivation.



(a)



(b)

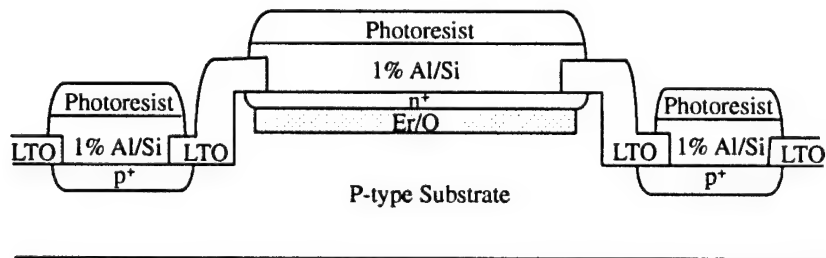


Figure 6.7: (a) Contact pattern and etch. (b) AlSi metal deposition. (c) AlSi metal pattern and dry etch.

raised to 900C and stabilized at this temperature before the wafers were loaded in. After the wafers saw 900C for 30 minutes, the wafers were boated out at 900C rather than cooling down to 800C. This modification of ICL furnace annealing procedure is important for effective Er annealing.

After Er annealing, a low temperature oxide was deposited to a thickness of a quarter wavelength (2500\AA) as a passivation layer as well as an anti-reflection coating for LED. Contact openings were then defined and $1\mu\text{m}$ 1% AlSi was sputter deposited. A final photolithography step followed by AlSi dry etch defined the LED metal contact pattern as shown in Figure 6.7. A 400C AlSi contact annealing in N_2/H_2 ambient improved the contact resistance and passivated previous processing damage. Al metal layer (96% reflectivity at $1.54\mu\text{m}$ [19]) was also deposited at the backside of the wafers to increase the light extraction efficiency by reflecting downwards light upwards.

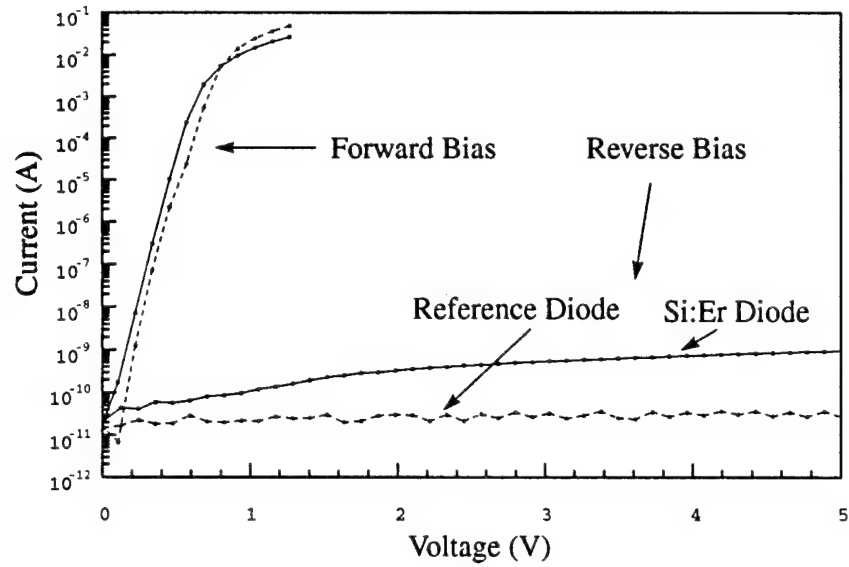
6.5 Electrical Characterization

Electrical characteristics of Si:Er LEDs and its reference diodes were measured by Keithley Yieldmax auto probe. Typical I-V curves of a Si:Er diode and a reference diode are shown in Figure 6.8(a). $1.28 \times 10^{-6} \text{A/cm}^{-2}$ leakage current at 5V reverse bias is observed for the Si:Er diode, while the leakage current is $3.72 \times 10^{-8} \text{A/cm}^{-2}$ for its reference diode. Ideality factors were calculated from I-V characteristics. The Si:Er LED has an average ideality factor of 1.25, while the reference diode has an average of 1.20. A higher ideality factor suggests the relative dominance of the recombination current over the diffusion current. The difference between Si:Er diodes and reference diodes is due to the residual Er implantation damage and the deep level states introduced by Er.

Due to the Er donor activity, junction doping profiles are different between the Si:Er diode and reference diode. Junction doping profiles were characterized by the spreading resistance profiling (SRP) technique. The junction depth of a Si:Er diode in a p-type CZ substrate ($1 \times 10^{16} \text{cm}^{-3}$) is defined by the Er implant rather than the implanted n^+ emitter. For a shallow arsenic n^+ emitter, an $n^+(\text{As}) / \text{p}(\text{substrate}) / \text{n}(\text{Er}) / \text{p}(\text{substrate})$ structure is formed as shown in Figure 6.8(b). As the emitter is driven closer to Er by the phosphorus implant or a high temperature drive-in of arsenic implant, an $n^+(\text{P or As}) / \text{n}(\text{Er}) / \text{p}(\text{substrate})$ junction profile was observed. Also shown in Figure 6.8(b) is the junction profile of the reference diode. A further detailed investigation of Er donor behavior will be presented in the next chapter.

Er introduces deep level states and is an effective recombination center [1, 4]. Recombination of electron-hole pairs at Er sites contributes to the diode recombination current. The existence of Er in the space charge region of the junction and residual implantation damage therefore lead to a higher leakage current and ideality factor.

Based on the I-V characteristics, the diode series resistance was calculated by plotting the voltage drop from the ideal value vs. current on a linear plot as shown in Figure 6.9 [20]. An average of 2.2Ω series resistance was obtained from a 3mm x 3mm Si:Er LED while the resistance was 1.6Ω for the reference diode. The residual Er implantation damage and the dopant compensation due to the Er donor activity



(a)

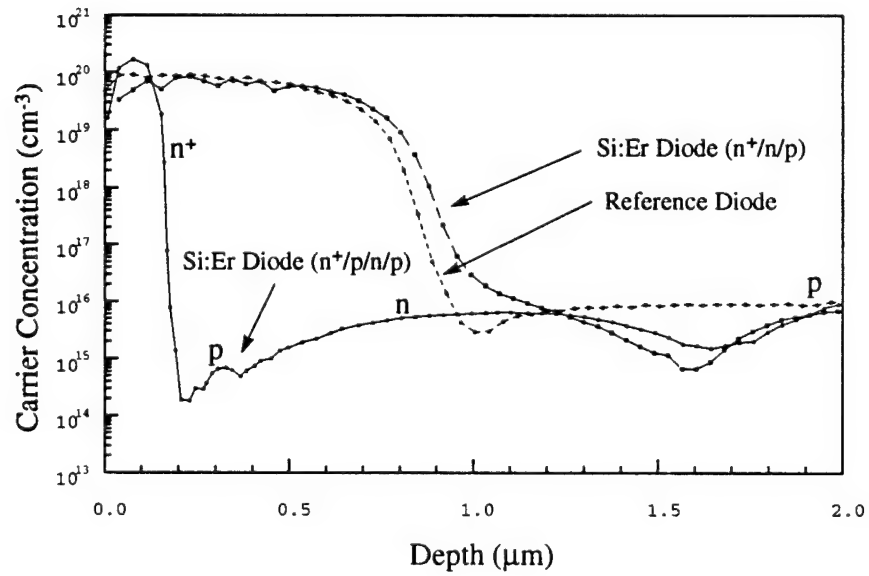
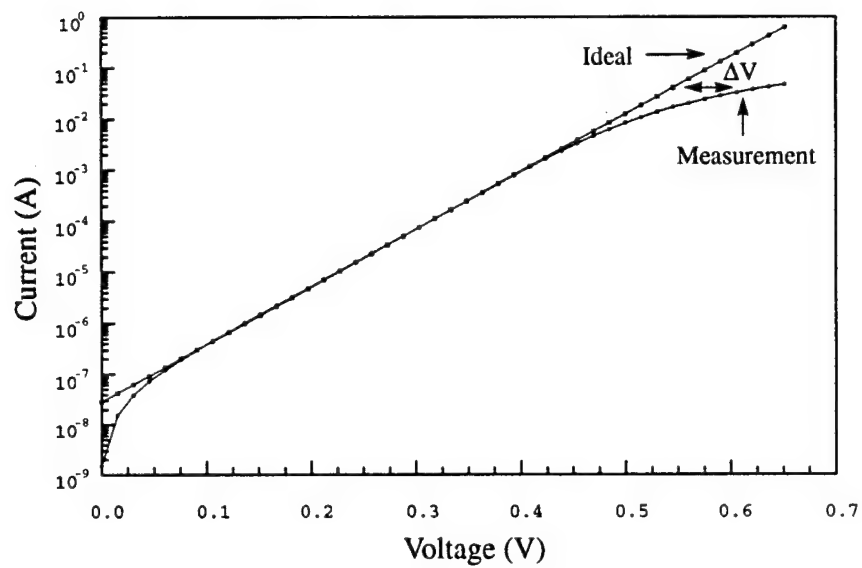


Figure 6.8: (a) Typical I-V characteristics of an Si:Er LED and a reference diode. (b) Junction profiles of two Si:Er LEDs with different n^+ emitter depth and a reference diode.



(a)

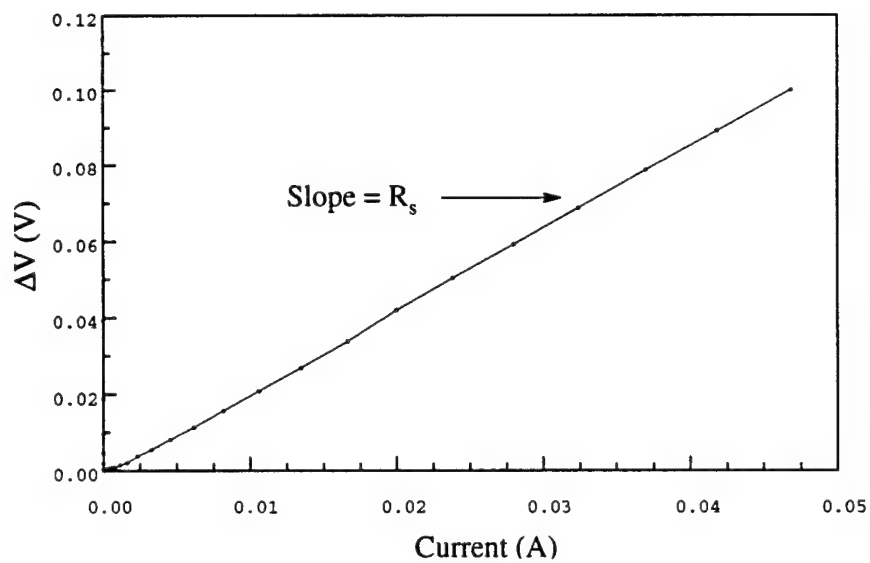


Figure 6.9: (a) Deviation of voltage drop (ΔV) from ideal. (b) ΔV vs. linear current to determine resistance R_s .

again contribute to the higher resistance.

Based on the spreading resistance profile, I-V characteristics of Si:Er diodes was simulated with the device simulator Medici. The spreading resistance profile (Figure 6.9 (b), $n^+/n/p$ Si:Er LED) was used as input for the Medici simulator as a junction doping profile with a junction depth at about $1.60\mu m$. SRH and free carrier Auger recombination was considered by assuming a default trap level in the middle of the bandgap, a default Auger coefficient of $2.8 \times 10^{-31} cm^6/s$ for electrons and $9.9 \times 10^{-32} cm^6/s$ for holes. The comparison of simulated and measured data is shown in Figure 6.10(a). A reasonable fit between the measurement and the simulation is observed. The discrepancy in the low bias region is probably due to two factors: (1) the default trap level defined in Medici is different from many deep levels introduced by Er, which leads to a different recombination current; and (2) the simulator does not take into account the dopant compensation.

A perimeter/area measurement of leakage current was carried out to determine the source of the leakage current. As shown in Figure 6.10(b), the leakage current scales linearly with the Er diodes area rather than their perimeter. This indicates that the leakage current is due to the bulk material rather than the Si mesa etch. The non intersection of the space charge region with the etched mesa surface and oxide passivation successfully eliminate the mesa etch damage as a source of excess leakage current.

6.6 Optical Characterization

6.6.1 Electroluminescence and Photoluminescence

Electroluminescence (EL) and photoluminescence (PL) spectroscopy was used as an important optical characterization tool for Si:Er LEDs. EL and PL have a similar experimental setup. The main difference is that in PL measurement a 488nm argon laser is used and in EL a square wave voltage output from a pulse generator is used to forward bias the LED. The setup is shown in Figure 6.11.

The fabricated wafers were cut with a die-saw and the diodes were then mounted on TO-5 headers. Electroluminescence measurements were performed by forward biasing the diode with a pulse generator (25 Hz modulation, 50 % duty cycle). The emitted light was dispersed using a 0.75m Spex monochromator and detected by a liquid nitrogen cooled Northcoast Ge detector. Low temperature measurements were performed by mounting the LED in an Oxford helium cryosystem (CF204).

Figure 6.2 shows typical electroluminescence spectra from a surface-emitting Si:Er LED, observed at both 100K and room temperature. A sharp luminescence linewidth (150 Å) at $1.54\mu m$ is observed at room temperature. No line shift of the peak wavelength with temperature is observed, consistent with the Er intra-4f shell transition. Also shown in Figure 6.3 is the PL spectrum of the same diode. The similarity of the spectra indicates that both EL and PL have the same electron-hole pair mediated excitation mechanism [2].

The EL spectra and intensities depend on the drive current density. Shown in

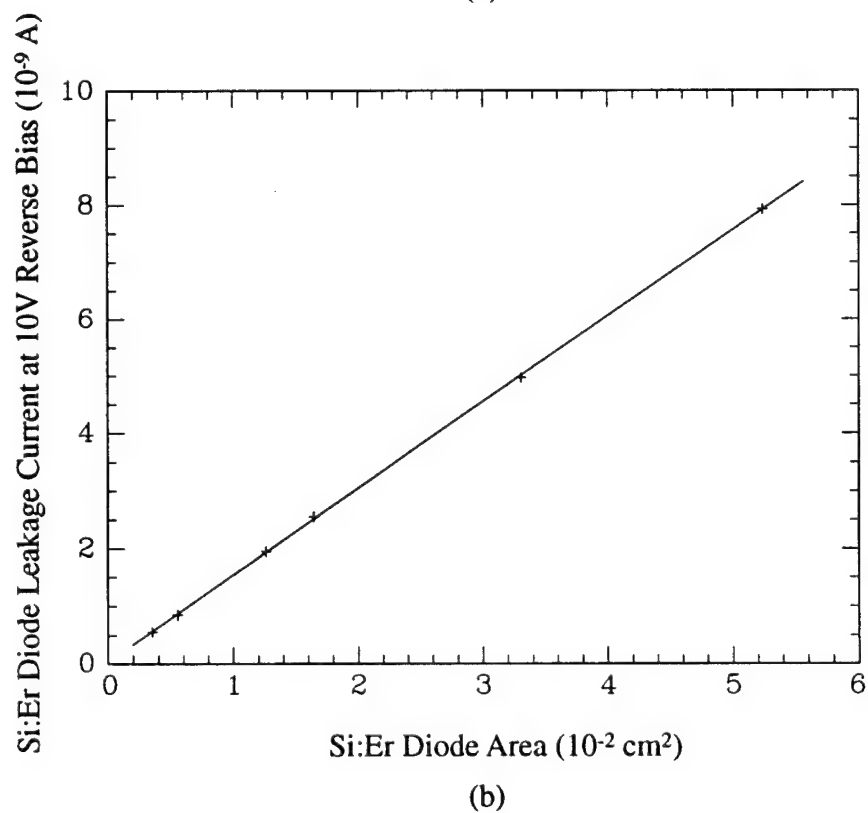
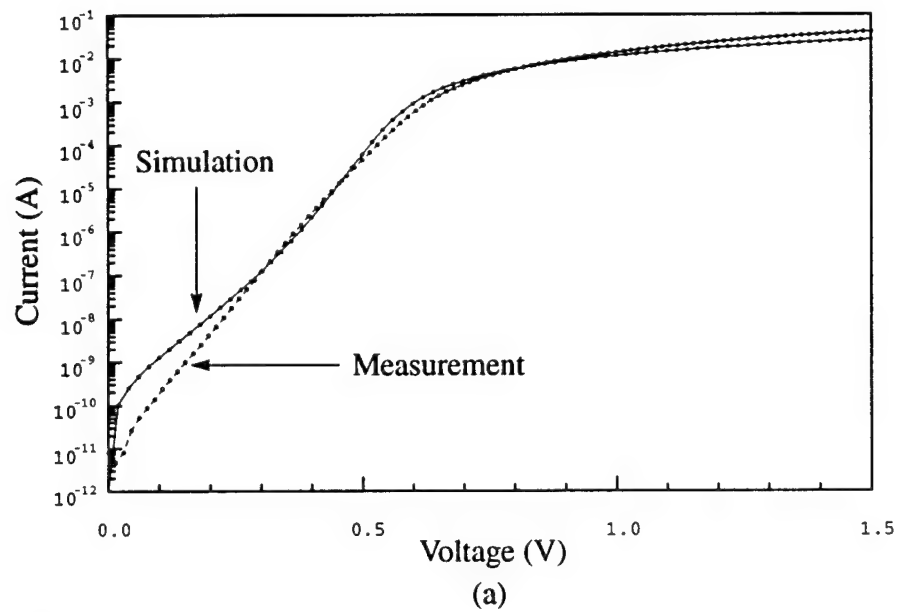


Figure 6.10: (a) Medici simulated and measured I-V curves for Si:Er diode. (b) Si:Er diode leakage current area dependence.

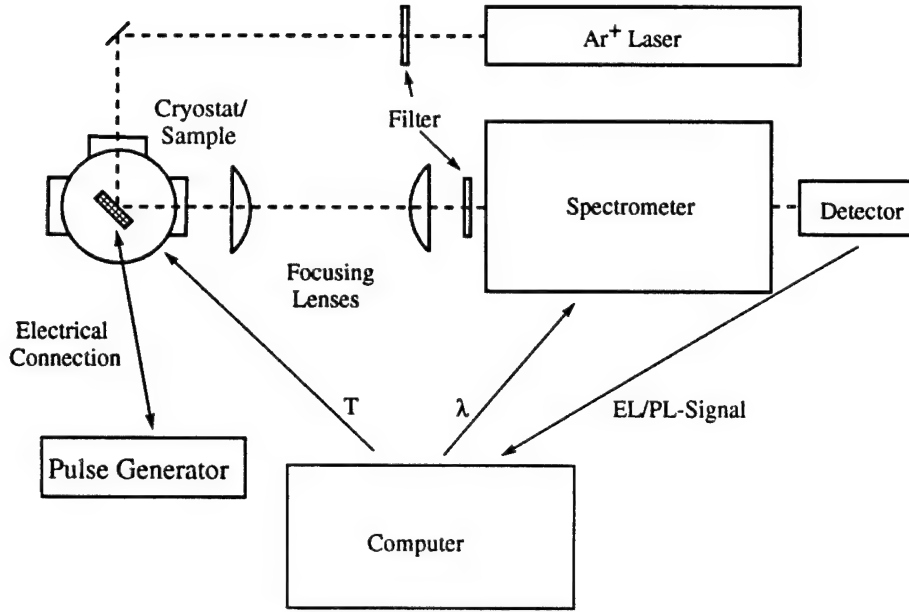


Figure 6.11: Photoluminescence and electroluminescence experimental setup.

Figure 6.12 are the EL spectra taken at 100K with different drive current densities. Only Er luminescence at $1.54\mu\text{m}$ is observed at low drive current density. At higher drive current density, the Er luminescence tends to saturation and free exciton and defect-related luminescence lines appear. The relative dominance of the Er luminescence at low drive current densities shows that the Er centers are efficient radiative recombination centers. The defect-related luminescence spectra are likely to be the dislocation related D-lines [6, 21, 22]. The two main peaks at $1.35\mu\text{m}$ and $1.44\mu\text{m}$ are close to the peak wavelength of D_3 ($1.33\mu\text{m}$) and D_2 ($1.42\mu\text{m}$), while the background feature around $1.54\mu\text{m}$ matches with D_1 ($1.53\mu\text{m}$). Absence of D-lines from reference diodes indicates that D-lines are Er related.

The dependence of the Er EL peak intensity on the drive current densities is shown in Figure 6.12. At 100K, the Er EL peak intensity starts to level off at a drive current density of about 1.5 A/cm^2 , while no saturation is observed at room temperature. The band-edge related luminescence peak intensity and D-lines peak intensity increase with the drive current density as expected, and no saturation is observed. The saturation of the Er EL intensity at 100K is due to the presence of a competing nonradiative impurity Auger backtransfer process at high injected carrier concentration. Er light emission is proportional to [15]:

$$EL \sim \frac{N_{Er}^*}{\tau_{rad}} \quad (6.5)$$

where N_{Er}^* is the optically active Er concentration and τ_{rad} is the spontaneous radiative lifetime of Er. From other measurements and simulations [15, 16], it is believed that the Er light emission is limited by the impurity Auger process and not by the amount of excitable Er ions. At low drive current density, the impurity Auger process

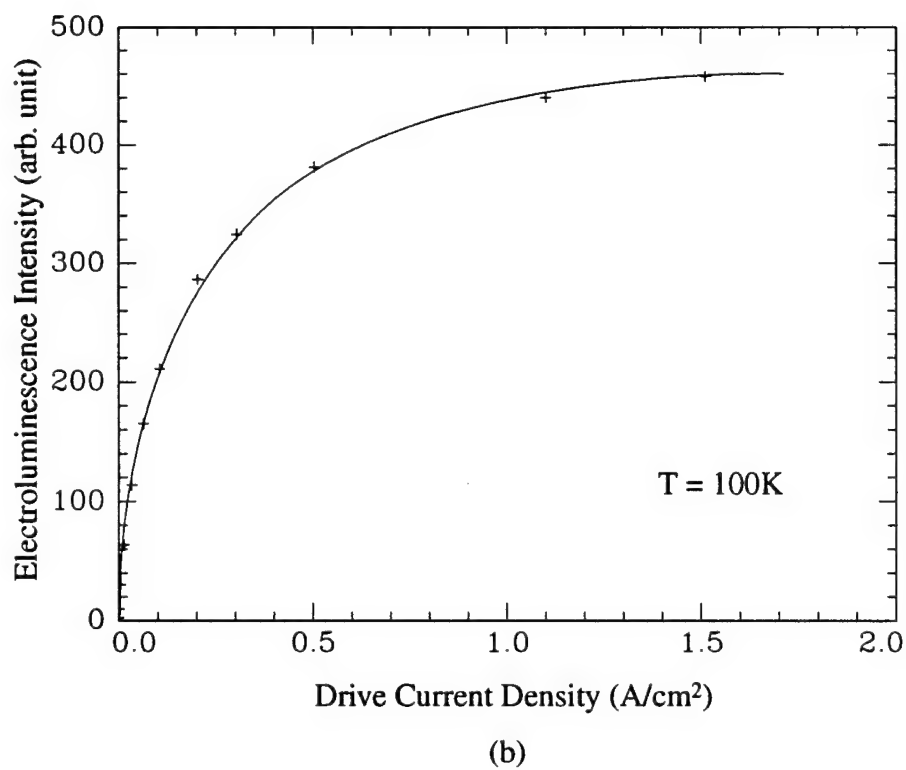
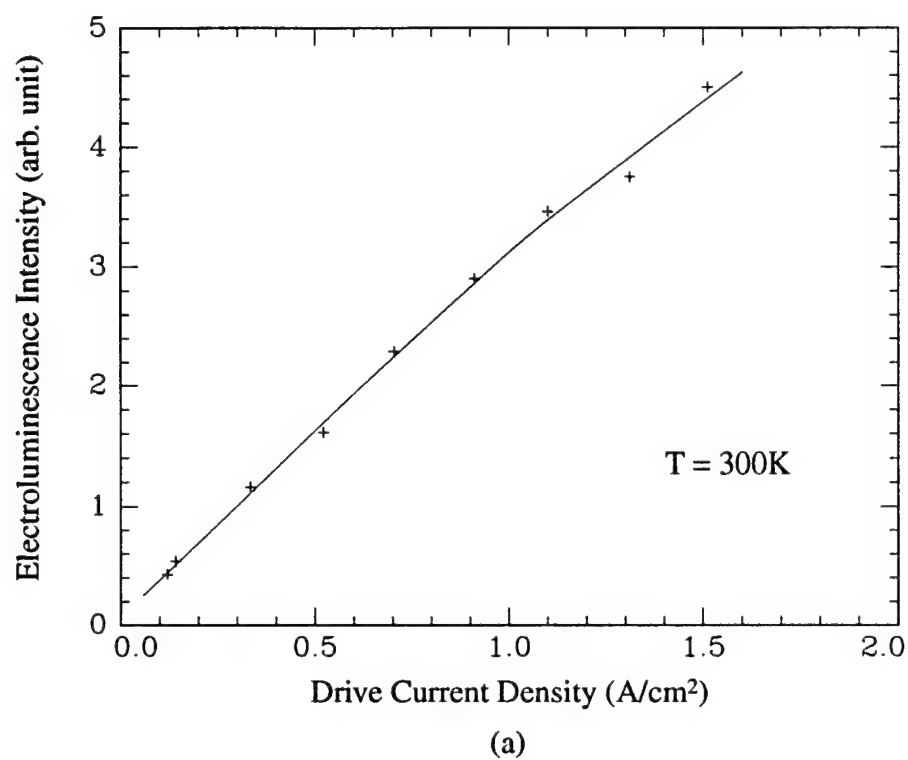


Figure 6.12: Si:Er LED EL drive current density dependence at both $T = 300\text{K}$ (a) and $T = 100\text{K}$ (b).

is not an important competing process for the Er radiative recombination process and an increase of Er light emission vs. current density is therefore observed. At high current density, the impurity Auger process becomes an efficient competing process to deexcite the excited Er atoms (N_{Er}^*) by transferring the energy nonradiatively back to the Si lattice instead of emitting photons. This backtransfer process causes the level off of Er light emission at high drive current density. At room temperature, another unidentified back transfer nonradiative recombination process becomes dominant [15], which leads to a less efficient pumping process for Er and therefore a much higher drive current density is needed to saturate the Er.

The Er EL peak intensity decreases significantly as temperature increases (Figure 6.4). The EL peak intensity was monitored near its saturation value with a constant forward bias current density over the entire temperature range. The linewidth of the Er luminescence at $1.54\mu m$ broadens slightly from 85\AA at 100K to 150\AA at 300K. The thermal quenching behavior is similar to that of the PL measurement [1, 2]. The detailed mechanism for thermal quenching is not clear. An impurity Auger process was identified as partially responsible for the thermal quenching. Nonradiative energy back transfer from the excited Er atom to Si lattice by this impurity Auger process significantly quenches the Er light emission intensity.

6.6.2 Quantum Efficiency

Light output power was measured with a Newport power meter. A 1:1 ratio collection optics was used to focus emitted light into the power meter. A $1.54\mu m$ narrow bandwidth (45nm) bandpass filter was used to filter out the dislocation lines and bandedge luminescence. Only part of the emitted light was collected and focused into the power meter. Based on the collection optics, the measured power output is used to calculate the total Er light emission power.

The optical efficiency η_{opt} of the Si:Er LED can be estimated as

$$\eta_{opt} = \eta_{abs} \times \eta_{ref} \times \eta_{cri} \quad (6.6)$$

$\eta_{abs} = \exp(-\alpha \times L)$, where α is the absorption coefficient of the Si material and L is the distance from the light-emitting site to the Si surface. Assuming a typical number of $1\mu m$ for L and 50 cm^{-1} for the α of degenerately doped n^+ layer [23], $\eta_{abs} = 0.9950$, i.e., the absorption is negligible.

$\eta_{ref} = 1 - R$, where R is the reflectivity at interface. At perpendicular incidence, the reflectivity of a ($n_1(\text{air}) \angle n_2(\text{oxide}) \angle n_3(\text{Si})$) sandwich layer becomes:

$$R = \left(\frac{n_1 n_3 - n_2^2}{n_1 n_3 + n_2^2} \right)^2 \quad (6.7)$$

The reflectivity can be minimized by selecting a layer of oxide with a quart wavelength thickness: $t_{oxide} = \frac{\lambda}{4n^2} = 2500\text{\AA}$. Therefore, $\eta_{ref} = 1 - R = 0.9552$, assuming a refractive index of 1.5 and 3.5 for oxide and Si, respectively.

Only a fraction of emitted light lying within the cone of critical angle θ_c can be extracted. $\eta_{cri} = 1 - \cos \theta_c = 1 - \left(1 - \left(\frac{n_2}{n_3} \right)^2 \right)^{-1/2} = 0.09649$.

Therefore $\eta_{opt} = \eta_{abs} \times \eta_{ref} \times \eta_{cri} = 9.17\%$, i.e, only 9.17% of the total generated light can escape from the Si substrate.

Given a 7.5 cm collection lens diameter and 9 cm distance between LED and lens, the collection angle of the lens can be calculated as: $\theta_{lens} = \arctan(\frac{7.5}{2 \times 9}) = 22^\circ$. Therefore the lens collection efficiency $\eta_{lens} = 1 - \cos 22^\circ = 0.072$, only 7.2% of the total emitted light is collected. The cryostat window consists of three quartz windows, each having a transmission coefficient of $T_{glass} = \frac{4 \times n}{(n+1)^2} = 0.96$. Furthermore there are two focussing lenses with a similar T_{glass} . The bandpass filter has a transmission coefficient of $T_{filter} = 0.75$ at $1.54\mu m$. Therefore, the transmission coefficient of the glass and filter is $\eta_{trans} = T_{glass}^5 \times T_{filter} = 0.6115$.

Therefore, only $9.17\% \times 7.2\% \times 61\% = 0.4\%$ of the total generated light was collected into the power meter. This 0.4% light extraction efficiency is a typical value for a planar surface-emitting LED [24].

The power meter has a diameter of 2mm light absorption area. Due to the use of 1:1 collection optics, only the identical size of the LED can be focused into the power meter. Therefore an area factor $\eta_{area} = \frac{A_{detector}}{A_{LED}}$ needs to be included.

Based on the above assumptions, the total light power generated from Er can be estimated from the measured power out as following:

$$P_{out}(Er) = \frac{P_{out}(measured)}{\eta_{opt} \times \eta_{lens} \times \eta_{trans} \times \eta_{area}} \quad (6.8)$$

The input power is calculated from the measured voltage across the diode and the current as:

$$P_{in} = voltage \times current \quad (6.9)$$

The internal quantum efficiency (η_{int}) is defined as:

$$\eta_{int} = \frac{P_{out}(Er)}{P_{in}} \quad (6.10)$$

Figure 6.13 shows Er power output ($P_{out}(Er)$) and quantum efficiency (η_{int}) versus drive current density. A higher η_{int} is observed at lower drive current density, where the maximum is 4×10^{-4} at 100K.

At high drive current density, a significant amount of heat was generated. $R = 2.2 \Omega$ series resistance was calculated from I-V measurement and the amount of heat was calculated as:

$$P_{heat} = I^2 \times R \quad (6.11)$$

By taking into account the generated heat, a higher η_{int} can be calculated as:

$$\eta_{int} = \frac{P_{out}(Er)}{P_{in} - P_{heat}} \quad (6.12)$$

The heat-adjusted η_{int} is also shown in Figure 6.13.

This 5×10^{-4} internal quantum efficiency is about 2 orders of magnitude higher than the 3×10^{-6} internal quantum efficiency reported by Polman [25]. However, orders of magnitude increase is needed for practical applications at room temperature.

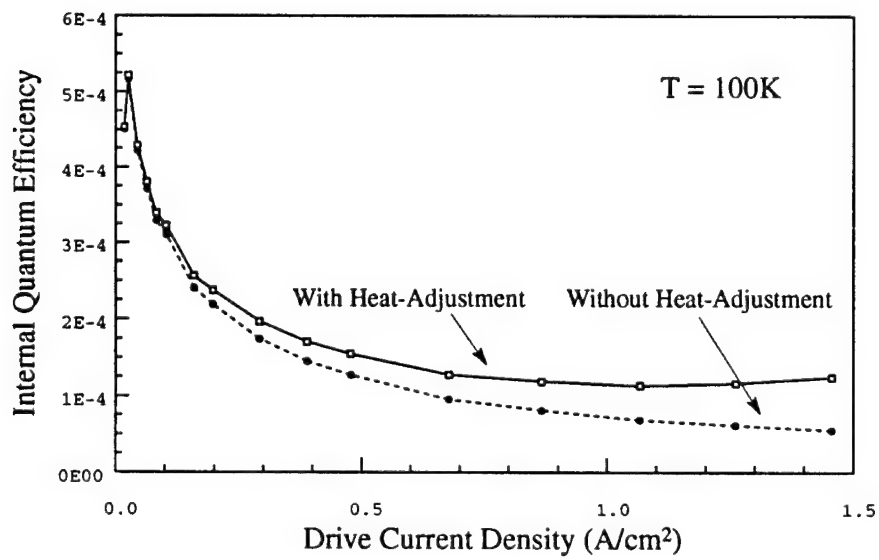
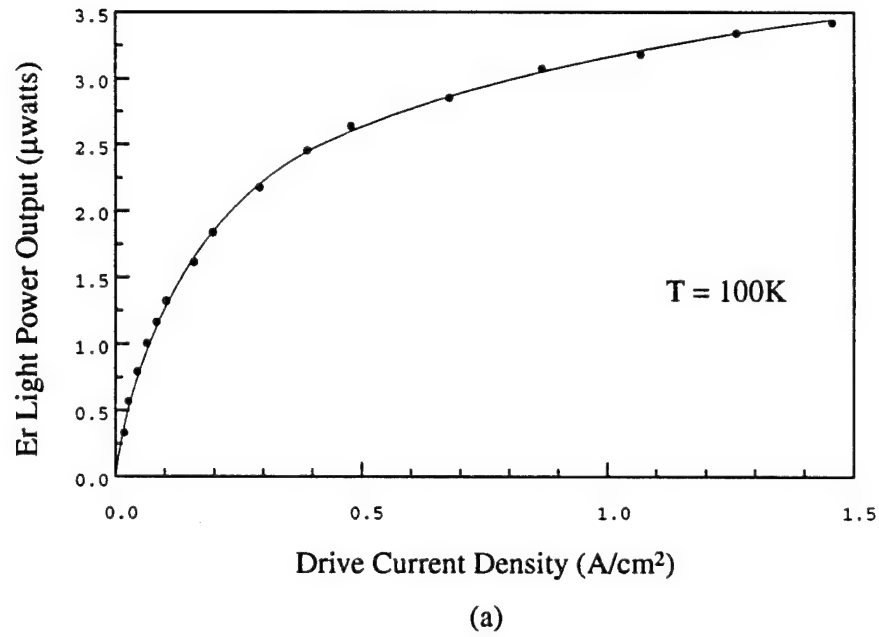


Figure 6.13: (a) Si:Er LED light power output at T = 100K. (b) Si:Er LED internal quantum efficiency at T = 100K.

The approaches to increase the internal quantum efficiency are likely to be through the engineering of Er micro-environment, such as different ligand field, to increase the Er capture cross section of electron-hole pair [3]. Also, the minimization of other competing processes which includes the minimization of D-lines are important. From the TEM pictures (will be discussed in next chapter), there are still considerable residual Er implantation damage. The removal of these damage should increase the efficiency by eliminating competing recombination channels.

The percentage of optically active Er can be estimated from the saturated Er light output power. At 100K, the Er saturation output power at $J = 1.5\text{A}/\text{cm}^2$ was $3.4\mu\text{W}$. The Er light output power can also be calculated as

$$P_{out}(Er) = \frac{[Er] \times h \times c}{\tau_{sp}} \quad (6.13)$$

where $P_{out}(Er)$ is the total power output of Er, $[Er]$ is the concentration of optically active Er, and τ_{sp} is the spontaneous lifetime. Assuming $\tau_{sp} = 1\text{ms}$ [3] [7], $[Er]$ is estimated to be 2.64×10^{10} atoms. Given the Er dose of $3.8 \times 10^{13}\text{cm}^{-2}$ and a LED area of $9 \times 10^{-2}\text{cm}^2$, a total of 3.42×10^{12} Er atoms was implanted. Therefore, the percentage of optically active Er at 100K can be estimated to $2.644 \times 10^{10}/3.42 \times 10^{12} = 0.78\%$.

6.6.3 Junction Profile

The effect of junction depth on Er light emission intensity was studied in two experiments. Due to the Er/O implantation related donor activity, the junction depth in p-type substrate was defined by the Er implant rather than by the implanted phosphorus or arsenic. To easily vary the junction depth, the junction depth variation experiment was first carried out in a n-type substrate. In n-type substrate, the junction depth was clearly defined by the implanted p^+ without the complication of Er donor activity. Junction depth can be varied by implanting boron at different energies. All the other processing conditions were kept constant so that a comparison of Er EL intensity and junction depth can be made.

EL comparison of Si:Er LEDs were done in identical experiment conditions. A typical L-J (light vs drive current density) curve at 100K is shown in Figure 6.14(a). The dependence of Er EL intensity on junction depth is shown in Figure 3.14(b). As the junction moves close to the Er region, an increase of Er light emission is observed. The EL intensity peaks at a junction depth of about $1.2\mu\text{m}$. As the junction moves across the Er peak, light emission actually decreases.

Shown in Figure 6.15(b) is a SIMS measurement of Er doping profile and four SUPREM-3 simulated junction profiles. As the junction moves toward Er, the injected minority carrier concentration at the Er sites increases. Recall that the electron-hole-Er Auger process is the main excitation mechanism. Therefore, this leads to an increase of Er excitation efficiency and Er light emission. At the same time, a major part of Er region is not covered by the heavily doped n^+ layer. However, as the junction moves over the Er im[plantation peak, a significant part of Er is covered by the heavily doped p^+ region. The p^+ region decreases the minority carrier lifetime

[17, 18] and therefore reduces the Er excitation efficiency. This leads to a decrease of Er light emission. The tradeoff between the carrier injection efficiency (move junction close to Er region) and the decrease of carrier lifetime due to high concentration (move junction away from Er region) leads to an optimum junction depth of about $1.2\mu\text{m}$ for maximum light emission.

This junction depth dependence can be modeled by making the following assumptions: (1) Er does not emit light when it is buried in the heavily doped p^+ region, (2) a characteristic diffusion length (L) describes the carrier recombination and diffusion process through the Er region, (3) the Er light output (P_{Er}) is proportional to the remaining Er dose ($[Er]$, not buried in heavily doped region) and the carrier injection efficiency at an Er peak depth of about $1.5\mu\text{m}$, therefore:

$$P_{Er} \sim [Er] \times \exp\left(\frac{-(1.5 - x_j)}{L}\right) \quad (6.14)$$

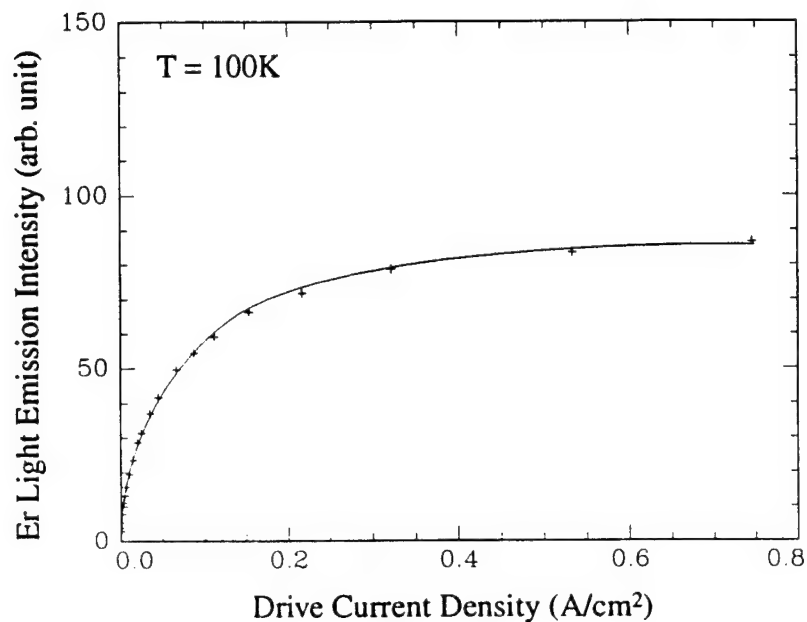
where x_j is the junction depth, and the Er peak depth is about $1.5\mu\text{m}$. A reasonable fitting between the measurement data and the above equation (Figure 3.14(b)) leads to the determination of the characteristic diffusion length $L = 0.5\mu\text{m}$. This small diffusion length in the Er region is probably due to the optical active Er, acting as a recombination center, and the residual Er implantation damage.

A second study on the effects of n^+ emitter depth variation on Er EL intensity in a p-type substrate was also carried out. Due to the Er donor activity, junction depth was defined by Er implant rather than n^+ implanted emitter in p-type CZ ($1 \times 10^{16}\text{cm}^{-3}$) substrate. Three Si:Er diodes with three different n^+ emitter depths were implanted with the same Er/O dose and annealed at the same conditions (900C/30mins/ N_2). However, two n^+ emitter (LED A and LED C) were implanted with arsenic and one n^+ emitter (LED B) was implanted with phosphorus. This different dopant emitter would introduce certain variation in the comparison.

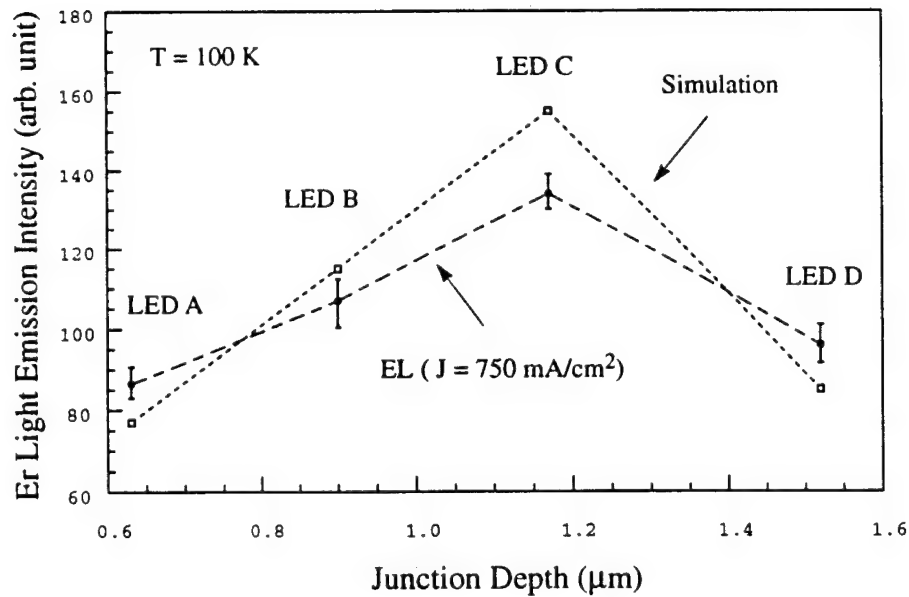
Spreading resistance profiles of three Si:Er diodes and Er SIMS profile are shown in Figure 6.16(a). SIMS shows that the majority of the Er region is not covered by the highly doped n^+ emitter region. As expected, the junction depth is similar for the three diodes. The n^+ emitter depth were $0.45\mu\text{m}$, $0.75\mu\text{m}$, and $1.0\mu\text{m}$ for LED A, B and C. A comparison of EL and PL under the same experiment conditions is shown in Figure 6.16(b). Er PL intensity of LEDs A and B were similar, given the difference of phosphorus and arsenic n^+ emitter. A slight decrease of Er PL intensity was observed from LED C, possibly due to the fact that the n^+ emitter of LED C covers more of the Er region than LED A and B. While the PL intensities are comparable among the three LEDs, a much larger EL intensity variation is observed. EL intensities increase as the n^+ emitter moves closer to the Er region as shown in Figure 6.16(b).

As the n^+ emitter moves closer to the Er region, even the junction depth has not changed, the injected electron concentration at the Er from the n^+ region increases. This leads to an increase of Er excitation efficiency and therefore an increase of Er light emission. This dependence can again be simulated using a similar approach. Assuming that:

$$P_{Er} \sim [Er] \times \exp\left(\frac{-(1.5 - x_e)}{L}\right) \quad (6.15)$$

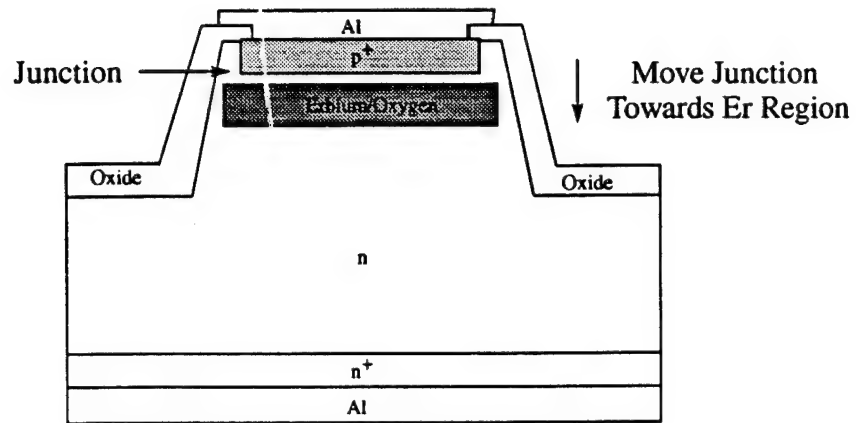


(a)

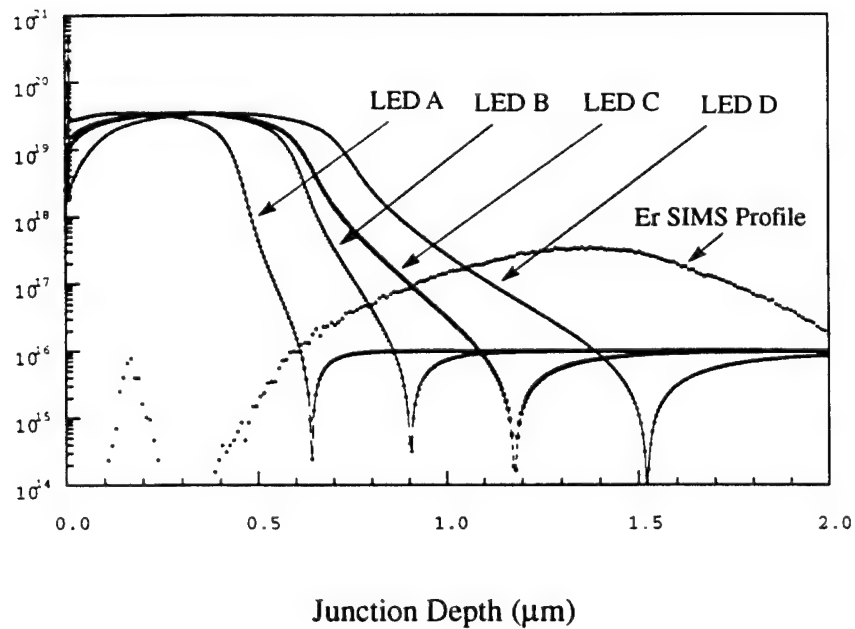


(b)

Figure 6.14: (a) A typical Er EL intensity vs. drive current density. (b) Si:Er LED light emission intensity vs. junction depth in n-type substrate. The dashed line with error bar is the measurement, and the dotted line is the simulation.



(a)



(b)

Figure 6.15: (a) Cross section view of an Si:Er LED on n-type substrate. (b) Suprem3 modeled junction depth profiles.

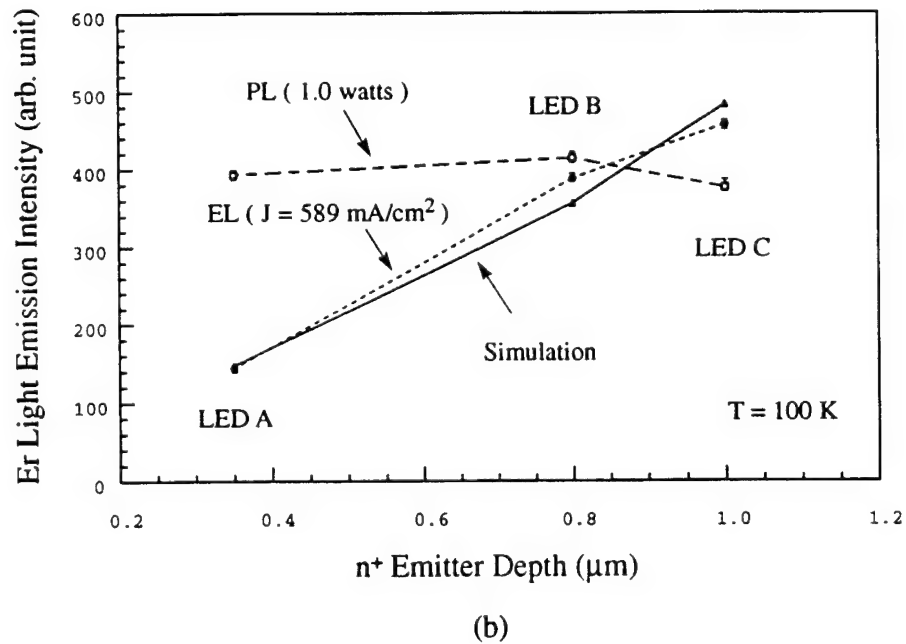
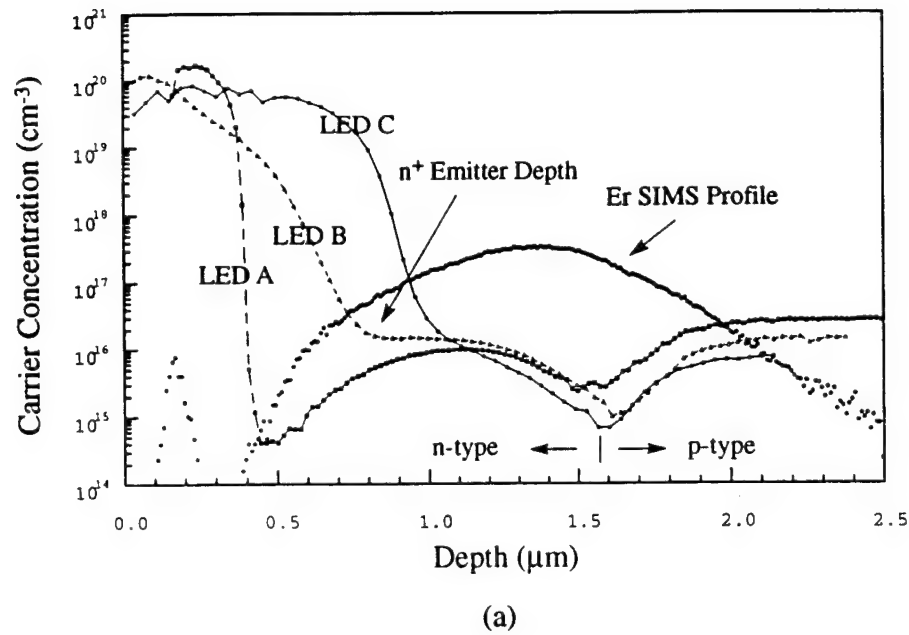


Figure 6.16: (a) Spreading resistance profiles of three Si:Er LEDs with different n^+ emitter depth. (b) EL and PL comparison of three Si:Er LEDs with different n^+ emitter depth. The center line is PL measurement, the dotted line is EL measurement, and the solid line is the simulation.

where x_e is the n^+ emitter depth. The fitting leads to a similar diffusion length $L = 0.5\mu m$ (Figure 6.16(b)). The very similar diffusion lengths obtained from both substrates indicate that indeed this characteristic diffusion length describes the carrier recombination and diffusion processes in the Er region. Given the carrier concentration of about $10^{16}cm^{-3}$, a much larger diffusion length of about $500\mu m$ is expected [26] for the Si only region. This three orders of magnitude decrease of diffusion length at the presence of Er indicates the effectiveness of Er as a recombination center and the presence of residual implantation damage.

A carrier lifetime of about $\tau = 2ns$ is estimated from the $0.5\mu m$ diffusion length [26]. From the equation:

$$\tau = (N_t \times v_{th} \times \sigma_{Er})^{-1} \quad (6.16)$$

where N_t is the carrier trap density and $v_{th} = 10^7 cm/s$ is the thermal velocity, the Er carrier capture cross section σ_{Er} can be estimated to be about $10^{-15}cm^{-2}$ by assuming that N_t is equal to the Er concentration of about $5 \times 10^{17}cm^{-3}$. A typical capture cross section for efficient recombination centers such as gold or iron is about $10^{-15}cm^{-2}$ [27]. Therefore the calculated fairly large capture cross section again indicates that Er is an efficient recombination center.

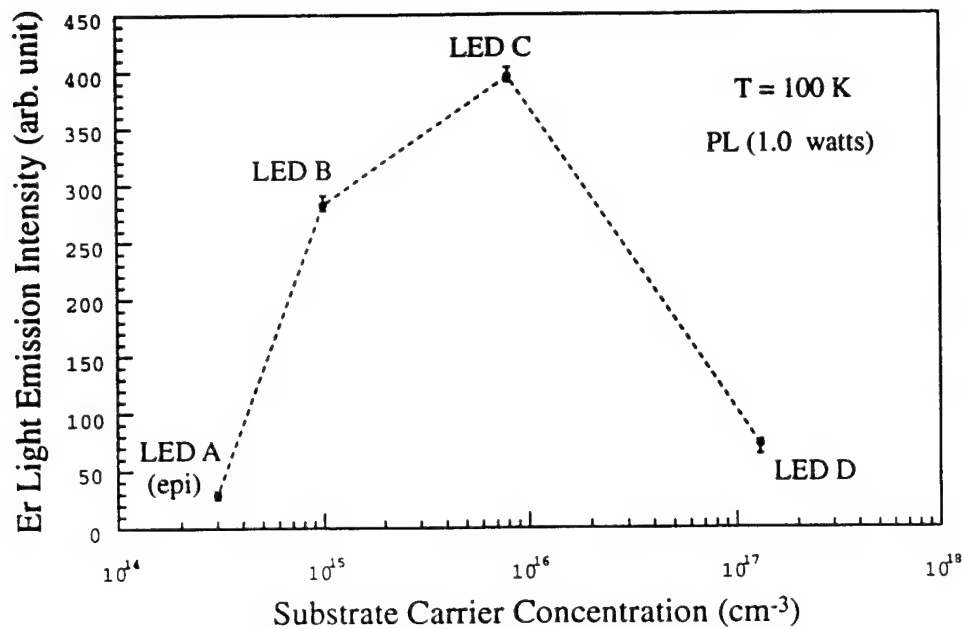
6.6.4 Substrate Concentration

High substrate concentration is desired for low series resistance. However, high substrate concentration also has a substantially lower minority lifetime due to free carrier Auger effect. This small carrier lifetime leads to low Er excitation efficiency and therefore low Er light emission.

Si:Er LEDs were fabricated similarly on a total of four different doping wafers: one p-type epi wafer ($3 \times 10^{14}cm^{-3}$, LED A) and three p-type CZ ($1 \times 10^{15}cm^{-3}$ for LED B, $1 \times 10^{16}cm^{-3}$ for LED C, and $2 \times 10^{17}cm^{-3}$ for LED D) wafers. Emitter implantation was first performed and the damage removed by annealing. Er and O were then implanted at a peak concentration of $5 \times 10^{17}cm^{-3}$ and $3 \times 10^{18}cm^{-3}$, respectively. Identical annealing at 900C for 30 minutes in N_2 ambient was used for Er activation.

Due to the limited Er donor activity, the junction depth was defined at about $1.6\mu m$ by the Er implant in LEDs A, B, and C. In LED D, the high background p-type concentration was only slightly compensated by the Er donor activity. Therefore, the junction was defined by the implanted n^+ emitter instead of Er. A shallower junction depth of $0.6\mu m$ was measured for LED D. This junction depth variation certainly complicates the concentration comparison. While the junction depth difference complicates the EL comparison, its effect on PL comparison is limited. This is supported by the n^+ emitter depth variation experiment in which PL intensities of LEDs with different n^+ emitter depth were comparable. Therefore this comparison is still expected to show the trend.

The comparison of Er PL intensities of four Si:Er LEDs were done under the same experiment conditions at 100K. The results are shown in Figure 6.17. Maximum Er light emission intensity was obtained from LED B ($1 \times 10^{16}cm^{-3}$). A sharp PL



(a)

Figure 6.17: Er PL intensity vs. substrate concentration.

intensity decrease was observed for high boron substrate concentration (LED D, $2 \times 10^{17} \text{ cm}^{-3}$). Both a lower carrier lifetime under high substrate concentration due to free carrier Auger effect and a non-radiative impurity Auger backtransfer process at high carrier concentration contribute to the decrease of Er PL light emission for LED D. The decrease of Er PL intensity at $1 \times 10^{15} \text{ cm}^{-3}$ concentration (LED B) is not understood.

A further decrease of Er light emission intensity is observed from LED A ($3 \times 10^{14} \text{ cm}^{-3}$, epi wafer). This drop is unlikely due to substrate concentration effect but due to a much lower oxygen concentration in the epi wafer (less than $1 \times 10^{16} \text{ cm}^{-3}$ in epi vs. $1 \times 10^{18} \text{ cm}^{-3}$ in CZ). Er was coimplanted with $3 \times 10^{18} \text{ cm}^{-3}$ oxygen, but due to a small straggle of oxygen implant compared to Er implant, a significant part of the Er is not covered by oxygen. The lack of oxygen is believed to be the main reason for a low Er light emission intensity in LED A. Relatively low Er light emission from epi wafers was also reported in literature [28].

6.7 Summary

The first room temperature Si:Er LED has been demonstrated by 4.5 MeV Er implantation. Various efforts have been made to characterize Si:Er LEDs and to increase its efficiency. However, a low quantum efficiency was measured and orders of magnitude increase is needed for practical room temperature application.

Bibliography

- [1] F. Ren, J. Michel, Q. Sun-Paduan, B. Zheng, H. Kitawa, D. C. Jacobson, J. M. Poate, and L. C. Kimerling, *Mat. Res. Soc. Symp. Proc.* Vol. 301, 87 (1993).
- [2] J. Michel, J. L. Benton, R. F. Ferrante, D. C. Jacobson, D. J. Eaglesham, E. A. Fitzgerald, Y. H. Xie, J. M. Poate, and L. C. Kimerling, *J. Appl. Phys.* 70, 2672 (1991).
- [3] B. Zheng, J. Michel, F. Ren, L. C. Kimerling, D. C. Jacobson, and J. M. Poate, *Appl. Phys. Lett.* 64, 2842 (1994).
- [4] F. Ren, Ph.D Thesis, MIT, 1994.
- [5] J. L. Benton, J. Michel, L. C. Kimerling, D. C. Jacobson, Y. H. Xie, D. J. Eaglesham, E. A. Fitzgerald, and J. M. Poat, *J. Appl. Phys.* 70, 2667 (1991).
- [6] R. Sauer, J. Weber, J. Stolz, E. R. Weber, K. H. Kusters, and H. Alexander, *Appl. Phys. A*, 36, 1 (1985).
- [7] P. B. Klein, and G. S. Pomrenke, *Electron. Lett.* 24, 1503 (1988).
- [8] J. Michel, F. Ren, B. Zheng, D. C. Jacobson, J. M. Poate, and L. C. Kimerling, *Proceedings of ICDS 17*, Gmunden, Austria, 1994.
- [9] I. N. Yassievich and L. C. Kimerling, *Semicond. Sci. Technol.* 7, 1 (1993).
- [10] H. Efeoglu, J. H. Evans, T. E. Jackman, B. Hamilton, D. C. Houghton, J. M. Langer, A. R. Peaker, D. Perovic, I. Poole, N. Ravel, P. Hemment, and C. W. Chan, *Semicond. Sci. Technol.* 8, 236 (1993).
- [11] H. Ennen, G. Pomrenke, A. Axmann, K. Eisele, W. Haydl, and J. Schneider, *Appl. Phys. Lett.* 46, 381 (1985).
- [12] B. E. A. Saleh, and M. C. Teich, *Fundamentals of Photonics*, Wiley-Interscience Publishing Company.
- [13] Y. H. Xie, E. A. Fitzgerald, and Y. J. Mii, *J. Appl. Phys.* 70 (6), 3223 (1991).
- [14] T. Tiedje, K. M. Colbow, Y. Gao, J. R. Dahn, J. N. Reimers, and D. C. Houghton, *Appl. Phys. Lett.* 61, 1296 (1992).

- [15] J. Palm, F. Gan, and L. C. Kimerling, submitted to J. Appl. Phys.
- [16] F. Gan Master Thesis, MIT.
- [17] J. Dziewior, W. Schmid, Appl. Phys. Lett. 31, 346 (1977).
- [18] W. Schmid, Phys. Stat. Sol. B. 84, 529 (1977).
- [19] Optical filters and coatings, Corion product catalog, (1991).
- [20] G. W. Neudeck, The PN Junction Diode, Modular Series on Solid State Devices, 2nd Edition, Addison-Wesley Publishing Company.
- [21] M. Suezawa, and K. Sumino, Phys. Stat. Sol. A. 78, 639 (1983).
- [22] G. Davis, Physics Reports (Review Section of Physics Letters), 176, 83 (1989).
- [23] W. Spitzer, and H. Y. Fan, Phys. Rev. Vol. 108, 268 (1957).
- [24] W. N. Carr, Infrared Phys. 6, 1, (1966).
- [25] A. Polman, G. N. van den Hoven, J. S. Custer, J. H. Shin, and R. Serna, submitted to J. Appl. Phys.
- [26] 6.720 class note, MIT.
- [27] R. S. Muller, and T. I. Kamins, "Device Electronics for Integrated Circuits", 223, Hohn Wily Sons Publisher, (1986).
- [28] P. N. Favennec, H. L'Haridon, D. Moutonnet, M. Salvi, and M. Gauneau, Jpn. J. Appl. Phys. Vol. 29, 4, L524 (1990).

Chapter 7

Si:Er LED Integration

7.1 Introduction

Process incompatibility between Si CMOS and III-V compound semiconductor LEDs has been a major obstacle for the integration of Si electronics and compound optoelectronics [1]. Si:Er promises to be fully Si CMOS compatible. Integration of LEDs with Si VLSI electronics and Si/SiO_2 waveguides is the backbone of Si based optical interconnection.

To demonstrate the concept of integrating Si:Er LEDs with VLSI electronics, a mini-circuit including a MOSFET driver in series with an Si:Er LED was processed in a CMOS process flow. A MTL twin-well CMOS baseline process was modified to incorporate an Si:Er LED process modular [2]. Functional MOSFETs and Si:Er LEDs were successfully integrated in a CMOS process and light emission from a MOSFET modulated Si:Er LED was observed up to $T = 200K$.

In this chapter, process design and fabrication is first described in section 5.2 and 5.3. Followed by electrical and optical characterization of the MOSFET integrated Si:Er LEDs in section 5.4 and 5.5.

7.2 Process Design

Having found many applications in IC electronics and micromaching, SOI is now finding a new home in integrated optics as an ideal material candidate for Si:Er LED/waveguide integration. Mainly there are two types of SOI wafers widely used in IC industry: SIMOX (Separation by IMplanting OXygen) and BESOI (Bond and Etch-back Silicon On Insulator). SIMOX has a buried layer of oxide formed by high dose oxygen implantation and subsequent annealing. Due to the limitation of oxygen implantation energy, the top device silicon layer is limited to be around 2000\AA . Since Si:Er LEDs require the depth of the silicon layer to be at least $2\mu m$ for 4.5 MeV Er implants, SIMOX is not used for Si:Er LED fabrication. BESOI has a flexible top silicon layer so it is more suitable for LED integration, though silicon epitaxy growth of SIMOX wafers has the same flexibility.

Si:Er LED/waveguides integration is the driving force for processing Si:Er LEDs

on BESOI substrate. Light emission from an edge-emitting Si:Er LED at $1.54\mu\text{m}$ on the top silicon layer is transparent in silicon. Due to the refractive index difference between top silicon layer ($n=3.5$) and buried oxide layer ($n=1.5$), light can propagate along the top silicon layer by appropriate selection of top silicon layer and buried oxide layer thickness.

Si/SiO₂ waveguide has been integrated with an edge-emitting Si:Er LED as shown in Figure 7.1(a). Light emitted from the edge-emitting Si:Er LED couples into the waveguide and can be detected at the end of the waveguide. Direct photolithographic pattern and the following Si dry etch define the LED/waveguide alignment limited only by photolithographic misalignment. The top silicon layer of the BESOI wafers is about $5\mu\text{m}$ with a 5000\AA buried thermal oxide layer. Simulations show that this slab waveguide structure supports multimode at $1.54\mu\text{m}$. Also shown in Figure 7.1(b) is a MOSFET integrated Si:Er LED fabricated on a BESOI substrate. The detailed fabrication and characterization will be presented in the following sections.

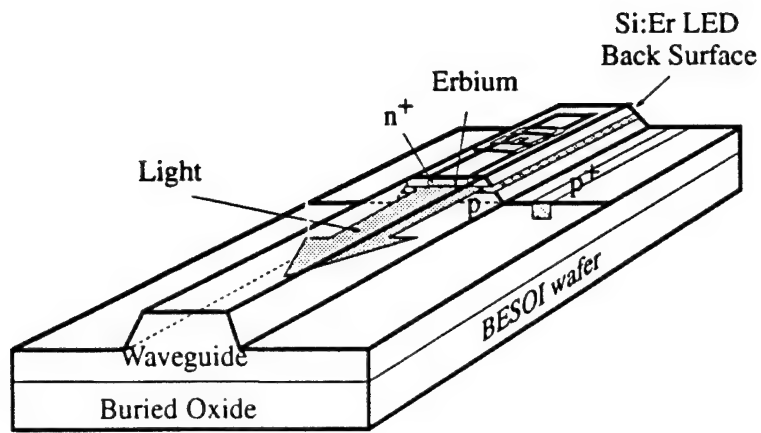
Process design emphasis was placed on the optimization of both MOSFETs and Si:Er LEDs. A standard $2\mu\text{m}$ design rule was used to ensure chip functionality. A p-well was chosen due to the requirement of p-type background for Si:Er LEDs. Two different p-wells were formed for the NMOS and the LED. The NMOS has a p-well concentration of $5\times 10^{16}\text{cm}^{-3}$ and a well depth of about $4\mu\text{m}$, while the LED p-well has a concentration of about $1\times 10^{16}\text{cm}^{-3}$ and a depth of $5\mu\text{m}$.

Arsenic was used to form the LED n^+ emitter. The choice of arsenic required a high temperature drive in to the move arsenic emitter close to the Er implant region (peak at about $1.5\mu\text{m}$ for 4.5 MeV Er implantation). This high temperature process can be incorporated into the CMOS p-well drive-in process. The p-well drive-in was splitted into two parts. Arsenic was implanted after the first half part of well drive-in, the 2nd half of well drive-in serves both as the drive-in of arsenic n^+ emitter and the p-well itself.

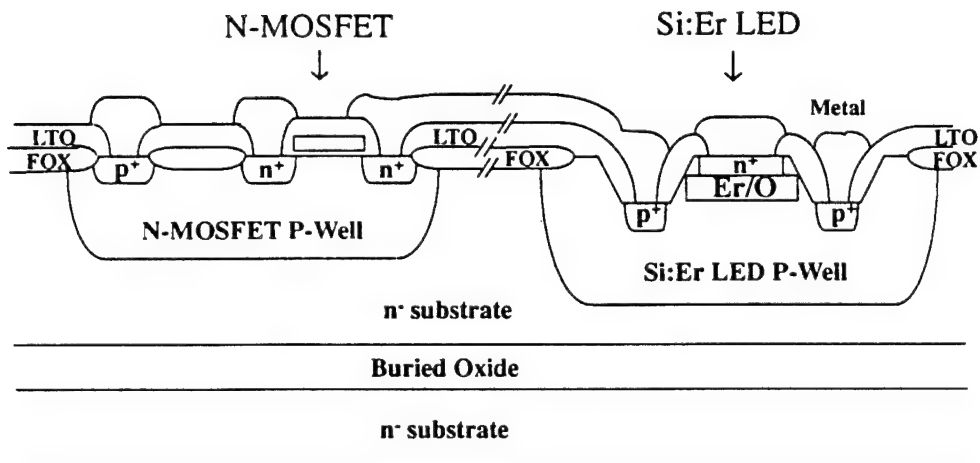
LED regions were always protected from MOS implants by photoresist. The LED arsenic regions were protected in field oxidation by nitride. Er was implanted at both 4.5 MeV and 400 keV after CMOS source/drain annealing due to its limited thermal budget. Therefore Er only saw its required thermal annealing. CMOS source/drain annealing is slightly reduced to accomodate the extra Er annealing so that at the end of the whole process MOSFETs get the same thermal budget. Therefore no MOSFET performance degradation is expected.

7.3 CMOS Fabrication

The starting wafers are n-type CZ and BESOI substrates. The resistivity of the substrates is typically between 10 and $20\Omega\text{cm}$. The top silicon layer of the BESOI wafers is about $5\mu\text{m}$. NMOS-p-well and LED-p-well are formed with two separate masks. First a stress relief oxide (SRO) of 430\AA is thermally grown followed by a 1500\AA LPCVD deposition of silicon nitride. The wafers are then patterned (mask 1), nitride dry-etched, and implanted with boron to form the NMOS-p-well. The unetched SRO serves as a screening oxide layer for the boron implantation. The



(a)



(b)

Figure 7.1: (a) Si:Er LED/waveguide integration on BESOI substrate. (b) Si:Er LED/MOSFET integration on BESOI substrate.

etched areas define p-wells while the photoresist (PR), nitride, and SRO block the boron implant. After stripping the PR the wafers undergo a second photolithographic step (mask 2) to define the LED p-well. By using two masks, both NMOS-p-well and LED-p-well concentration and profile can be optimized for each specific purpose.

After LED-p-well boron implantation and PR strip, a high temperature drive-in (1150C) in an oxidizing ambient drives the well half way to its required depth. A LED n^+ arsenic emitter formation is carried out for the 4.5 MeV Er implantation wafers. For the 400 keV Er wafers, the well drive-in is completed in one run rather than splitted into two runs. Wafers are patterned (mask 3) for LED n^+ arsenic emitter implant. Oxide under the open area is etched down to about 200Å. The remaining 200Å oxide serves as an arsenic implant screening layer. Arsenic is then implanted at an energy of 80keV and a dose of $5 \times 10^{15} \text{cm}^{-2}$ to form LED n^+ emitter as shown in Figure 7.2. After photoresist strip, second half p-well drive-in is carried out in nitrogen ambient. Nitrogen ambient was chosen to effectively anneal out arsenic implantation damage. The second p-well drive-in also drives arsenic emitter to the desired depth. At the conclusion of drive-in processes the well impurity concentration gradient within the well is rather small.

The nitride is wet stripped and a phosphorus field threshold-adjust photomask (mask 4) and implant is carried out. The photo mask is designed so that only the n-type region is implanted. The surface is then stripped of oxide, and a standard LOCOS (local oxidation of silicon) process forms the device active regions as shown in Figure 7.3. First a SRO/nitride sandwich is formed followed by an active area pattern (mask 5) and nitride dry etch. Before stripping the photoresist a second layer of photoresist is added and patterned (mask 6) followed by a boron p-field threshold-adjust implant. A wet field oxide is then grown, after which the SRO/nitride layer is removed from the active device regions.

Next a sacrificial gate oxide is grown to serve as a screen layer for the subsequent threshold implant. Both types of MOSFET receive a threshold-adjust and punchthrough implant. Prior to the implants, two masks (mask 7 and mask 8) are used to open the appropriate region for each implant as shown in Figure 7.4. Following the threshold implants the screen oxide is stripped in a 50:1 HF dip performed during a modified RCA clean. A 220Å gate oxide is then carefully grown followed by the immediate deposition of 5000Å polysilicon at 625C. The polysilicon is then degenerately doped n^+ with POCL_3 and patterned (mask 9). Before the polysilicon etch, the wafers are dipped in BOE (buffered oxide etch) to remove any oxide. After etching the polysilicon the wafers are patterned (mask 10) for the n^+ implant. This implant forms the NMOS source/drain and n-substrate contact as shown in Figure 7.5.

The wafers are then patterned (mask 11) for Si:Er LED mesa etch as shown in Figure 7.6. The mask is a dark field pattern which enables the MOSFETs regions to be covered by photoresist. The mesa etch is a low power semi- isotropic SF_6/CCL_4 silicon etch and must be preceded by a short BOE dip to remove oxide. A depth of about $3\mu\text{m}$ is formed by timing etch. A slope of 75 degree is obtained to ease the following metal step coverage. Mask 12 is then used to pattern the LED p^+ implant. This implant also forms the PMOS source/drain and p-well contact plugs. All the

implants are annealed with a 900C reoxidation followed by a 950C junction drive-in.

A 4 μ m thick photoresist is patterned (mask 13) to define the Er/O implantation region. The implantation is carried out at ATbrought back to MTL for a 900C/30mins anneal to activate Er optically. Some of the wafers which have no LED n^+ arsenic emitter formed are implanted with arsenic at a dose of $1 \times 10^{15} \text{cm}^{-2}$ and an energy of 10 keV at Implant Science. Er and O are then implanted at an energy of 400 keV. The thermal annealing for 400 keV Er/O and arsenic is carried out at 800C for 30 minutes in N_2 ambient.

CVD LTO is deposited to serve as a dielectric layer between metal and polysilicon. The backside is then stripped of LTO, polysilicon, and field oxide. Later the contacts are patterned (mask 14) and etched. Once the contact resist pattern is removed the wafers undergo a piranha clean to eliminate any residual organic. The wafers are dipped into 50:1 HF for 30 seconds to clean up any residual native oxide in the contact openings and then deposited with 1 μ m 1% AlSi metal layer. Next, the wafers are patterned (mask 15) and etched using a $BCl_3/CHCl_3$ chemistry. A final 400C anneal in a forming gas ambient (N_2/H_2) finishes the CMOS/LED process.

7.4 Electrical Characterization

A cross section view of a MOSFET/LED structure is shown in Figure 7.7. A Si:Er LED is in series with a NMOS and an isolated PMOS is also fabricated to demonstrate the full compatibility of LED with CMOS. The process flow was simulated with TMA SUPREM-3 to ensure the correct doping profiles. The device characteristics for the NMOS and PMOS transistors are similar to those of the MOS transistors of the MTL CMOS baseline process [2]. Plots of I_{ds} vs. V_{ds} curves are shown in Figure 7.8. A typical threshold voltage 0.55V and -0.79V were measured for NMOS and PMOS transistors. The subthreshold slopes of NMOS and PMOS transistors are 81 mV/decade and 85 mV/decade (Figure 7.9). A typical transconductance of 9×10^{-4} siemens and 4×10^{-4} siemens at 3 volts gate bias were measured for the NMOS and PMOS transistors as shown in Figure 7.10.

I-V characteristics of a typical 4.5 MeV Si:Er LED is shown in Figure 7.11. An ideality factor of 1.27 was measured. The observed I-V characteristics of the MOSFET integrated Si:Er LEDs was similar to that of the discrete Si:Er LEDs.

7.5 Optical Characterization

Light emission from 4.5 MeV Si:Er LEDs on both CZ and BESOI wafers after CMOS process flow was observed up to $T = 200\text{K}$. The decrease of light emission intensity is due to the carrier lifetime degradation after CMOS processing. The MOSFET was turned on by a constant 2V gate bias and the power supply voltage (LED anode) was varied to vary the LED current density. Similar Er EL spectra of MOSFET integrated Si:Er LEDs at 100K from both CZ wafer and BESOI wafer were observed. Figure 7.12 shows a typical Er EL spectra at low and high drive current densities

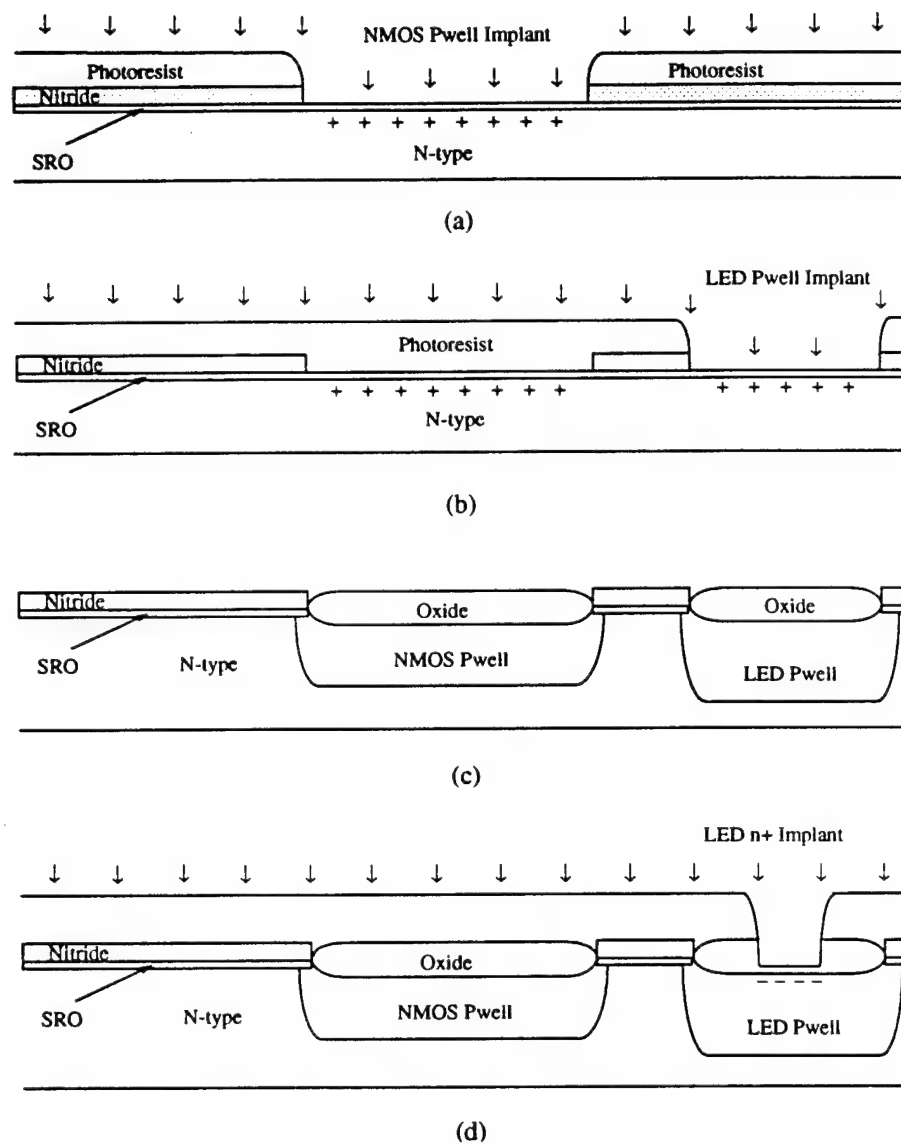
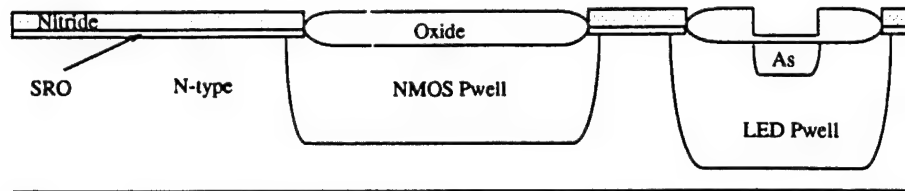
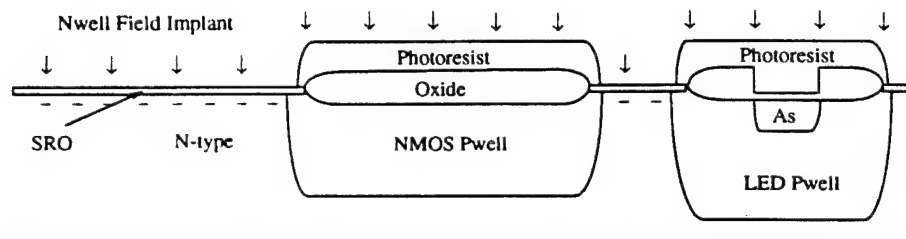


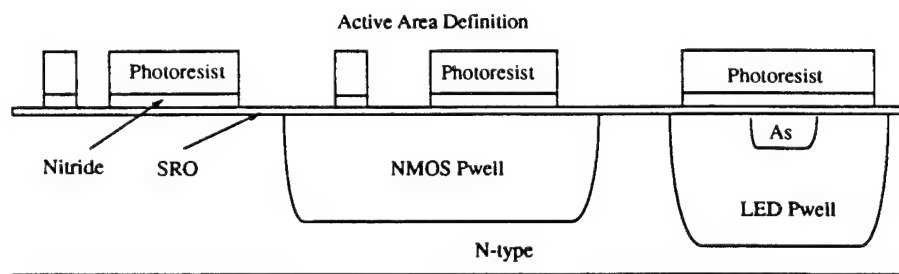
Figure 7.2: (a) NMOS p-well pattern and implant. (b) LED p-well pattern and implant. (c) p-well first half drive-in. (d) LED n^+ arsenic pattern and implant.



(a)

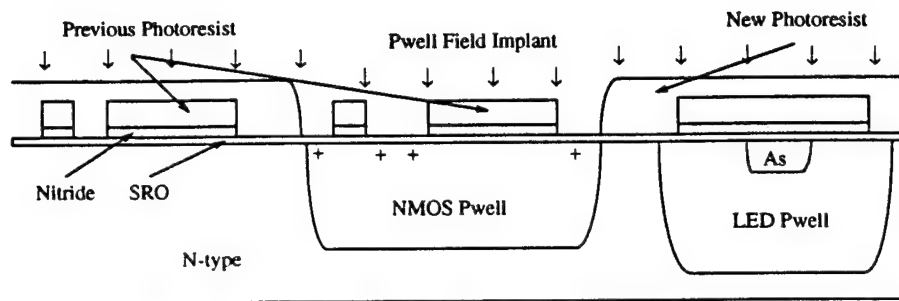


(b)

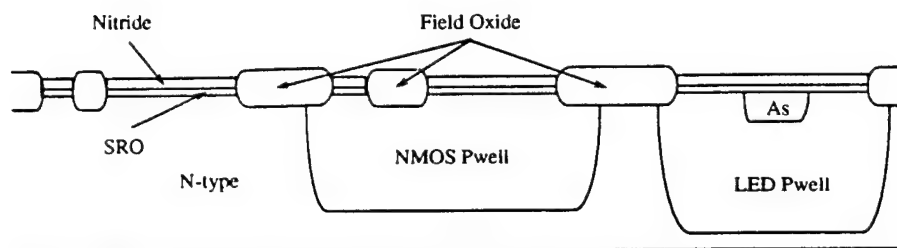


(c)

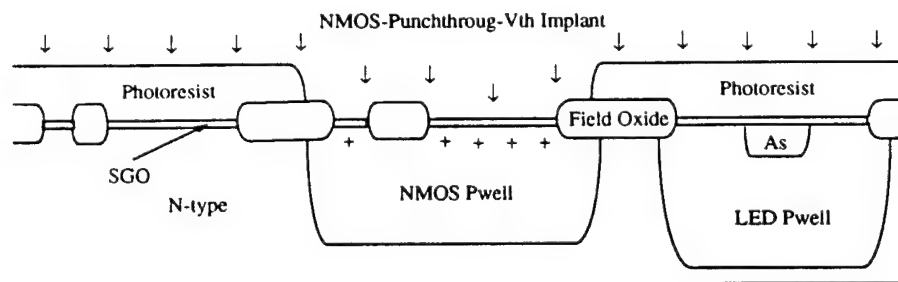
Figure 7.3: (a) LED arsenic/p-well drive-in. (b) n-well field threshold pattern and implant. (c) Active area pattern and nitride etch.



(a)



(b)



(c)

Figure 7.4: (a) p-well field pattern and implant. (b) LOCOS isolation. (c) NMOS threshold and punchthrough pattern and implant.

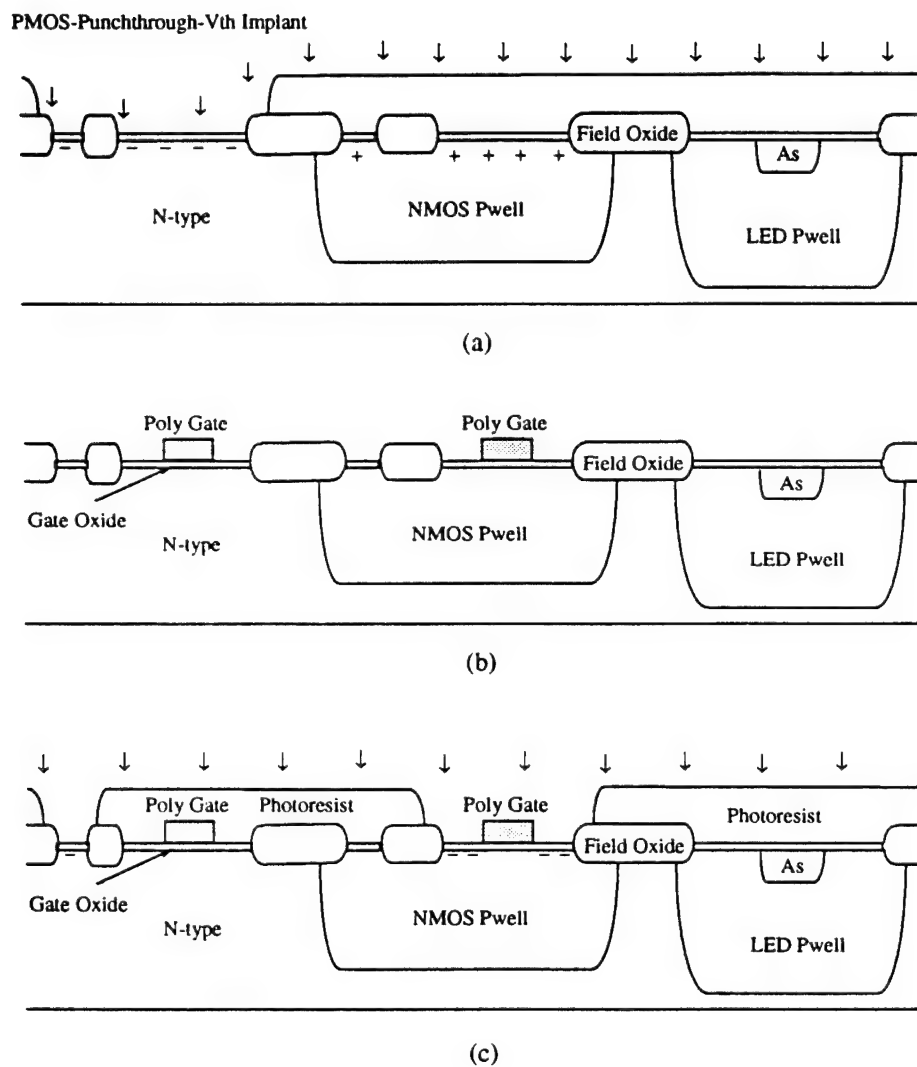
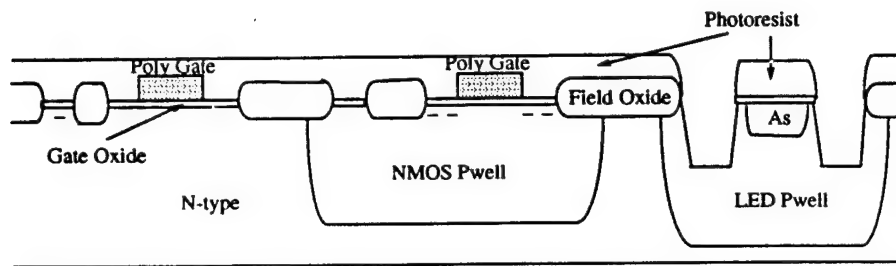
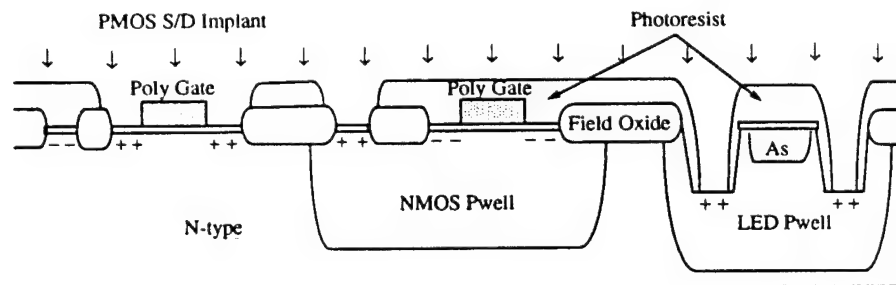


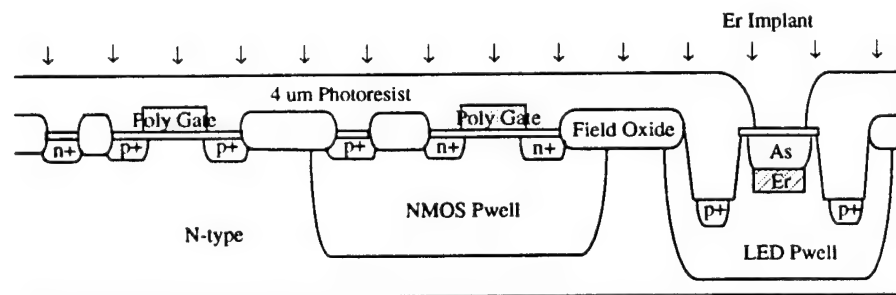
Figure 7.5: (a) PMOS threshold and punchthrough pattern and implant. (b) Gate oxidation and polysilicon gate pattern and etch. (c) NMOS source/drain and nwell contact pattern and implant.



(a)



(b)



(c)

Figure 7.6: (a) LED mesa pattern and etch. (b) PMOS source/drain and p-well contact pattern and implant. (c) Er/O pattern and implant.

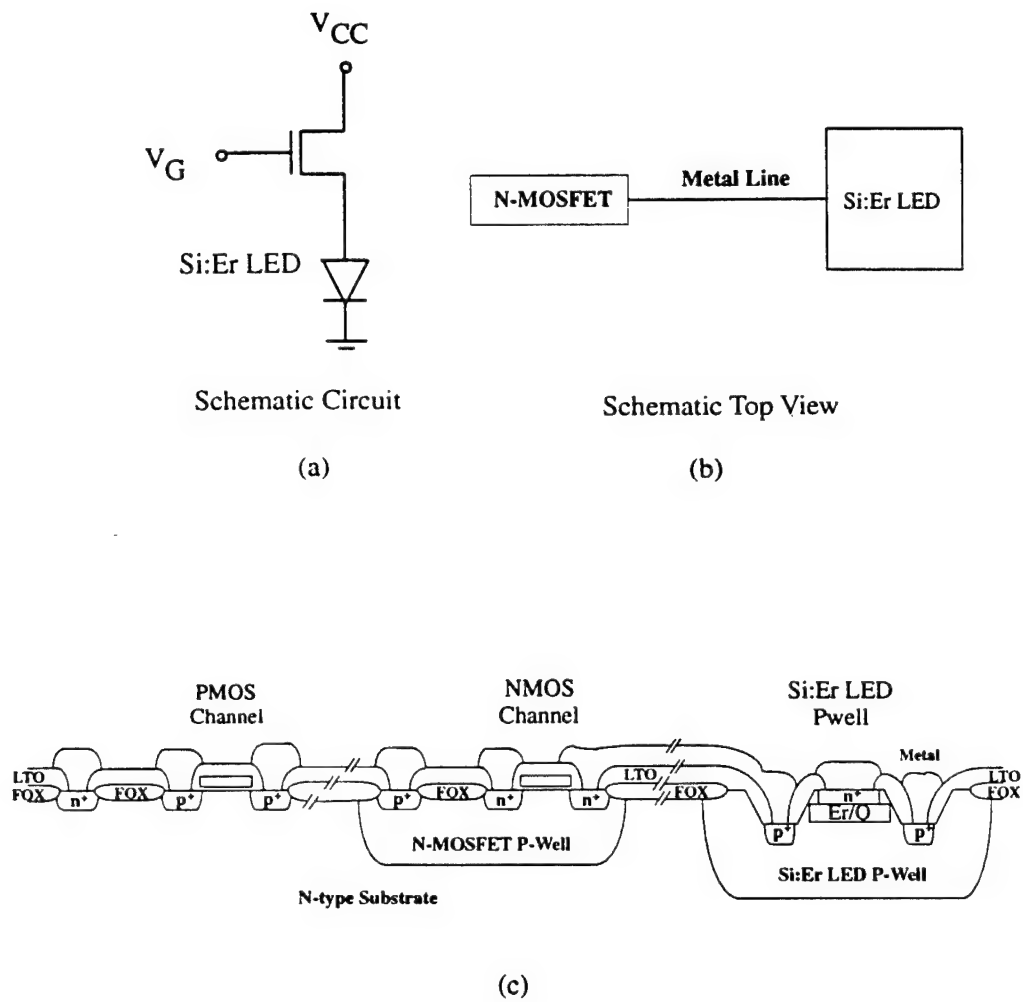


Figure 7.7: (a) Schematic circuit configuration showing MOSFET in series with Si:Er LED. (b) Schematic top view of the circuit. (c) CMOS/Si:Er LED cross section view.

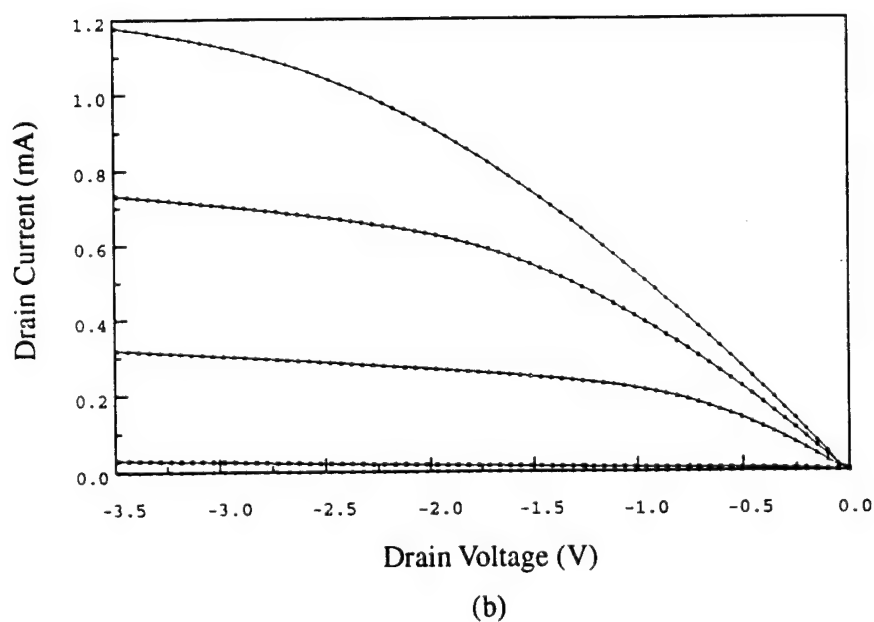
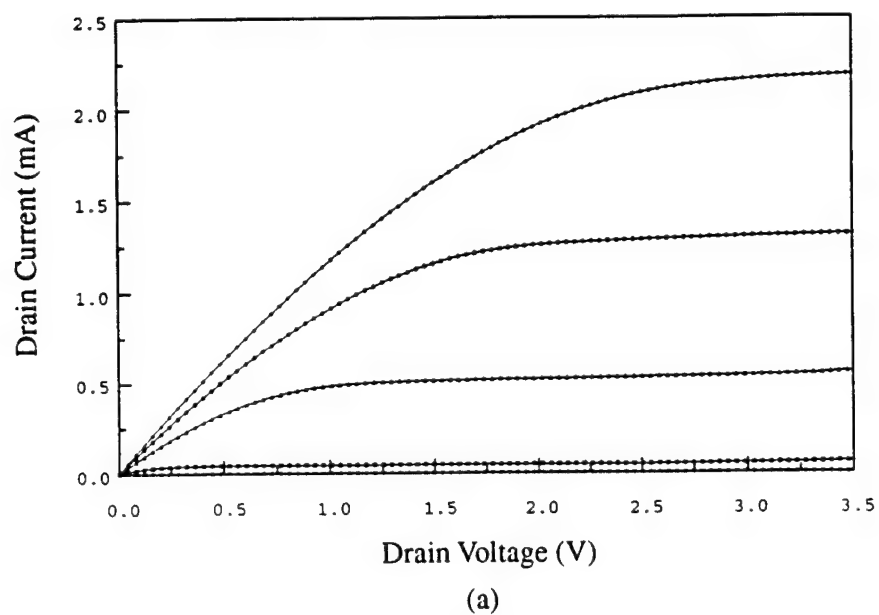
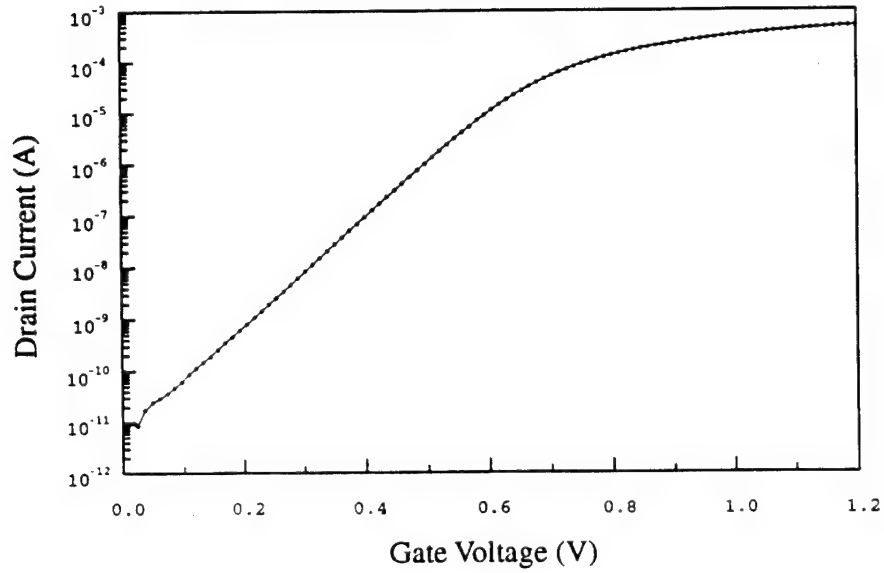
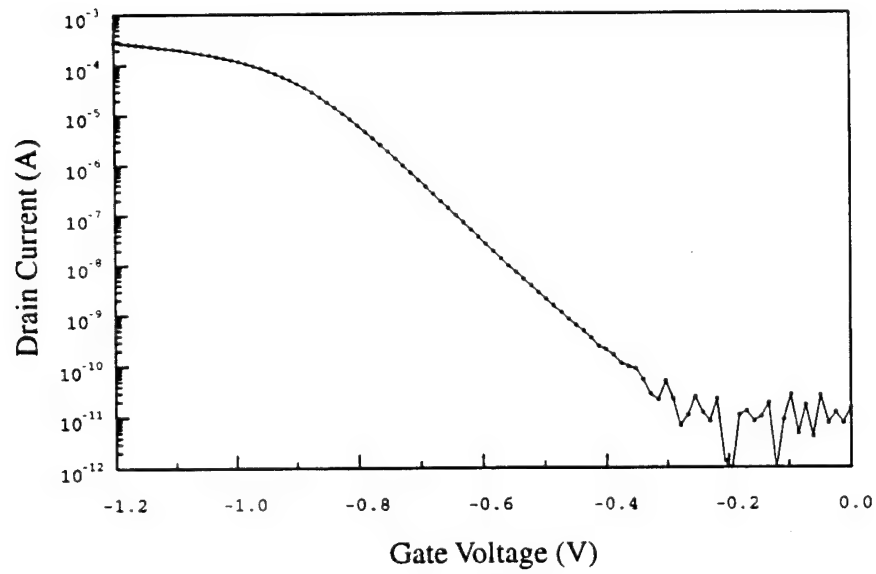


Figure 7.8: (a) Drain current vs. drain voltage for n-channel $W/L = 20/2$, $V_b = 0V$, $V_G = 1V$ to $5V$. (b) Drain current vs. drain voltage for p-channel $W/L = 30/3$, $V_b = 0V$, $V_G = -1V$ to $-5V$.



(a)



(b)

Figure 7.9: (a) Subthreshold slope = 81 mV/decade for n-channel, $W/L = 20/2$, $V_{ds} = 50$ mV. (b) Subthreshold slope = 85 mV/decade for p-channel, $W/L = 30/3$, $V_{ds} = -50$ mV.

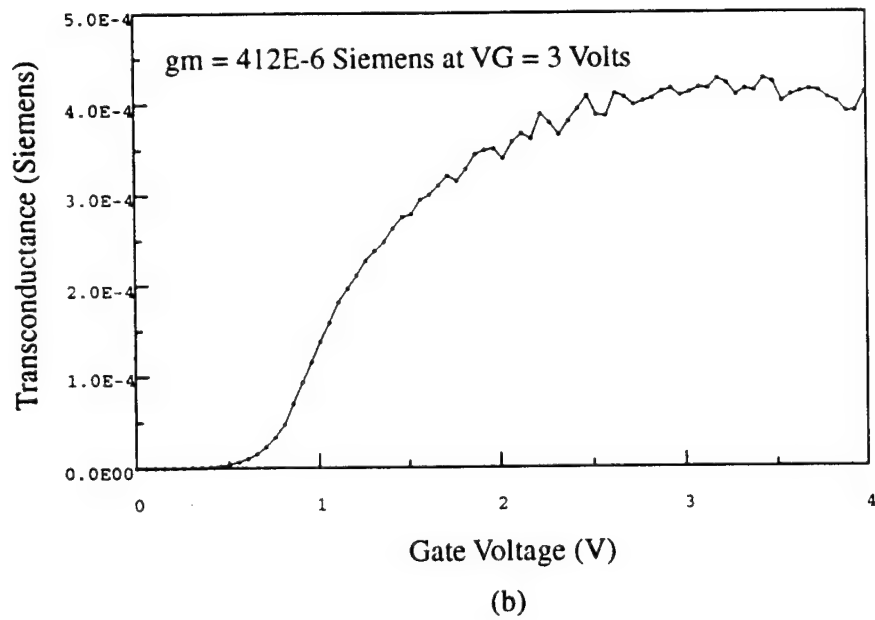
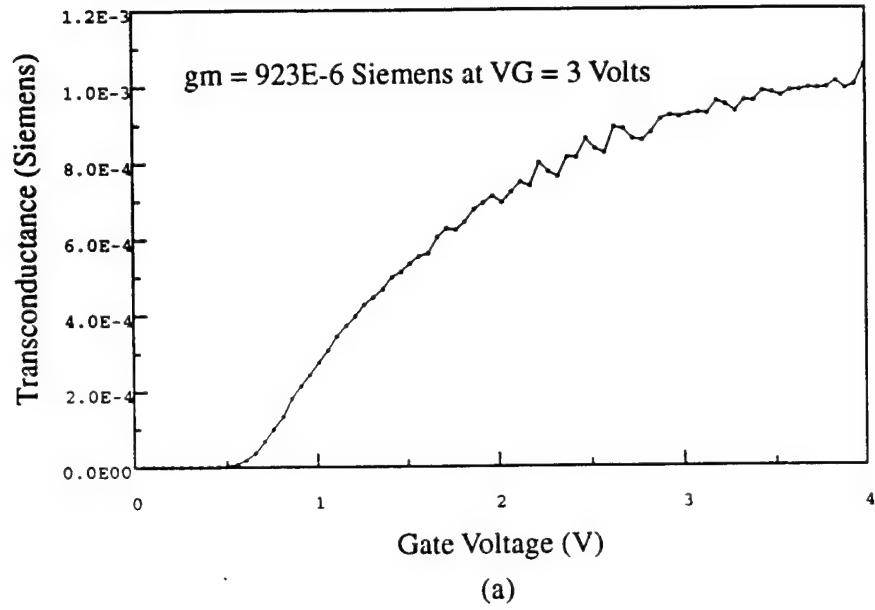


Figure 7.10: (a) Transconductance vs. gate voltage for n-channel, $W/L = 20/2$, $V_d = 3\text{V}$. (b) Transconductance vs. gate voltage for p-channel, $W/L = 30/3$, $V_d = -3\text{V}$.

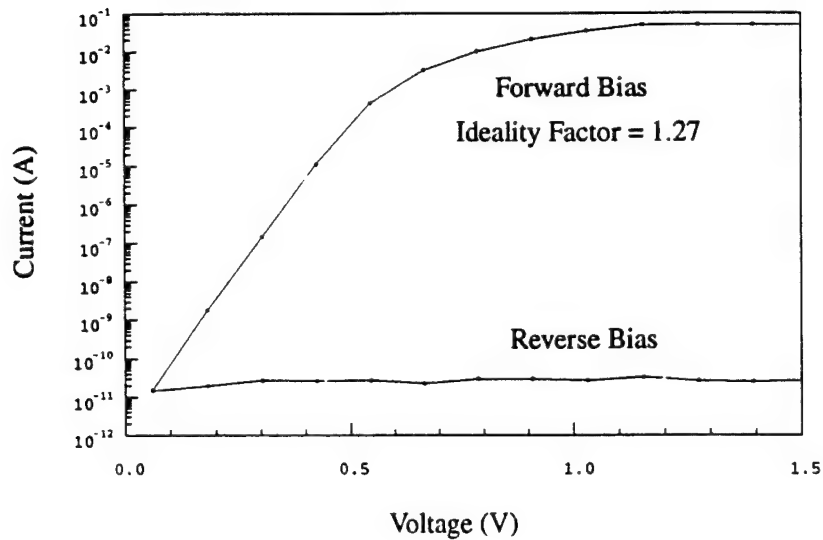


Figure 7.11: A typical I-V curve of a MOSFET integrated Si:Er LED

at $T = 100\text{K}$. The characteristic D-lines associated with discrete 4.5 MeV LEDs was also observed. The light vs. drive current density from the MOSFET integrated Si:Er LED on BESOI is shown in Figure 7.13(a). The characteristics are similar to those of discrete Si:Er LEDs.

Light modulation by the MOSFET is demonstrated at $T = 100\text{K}$. The power supply voltage (LED anode) is kept constant and the MOS gate voltage is varied. Below a certain voltage, the MOSFET is in cut off mode, no current flows and therefore no light emission from the LED is observed. After the MOSFET turn-on, a dramatic increase of light emission from LED is observed. Light emission from Si:Er LED vs. MOS gate voltage is shown in Figure 7.13(b). Light saturation was observed for further increase of the MOSFET gate voltage. Light emission can be modulated on and off by varying gate voltage around this threshold voltage.

The modulation speed is limited by the lifetime of the first excited state. The spontaneous radiative lifetime of Er is estimated to be 1ms [3]. Due to other non-radiative recombination channels, the measured effective lifetime is around $100\mu\text{s}$. This effective lifetime limits the maximum modulation speed of the LED to be below 100kHz. A direct measurement of the frequency response of the Si:Er LED was carried out to confirm the above estimate. A high speed liquid nitrogen cooled GaInP detector instead of slower Ge detector, a current amplifier, and a digital oscilloscope were used in the measurement. The measured data is shown in Figure 7.14. The measurement system response time is mainly limited by the current amplifier to be about $20\mu\text{s}$. As a result, only the initial response decay at frequencies slower than about 50 kHz ($50\text{ kHz} = 1/20\mu\text{s}$) is due to Er light emission decay. The response decay at frequency higher than 50 kHz is limited by the measurement system. The order of magnitude (kHz) result of this frequency measurement is consistent with the estimate from lifetime measurement.

The slow modulation speed of Si:Er LEDs requires an external modulator for

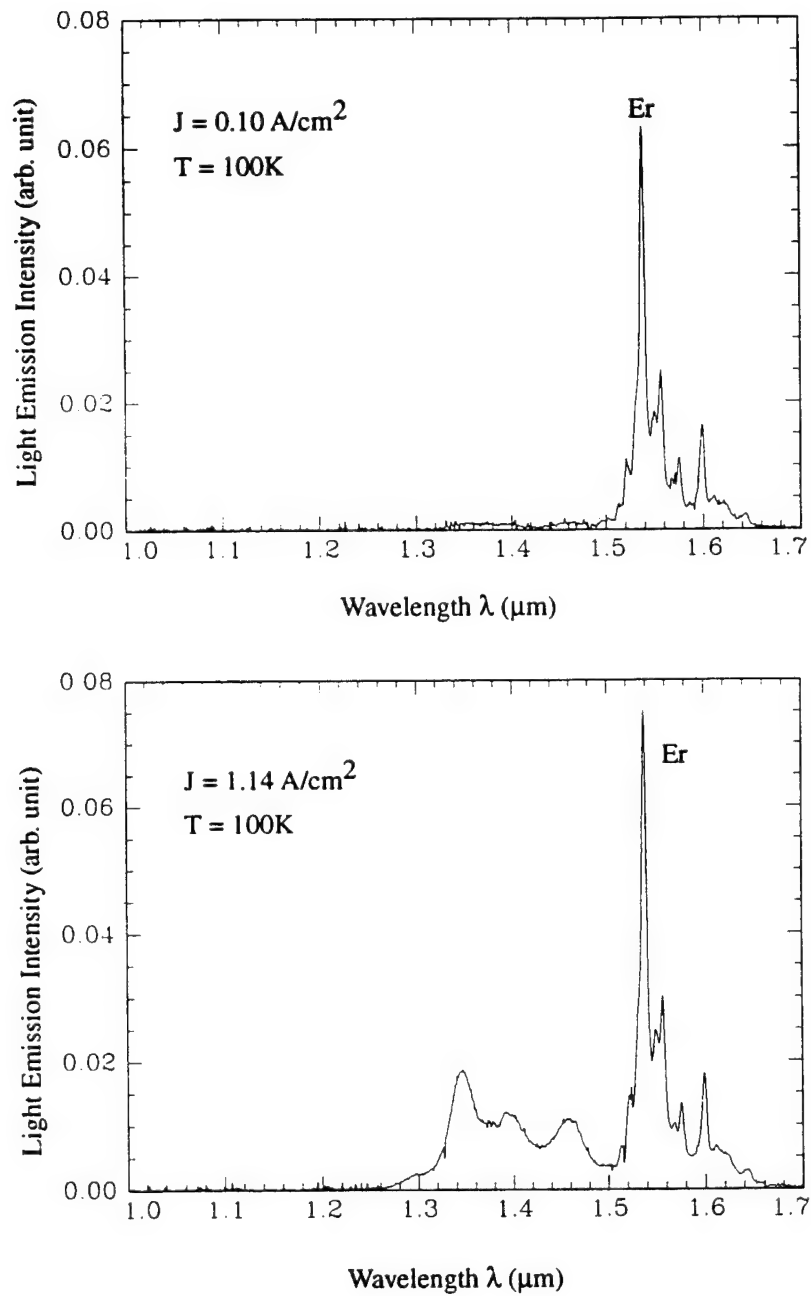
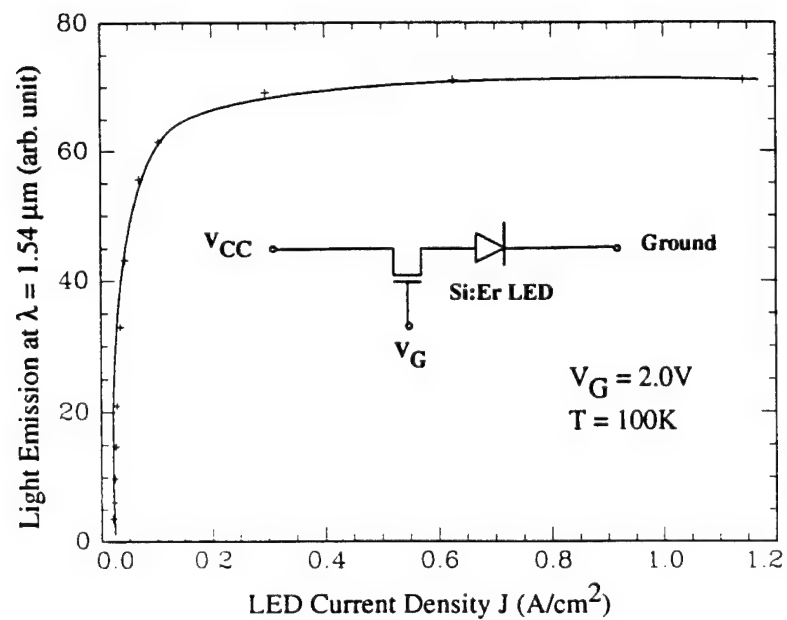
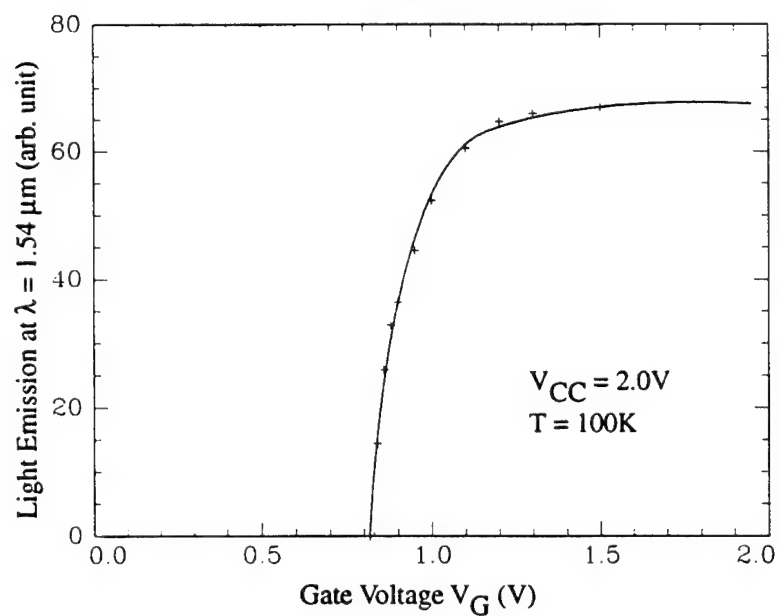


Figure 7.12: Light emission from a MOSFET integrated Si:Er LED on BESOI substrate at high and low drive current densities.



(a)



(b)

Figure 7.13: (a) Er light emission intensity vs. drive current density. (b) Er light modulation by MOSFET gate voltage.

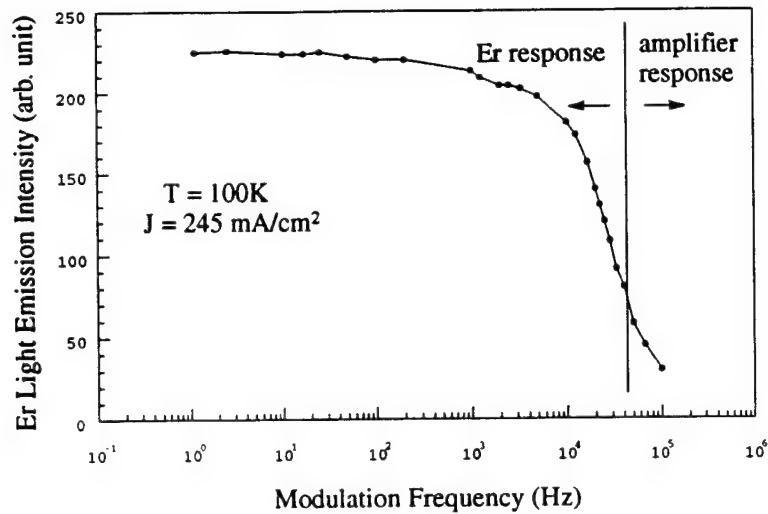


Figure 7.14: Er light emission modulation frequency curve. The intensity decrease at frequencies below about 50 kHz is due to Er, the drop beyond 50 kHz is due to the measurement system response time.

high speed application. The perceived integrated system plans to use an external modulator to modulate the DC light emission from on-chip Si:Er LEDs. A free carrier absorption type Si optical modulator is a potential candidate for the system integration [4].

7.6 Summary

A CMOS/LED process which integrates an Si:Er LED modular process into a $2\mu\text{m}$ CMOS process has been described. The device characteristics of the MOS transistors are similar to those from the MTL CMOS baseline process. A functional MOSFET integrated Si:Er LED is demonstrated up to $T = 200\text{K}$ on both CZ and BESOI wafers.

The concept of LED integration with Si VLSI electronics was demonstrated by integrating Si:Er LEDs with MOSFETs in a CMOS process flow. No fundamental processing limitations are observed for further implementation of complex CMOS circuits.

Bibliography

- [1] H. K. Choi, G. W. Turner, T. H. Windhorn, and B. Y. Tsaur, IEEE Electron Device Lett. Vol. 7, 500 (1986).
- [2] P. K. Tedraw, and C. G. Sodini, Twin Well CMOS Process, MTL Technical Report 1.2, 1989.
- [3] Y. H. Xie, E. A. Fitzgerald, and Y. J. Mii, J. Appl. Phys. 70 (6), 3223 (1991).
- [4] B. N. Kurdi, and D. G. Hall, Opt. Lett. 13, 175, (1988).

Chapter 8

UHV-CVD Reactor

8.1 Introduction

In order to fabricate erbium-doped silicon based optoelectronic devices, several thermodynamic and kinetic issues have to be resolved. The most important of these are the concentration of optically active erbium which can be achieved in silicon and an improved quantum efficiency. Xie [1] has estimated that erbium concentrations in excess of three orders of magnitude above its solubility limit ($\sim 5 \times 10^{16}/\text{cm}^3$ at 1250°C) are needed for sufficient device output power. For the erbium to be optically active, it has to have co-dopants such as oxygen or fluorine surrounding it. The difficulty is introducing these co-dopants so that they are only localized around the erbium and not forming defects in other parts of the device.

We have designed and built an ultra-high vacuum chemical vapor deposition (UHV-CVD) reactor which addresses both of these issues. UHV-CVD is a process which relies on a hydrofluoric acid pre-growth clean and very low partial pressures of oxygen and water ($\leq 10^{-10}$ torr) to grow at low temperatures [2]. Meyerson [3] has reported growing single crystal silicon as low as 550°C using this process. We believe that at these temperatures, erbium will not precipitate due to kinetic constraints. The source of erbium in this reactor is a metallorganic compound which also has the other ligands (such as oxygen or fluorine) in it. These ligands can reduce the already low diffusivity of erbium by complexing with it and further aid in obtaining metastable concentrations. By varying the local environment of the erbium through processing and a careful choice of the precursor, the quantum efficiency can also be improved. This could be attributed to a shift of the erbium-ligand state in the band gap which alters its ability to capture and emit carriers. Quantum efficiency will also be improved by growing Er-doped $\text{Si}_{1-x}\text{Ge}_x$ in $\text{Si}/\text{Si}_{1-x}\text{Ge}_x$ heterostructures. Since the index of refraction is higher in $\text{Si}_{1-x}\text{Ge}_x$ than Si, the light produced in the alloy will be guided in the quasi one dimensional mesa structure for better collection. The large valence band offset in strained $\text{Si}_{1-x}\text{Ge}_x/\text{Si}$ system will strongly confine the holes around the erbium. Coulomb attraction, along with a slightly favorable conduction band offset, should also localize the electrons in the same area, allowing for stronger pumping of the erbium.

8.2 Description of System

This reactor consists of three basic parts; a gas manifold system, load lock and growth chamber. The gas manifold is further divided into the gas cabinets and a regulation/control system. The process gases used are SiH_4 , GeH_4 (3% in argon), B_2H_6 (5000 ppm in SiH_4), and either AsH_3 or PH_3 (in SiH_4 or H_2 respectively). These gases are outside the class 100 clean room where the reactor is located and are piped to the control cabinet which sits beside the reactor. The control cabinet, custom made by Applied Energy Systems, contains further regulation, mass flow controllers (MFC's), purifiers, manual, check and pneumatic valves. The Nanochem filters are designed to reduce the water and oxygen content to below 1 ppb and are on all gas lines except the diborane (no filter is available for that gas). The all metal MFC's are made by MKS Instruments (series 1459C) and only allow for a maximum flow for process gases of 10 standard cubic centimeters per minute (sccm). The SiH_4 and GeH_4 lines have by-pass valves around the MFC's for faster purging. Hydrogen dilution of the dopant lines was incorporated to have finer control over the doping concentration. This is accomplished by inserting hydrogen between two MFC's on both doping lines. By balancing the settings of the downstream MFC and an excess venting MFC, the dilution can be controlled.

Lag time in gas switching has been minimized to obtain abrupt interfaces by design. On the downstream side of the MFC's, the gas lines are split into two lines, named 'reactor' and 'by-pass', which empty into two trunk lines. All of the 'reactor' lines go to the trunk line that is connected to the upstream side of the growth chamber, while the 'by-pass' lines go to the line attached just above the process turbomolecular (turbo) pump. For each process gas line, the pneumatic valves on the split lines are wired together such that when one valve is closed, the other simultaneously opens. Since both of the split lines have the same pressure on the downstream side, no large transient spikes occur when switching in a gas from by-pass to the reactor. In addition, a second SiH_4 line was added to ensure rapid switching between two different compositions of $\text{Si}_{1-x}\text{Ge}_x$. This is accomplished by setting up a second silane flow in the by-pass line for a desired composition while another composition is being grown. To initiate the new growth, the first silane line is switched out of the reactor while the second is simultaneously switched in. This avoids resetting the silane flow during growth with the resulting gradation of the $\text{Si}_{1-x}\text{Ge}_x$ alloy. Finally, the proximity of the valves and MFC's helps to shorten the switching times.

The erbium source used in the reactor is an organometallic compound which is bubbled through a hydrogen line. The bubbler is capable of heating the source to 300°C with control of $\pm 1^\circ$. High temperature valves are downstream from the bubbler so that the gas line can be heated to prevent condensation of the erbium. The hydrogen MFC for the bubbler is able to flow 500 sccm for higher erbium incorporation. Temperature fluctuations in the bubbler have the ability to create large changes in the precursor's vapor pressure. To prevent this from affecting the concentration in the film, a needle valve was placed in-line downstream of the bubbler. The pressure drop across this valve dampens the oscillations.

The load lock is pumped by a Balzers TPU 330 liters/sec turbo pump, backed

by an Alcatel mechanical pump. Conflat fittings are used everywhere except for the load lock door, which has a viton o-ring. The base pressure is 2×10^{-7} torr and is achieved after 10 hours of pumping. An activated alumina trap is located between the two pumps to prevent oil backstreaming. A pirani and cold cathode pressure gauge are dedicated for the load lock. Transfer of the sample into the growth chamber is accomplished with the use of a magnetic transfer arm.

Growth occurs in a hot-walled reactor. A three zone furnace, made by Mellon, heats a 130 mm inner diameter quartz tube. This size of tube is necessary for processing 4 inch wafers, but quartz to metal seals are not practical for these dimensions. As a result, a coupling assembly using viton o-rings was used. Each end of the tube has a vacuum in a small area outside an 'interior' o-ring created by a small Alcatel mechanical pump. This should significantly reduce the leak rate into the system through these o-rings. All other fittings are UHV compatible conflat. The chamber has a ion gauge and capacitance manometer to measure pressure from 1 torr to vacuum. A thermistor gauge, which can measure from about atmosphere to 1 mtorr can be exposed to the chamber depending on the valving. Partial pressures of gases can be determined from a Leybold-Inficon residual gas analyzer (RGA). The RGA can detect fragments up to 200 amu/charge and partial pressures as low as 10^{-13} torr. The pumps on the chamber include Leybold's S60A mechanical pump, WA500 roots pump, and a Balzer's 510 liters/sec turbo pump. They are valved so that the mechanical and roots pump can either back the turbo pump or directly pump on the chamber. A stainless steel trap sits between the two pumps to prevent the mechanical pump from backstreaming. All pumps have fomblin oil to prevent a reaction with the process gases. The base pressure of the growth chamber at room temperature is 8×10^{-9} torr, rising to 2×10^{-8} torr at 850°C . The partial pressure of water and oxygen are usually in the low 10^{-10} torr range.

8.3 Safety Features

Since such toxic and pyrophoric gases are used in this system, safety is a critical concern. Because most of the process gases can ignite if large flow rates occur, limiting orifices are on all cylinders. High pressure pneumatic valves are at the outlets of all the cylinders which will close upon the detection of a leak. The MDA unit, which monitors for leaks, has sensing points in the gas cabinet, gas manifold, at both ends of the quartz tube and outside the exhaust system. An extensive interlock system has been built into the control cabinet as well. Besides leak detection, exhaust failure and overpressure will automatically shut off all gases. Additionally, the gate valve above the turbo closes with overpressure to protect it from a possible catastrophic tube failure. Two emergency shut-off switches control the gas manifold and the reactor equipment. The RGA is also continuously used for monitoring the system itself for leaks. Any sign of increasing partial pressures of nitrogen and oxygen result in a full system leak check.

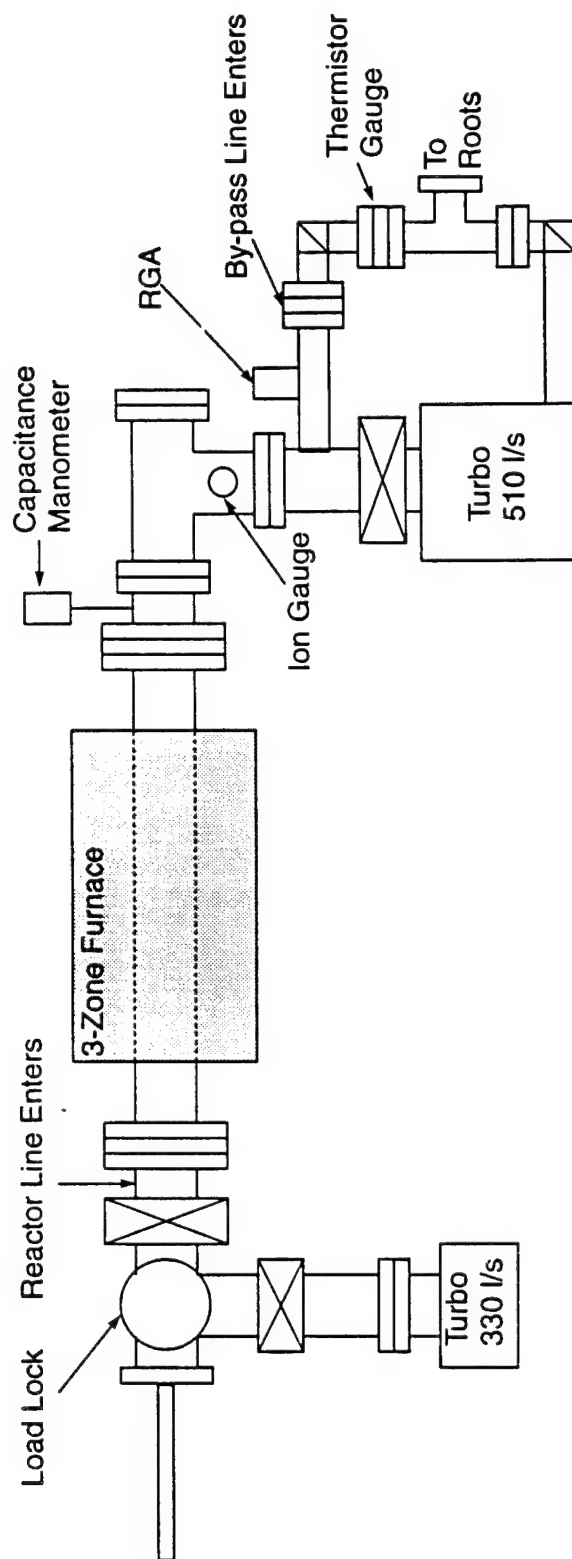


Figure 8.1: UHV-CVD reactor

8.4 Growth of Si and $\text{Si}_{1-x}\text{Ge}_x$ Films

We have used SIMS, spreading resistance (SR), scanning electron microscopy (SEM), transmission electron microscopy (TEM), photoluminescence (PL), electron beam induced current (EBIC) and Rutherford backscattering spectroscopy (RBS) to characterize the films.

8.4.1 Silicon Films

We have grown both undoped and doped silicon films. The PL spectra (Figure 8.2) show a low background with peaks only for excitons in the substrate and film and a feature due to poor surface cleaning. This last peak, which appears at $1.615\ \mu\text{m}$, is only seen in films where the thickness is less than about $1\ \mu\text{m}$ due to absorption in the film. An improved heat treatment has significantly reduced the intensity of this peak, and a different cleaning procedure should eliminate it completely. RBS was done on some of the first films to check for crystal quality. The silicon films had χ_{min} 's $\cong 3\%$, indicating high quality material. SR measurements have been made to determine electrically active doping concentrations. They indicate that the heaviest p-type doping we can achieve at high temperatures (850°C) is $1 \times 10^{20}/\text{cm}^3$. For this sample, SIMS showed a concentration of $8 \times 10^{20}/\text{cm}^3$, so only a fraction of the dopant is electrically active. Precipitation of boron did not appear to be the cause of this since the film looked relatively free of defects in XTEM. Growth rates for p^+ films are about $15\ \text{\AA}/\text{min}$, which is far below the $120\ \text{\AA}/\text{min}$ rate reported by Meyerson [4] for $1 \times 10^{20}/\text{cm}^3$ boron at 775°C . Work is in progress to understand this inhibition. In order to have more independence in p-type doping, a new mixture of 1% diborane in H_2 will be used in the future. Doping with arsine has also severely reduced growth rates, but this effect has previously been reported. Both SIMS and EBIC confirm that growth rates for the highest n-type doping flows at 850°C are about $10\text{--}15\ \text{\AA}/\text{min}$. The incorporation of As in these samples was approximately $10^{18}/\text{cm}^3$. Since phosphorus has been shown to not suppress the growth rate as much as arsenic [5], we have started to use 1% phosphine in H_2 .

8.4.2 $\text{Si}_{1-x}\text{Ge}_x$ Films

Several compositions and structures have been grown with $\text{Si}_{1-x}\text{Ge}_x$. The majority of films grown have had compositions between 5 and 40% Ge. The evolution of surface morphology of these films agrees with previous studies. At lower Ge content, planar surfaces are grown. As the germanium concentration reaches 15-20%, ripples are seen in SEM on the surface. These undulations form to reduce the strain in the film due to the lattice mismatch between Si and Ge. XTEM of the films shows that faceting is occurring on these ripples but we have not done a systematic study to determine the orientation. Faceting on (105) faces has been reported by others. Calibration growth runs have been done at 875 , 850 and 600°C for composition and growth rates. We are planning to calibrate at 550°C since low growth temperatures are needed to suppress surface undulation formation. RBS done on the first alloyed films grown

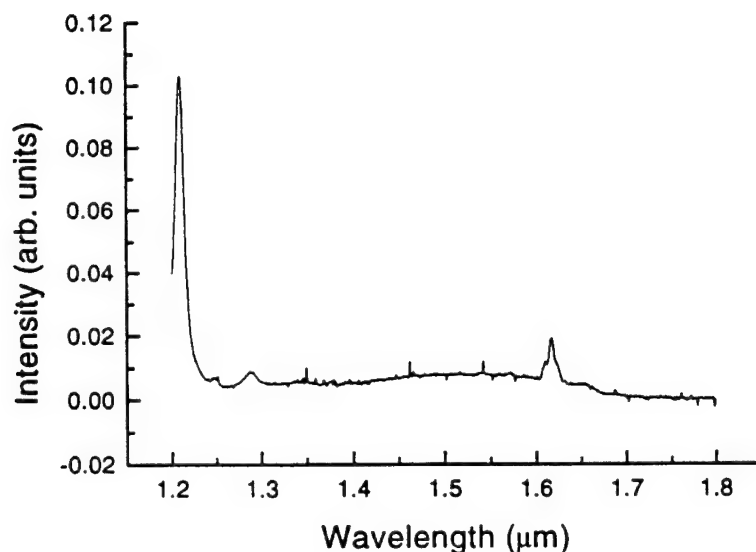


Figure 8.2: PL (at 4K) of Si grown at 575C for 30 min.

at temperatures between 575 and 650°C gave χ_{\min} 's of 20-40. Further RBS will be done on recent growths to examine the effect of better surface cleaning on the crystal quality. PL done on that material shows no features relating to defects (Figure 8.3), so channeling improvement is expected. $\text{Si}_{1-x}\text{Ge}_x$ films doped p-type have been grown at 700 and 850°C and for different compositions at the higher temperature. Boron incorporation increased with increasing Ge content and temperature in this process window. It might be possible to achieve higher doping at lower temperatures, however, due to kinetic constraints on precipitation.

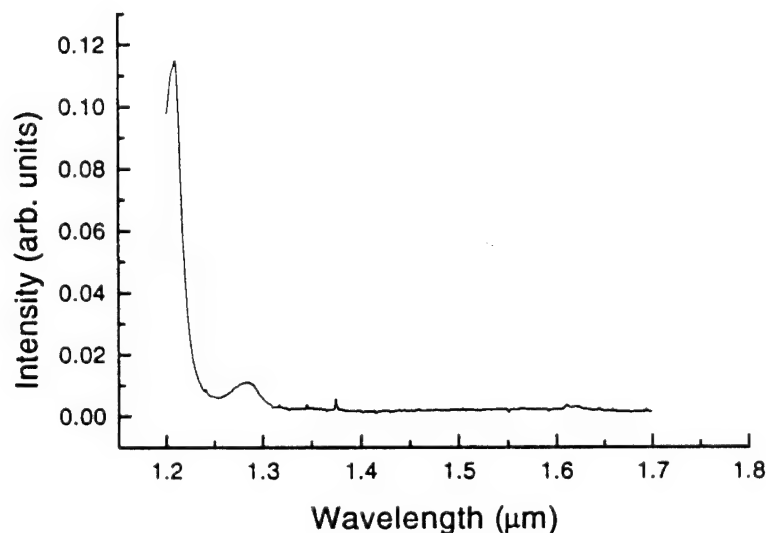


Figure 8.3: PL (at 4K) of $\text{Si}_{0.95}\text{Ge}_{0.05}$ grown at 850C for 60 min.

Finally, multiple quantum well structures of $\text{Si}/\text{Si}_{1-x}\text{Ge}_x$ have been grown to test

the switching capability of the system (Figure 8.4). $\text{Si}_{1-x}\text{Ge}_x$ thicknesses of 35 Å have been achieved. XTEM of the quantum well samples grown at 800°C show abrupt interfaces with some undulations at the top $\text{Si}_{1-x}\text{Ge}_x$ surface. Lower growth temperatures will be used in the future to kinetically restrain this phenomenon.



Figure 8.4: XTEM of SiGe quantum wells (35 Å) grown at 750 C

Bibliography

- [1] Y.H. Xie, E.A. Fitzgerald, Y.J. Mii, JAP 70, 3223 (1991).
- [2] B.S. Meyerson, E. Ganin, D.A. Smith, T.N. Nguyen, J. Electrochem. Soc. 133, 1232 (1986).
- [3] B.S.Meyerson, K. J. Uram, F. K. LeGoues, APL 53, 2555 (1988).
- [4] B.S. Meyerson, F.K. LeGoues, T.N. Nguyen, D.L. Harnage, APL 50, 113 (1987).
- [5] S.M. Sze, VLSI Technology (McGraw-Hill, New York, 1988).

Chapter 9

Polysilicon Waveguides for Optoelectronics Integrated Circuits

9.1 Introduction

The ability of Si-based electronics to achieve higher data rates while maintaining low power consumption is critically limited by existing interconnection technology. This limitation has driven the investigation of integrated optical interconnection in Si. Optical interconnection offers a low power-consumption, low-skew, high-bandwidth alternative to standard electrical interconnection. The obstacles facing the implementation of optical interconnection in Si are its apparent exotic nature, the need for emitters and detectors at $\lambda = 1.3\mu\text{m}$ or $1.55\mu\text{m}$ in Si, and the lack of design rules that would make optical interconnection accessible to circuit designers. In order to develop an optical interconnection scheme that closely follows existing electrical interconnection methods, we are investigating waveguides consisting of polysilicon (polySi) clad with deposited SiO_2 . The polySi/ SiO_2 materials system allows several layers of interconnection, similar to existing multi-level-metal, and uses processing techniques available in standard Si integrated circuit fabrication.

While our work with polySi waveguides is unique, the investigation of Si as a waveguide material started at least as early as 1985 [1]. Since that time a number of waveguide technologies have been considered for Si interconnection; however, each approach requires a significant change from existing circuit layout considerations. The published work centers primarily on the use of SOI (Silicon On Insulator) material [2, 3, 4, 5, 6, 7], which requires the optical interconnection to occupy the same level of Si as the electronic devices. This combination of devices and interconnection on a single layer limits the real estate available for devices and requires the use of regrowth techniques for the integration of emitters and detectors.

Other waveguide designs—including ARROW (Anti-Resonant Reflector Optical Waveguide)[8], glass waveguides on Si [9], and lightly-doped Si layers [1]—face more serious limitations. Fabrication of multi-layer ARROW is possible [10], but only

planar geometries have been demonstrated. Glass and lightly-doped Si waveguides provide only small index contrasts and, therefore, require large cross-sectional dimensions. PolySi waveguides avoid all of these problems: multiple layers of polySi/SiO₂ can be deposited, no regrowth is required for integration, and small waveguide dimensions are feasible because of the large index contrast (3.5/1.5 for polySi/SiO₂). For single-mode waveguides, polySi thicknesses of 0.2 μ m and waveguide widths of 0.6 μ m have been designed [11].

No work to our knowledge has been carried out using polySi as a waveguiding medium. This neglect of polySi/SiO₂ can be attributed to reports that polySi absorbs at wavelengths typically used for optical communication (1.3 and 1.5 μ m). The published absorption measurements are near 1000dB/cm at these wavelengths [12, 13]. Scattering due to surface imperfections and grain boundaries are thought to limit the usefulness of polySi as a lightguiding material. We have begun a systematic investigation of these claims, and this chapter details our initial results.

9.2 Experimental Methods

To assess the losses in polySi waveguides we fabricated waveguides from deposited polySi, annealed amorphous Si, and BESOI (Bond and Etchback Silicon On Insulator) materials. The materials provide variations in surface roughness, crystalline quality, and absorption that allow us to determine the relative loss contributions from the different loss sources. All of the waveguides tested were of the buried strip geometry. The core of the strip was either polySi or crystalline Si; the cladding in all cases was deposited SiO₂. The fabrication sequence for the polySi guides consisted of LPCVD deposition of 3 μ m of SiO₂ on a Si substrate, followed by LPCVD deposition of 1mm of core (polySi at 625C or amorphous Si at 560C or 580C). CMP was performed on several of the 625C samples to reduce the roughness of the polySi surface. Samples (including BESOI) were then plasma etched in SF₆ to transfer the strip pattern, and clad with an upper layer of SiO₂ approximately 1 μ m thick. Finally, the samples were annealed at 600C for 16 hours to transform the amorphous Si samples into polySi.

Each waveguide sample consisted of 20 8 μ m wide guides. These waveguides are multimode, but the information determined concerning polySi waveguide performance is applicable to single-mode waveguides. Reducing the waveguide dimensions will, however, change the interaction of the guided mode with the waveguide surfaces. The optical mode of smaller waveguides extends further from the core and the light intensity at the waveguide surface is greater. The increased light intensity at the waveguide surfaces increases the amount of light lost to surface imperfections. The most critical step in the waveguide preparation is facet production. Si, unlike GaAs, is not easily cleaved. Researchers have successfully cleaved (100) Si by thinning the Si substrate to 90 μ m before cleaving [15] and have also successfully cleaved (110) oriented Si on perpendicular (111) crystal planes [16]. To maintain compatibility with integrated circuit substrates we limit ourselves to unthinned, (100) Si substrates. We have developed a polishing technique that produces excellent facets repeatably and with high yield. The polishing technique follows TEM sample preparation using a

tripod polisher [17]. Using this technique we achieve standard deviations in output power of only 3% in measurements over 20 waveguides of the same width.

To perform the cutback measurements, waveguides of different lengths were prepared and the transmission of $\lambda = 1.55\mu\text{m}$ light through the waveguide was measured. We use a laser diode source coupled into an optical fiber to inject light into our waveguides. The fiber feeds into a 90-10 power splitter: 90% of the laser power goes to the waveguide, 10% goes to a detector that monitors the input power. The 90% arm of the splitter terminates in a conically tipped optical fiber mounted on a piezoelectrically controlled 3-axis translation stage. The fiber is butt-coupled into the waveguide under test, which is mounted on an x-ray goniometer and 3-axis translation stage allowing control of six degrees of freedom. Using two CCD cameras and an optical power meter, we can image the light scattered from the surface of the waveguide, image the light exiting the output facet of the waveguide, and measure the power out of the waveguide.

9.3 Results

The 625C polySi waveguides exhibit the highest loss (77dB/cm), the 560C annealed amorphous Si loss is noticeably lower (35dB/cm), and the BESOI has losses of less than 1dB/cm (this is the lower limit of detection of our measurement). The loss measurements are summarized in Table 9.1. Images of the surface of the polySi waveguides during testing showed light scattering at the rough surfaces of the waveguide. SEM investigation revealed the rough nature of the polySi surface. To quantitatively assess the magnitude of the surface roughness we used Specular Reflectance (SR) and Atomic Force Microscopy (AFM) measurements.

Sample	RMS Roughness (nm)	Measured Loss (dB/cm)	Calculated Loss (dB/cm)
BESOI	--	1.0	--
560°C	3.7	37.0	1.5
580°C	14.9	71.0	24.0
625°C	20.1	77.0	43.6
625°C CMP	6.8	35.0	5.0
Δ Loss (dB/cm)		42.0	38.6

Table 9.1: Loss and surface roughness measurements.

Specular reflectance is related to the rms surface roughness by the following equation [18]:

$$R/R_o = \exp - (4\pi \cos\phi \frac{\sigma}{\lambda})^2 \quad (9.1)$$

where R is the measured reflectance, R_0 is the reflectance of a baseline sample (a Si wafer in this case), ϕ is the angle of incidence of the measured beam, σ is the rms surface roughness, and λ is the wavelength of the incident beam. This relation holds under the condition that the rms roughness is much smaller than the wavelength of the incident light. Figure 9.1 shows the square of the reflectance of crystalline Si, 625C polySi, and 560C annealed amorphous Si plotted against the wavelength of the incident illumination. The 560C sample exhibits a spectrum similar to that of the crystalline Si sample, indicating a smooth surface, while the reflectance of the 625C sample is greatly reduced by its rough surface. The SR data provides rms roughness values of 4.5nm and 19.5nm for the 560C and 625C samples respectively. Direct AFM measurement of the surface roughness gives values of 3.5nm for the 560C sample and 20.1nm for the 625C sample; these values agree well with the SR measurements. AFM roughness data for all of the samples are given in Table 9.1.

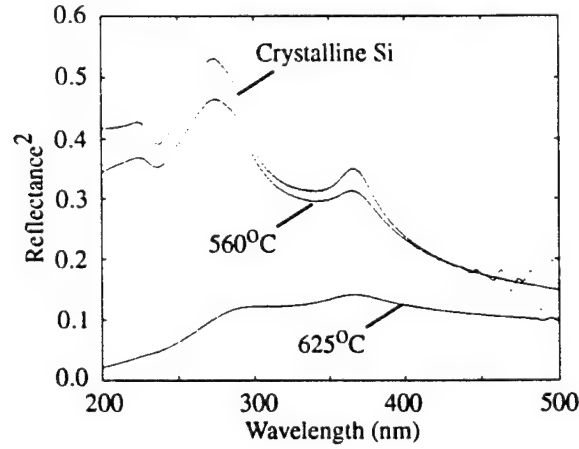


Figure 9.1: Spectral Reflectance data for crystalline Si, 560C and 625C polySi. The 560C sample exhibits reflectance similar to that of crystalline Si, indicating that its surface is less rough than the polySi deposited at 625C.

To determine the relative contribution of loss from the surface roughness, we follow an analysis developed by Tien [14]. From a knowledge of the modal characteristics of the waveguide [19], Tien's analysis gives an expression for the loss due to scattering at the waveguide surface:

$$\alpha = A^2 \left(\frac{1}{2} \frac{\cos^3 \theta}{\sin \theta} \right) \left(\frac{1}{t_g + \frac{1}{q} + \frac{1}{p}} \right) \quad (9.2)$$

In this expression θ is the angle of the rays propagating in the waveguide, $1/p$ and $1/q$ are the penetration depths of the mode into the cladding (in our symmetric case $p = q$), t_g is the guide thickness, and A is a measure of the surface roughness [20]. The relation for A is given by:

$$A = \frac{4\pi}{\lambda_2} (\sigma_{12}^2 + \sigma_{23}^2)^{1/2} \quad (9.3)$$

where σ_{12} and σ_{23} are the rms roughness of the polySi/SiO₂ interfaces at the top and bottom of the waveguide respectively and λ_2 is the wavelength in the core material.

We use simplifying assumptions to estimate the contributions of scattering. First we consider only slab waveguides (edge roughness is neglected). Second, we assume that the roughness of the lower interface between the polySi and SiO₂ is negligible. Third, we assume that we measure only the power in the fundamental mode. The last assumption is based on the high loss of higher order modes, which makes their contribution to the total output power negligible. Analytic considerations additionally show that only the fundamental mode can be coupled out of the polySi/SiO₂ structure [21].

Using the AFM surface roughness values we estimate scattering losses of 43.6dB/cm and 5.0dB/cm for the 625C and 625C CMP samples, respectively. The calculation results are summarized in Table 9.1. Surface scattering cannot account for all measured loss, however it does account for the difference in measured loss for the 625C and 625C CMP waveguides. The measured difference is 42.0dB/cm and the calculated difference is 38.6dB/cm. The larger measured difference may be due to edge roughness, which will be worse for samples with rough surfaces due to photolithographic pattern transfer of the surface roughness to the waveguide walls. The agreement between the measured and calculated values shows that surface roughness is a dominant source of loss in polySi waveguides.

To determine the bulk microstructure contributions to the total loss, it is necessary to remove surface scattering loss from the total measured loss. Figure 9.2 shows the measured and calculated losses as a function of surface roughness. Subtracting the calculated scattering loss from the total loss gives an estimate of the bulk loss for each sample. Figure 9.3 shows the dependence of this estimated bulk loss on deposition temperature. The 625C deposition exhibits the lowest loss. The bulk loss of the 580C sample is markedly higher, while the 560C sample shows losses similar to the 625C sample. By controlling the grain size through the deposition temperature one can optimize the performance of polySi as a light guiding material.

In conclusion, we have measured the losses in polySi waveguides and found them to be two orders of magnitude lower than the published absorption data for polySi. Control of the surface roughness of the polySi is critical to achieving low losses. PolySi deposited at 625C and polished by CMP exhibits losses of 35dB/cm compared to losses of 77dB/cm measured for unpolished 625C polySi. The reduction in loss correlates well with calculated losses by surface scattering. Estimates of bulk losses for the polySi waveguides show a dependence of the loss on the film deposition temperature.

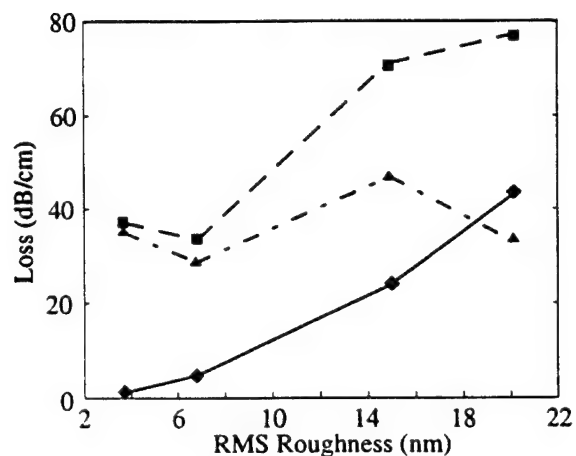


Figure 9.2: Measured loss (squares), calculated loss due to surface roughness (diamonds), and estimated bulk loss (triangles) as a function of surface roughness. The estimated bulk loss is determined by subtracting the calculated loss from the measured loss. Samples (from left to right) are 560C, 625C CMP, 580C and 625C. Differences in estimated bulk loss are attributed to microstructural effects.

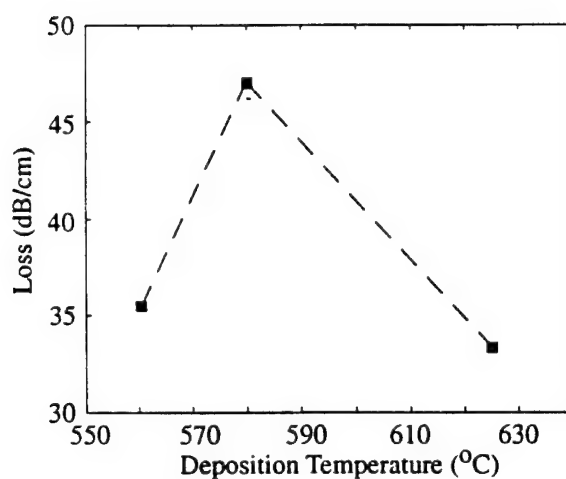


Figure 9.3: Estimated bulk loss dependence on deposition temperature.

Bibliography

- [1] R. A. Soref and J. P. Lorenzo, IEEE J. of Quant. Electron. QE-22, 873 (1986).
- [2] B. N. Kurdi, D. G. Hall, Opt. Lett. 13, 175 (1987)
- [3] B. L. Weiss, G. T. Reed, S. K. Toh, R. A. Soref, F. Namavar, IEEE Phot. Technol. Lett. 3, 19 (1991).
- [4] J. Schmidtchen, A. Splett, B. Schuppert, and K. Petermann, Electron. Lett. 27, 1486 (1991).
- [5] R. M. Emmons, B. N. Kudi, and D. G. Hall, IEEE J. of Quant. Electron. 28, 157 (1992).
- [6] A. Rickman, G. T. Reed, B. L. Weiss, and F. Namavar, IEEE Phot. Technol. Lett. 4, 633 (1992).
- [7] R. A. Soref, E. Cortesi, F. Namavar, and L. Friedman, IEEE Phot. Technol. Lett. 3, 22 (1991).
- [8] Y. Kokbun, T. Baba, T. Sakaki, Electron. Lett. 22, 892 (1986).
- [9] R. Adar, Y. Shani, C.H. Henry, R. C. Kistler, G. E. Bonder, and N. A. Olsson, Appl. Phys. Lett. 58, 444 (1991).
- [10] S. Asakawa, Y. Kokubun, M. Ohyama, and T. Baba, Elect. Lett. 29, 1485 (1993).
- [11] D. Lim, M. S. Thesis, Massachusetts Institute of Technology, 1994.
- [12] W. B. Jackson, N. M. Johnson, and D. K. Biegelsen, Appl. Phys. Lett. 43, 195 (1983).
- [13] R. E. Jones, Jr., S. P. Wesolowski, J. Appl. Phys. 56, 1701 (1984).
- [14] P. K. Tien, Appl. Opt. 10, 2395 (1971).
- [15] L. S. Yu, F. Guan, Q. Z. Liu, and S. S. Lau, Appl. Phys. Lett. 66, 2016 (1995).
- [16] K. Bernhard-Hofer, A. Zrenner, J. Brunner, and G. Abstreiter, Appl. Phys. Lett. 66, 2226 (1995).
- [17] J. Benedict, R. Anderson, and S. J. Klepeis, MRS Symp. Proc. 254, 121 (1992).

- [18] K. L. Chiang, C. J. Dell'Oca, F. N. Schwettmann, J. Electrochem. Soc. 126, 2261 (1979).
- [19] H. Kogelnik in Guided-Wave Optoelectronics, ed T. Tamir (Springer Verlag, New York, 1988).
- [20] R. G. Hunsperger, Integrated Optics: Theory and Technology (Springer Verlag, New York, 1985).
- [21] B. L. Weiss and G. T. Reed, Opt. and Quant. Electron. 23, 1061 (1991).

Appendix A

Papers and Talks

A.1 Papers

"The Mechanisms of Electronic Excitation of Rare Earth Impurities in Semiconductors", I. N. Yassievich and L. C. Kimerling, *Semiconc. Sci. Technol.* 7, 1 (1993).

"IC Compatible Processing of Si:Er for Optoelectronics", F. Y. G. Ren, J. Michel, Q. Sun-Paduano, B. Zheng, H. Kitagawa, D. C. Jacobson, J. M. Poate, and L. C. Kimerling, *Mater. Res. Soc. Symp. Proc.* 298, 415 (1993).

"The Physics and Application of Si:Er for Light Emitting Diodes", J. Michel, F.Y.G. Ren, B. Zheng, D.C. Jacobson, J.M. Poate, and L.C. Kimerling, *Materials Science Forum* Vol. 143-147 (Trans Tech Publications, Aedermannsdorf, Switzerland 1994) p. 707 (1993).

"Fluorine-Enhanced Si:Er Light Emission", F. Y. G. Ren, J. Michel, D. C. Jacobson, J. M. Poate, and L. C. Kimerling, *Mater. Res. Soc. Symp. Proc.* (1993).

"Erbium-Doped Silicon for Integrated Optical Interconnects", L. C. Kimerling, D. M. Koker, B. Zheng, F. Y. G. Ren, and J. Michel, in: "Semiconductor Silicon/1994," ed. by H. R. Huff, W. Bergholz, and K. Sumino, (The Electrochemical Society, Pennington, NJ, 1994) p. 486.

"Room Temperature Sharp Line Electroluminescence at $\lambda = 1.54\mu m$ from an Erbium-doped, Silicon Light-emitting Diode", B. Zheng, J. Michel, F. Y. G. Ren, D. C. Jacobson, J. M. Poate, and L. C. Kimerling, *Appl. Phys. Lett.* 64, 2842 (1994).

"Erbium-doped Silicon for Integrated Optical Interconnects", L. C. Kimerling, D. M. Koker, B. Zheng, F. Y. G. Ren, and J. Michel, *Proceedings of the 4th Biennial Department of Defense Fiber Optics and Photonics Conference (AFCEA, Washington, 1994)*.

"Erbium in Silicon: A Defect System For Optoelectronic Integrated Circuits," J. Michel, J. Palm, F. Gan, F.Y.G. Ren, B. Zheng, S.T. Dunham, and L.C. Kimerling, Proceedings to the 18th International Conference on Defects in Semiconductors, ICDS, Sendai, Japan, July 23-28, 1995.

"Electronic Structure of Erbium Centers in Silicon," F. Gan, L.V.C. Assali, and L.C. Kimerling, Proceedings to the 18th International Conference on Defects in Semiconductors, ICDS, Sendai, Japan, July 23-28, 1995.

A.2 Talks

- 2/9/93 Lionel C. Kimerling, 'Silicon Optoelectronics',
DARPA Optics Review, Hilton Head, SC
- 4/12/93 INVITED TALK: Lionel C. Kimerling, 'IC Compatible Processing
of Si:Er for Optoelectronics', MRS Conference, San Francisco, CA
- 5/27/93 Lionel C. Kimerling, 'Optical Interconnects in Silicon',
AT&T Bell Labs, Murray Hill, NJ
- 6/23/93 Bo Zheng, 'Integration of Silicon LED/Waveguide Structures
for $\lambda = 1.54\mu\text{m}$ Operation', EMC Conference, Santa Barbara, CA
- 7/20/93 INVITED TALK: Jurgen Michel, 'The Physics and Applications of
Si:Er for Light Emitting Diodes', International Conference on Defects
in Semiconductors, Gmunden, Austria
- 8/31/93 INVITED TALK: Lionel C. Kimerling, 'Why, How and When:
Silicon Optical Interconnects', AGED Workshop, Austin, TX
- 10/20/93 INVITED TALK: Lionel C. Kimerling, 'Materials Challenges for
Electronics and Optoelectronics', NSF, Future of Electronic Materials,
Washington, DC
- 11/29/93 Lionel C. Kimerling, 'Silicon Optoelectronics',
AFOSR Research Review, Boston, MA
- 12/2/93 Frank Ren, 'Fluorine-Enhanced Si:Er Light Emission',
MRS Fall Meeting, Boston, MA
- 12/6/93 INVITED TALK: Jurgen Michel, 'The Physics and Application of Si:Er
for Light Emitting Diodes', AT&T Bell Laboratories, Murray Hill, NJ
- 2/14/94 Lionel C. Kimerling, 'Photonic Materials Research at MIT',
Rockwell Science Center Meeting, MIT, Cambridge, MA
- 3/17/94 Lionel C. Kimerling, 'Silicon Light Emitting Diodes', Hanscom AFB, MA
- 3/22/94 Lionel C. Kimerling, 'Erbium-doped Silicon for Integrated Optical
Interconnects', DoD Fiber Optics and Photonics Conference, McLean, VA
- 5/23/94 INVITED TALK, Lionel C. Kimerling, 'Silicon Optical Interconnection',
Electrochemical Society Meeting, San Francisco, CA
- 6/15/94 Lionel C. Kimerling, 'Silicon Microphotonic Technology',
ARPA Optics Review, Monterey, CA

- 6/24/94 Jurgen Michel, 'Er-O and Er-F Reactions in Silicon',
Electronic Materials Conference, Boulder, CO
- 7/22/94 INVITED TALK, Lionel C. Kimerling, 'Light Emission from Si:Er
System', 13th Symposium on Alloy Semiconductor Physics and
Electronics, Izu-Nakaoka, JAPAN
- 10/17/94 INVITED TALK, Lionel C. Kimerling, 'Silicon: A New Material
for Photonics', First International Conference on Materials for
Microelectronics, Barcelona, Spain
- 10/25/94 INVITED TALK, Jurgen Michel, 'Rare Earth Doped Silicon Emitters',
AVS (American Vacuum Society) 41st National Symposium, Denver, CO
- 11/1/94 INVITED TALK, Lionel C. Kimerling, 'Silicon Optical Interconnection',
Georgia Institute of Technology, Atlanta, GA
- 11/22/94 INVITED TALK, Lionel C. Kimerling, 'Silicon Optical Interconnection',
University of Massachusetts, Amherst, MA
- 12/1/94 INVITED TALK, Lionel C. Kimerling, 'Erbium-implanted Silicon LEDs',
Materials Research Society Fall Meeting, Boston, MA
- 12/12/94 INVITED TALK, Jurgen Michel, 'Erbium Doped Silicon Light Emitters',
IEDM (International Electron Devices Meeting), San Francisco, CA
- 2/ 7/95 INVITED TALK, Lionel C. Kimerling, 'Silicon LEDs',
SPIE Conference, San Jose, CA
- 4/17/95 INVITED TALK, Jorg Palm, 'Defects and Future Silicon Technology',
Materials Research Society Spring Meeting, San Francisco, CA
- 5/21/95 INVITED TALK, Lionel C. Kimerling, 'Materials Challenges for ULSI',
Electrochemical Society Meeting, Reno, Nevada
- 6/22/95 Bo Zheng, 'Process Integration of MOSFETs and Erbium-Doped Silicon
Light-Emitting Diodes,' Electronic Materials Conference,
Charlottesville, VA
- 6/22/95 Jim Foresi, 'Characterization of Crystalline and Polycrystalline Silicon
Waveguides for Optical Integration and Interconnection,'
Electronic Materials Conference, Charlottesville, VA
- 7/27/95 Jurgen Michel, 'Erbium in Silicon: A Defect System For Optoelectronic
Integrated Circuits', 18th International Conference on Defects in
Semiconductors, ICDS, Sendai, Japan
- 8/1/95 Lionel C. Kimerling, 'Silicon Microphotonic Technology',
ARPA Review Meeting, Big Sky, Montana
- 8/17/95 INVITED TALK, Lionel C. Kimerling, 'Silicon: A New Material for
Photonics,' Texas Instruments Colloquium, Dallas
- 9/1/95 INVITED TALK, Lionel C. Kimerling, 'Silicon Microphotonic Materials
Technologies,' KSEA International Technical Conference on Globalization
and Technology Frontiers, San Francisco, CA
- 11/8/95 INVITED TALK, Jurgen Michel, 'Er doped Si for LED's',
ESF Workshop on Electroluminescence in Silicon, Munich, Germany

DISTRIBUTION LIST

addresses	number of copies	
DR. RICHARD A. SOREF ROME LABORATORY, EROC 50 SCOTT DRIVE HANSCOM AFB, MA 01731-2909	5	
MASSACHUSETTS INSTITUTE OF TECH MATERIALS SCIENCE & ENGINEERING TECHNOLOGY	5	
ROME LABORATORY/SUL TECHNICAL LIBRARY 26 ELECTRONIC PKY ROME NY 13441-4514	1	2
ATTENTION: DTIC-OCC DEFENSE TECHNICAL INFO CENTER 8725 JOHN J. KINGMAN ROAD, STE 0944 FT. BELVOIR, VA 22060-6218	2	4

***MISSION
OF
ROME LABORATORY***

Mission. The mission of Rome Laboratory is to advance the science and technologies of command, control, communications and intelligence and to transition them into systems to meet customer needs. To achieve this, Rome Lab:

- a. Conducts vigorous research, development and test programs in all applicable technologies;
- b. Transitions technology to current and future systems to improve operational capability, readiness, and supportability;
- c. Provides a full range of technical support to Air Force Materiel Command product centers and other Air Force organizations;
- d. Promotes transfer of technology to the private sector;
- e. Maintains leading edge technological expertise in the areas of surveillance, communications, command and control, intelligence, reliability science, electro-magnetic technology, photonics, signal processing, and computational science.

The thrust areas of technical competence include: Surveillance, Communications, Command and Control, Intelligence, Signal Processing, Computer Science and Technology, Electromagnetic Technology, Photonics and Reliability Sciences.